THE UNIVERSITY OF CHICAGO

CONTROL OF SPIN QUBITS IN A CLASSICAL ELECTRONICS MATERIAL

A DISSERTATION SUBMITTED TO
THE FACULTY OF THE PRITZKER SCHOOL OF MOLECULAR ENGINEERING
IN CANDIDACY FOR THE DEGREE OF
DOCTOR OF PHILOSOPHY

BY
ALEXANDRE BOURASSA

CHICAGO, ILLINOIS
MARCH 2021

To my family.

Table of Contents

List of Figures

List of Tables

ACKNOWLEDGMENTS

None of the work presented in this dissertation would have been possible without the support of my mentors, colleagues, friends, and family.

First, I would like to thank my advisor David Awschalom. I am amazed every day at David's ability to simultaneously manage a world-class research group while consistently building new large-scale collaborative efforts. Between his recent roles in building an exceptional PME quantum faculty team, establishing the Chicago Quantum Exchange, and his involvement in the National Quantum Initiative, David's contributions to the quantum physics community are truly astounding. Through my years in the PME, I've witnessed David's unwavering trust in his student demonstrated every day through his constant and dependable support of grass root scientific efforts. Additionally, David's uncanny ability to quickly identify and contextualize the most impactful elements of a study has helped me and others home-in to the most critical aspect of our research. Overall, I feel very lucky to have been part of the Awschalom group and it has afforded me opportunities and support that is scarcely available anywhere else.

Thank you to all the members of my thesis committee (Andrew Cleland, David Schuster, and Giulia Galli) for the thoughtful discussion throughout this PhD journey. Having such an awesome quantum faculty team made the University of Chicago the obvious place for me to choose when deciding where to pursue my graduate studies.

I would also like to thank all my colleagues in the Awschalom group whom I've had the chance to work with through the years.

First and foremost, I would like to give special thanks to Chris Anderson. Chris and I have worked closely together since day one, and the work presented in this dissertation would not have been possible without him. I am continuously impressed by his unwavering dedication to science (extending well past normal hours!), his natural inclination/ability to initiate and sustain collaborative endeavor (both within and outside the group), and the depth and breadth of his mastery of the scientific literature. These skills have made Chris a critical asset to the whole group and I am convinced they will serve him well in the years to come. I could not have asked for a better scientific partner. Above all, thank you Chris for your friendship through the years.

I would also like to give a shoutout to the original LL213 team! Thanks to Alex Crook. In addition to being our in-house nanofabrication expert; Alex's scientific persistence, meticulous attention to details, and insistence on deconstructing complex scientific issues into clear and simple ideas have been invaluable to the SiC efforts. Your expertise combined with your approachability, humor, and humility makes working with you a true pleasure. Thanks to Kevin Miao. Starting from an empty lab, Kevin and I, built together the core experimental infrastructure underlying every result presented in this thesis. Thank you for your contributions and, between all of the recent "singles" SiC results, I am glad to see that our early time investments to build out these setups finally paid off.

I would also like to give a special shoutout to Elena Glen and Cyrus Zeledon who have recently picked up these SiC experiments and are currently pushing them to the next level! When I first met Elena (through her REU in the group), I was impressed by how quickly she integrated into the project and took charge of it. I am convinced that your drive, your capacity to communicate and reach out to others, and your leadership abilities will take you far. Thank you for being so easy to work with. Cyrus is the latest addition to our SiC dream team! So far, I've been very impressed by all of your hard work throughout the development of our new optical setup. I have really enjoyed working with both of you and I can't wait to see what you accomplish next!

Thanks to all the members of the SiC team whom I've had the chance to work with. Sam Whiteley, with whom I've had the pleasure to work with on the mechanical spin drive experiments. Your diligence and enthusiasm in the cleanroom are truly impressive, and you've made my day more than once with your ability to get yourself in, and occasionally out of, awkward social interactions! Gary Wolfowicz, whose work UV enhancement of divacancies established a basis for some of the charge dynamic studies presented in this thesis. Your dependable critiques made you a great person to test ideas against. I'm glad I finally got you to listen to at least one Quebec track! Peter Mintun, my fellow Villager whose puns and jokes were always a refreshing breath of joy. Your scientific knowledge combined with your financial acumen always makes for incredibly interesting conversation, and your humor made it all the more enjoyable. Berk Diller, whose negotiation skills are a force to be reckoned with. Your inquisitive mind makes you a great person to talk to and I've always appreciated your heteroclite conversation starters ranging from science fiction to scientific trivia. And Sam Bayliss, the much needed LL213 parental supervision whom we scared away into a prosperous land of molecules. Sam's organization, clarity of thought, and depth of knowledge never ceases to amaze me. Thank you for the scientific insight you've passed along to me and thank you for being such a great person to work with!

Thank you to the previous generation of the SiC students who laid the groundwork for us and were early mentors. You guys are legends! Paul Klimov, whose wits and work intensity as a scientist are only matched by his patience as a teacher. The 2 weeks "Klimov Classes", I was lucky enough to attend before you left, single-handedly allowed me to get up to speed with what I needed to know about optics and spins! Little did I know then that you would once again be the one to show me the way into a whole new field of science at Google. I am thankful for both of these opportunities to learn from you and I hope our paths cross again in the future! David Christle who's work on single divacancy defects was a direct predecessor to the results presented here. Thank you for your eternal wisdom, technical know-how, as well as your always entertaining social media posts. As an early supporter of Python in the group, I think you'd be proud of our software infrastructure and experimental automation. Will Koehl, who pioneered SiC defects and always had something interesting to say about all matters of conversations. Thanks for bringing me on to your project when I joined the group and allowing me to make my very first experimental contribution.

Thanks to all the other post-docs and older graduate students who have given me so many tips and tricks to make my experiment work better. Joseph Heremans, who I was lucky enough to meet in the PME labs before he so seamlessly transitioned to lead a new and impressive effort at ANL. Thanks for transmitting the group's accumulated knowledge. Brian Zhou, whose calm and friendly demeanors are only matched by the depth of his expertise. Thanks in particular for teaching me how to work with cryogenic equipment. Charlie de las Casas whose brief excursion into the land of SiC was a welcome infusion of know-how to our nascent setups. Thanks for teaching me all about spin control sequences and being a great person to work with. A huge thanks to Paolo Andrich, Chris Yale, and Andrew Yeats, who all thought me so much about research and were generally awesome people to have around the labs.

Thanks to my fellow classmates who join the PME (IME at the time) with me in the early days of the department. Special shoutouts to my teammates in the Awschalom group. Masaya Fukami, your theoretical prowesses are extraordinary and I can only ever aspire to learn half of the things you know about physics. Paul Jerger, you are the best of us. Your intellect is only matched by your humility and kind spirit. Thanks for being such an awesome lab mate and I truly hope I get to work with you again in the future. Erzsebet Vincent, your creative mind infused the group with a wealth of originality and out-of-the-box thinking. I particularly enjoyed the occasional spoken words and theatrical group meeting presentation. The way you mesh science and arts is truly unique and amazing. A special shoutout to my other quantum classmates: Hung-Shen Chang, Joel Grebel, and Youpeng Zhong. It was an honor to study with all of you and thanks for being awesome ERC basements neighbors!

Thanks to the whole Awschalom team at the PME and at ANL. To Jacob and Michael, thank you for being such awesome stewards of NSpyre and for continuing to grow it in the community-oriented spirit in which it was designed. To Leah, Yeghishe, Nazar, and Sean, our current powerhouse of a postdoc team, thanks for all the great scientific discussions and I look forward to following from afar all the various projects you've put together. To the next generation of graduate students: Grant, Jonathan, Ben, Pratiti, and Joseph, the lab is in good hands with you all and I can't wait to see what you accomplish next! And thank you to all the undergraduates who have contributed either directly or indirectly to the work presented here. In particular, thanks to Agnetta Cleland, Thomas Kiely, Hope Lee, Ananya Pillutla, and Marie Wesson, with whom I've had the chance to work more closely.

I would also like to thank our collaborators. Thanks to Mykyta Onizhuk, He Ma, and all the Galli group, whose theoretical insights were critical to this work. Thanks to N.T. Son, Takeshi Ohshima, Michael Flatté, Adam Galli, and their respective teams, who provided valuable SiC materials, electron irradiations, and scientific discussions.

More broadly thank you to all the folks I've met here in Chicago (in the PME and PSD departments, as well as outside the university). You've all made my experience here phenomenal and I hope to meet you all in person again (once the global pandemics subsides) very soon. Thanks in particular to Cody Castle. I couldn't have asked for a better roommate. Thanks for showing me everything that Chicago has to offer. You are a true renegade! And to my other roommates over the years (Lucio, Arthur, and Hugo), thanks for all the memories! It was great to get to know every one of you. Thank you to my climbing friends (Kyle, Yu, Jeff, Jamie, Marissa, Jiayi, Will, Trista, Audrey, Anna, Sasha, Olivier, and Hannes). It was great to learn this sport from all of you. A special thanks to Etienne and Laureen Dumur, who both were awesome and reliable climbing partners and friends. I really hope I get to visit you on the Old Continent sometime soon!

Thanks to all the mentors I've had over the years. Thank you to Jack Sankey and Lily Childress at McGill for introducing me to the field of quantum science. I will forever be grateful to you both for taking me into your groups and teaching me so much about experimental physics. And thanks to all my teammates there who built the experiments in these labs from the ground up (Christoph, Tina, Simon, Abeer, Max, Erika, Zach, Chris, and many more!). Thanks to Dalziel Wilson and Tobias Kippenberg's team at EPFL for an awesome summer of research in Switzerland. And thank you to the whole team at Google Quantum AI and especially to Paul Klimov and Julian Kelly. It's been really great to learn all about scaling superconducting systems and how research is done in an industry setting. I hope to get the chance to meet you all in person at some point!

Thank you to my friends in Quebec who have always been there for me. Thanks to my electrical engineering friends (Phillipe, Viviana, David A., David Z., Annie, Sasha, Karim) who've made my undergraduate experience so enriching and enjoyable. Thanks to all the friends and mentors whom I've met through my years of gymnastics. A special thanks to my long-time friend "Big Alex" and his whole family who have been, through the years, like a second family to me.

To Kate, thank you for always pushing me toward a better life balance. You are smart and kind, and with a little bit of patience, I know you will get to see, taste, and experience all that the world has to offer. I will always cherish the memories we have made in Chicago (and around the globe!) and I'm excited to see what lies ahead! And finally, thanks to my entire family for always being there for me. My only regret through this adventure is to have been so far from all of you for so long. Thank you to my late grandparents who taught us the value of hard work, integrity, and looking out for one another. Thank you to Lysane and Yannick. I know I will always be able to count on you both and I am so proud of the people you have become. And thank you to my parents, Marie-José and Jean, for guiding me through life and for instilling in me a deep appreciation for knowledge and rational thinking. Your reliable and unconditional support is the foundation that underpins everything I do. You all are my home and I embrace every moment I get to spend with you.

ABSTRACT

Over the last century, innumerable technological advances in communication and computation have resulted from combining the abstract notion of digital information (bits) with its physical realization in semiconductors. We now stand at the crossroad of a new information paradigm based on the abstract notion of the quantum bit (qubit) which proposes fundamentally new ways of exchanging information and performing computations. We must now find physical systems which can physically implement these qubits.

Here we will discuss one of these systems: the neutral divacancy (VV^0) in silicon carbide (SiC). Throughout this dissertation, we will explore both the spin and optical properties of the VV^0 which makes this defect system particularly well suited for quantum communication applications.

In particular, we will argue that SiC is a technologically advantageous host due to its prevalence in the semiconductor electronics industry. This enables the integration of VV^0 in scalable classical electronic devices such as p-i-n diodes. We demonstrate that this simple integration can allow us to engineer the electrical environment around the defect. This results in a narrow and widely tunable optical interface and deterministic control of the defect charge state.

Moreover, this dissertation also explores nuclear spins as critical resources to build robust quantum memories and multi-qubit systems. Here we will show how isotopic engineering of the host material can be used to both increases the coherence of the VV^0 electronic spin and at the same time maximize the number of available nuclear memories.

Overall, we believe that the VV^0 in SiC is particularly well suited for building quantum communication and quantum repeater devices. Accordingly, the work in this dissertation is framed from that perspective and addresses some of the leading challenges and opportunities related to the realization of quantum communication devices in a scalable semiconductor material.

CHAPTER 1

INTRODUCTION

1.1 Classical information

1.1.1 Theory of Communication

At Bell Labs in 1948, Claude Shannon, one of the century's most influential mathematician and electrical engineer, proposed the idea of disentangling the abstract notion of information from its physical implementation [121]. Originally called "Theory of Communication" and later dubbed "Information Theory", Shannon's idea suggested that information was any means by which a receiver could distinguish a particular message (coming from a sender) from the "set of all possible messages". As he saw it:

> *"The fundamental problem of communication is that of reproducing at one point either exactly or approximately a message selected at another point."* - Claude Shannon, 1948

He suggested that messages, independent of their physical representation (telegraph, telephone calls, written words, etc...), could conveniently be expressed as sequences of 0s and 1s which he called "bits" (an abbreviation for "binary digits" he borrowed from a colleague). This was a powerful idea since digital messages were inherently robust to noise in the communication channel. This theory, along with Shannon's many other ideas (such as boolean algebra for switching circuits and error correction codes), was prescient and led the way towards the new Information Age.[1]

---

[1] It is remarkable to note how these problems (or some version of them at least) are still very relevant today and at the center of cutting-edge research into quantum technologies. This speaks to the fundamental nature of the questions Shannon was putting forward. Moreover, because most of the work presented in this dissertation is aimed at solving quantum communication problems, it is inspiring to note that the luminaries that brought forth the digital world were also concerned with the problem of communication.

Although mostly conceptual at the time, digital technologies are now ubiquitous and heterogeneous data of all kinds (sounds, images, videos, Ph.D. dissertations, etc...) are now regularly reduced to a bunch of 0s and 1s. This abstract "bit" representation is then mapped onto physical states such as magnetic domains (hard drive), charge (RAM/SSD), or electromagnetic waves (light in fiber optics, radio transmission, wifi, ...) for example. This means that there exists a one-to-one correspondence between the original physical quantities of the message, the abstracted sequence of 0s and 1s, and the physical implementation of that "bit string". It is truly astounding to think of the myriads of ways in which the same information is regularly physically encoded!

One might ask: Can *any* physical state be encoded and transmitted to a receiver using a string of bits? The answer is: surprisingly no! In fact, when using physical systems that obey the laws of quantum mechanics, we can build states that could never be transmitted to a receiver using only classical bits. We will explore this idea in more detail in section 1.3.1.

1.1.2 Computing with bits

Besides using bits for encoding and transmitting messages, one can also use them to compute. In fact, roughly 12 years before Shannon's seminal paper, Alan Turing laid the foundation for computing with discrete machines [134].

Today, most computers (more precisely "classical computers") use solid-state semiconducting electronic circuits to perform computations. In this type of computer, bits are physically represented by voltages at different nodes in the circuit, and gates are implemented using transistors (more on semiconducting devices in section 2.3).

In general, classical algorithms can be expressed in terms of Boolean operators that operate on 1 or 2 bits at a time. A set of Boolean operators is said to be functionally complete if (and only if) we can combine the operators in that set to express any Boolean function. Such functionally complete set include the {NAND} and {NOR} sets [122]. Here let's use the NAND operator for illustration.

1.1.3 The universal NAND gate

The NAND operation is one that returns 0 if both inputs are 1 and 1 otherwise. This gate can be implemented using any switching element but is most commonly built out of transistors (shown in Fig 1.1).

The NAND gate is said to be universal because, in theory, any Boolean function can be expressed using only that operation. Another way to say this is that, by combining NAND gates we can implement any two-bits truth table, and by extension, any N-bits truth table as well. Following Turing's definition of the "a-machine", we can combine such a circuit with a memory (which can in fact be built out of NAND gates as well (SR latch)!) to implement any Turing computable algorithms.

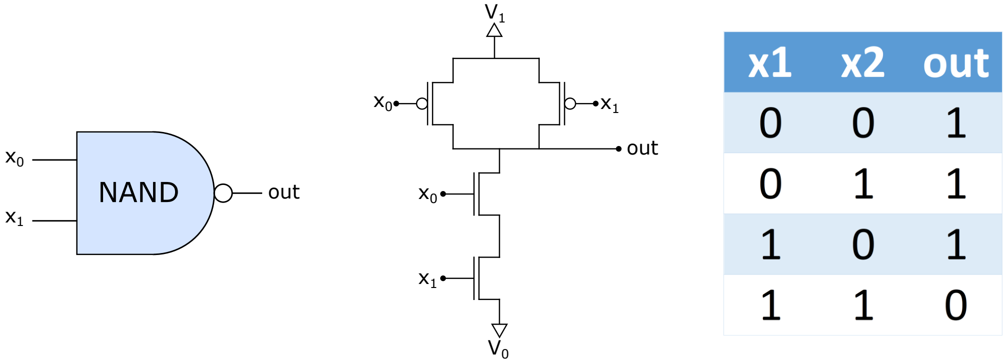

x1	x2	out
0	0	1
0	1	1
1	0	1
1	1	0

(a) (b) (c)

Figure 1.1: (a) Symbol used to represent the universal NAND gate. (b) CMOS circuit implementing a NAND gate (c) Truth table of the NAND gate

1.1.4 Classical computing in the language of linear algebra

The mathematics of switching circuits are usually (and much more usefully!) written in terms of Boolean algebra operation. However, in an analogy to its quantum operation counterparts, let's try to ask how classical operations could be expressed in the language of linear algebra. In that framework, one could express the binary states as:

$$0 : \begin{pmatrix} 1 \\ 0 \end{pmatrix} \qquad 1 : \begin{pmatrix} 0 \\ 1 \end{pmatrix} \tag{1.1}$$

And then expand to larger numbers of bits using the tensor product operation ($\otimes$). For example, a two-qubit state would look like:

$$x_1 x_2 : \begin{pmatrix} \overline{x_1} \cdot \overline{x_2} \\ \overline{x_1} \cdot x_2 \\ x_1 \cdot \overline{x_2} \\ x_1 \cdot x_2 \end{pmatrix} \tag{1.2}$$

where x_i are boolean variables, "$\cdot$" denotes the AND operator and the overbar denotes negation. We note that there is always one (and only one) entry with a 1 and every other entry is 0 (it's a very inefficient representation!).

Now we can start to write operators as matrices. For example, we could write the NAND operator as:

$$\text{NAND} : \begin{pmatrix} 0 & 0 & 0 & 1 \\ 1 & 1 & 1 & 0 \end{pmatrix} \tag{1.3}$$

Interestingly, this is not by itself sufficient to write an arbitrary circuit in this linear algebra formulation of classical logic. This is because, in general, there is a "trivial" operation that is generally omitted from the universal set: the copy operator. Such an operation acts on a single bit and expands the Hilbert [2] space:

---

[2] Mathematically a Hilbert space represents a "complete vector space with a defined inner product operation which specifies the square of the norm". This is formally broken down into 9 specific criteria (8 defining a vector space, plus the inner product requirement), but roughly speaking, this simply means that a Hilbert space corresponds to a set of objects with defined operations (addition, inner product, and multiplication by scalars) which behaves in a "standard" way (associativity, commutativity, etc...). Hilbert

$$\text{COPY} : \begin{pmatrix} 1 & 0 \\ 0 & 0 \\ 0 & 0 \\ 0 & 1 \end{pmatrix} \tag{1.4}$$

Alternatively, one may think that we could simply start with more copies of the inputs. However, in general, it is not possible to know in advance how many copies we would need (because of considerations related to the halting problem).

From this formulation, we can make a few interesting observations and comparison with the linear algebra of quantum mechanics (reader unfamiliar with the mathematics of quantum mechanics can refer to section 1.2.2 for a brief overview):

1. States in this formulation are deterministic (ie entries always 1 or 0), this is in stark contrast to quantum mechanical states which are generally probabilistic. One could think of expanding this framework to probabilistic classical bits (p-bits) [32], but even then, the probability described by such a system would be critically different from the probability amplitudes of a quantum state.

2. Operations in that formulation are not unitary. In particular, the size of the Hilbert space is not conserved. This means that classical operations are not in general time-reversible. For instance, from the output of a NAND gate, we cannot recover its input.

3. States can explicitly be copied exactly (using the COPY operator). This is, again, in contrast to quantum states which can never be copied (according to the no-cloning theorem [151]).

---

spaces are often used in quantum mechanics to represent the set of all possible qubit states.

1.2 Quantum information

Quantum information is sometimes used to refer specifically to the branch of mathematics interested in extending the original ideas of Shannon's information theory to deal with the realities of quantum physics. However, in this chapter, I will broaden that definition and discuss more generally some of the ideas which form the basis of quantum technologies including quantum computation, quantum communications, and quantum sensing.

1.2.1 The quantum bit: qubit

First, let's take a look at the fundamental unit of quantum information: the qubit.

Just like the classical bit, the qubit is an abstract representation of a system that can be in exactly two distinct states (let's label them 0 and 1). Qubit states are often denoted using the Dirac notation (or "Bra-Ket" notation) as $|0\rangle$ and $|1\rangle$. It's important to remember that these are simply labels that we give to our state in order to abstract away the physical system. In later chapters, we will in fact substitute these labels for more physically meaningful ones (such as $\{|m_s = -1\rangle, |m_s = 0\rangle\}$ or $\{|\uparrow\rangle, |\downarrow\rangle\}$).

Unlike its classical counterpart, however, a qubit is a fundamentally probabilistic unit of information. This means that, in general, a qubit state must express both the probability that the qubit will take the value $|0\rangle$ when measured and the probability that it will take the value $|1\rangle$. More precisely, a qubit state is fully specified by the "probability amplitude" of both the $|0\rangle$ and $|1\rangle$ state.

1.2.2 The mathematics of the qubit

More formally, any pure quantum state can be described as unit length vectors in an N-dimensional Hilbert space, where N is the number of possible orthogonal states[3]. This

---

[3] Note that we will focus here on discrete quantum state expressed in the language of matrix mechanics. For continuous quantum variables, such as position and momentum, the linear algebra can be substituted

means, that any arbitrary quantum state can be expressed as:

$$|\Psi\rangle = \sum_{i=0}^{N} c_i |i\rangle \qquad c_i \in \mathbb{C} \tag{1.5}$$

Where we must satisfy the constraint $\sum |c_i|^2 = 1$ (unit length). Additionally, since all physical measurable quantities are expressed as $\langle\Psi| A |\Psi\rangle$ the global phase for $|\Psi\rangle$ is unphysical and can thus be chosen arbitrarily (ie $\left(e^{-i\phi} \langle\Psi|\right) A \left(e^{i\phi} |\Psi\rangle\right) = \langle\Psi| A |\Psi\rangle$ implies that for all intents and purposes $e^{i\phi} |\Psi\rangle$ is the same as $|\Psi\rangle$). Since all complex numbers can be expressed as 2 real numbers and taking into account the unit length and arbitrary phase, we find that quantum states in an N-dimensional Hilbert space can be fully described by 2N-2 real numbers.

For a qubit (N=2):

$$|0\rangle = \begin{pmatrix} 1 \\ 0 \end{pmatrix} \qquad |1\rangle = \begin{pmatrix} 0 \\ 1 \end{pmatrix} \tag{1.6}$$

and any single-qubit states can thus be written as:

$$|\Psi\rangle = \alpha |0\rangle + \beta |1\rangle = \begin{pmatrix} \alpha \\ \beta \end{pmatrix} \tag{1.7}$$

where α and β are complex numbers. Since $|\alpha|^2 + |\beta|^2 = 1$ (pure state), without loss of generality we can express $|\alpha| = \cos(\theta/2)$ and $|\beta| = \sin(\theta/2)$. Then, choosing the global phase such that $\alpha \in \mathbb{R}$, we can write:

$$|\Psi\rangle = \cos\left(\frac{\theta}{2}\right) |0\rangle + e^{i\phi} \sin\left(\frac{\theta}{2}\right) |1\rangle \qquad \theta \in [0, \pi],\ \phi \in [0, 2\pi[\tag{1.8}$$

This form makes it clear that there is a unique mapping between any qubit state and a point

---

by Schrödinger's wave formulation. This formulation is essentially equivalent to the matrix mechanics when the matrix dimension goes to infinity. We may also use the continuous formulation in later chapters.

on the surface of a unit sphere (see 1.2). This geometrical representation is called Bloch sphere.

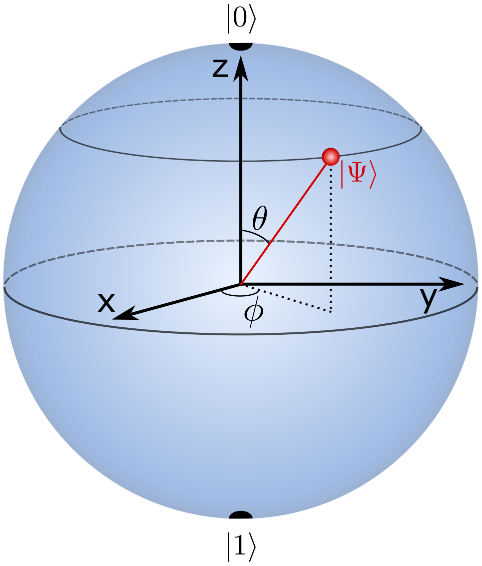

Figure 1.2: Visual representation of the qubit vector using the Bloch sphere

Once we have represented our state as a vector, we can now start to describe operators which, in the language of linear algebra, would be expressed as matrices. Interestingly, the concepts of operation and measurements in quantum mechanics are intimately related. For example, in a spin-half system the same matrix that represents a π-rotation around the x-axis (σ_x), can also be used to express a measurement of the magnetic moment along the x-axis ($\langle\Psi|\sigma_x|\Psi\rangle$) (more generally for arbitrary angle one would exponentiate σ_x...). Thus, operators serve the dual purpose of describing both the time-evolution of the quantum state (or gates) and specifying quantities that could in principle be measured. Additionally, two important properties of operators in quantum mechanics are:

1. Operators that describe the time evolution of pure states must also be unitary. This ensures both that:

   (a) the state remains of unit length in the Hilbert space.

   (b) the inner product of states is conserved (implying that states which are orthogonal at one time, will remain orthogonal forever). This means that quantum operations in closed systems are always reversible.

   (c) the dimension of the Hilbert space is conserved before and after the operation.

2. Operators are generally Hermitian which implies real eigenvalues. This ensures that measured quantities are always expressed as real values.

A common set of matrices used to described single-qubit operations are the Pauli matrices. Along with the identity operator, these form a set which can be linearly combined to construct any other arbitrary Hermitian matrix:

$$\begin{aligned} \sigma_0 = \mathbb{I} &= \begin{pmatrix} 1 & 0 \\ 0 & 1 \end{pmatrix} & \qquad \sigma_1 = \sigma_x &= \begin{pmatrix} 0 & 1 \\ 1 & 0 \end{pmatrix} \\ \sigma_2 = \sigma_y &= \begin{pmatrix} 0 & -i \\ i & 0 \end{pmatrix} & \qquad \sigma_3 = \sigma_z &= \begin{pmatrix} 1 & 0 \\ 0 & -1 \end{pmatrix} \end{aligned} \tag{1.9}$$

Another important single qubit gate (1Q gate) is the Hadamard gate which maps $|0\rangle \rightarrow |+\rangle = \frac{|0\rangle+|1\rangle}{\sqrt{2}}$ and $|1\rangle \rightarrow |-\rangle = \frac{|0\rangle-|1\rangle}{\sqrt{2}}$

$$H = \frac{1}{\sqrt{2}} \begin{pmatrix} 1 & 1 \\ 1 & -1 \end{pmatrix} \tag{1.10}$$

All of these are of course only special cases of the more general rotation operator, which can, in general, be written as:

$$ROT_{\hat{n}}(\alpha) = R_{\hat{n}}(\alpha) = \exp\left[-i\,\alpha\,\hat{n}\cdot\hat{\sigma}\right] \tag{1.11}$$

Besides 1Q gates, one also needs two-qubit gates (2Q gates) two build arbitrary quantum circuits. A few interesting examples fall in the class of controlled unitaries ($C_1(U_2)$) which effectively apply a unitary U to qubit 2 if and only if qubit 1 is $|1\rangle$

$$C_1(U_2) = \begin{pmatrix} 1 & 0 & 0 & 0 \\ 0 & 1 & 0 & 0 \\ 0 & 0 & u_{00} & u_{01} \\ 0 & 0 & u_{10} & u_{11} \end{pmatrix} \qquad \text{for} \quad \mathrm{U} = \begin{pmatrix} u_{00} & u_{01} \\ u_{10} & u_{11} \end{pmatrix} \tag{1.12}$$

A notable example of this type of 2Q gates is the CNOT gate

$$\begin{gathered} C_1NOT_2 = C_1(\sigma_{x,2}) = \begin{pmatrix} 1 & 0 & 0 & 0 \\ 0 & 1 & 0 & 0 \\ 0 & 0 & 0 & 1 \\ 0 & 0 & 1 & 0 \end{pmatrix} \\ C_2NOT_1 = C_2(\sigma_{x,1}) = \begin{pmatrix} 1 & 0 & 0 & 0 \\ 0 & 0 & 0 & 1 \\ 0 & 0 & 1 & 0 \\ 0 & 1 & 0 & 0 \end{pmatrix} \end{gathered} \tag{1.13}$$

Or more generally the C_iROT_j which can rotate qubit j based on qubit i. We should also note that there may be instances where it is more natural to apply U when qubit 1 is $|0\rangle$. These would have a slightly different matrix representation, but they are, of course, just as valid.

Finally, just like there were different sets of classical gates that were deemed universal, we can also construct sets of quantum gates that can be used to construct any quantum circuits with arbitrary precision. For example, one could pick the following discrete set of gates: H, CNOT, $R_{\hat{n}}(\frac{\pi}{8})$ - and use it to approximate any arbitrary circuit.

1.2.3 Quantum circuits

Classical circuits are often depicted as a network of gates linked with vertices that represent the flow of information from one part of the circuit to the next (see figure 1.3). Quantum circuits can also be represented in a similar way. However, in the case of quantum circuits gates are "mostly" unitary (with the exception of initialization and readout operations) which means that the number of qubits is conserved. For that reason, it can conveniently be represented as a series of parallel lines representing the evolution of specific qubits (see figure 1.3).

1.3 Classical vs quantum information

We have already highlighted a few similarities and differences between classical and quantum information. In this section, we want to add a few more comparisons to highlight some of the novel aspects of quantum states with respect to their classical analogs.

1.3.1 Quantum communication

When explaining the differences between classical and quantum physics, many concepts (e.g. superposition, interference, uncertainty, etc...) are used to describe the unique nature of quantum states. In this section, I will focus on the ideas of superposition and entanglement to try to show how quantum states differ from classical ones in practice.

In particular, we can go back to Shannon's ideas, and try to see what it is about quantum states which cannot be reduced to a string of binary digits and sent over a classical channel.

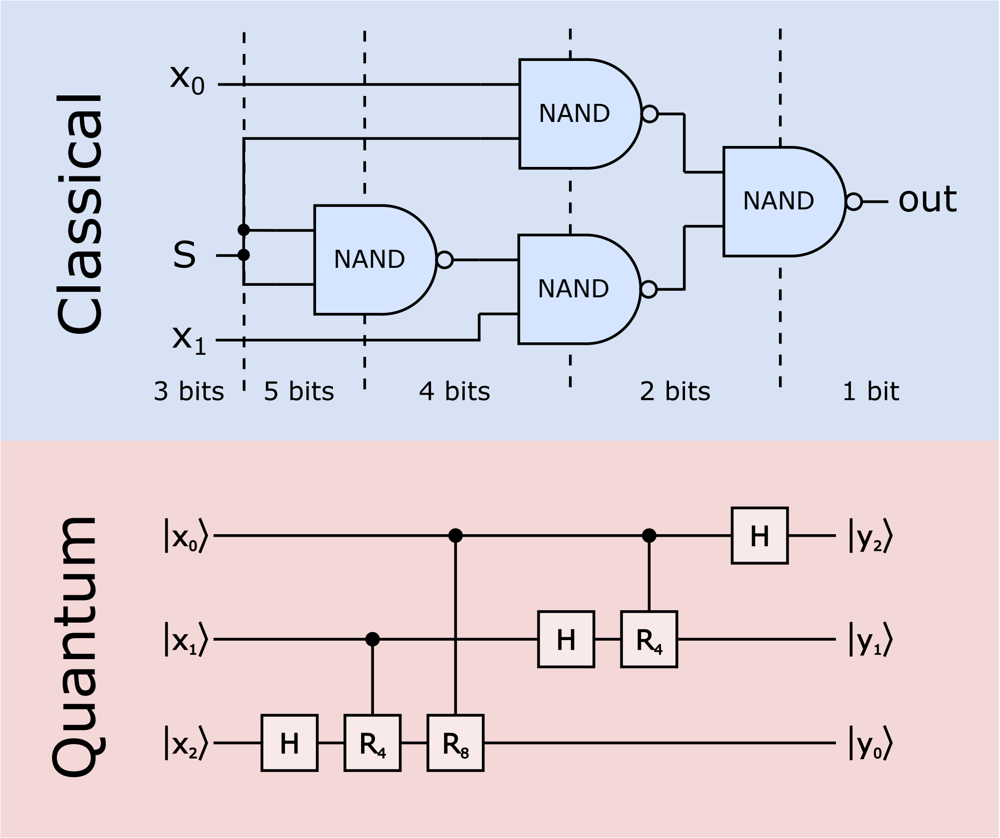

Figure 1.3: (Top) Classical circuit showing a multiplexer circuit made entirely of COPY (represented by the dot at the junction of wires) and NAND operations. Here we can see that the effective number of bits changes through the circuit.(Bottom) [Image source [19]] Quantum Fourier Transform circuit showing the "parallel line" representation of quantum circuits. In this representation, the number of qubits never changes.

Superposition

To begin, let's consider the idea of superposition. In particular, we can consider two scenarios:

1. What if we want to send a known arbitrary quantum state?
2. What if we want to send an unknown arbitrary quantum state?

In the first case, we assume that we know the quantum state we have (ie we know all of the complex probability amplitudes characterizing that state). In this case, one could simply send all of these amplitudes with arbitrary precision through a classical channel and reproduce the state exactly on the other side. Note, that this can be accomplished for any arbitrary superposition of states. So, does that mean we can always use classical information to encode our quantum state? Well, no. And to see this let's move on to our second case.

In the second case, we assume we find ourselves in possession of a single copy of an unknown quantum state. In this case, we have no way to know exactly the value of all the probability amplitudes. If we try to measure the state we will simply get a single sample of the probability distribution which would not give enough information to reproduce the state in any meaningful way.

Entanglement

Another way to distinguish classical information from quantum information is by talking about entanglement. I would argue this is perhaps the best way to exemplify how quantum states are different from classical ones. The key ideas here are the inseparability and non-locality of quantum states.

In particular, let's assume that we prepared a two-qubit state in the $|00\rangle + |11\rangle$ state (forget about state normalization for now...). Now we want to transmit one of the qubits (say qubit 2) to a receiver while keeping the other (qubit 1). The question is: can we accomplish this by transmitting some information to the receiver using only a classical communication channel and do so while maintaining the correlations between qubit 1 and qubit 2 (so that measurement are still probabilistic, with a 50-50 chance of yielding 0 or 1, but always yields the same results for both qubits)? The answer is that we cannot!

Indeed if we tried to send for example the following classical information: "Qubit 2 is currently in the $|0\rangle + |1\rangle$ state", the state that we will produce after the receiver gets this message is going to be $(|0\rangle + |1\rangle) \otimes (|0\rangle + |1\rangle)$ which is a very different state then $|00\rangle + |11\rangle$. At the end of the day, this is because the state $|00\rangle + |11\rangle$ is not separable which means that it cannot be fully described by looking only at one qubit at a time (this is in stark contrast to classical information which is always separable).

This inseparability also implies that the state is delocalized in space which means that components of a single state can be very far from one another and still be part of a single system.

1.3.2 Exponential complexity of quantum states

Another way to think about how quantum information differs from classical information is to refer to the exponential nature of the quantum Hilbert space. This is particularly relevant for applications such as quantum computation and it explains why classical computers cannot efficiently reproduce arbitrary quantum algorithms. In particular, one can discuss this complexity by counting how many "numbers" are necessary to represent a state made up of n bits/qubits.

For a n-bits classical state, you simply need n integer (0 or 1). In fact, you could even represent the entire state with a single integer between 0 and 2^n! This is because classical bits have a discrete set of valid states (0 or 1).

For a n-qubits pure quantum state, however, you need $2^n - 1$ complex number or $2 \cdot (2^n - 1)$ real number to fully specify the state. This means that the quantity of "numbers" that you need to fully specify a state becomes exponentially large as you add more qubits. This is in essence why arbitrary quantum algorithms with more than a few qubits are so hard to compute on classical computers.

In short, even a relatively small number of qubits can encode an exponentially complex state (requiring a large number of scalars to store), whereas the number of scalars needed to encode a classical system must increases linearly with the size (in bits) of that system.

CHAPTER 2

SEMICONDUCTING TECHNOLOGIES

In addition to being the birthplace of Shannon's Information Theory, Bell Labs was also a pioneer in developing the practical building block of all modern electronics: the transistor. In 1947, John Bardeen and Walter Brattain first demonstrated that they could use a piece of germanium between two gold contacts to produce electrical amplification. The idea was later refined by William Shockley who suggested that similar behavior could also be achieved at the junction of layers of semiconductors with different types of impurities. A few years later, Tanenbaum et al. [130] succeeded in making the first n-p-n transistor by producing high-quality single crystals with a rate varying growth technique.

Initially one of the main motivations behind developing a silicon-based transistor was to improve reliability, especially at higher temperatures. However, it became clear over the years that there was another major advantage: the ease of growing native silicon oxide. This eventually led to the realization of MOSFET (metal-oxide-semiconductor field-effect transistor). This technology and its descendant (such as the FinFET), made it possible to scale down the size of transistors, which eventually led to the modern nanometer-scale technologies.

2.1 Semiconductors

So, what is so special about semiconductors? As their name implies, semiconductors occupy a special place in the spectrum of materials at the border between an insulator and a conductor.

Insulators are materials that do not allow current to flow within them. In most insulators (excluding Mott insulators), electrons are tightly bonded to specific atoms or atomic bonds and would require large energy to leave these locations. In the language of band theory, we can say that insulators have a completely full valence band, no electrons within their conduction band and that these two bands are separated by a large energy gap.

Conductors, on the other hand, are materials that allow current to flow. There is generally no gap (or negligible gap) between the valence band and the conduction band. In such a material, electrons occupy non-localized states which enables them to move freely.

Finally, semiconductors are somewhere in between. In particular, they generally have a non-negligible (but relatively small) gap between the valance and conduction bands. This means, that the effect of dopants and external electric fields can be sufficient to tilt the balance more toward conducting or isolating states.

In particular, the electrical properties of semiconductors are often entirely dominated by amazingly few impurities in the crystal. In fact, any dopants concentration significantly greater than the intrinsic carrier concentration (for Si $n_i = 1.45 \cdot 10^{10}$ cm^{-3} [39]) should be considered important to describe the electrical properties. For instance, a crystal of silicon ($5 \cdot 10^{22}$ (Silicon atoms)/cm^3), with only 10^{13} (Boron atom)/cm^3 would be considered p-doped. For comparison, we could scale atoms to be the size of a ping pong ball and used a red ball to represent a boron dopant and white balls to represent the silicon atoms. Then, this ratio of atoms would be like placing a single red ball in a volume of 100 Olympic swimming pools filled to the rim with white balls!

In the case of semiconductors, that single “red boron ball” completely changes the electrical characteristics of the whole material! This is one of the reasons why materials engineering of semiconductors is so sensitive and complex.

2.2 Band theory

The physics of solid-state materials is often understood using band diagrams . In this section, we aim to provide a “broad line” derivation of what these bands correspond to. Our goal will be to provides sufficient background to understand the origins of the band diagram and what they physically represent.

2.2.1 The origins of bands: Periodic potential

At its core, band theory is a method for computing the energy of electrons in a solid-state crystal (in particular we will focus on the electrons in the outermost shells of the atoms). By crystal, we mean a periodic arrangement of atoms. Here we can take any finite size arrangement of atoms (call it a unit cell) and tile it across space to create an infinite and periodic lattice. For the purposes of this section, we will simplify the problem to solve for the energies of non-interacting electrons (i.e. we will ignore electron-electron correlations).

Then our goal will be to get an idea of how one could compute the energy levels associated with this solid-state crystal. In short, we want to find the eigenvalues associated with the Schrödinger equation. This is reminiscent of the "particle in a box" or "simple harmonic oscillator" problems, but we now have a more complex (and 3 dimensional) potential energy landscape $V(\vec{r})$. One could think of the potential landscape as an infinite arrangement of quadratic wells each centered at the position of one of the atoms.

Of course, the reality is slightly more complex. For example, if we have different types of an atom (e.g.: Si and C) the wells associated with each may be of different depth.

Whichever way we construct the potential of a single lattice site, one thing is certain: since the lattice of atoms is periodic the potential landscape will also itself be periodic. In fact, by symmetry, we can also state that the wavefunction associated with this energy landscape will also be periodic in magnitude (but importantly it can vary in phase!). Thus, without loss of generality, this problem is generally solved by using a Bloch function as an ansatz for the wave function:

$$\psi(\vec{r}) = e^{i\vec{k}\cdot\vec{r}}u(\vec{r}) \tag{2.1}$$

Once we made this assumption, we generally need to make additional approximations to solve the energies. These sometimes come in the form of analytical simplification (e.g. the tight bonding model or the nearly free electron model). These approximations can also be embedded into numerical simulations such as density functional theory (DFT).

Once we have calculated, these energy eigenstates we can plot them as a function of wavevector ($\vec{k}$). If we disregard the momentum value ($\vec{k}$) and are simply interested in what energy levels are possible we can collapse this 3D energy representation into a density of possible energies (called "density of states"). And finally, we can simplify further to draw bands that only distinguish between areas of zero and non-zero density of states.

Finally, we note that these bands can vary over macroscopic space. This may seem like a contradiction with the assumption of the infinite periodicity of the wavefunction. However, importantly, these two statements generally apply to very different length scales (quasi-infinite periodicity at an atomic scale, but no assumed periodicity at larger scales).

2.2.2 Filling up the bands of semiconductors

A charge-neutral pure crystal of semiconductor (e.g. Si or SiC) generally has exactly the right number of electrons to fill up the valance band. So in its lowest energy state (ground state), we would expect a completely full valence band and completely empty conduction band. In this state, the semiconductor is insulating. In practice, however, we always operate at a non-zero temperature which means we are never truly in the ground state. One can compute the number of electrons that will jump from the ground state to the excited state (intrinsic carrier concentration n_i) as [138]:

$$n_i = \sqrt{N_C N_V} e^{\frac{-E_g}{2k_B T}} \tag{2.2}$$

where N_C (N_V) corresponds to the effective density of state of the conduction (valance) band, E_g is the size of the energy bandgap, k_B is the Boltzmann constant and T is the temperature.

Around room temperature (300 K), the n_i of Si is $1.45 \cdot 10^{10}$ cm^{-3} [39]. Amazingly, in 4H-SiC, n_i is almost 20 orders of magnitude smaller[1]! At 300K, n_i of 4H-SiC is $5.64 \cdot 10^{-9}$

---

[1] It still amazes me how big of a difference there is in the n_i of Si and SiC!

cm^{-3} [6]. This is due, in part, to the larger E_g and is one of the reasons why SiC is a good semiconductor for high-temperature and power electronics. Generally, these relatively low intrinsic concentrations (even in Si) by themselves result in very little electron conduction and thus, the semiconductor is considered insulating in this state.

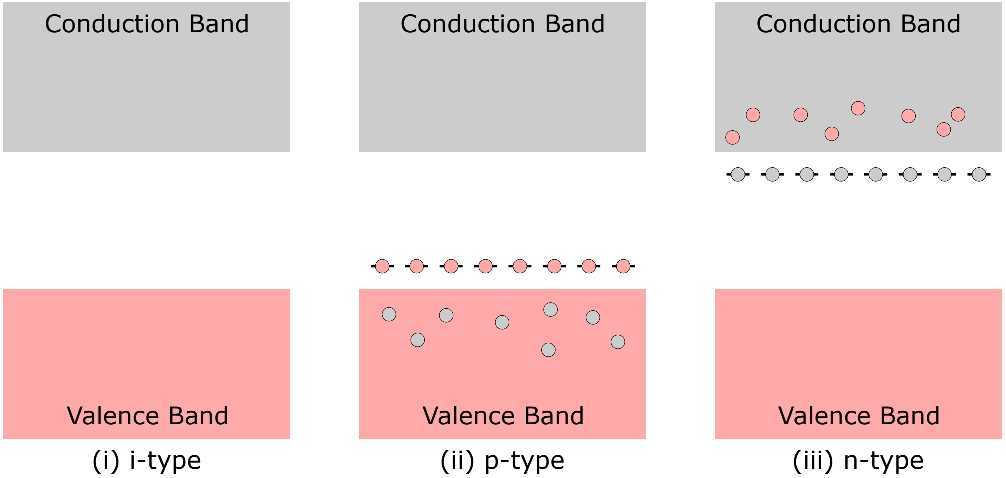

Figure 2.1: **Band diagram of semiconductors.** Red regions represent states filled with electrons and gray regions represent states filled with holes. (i) An intrinsic semiconductor with a valence band filled with electrons and an empty conduction band. This material is insulating because it contains no mobile charge carriers. (ii) p-type semiconductor showing the additional states resulting from the added p-type dopant. Since these states are so close to the valence band electrons are easily thermally excited leaving free holes as charge carriers in the valence band. (iii) N-type semiconductor showing the additional states resulting from the added n-type dopant. Excess electrons from these dopants are easily excited to the conduction band where they can act as charge carriers.

However, interesting changes start to happen when we introduce some defects to the semiconductors. These defects can be intrinsic (e.g. Vacancy complex ($\mathrm{V_{Si}}$, $\mathrm{V_C}$, $\mathrm{V_CV_{Si}}$, etc..)) or extrinsic (e.g. additional dopant atom of Nitrogen, Aluminum, Boron, Phosphorous, etc...). When we add such defects, we are in effect adding new states in which the electrons can now reside (states that were not part of the band diagram of the pure semiconductor crystal).

Certain defects (particularly the dopant atoms) add states close to the edge of the valence (or conduction) band and can trap (or release) electrons at a very low energy cost. These are called acceptors (or donors) and they result in holes easily hopping to the valence band (or electrons easily hopping to the conduction band). Either way, these additional carriers are now free to move in the crystal and result in a conductive material.

In general, semiconductor devices are operated at a temperature where most dopants are ionized thermally. Thus at thermal equilibrium, the following assumptions are usually made:

- In p-type material: the density of holes in the valence band (p_p) is approximately the same as the acceptor dopant density (N_a). The density of electrons in the conduction band (n_p) is very low and is approximately n_i^2/N_a.[2]
- In n-type material: The number of electrons in the conduction band (n_n) is approximately the same as the donor dopant density (N_d). The density of holes in the valence band (p_n) is very low and is approximately n_i^2/N_d.

In section 2.4, we will also treat some relevant cases where these assumptions do not necessarily hold.

2.3 Junction Devices

In this section, we will explore different types of semiconductor devices that can be built by combining layers with different dopings, along with metals and oxides. We will first focus on the simple p-n junction, then will expand our analysis to the p-i-n junction and finally, we will give a cursory overview of a few more interesting devices. We will focus here on specific aspects of junction devices that will underline the work presented in chapter 5. For more information on the basis of junction devices, the reader can also refer to [104, 138].

---

[2] This follows from the fact that $p = N_C \exp\left[\frac{-(E_C-E_F)}{k_BT}\right]$ and $n = N_V \exp\left[\frac{-(E_F-E_V)}{k_BT}\right]$ where the energies are labeled E_C for the conduction band minimum, E_V for the valence band maximum and E_F for the Fermi energy. These relation hold regardless of doping and therefore, $n \cdot p = N_C N_V e^{\frac{-E_g}{k_BT}}$ which is simply n_i^2 (as per equation 2.2). So $n \cdot p = n_i^2$ regardless of doping and $n_p = n_i^2/p_p$

2.3.1 p-n junction diode

When we put a piece of p-doped semiconductor in contact with an n-doped semiconductor we create p-n junction (or p-n diode). In this configuration, two things start to happen:

1. **Diffusion**: Excess electrons from the n-region will tend to diffuse toward the p regions where lower energy empty states are available constantly depletes the conduction band. Pictorially, we can imagine putting (ii) and (iii) from figure 2.1 together and seeing how the "red electron" in the n-type conduction band will tend to diffuse in the empty conduction band of the p-type material and then "fall" to the valence band (conversely one can also think of the holes from the p-type diffusing into the valence band of the n-type material and then "bubbling up" into the conduction band). This diffusion will tend to create a charge imbalance between the two sides of the junction: the p-side will have excess electrons (negatively charged) and the n-side will have excess holes (positively charged).

2. **Drift**: This charge imbalance will create a voltage difference between the two sides of the junction which will tend to force the electron back into the n-type (and the holes back into the p-type).

These two competing effects will eventually reach a thermal equilibrium where the voltage difference between the two sides will cause a drift rate that exactly cancels out the diffusion rate.

Critically, with this voltage difference will come an electric field in the junction. This electric field will force the carriers (electrons and holes) to go to one side of the junction and thus will create and charge carrier depletion inside the junction while leaving ionized atoms as static charges. This depletion region will be critical to the work presented in this thesis.

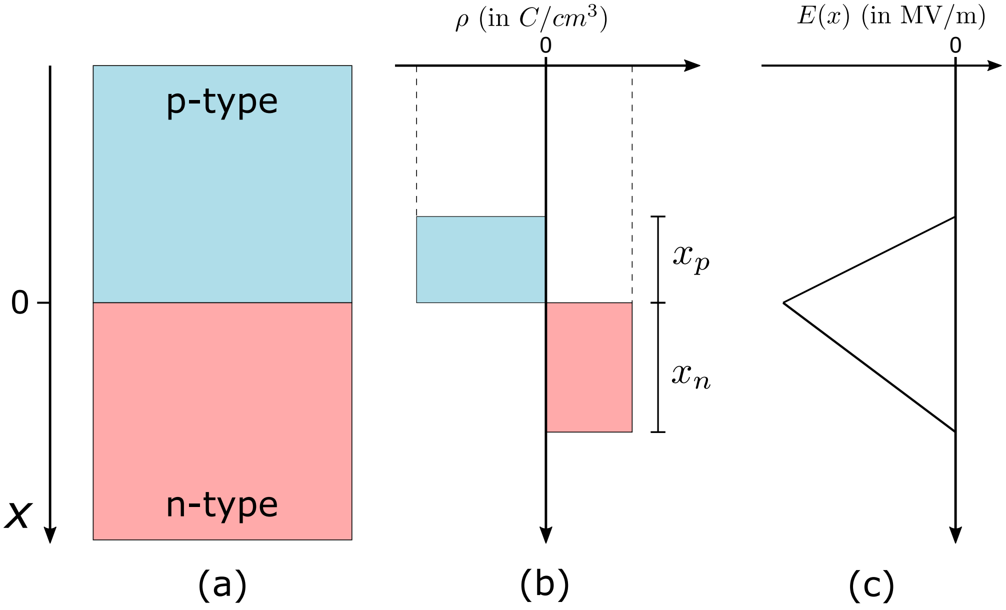

Figure 2.2: **Diagram of a p-n junction.** (a) Layers of the p-n junction with the interface located at x=0 (b) Charge distribution across the device. (c) Electric field distribution across the device.

Built-in voltage

This special equilibrium voltage is called the "built-in voltage" (V_b). Assuming two infinite planes of p and n layers, the problem is essentially 1 dimensional (p-doped material from $x = -\infty$ to 0 and n-doped material from $x = 0$ to ∞). We can then derive V_b as follow.

First, we can write the expected rate of electron diffusing to the p-side (Γ_{diff}):

$$\Gamma_{\text{diff}} = D_e \frac{dn}{dx} \tag{2.3}$$

where $n(x)$ is the concentration of electrons at position x in the junction (see figure 2.2 for illustration) and D_e is the electron diffusion coefficient and is related to the electron mobility (μ_e) by the Einstein relation $D_e = \mu_e k_B T/q$ (where q is the charge of an electron).

Then, we can write the expected rate of drift (Γ_{drift}) as a function of the electric field ($E(x)$):

$$\Gamma_{\text{drift}} = \mu_e n(x) E(x) \tag{2.4}$$

Then setting the drift equal to the diffusion (at equilibrium) we get the electric field as:

$$E(x) = \left(\frac{D_e}{\mu_e}\right)\left(\frac{1}{n(x)}\right)\frac{dn}{dx} = \left(\frac{k_B T}{q}\right)\left(\frac{1}{n(x)}\right)\frac{dn}{dx} \tag{2.5}$$

Finally, we find the built-in voltage by integrating the electric field over all x (integrating until far away from the interface):

$$V_b = -\int_{-\infty}^{\infty} E(x)dx = \left(\frac{k_B T}{q}\right)\int_{-\infty}^{\infty}\left(\frac{1}{n(x)}\right)\frac{dn}{dx}dx = \left(\frac{k_B T}{q}\right)\int_{n(-\infty)}^{n(\infty)}\left(\frac{1}{n}\right)dn \tag{2.6}$$

And since we know that $n(-\infty) = n_p = n_i^2/N_a$ and $n(\infty) = n_n = N_d$, we have

$$V_b = \left(\frac{k_B T}{q}\right)\ln\left(\frac{N_a N_d}{n_i^2}\right) \tag{2.7}$$

At room temperature, and using the doping levels outlined in section 5.3 ($N_d = 5e18cm^{-3}$ and $N_a = 7e18\ cm^{-3}$), we get $V_b \approx 3.2V$.

Importantly, this value only depends on $n(-\infty)$ and $n(\infty)$. Another way to put this is that the Fermi-Level must be equal across the device and thus the built-in potential can also be found by the difference in where the Fermi level lies in the gap of the p- and n-type layers. This will be important in section 2.3.2, where we will be able to use the same V_b derived here for p-i-n devices.

Electric Field

As discussed earlier in this section, the built-in voltage establishes a charge depletion region in the junction. By definition, this charge depletion implies that all the free electrons and holes are swept away leaving behind the ionized dopants (donors and acceptors). This creates regions of non-zeros charge density corresponding to the number of ionized impurities (at room temperature we usually assume that all dopants are ionized).

Then, the electric field in the junction can be easily found by Maxwell's equation:

$$\nabla \cdot \mathbf{E} = \frac{\rho}{\varepsilon} \tag{2.8}$$

where ε is the permittivity in the material and ρ is the charge density where:

$$\rho = \begin{cases} -qN_a & \text{for } \text{-}x_p < x \leq 0 \\ qN_d & \text{for } 0 \leq x < x_n \\ 0 & \text{for } x \notin [\text{-}x_p, x_n] \end{cases} \tag{2.9}$$

where x_p and x_n are the size of the depletion region in the p- and n-type regions.

Therefore, in our 1D problem

$$E(x) = \int_{-\infty}^{x} \frac{\rho}{\varepsilon} dx = \begin{cases} \frac{-qN_a}{\varepsilon} \cdot x & \text{for } \text{-}x_p < x \leq 0 \\ \frac{qN_d}{\varepsilon} \cdot x + K & \text{for } 0 \leq x < x_n \\ 0 & \text{for } x \notin [\text{-}x_p, x_n] \end{cases} \tag{2.10}$$

where $K = \int_{-\infty}^{0} \frac{\rho}{\varepsilon} dx = \frac{-qN_a x_p}{\varepsilon}$. Since $E(x)$ must be continuous at $x = x_n$, we find that $N_d x_n = N_a x_p$. We could also find the total depletion width $W = x_n + x_p$ by solving for $\int_{-\infty}^{\infty} E(x) dx = V_b$ using the E(x) from Eq 2.10 and the V_b found Eq 2.7. We'll leave this as an exercise for the reader, but the solutions are:

$$W = x_p + x_n = \sqrt{\frac{2\varepsilon V_b}{q}\left(\frac{1}{N_a} + \frac{1}{N_d}\right)} \tag{2.11}$$

And thus we know $x_p = W\left(\frac{N_d}{N_a+N_d}\right)$ and $x_n = W\left(\frac{N_a}{N_a+N_d}\right)$. Finally, the maximum amplitude electric field (at x=0) is then:

$$E(0) = \frac{-qN_a}{\varepsilon} \cdot x_p = -\sqrt{\frac{2qV_b}{\varepsilon\left(\frac{1}{N_a} + \frac{1}{N_d}\right)}} \tag{2.12}$$

At room temperature, and using the doping levels outlined in 5.3, we get $E(0) \approx 3.2V$.

2.3.2 p-i-n junction diode

Dopant-free i region

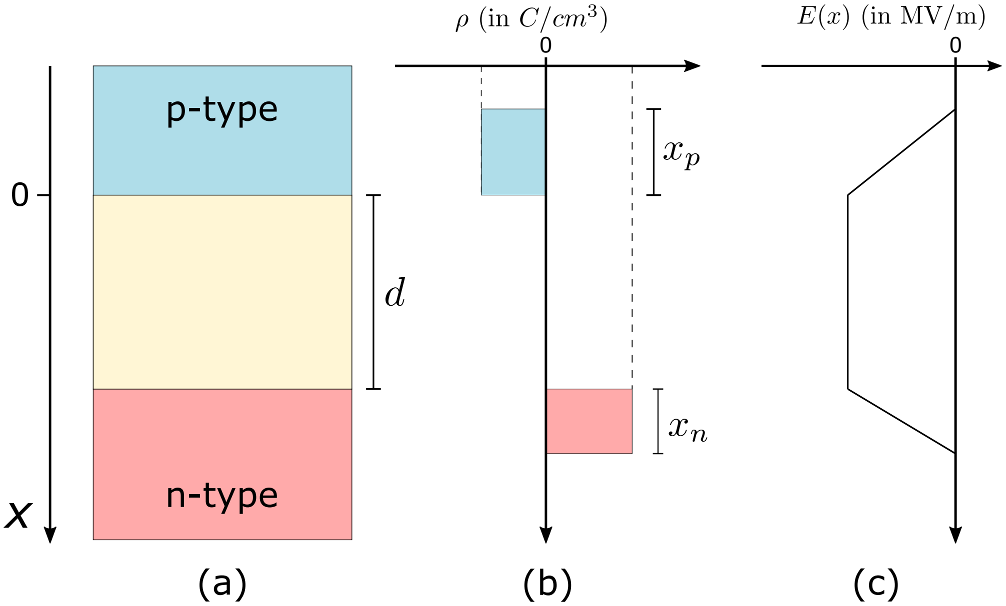

Figure 2.3: **Diagram of a p-i-n junction with no dopants in the i-layer.** (a) Layers of the p-n junction with the interface located at x=0 (b) Charge distribution across the device. (c) Electric field distribution across the device.

Now let's see what happens if we insert a dopant-free layer of thickness d between the p- and n-type layers (let's set the x=0 to be the p-i interface). As mentioned at the end of section 2.3.1, this change will not modify the total built-in voltage V_b. Moreover, since there are no dopants in the i region $\rho = 0$ and the electric field is constant. More specifically, we now have:

$$E(x) = \int_{-\infty}^{x} \frac{\rho}{\varepsilon} dx = \begin{cases} \frac{-qN_a}{\varepsilon} \cdot x & \text{for } \text{-}x_p < x \leq 0 \\ K & \text{for } 0 < x \leq d \\ \frac{qN_d}{\varepsilon} \cdot x + K & \text{for } d \leq x < d + x_n \\ 0 & \text{for } x \notin [\text{-}x_p, d + x_n] \end{cases} \tag{2.13}$$

Again we can use the fact that $-\int_{-\infty}^{\infty} E(x)dx = V_b$ to get an exact solution, but in the cases where d is much greater then W obtained in the p-n section^3 (Eq 2.11) we can effectivelly make the approximations $W \approx d$ and then

$$-V_b = \int_{-\infty}^{\infty} E(x)dx \approx K \cdot d \tag{2.14}$$

So, $K = -V_b/d$ and

$$E(x) = \begin{cases} \frac{-qN_a}{\varepsilon} \cdot x & \text{for } \text{-}x_p < x \leq 0 \\ \frac{-V_b}{d} & \text{for } 0 < x \leq d \\ \frac{qN_d}{\varepsilon} \cdot x - \frac{V_b}{d} & \text{for } d \leq x < d + x_n \\ 0 & \text{for } x \notin [\text{-}x_p, d + x_n] \end{cases} \tag{2.15}$$

Using the doping levels (except for the i-layer which we assume to be dopant free for now) and layer thickness from 5.3, we find that at 300K the electric field is at its largest magnitude in the i-layer where $E(x) = \frac{-V_b}{d} \approx -0.3MV/m$. This is indeed much smaller than the $188MV/m$ expected in a similarly doped p-n junction.

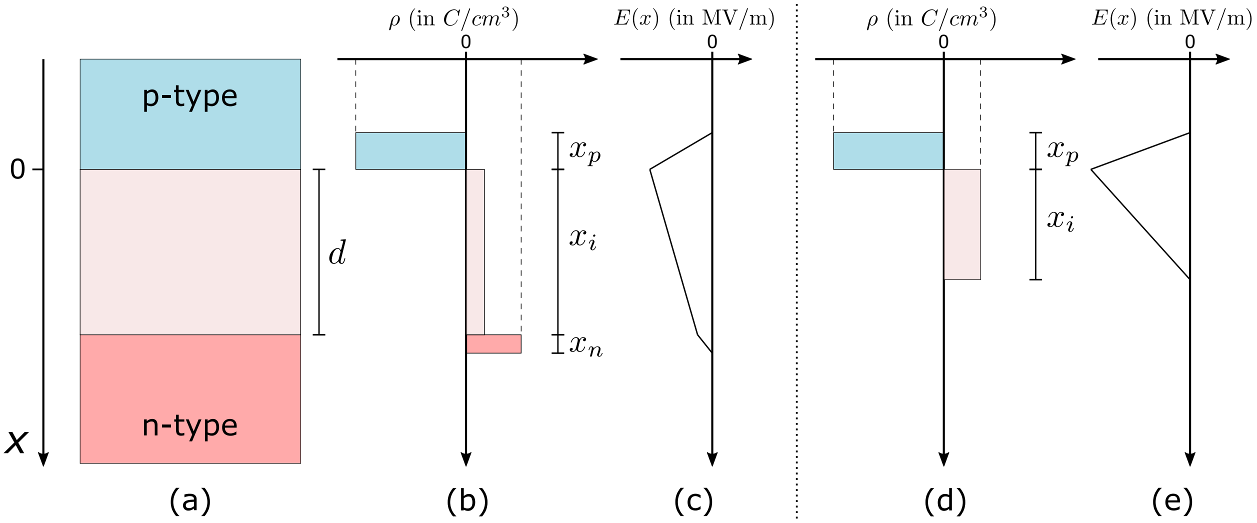

Figure 2.4: **Diagram of a p-i-n junction with some dopants in the i-layer.** (a) Layers of the p-n junction with the interface located at x=0 (b and c) Charge distribution and electric field when the dopant in the i-layer is sufficiently small such that $x_i = d$ (d and e) Charge distribution and electric field when the dopant in the i-layer is sufficiently large such that $x_i < d$.[5]

I-region with accidental doping

In practice, it is prohibitively difficult to grown pure dopant-free layers (especially in a chamber where we just grew highly doped layers). Thus, we now need to consider the more realistic case where the i-layer is slightly doped. For this example, we will assume a slight concentration of n-dopants in the i-layer (since this is what we expect in our samples in section 5), but of course, the reasoning is similar for slight p-type dopants.

In this scenario, there will be some (but not a lot) ionized dopants (or charge density ρ) in the i-layer to give the electric field a slope.

---

3. Here we use the equation from the p-n junction because $x_p + x_n$ in the p-i-n is always smaller or equal than W of an equivalently doped p-n. This follows from the fact that $\max(|E(x)|)$ is smaller in a p-i-n.

$$E(x) = \int_{-\infty}^{x} \frac{\rho}{\varepsilon} dx = \begin{cases} \frac{-qN_a}{\varepsilon} \cdot x & \text{for -}x_p < x \leq 0 \\ \frac{qN_{d,i}}{\varepsilon} \cdot x + K_1 & \text{for } 0 < x \leq x_i \\ \frac{qN_d}{\varepsilon} \cdot x + K_2 & \text{for } d \leq x < d + x_n \\ 0 & \text{for } x \notin [\text{-}x_p, x_i + x_n] \end{cases} \tag{2.16}$$

where the ionize dopant density in the i-layer is $N_{d,i}$ and x_i is the size of the depletion region in the i-layer. We also have $x_i \leq d$ and $x_n = 0$ when $x_i = d$. Here we could of course solve for K_1 and K_2 by using the fact that E(x) is countinous at x=0 and x=d, and using the relation between E(x) and V_b ($-\int_{-\infty}^{\infty} E(x)dx = V_b$).

Here we point out three different regimes:

1. $d \gg \frac{N_{d,i}}{N_a}$: the junction is fully described as a p-n junction (where the i-layer acts as the n-side of the junction) and the n-layer does not participate (see figure 2.4 (d) and (e)).

2. $d \ll \frac{N_{d,i}}{N_a}$: the junction essentially behaves the same as a dopant-free p-i-n junction (see figure 2.3).

3. d similar magnitude as $\frac{N_{d,i}}{N_a}$: the electric field has two distinct slopes (see figure 2.4 (b) and (c)).

2.3.3 The effects of applying a voltage to junction devices

In the previous sections, we have discussed how to analyze junction devices in the absence of externally applied potential. However, in practice junction devices are generally used in electrical circuits where external voltages are applied.

It is fairly straightforward however to adapt the analysis from the previous sections to the case where we do have externally applied voltage (V_a where positive values imply a higher potential on the p-side). In this case, we can use essentially the same equations for E(x) as before, but we can now solve for the constants (K, K_1, K_2, x_p, x_n and x_i) by using:

$$V_b - V_a = -\int_{-\infty}^{\infty} E(x)dx \tag{2.17}$$

Although we will not go into much more details here there are a few remarks to make here:

- In the forward bias regime ($V_a > 0$), we find that increasing V_a to the built-in voltage value (V_b) and beyond results in an exponential rise in the current flowing from $x = -\infty$ to $x = \infty$. This non-linear behavior is a key feature of semiconductor devices and is ultimately responsible, in devices such as the transistor, for signal amplification and switching logic.

- In the reverse bias regime ($V_a < 0$), we find that decreasing V_a (increasing $|V_a|$) results in very little change in the current flowing in the junction. Instead, we find that this larger $|V_a|$ adds to V_b to increase the magnitude of the electric field ($|E(x)|$) in the junction.

- When we go very far in the reverse bias regime we eventually see a sharp rise in current flowing from $x = \infty$ to $x = -\infty$. This is often referred to as the "breakdown regime" and is a result of reaching the breakdown field in the semiconductor.

2.4 Non-equilibrium dynamics

So far, in this chapter, we have always assumed a room temperature thermal equilibrium. However, in the experiments, we will present in this thesis, these conditions are rarely satisfied. In particular, we usually operate at low temperatures and under occasional optical illumination. In this section, we will quickly explore how these two conditions affect the analysis described in this chapter.

2.4.1 Low temperature and carrier freeze-out

Now let's discuss the effects of temperatures on semiconductor materials. First, we'll address the effect of temperature on intrinsic carriers and then, we'll discuss the effect of temperature on dopant ionization.

The effect of temperature on intrinsic carriers (n_i)

As we previously discussed (eq. 2.2), the intrinsic carrier concentration (n_i) comes from the semiconductor levels itself (as opposed to dopants induced levels), and it increases exponentially with temperatures.

- At high temperature, this means that the material becomes dominated by these intrinsic carriers, making the doping type irrelevant (N_a or $N_d \ll n_i$) and breaking the functionality of most junction devices.
- At low temperature, the intrinsic carriers becomes exceedingly small, because the thermal energy is much smaller than the bandgap (E_g). In fact, if we carry out the calculation for Si at 4.2K, we find $n_i \approx 10^{-686}\, cm^{-3}$ [79]. [6]

From this, we can safely conclude that at cryogenic temperature thermal intrinsic carriers are completely absent.

The effect of temperature on dopant ionization

Now, let's discuss the effect of temperature on the carrier produced by dopant ionization. At room temperature, we had assumed that all dopants were ionized (for example $n_n \approx N_a$). However, as we lower the temperature this assumption may no longer hold. The figure

---

[6] Incidentally, this number is so unbelievably small that there is no physical analogy to be drawn. Even we consider a piece of Si the size of the observable universe this means that the probability of finding a single thermal electron in the conduction band would still only be about 1 in 10^{600}!

of merit here is the ionization energy of the dopant. Each dopant has different ionization energies. In 4H-SiC, for example, Nitrogen has ionization energies of 61 meV (h site) and 126 meV (k site), while Aluminum has a ionization energy of roughly 200meV on both sites [81]. Since these energies are much smaller than E_g the dopants are more readily ionized. Nevertheless, once we get below roughly 100K the number of carriers produced from thermally ionized dopants also starts to drop significantly [28] (see figure 2.5). At 4.2K we once again have essentially zero carriers produced thermally.

Therefore, since both intrinsic and dopant induced carriers are essentially absent, the cryogenic operation of semiconductor diodes will be significantly impacted and, in the absence of illumination, charges are unlikely to flow. For this reason, low-temperature CMOS electronics is still a challenging and active area of research [65].

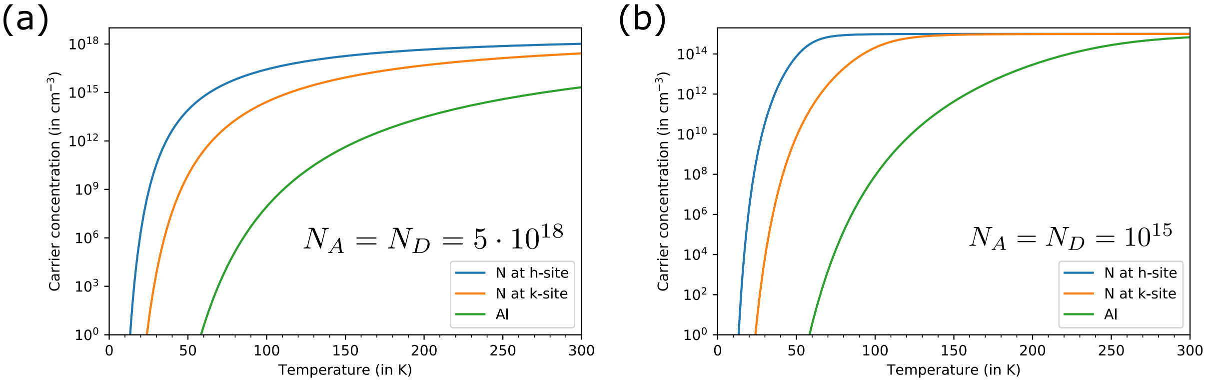

Figure 2.5: **Carrier freeze-out of dopants in SiC.** Plot of carrier concentration due to ionized dopant as a function of temperature. (a) Shows carrier concentration of $5 \cdot 10^{18}$ (similar to concentrations in the work presented in section 5) (b) Shows carrier concentration for a more "standard" dopant concentration of 10^{15}. These calculations were performed using the equations from [28]

2.4.2 Optical illumination of low-temperature SiC devices

As we just saw, semiconductor devices at low temperatures behave quite differently than their room-temperature counterpart. In particular, in thermal equilibrium at 4-5K, all electrons are essentially static and in their ground states, which results in the absence of free charge carriers. However, the situation becomes very interesting when we add optical illumination to the picture.

The idea is that electrons can be excited to higher energy levels by optical photons. This pushes the material out of thermal equilibrium by exciting electrons and producing free carriers. We note here that, importantly, the fact that we are out of equilibrium means that notions and concepts derived from equilibrium assumptions (such as Fermi level for example) will generally not be relevant here.

To a first-level approximation, one could think of the optical illumination as establishing an "effective semiconductor electron temperature" which is higher than the phonon temperature. This model attempts to bring back a certain notion of equilibrium (under optical drive). However, ultimately, this model is incomplete since it does not account for the fact that photons are quantum objects with discrete energy and thus, only certain transitions are allowed.

Therefore to arrive at a more correct description of low-temperature semiconductors under illumination, we must carefully examine all the possible transitions and determine which ones are allowed and which ones aren't (see figure 2.6).

In general, since the dopants are so close to the bands they can be excited with very low energy mid-infrared photons (we expect to need $6.2\mu m$ for Al and $20.3\mu m$ for $\mathrm{N}_{(h)}$). This means that even though in thermal equilibrium we would expect no free carriers, this assumption does not hold in most experiments we will present in this dissertation (which will also always involve optical illuminations with wavelengths anywhere from the ultraviolet (UV) to the near-infrared (NIR)). In fact, at these energies, black-body radiation from 300K (from our objective for example), has a wavelength that is sufficient to excite these shallow dopants.

As for the deeper levels, we will do a more careful analysis of the impact of NIR and red light on the stable charge state of deep level defects in chapter 5 and appendix 5.3.

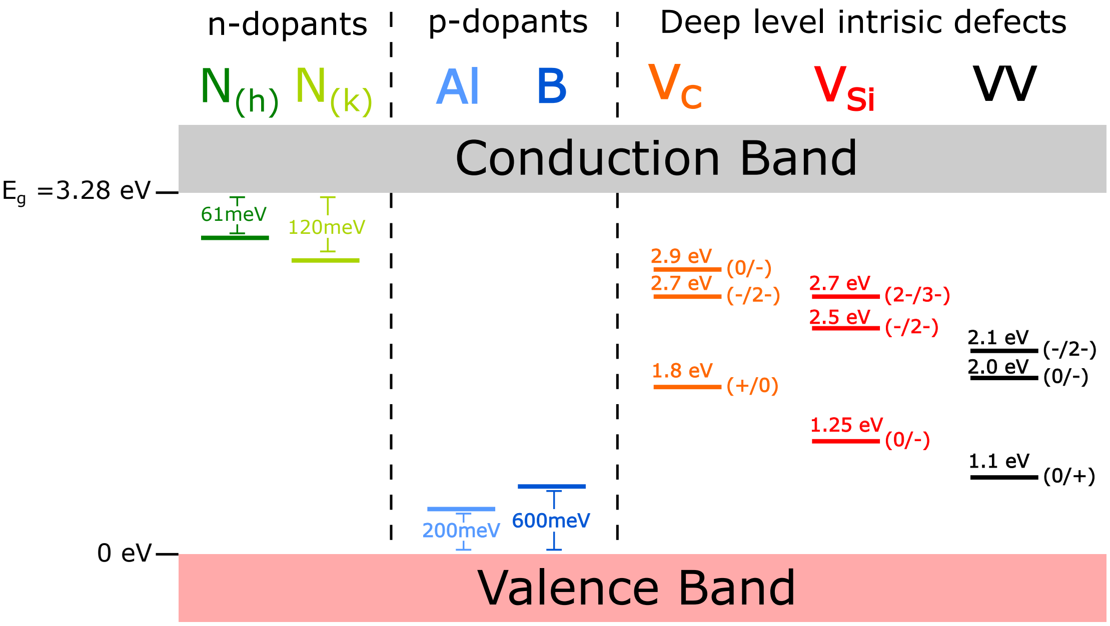

Figure 2.6: **Ionization energies of defects and dopants in SiC.** Diagram representing the different ionization energies for n- and p-type dopant and deep intrinsic defect levels. For the dopants, we've labeled the energy to the closest band. For the deep defect levels, we've labeled the energy with respect to the valence band maximum. We have identified here the two different sites for Nitrogen (because the ionization energies are quite different relatively), but it's worth remembering that all of the dopant/defect shown above have different possible locations (h and k sites) and orientation (for VV) with slightly different ionization energies which are not shown here. Values were taken from [95] and [81].

CHAPTER 3

FROM DEFECT TO QUBIT

3.1 The divacancy defect in SiC

Silicon carbide (SiC) is a semiconductor material composed of carbon and silicon atoms (with a 1:1 ratio). A vast number of possible arrangements of atoms are possible. These distinct crystal forms are called polytypes. The most common polytypes of silicon carbide are 3C, 4H, and 6H. Throughout this dissertation, we will discuss a point defect produce by a missing Si atom (V_{Si}) next to a missing C atom (V_C) (see figure 3.1 for two examples of this structure). This defect, in its electrically neutral form, is aptly named: neutral divacancy (VV^0. The neutral divacancy in SiC has been observed in several of these polytypes [47], but for the purpose of this dissertation, we will focus on 4H-SiC. This polytype is the results of stacking hexagonal sheets of SiC (along the c crystal axis) with either no rotation (h) or a 60-degree rotation (k) between these layers [49, 10]. By alternating between a hexagonal (h) and cubic (k) stacking, we produce a self-similar crystal with a periodicity of 4 layers (ABCB-ABCB-...).

In such a crystal, there are thus two types of lattice locations for each atom which we identify using the labels (h and k) associated with how they stack to the next/previous layer. Consequently, there are 4 possible divacancy defects: *hh*, *kk*, *hk* and *kh* (with the first letter representing the V_C site and the second the V_{Si} site). These defects are each associated with a specific photoluminescence line and are thus also sometime refered to as PL1 (*hh*), PL2 (*kk*), PL3 (*hk*) and PL4 (*kh*).

The hh and kk defects are by definition along the c-axis of the crystal and have a C_{3v} symmetry whereas the *hk* and *kh* defects are basal and have a C_{1h} symmetry. All three of these defects form spin singlets (S=0) and spin triplets (S=1) states which can be used to store, manipulate, and readout quantum information. In this section, we will expand on how these properties can be qualitatively arrived at from first principles.

3.2 Energy level structure of the divacancy

This section is intended to give some qualitative idea of how one can arrive at the properties of the divacancies from first principles. Here we will go through a group theoretical type of derivation, but we will try to avoid taking the usual shortcut that group theory usually affords. This approach is intended to give the intuition behind the divacancy's energy level to a reader who might not be familiar with group theory. For conciseness, we will use the *hh* defect for this derivation and simply state that the derivation for the *kk* is nearly identical. For the basal defects (ie *hk* and *kh*), the derivation will use similar principles, but will be slightly different because of the C_{1h} symmetry.

Note that for a more formal analysis of the energy level structure of defects, there are detailed publications on discussing both the NV center[97] and the divacancy[53].

3.2.1 The geometry and symmetries of the divacancy

We begin by taking a look at the geometrical structure of the divacancy (see figure 3.1). Defining $\{c_1, c_2, c_3\}$ and $\{s_1, s_2, s_3\}$ as the dangling bonds of the neighboring C and Si atoms respectively (these are essentially the sp^3 orbitals of the associated C and Si atoms). We know that ultimately we will need to distribute 6 electrons in the orbitals left vacant by these dangling bonds.

The next step is to enumerate the possible geometrical transformation that would results in a self-similar picture (let's call the set of these symmetries $\mathbb{S}$). In this case, these are:

- Do nothing. This trivial transformation must be included (as the identity element of the group) for the completeness of the group (labeled E).

- Rotation by ±120 degrees around the c-axis (labeled C_3^+ and C_3^-).

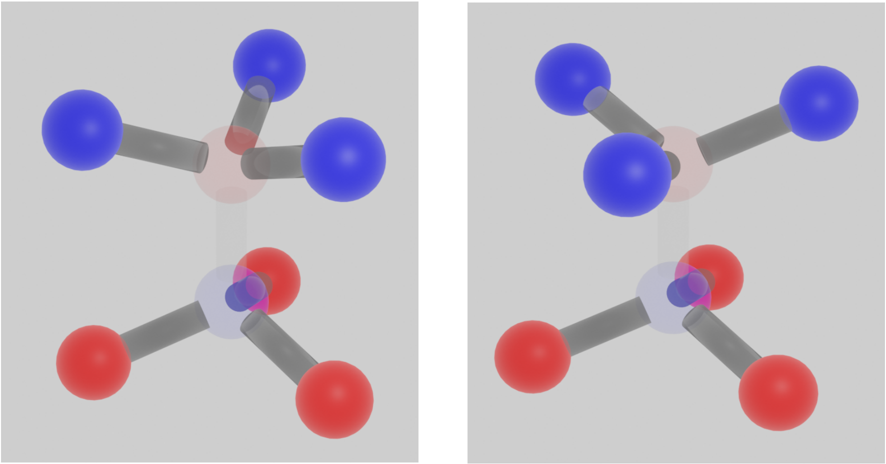

Figure 3.1: **3D representation of the divacancy.** 3D rendering of the c-axis divacancy defect (*hh* on the left, and *kk* on the right). The difference here is the 60° twist between the C (in blue) and Si atoms (in red) in the case of the *kk*. The transparent spheres represent the missing attoms forming the divacancy.

- Reflection in one of 3 different planes which can be constructed by using the two vacancies and one of the C (or Si) atom as points on that plane (labeled σ_v, σ_v' and σ_v'').

Since the atoms in the lattice have these symmetries, the orbitals of the defect state will also necessarily have the same symmetries. This is because the symmetries of the potential energy landscape must be reflected in the eigenfunction solutions to the associated Schrödinger equation.

Importantly, this also means that only states which cannot transform into each other by one of these symmetries can have different energies. For example, a state Ψ_1 which is the mirror image of another state Ψ_2 across σ_v must have the same energy since it sees the same potential.

Since we know that the basis states (orbital wavefunctions) must be orthogonal, and we also know that they are self-similar under any transformation in $\mathbb{S}$, it follows that the orbital states we are looking for cannot transform into one another using any transformation in $\mathbb{S}$.

3.2.2 The single electron levels

So now we want to find states in the space spanned by $B = \{c_1, c_2, c_3, s_1, s_2, s_3\}$ which cannot transform into one another under any of the transformations in $\mathbb{S} = \{E, C_3^+, C_3^-, \sigma_v, \sigma_v', \sigma_v''\}$. Let's first see how each of these transformation act on our dangling bonds.

For instance, if we apply σ_v (mirror across the plane formed by V_C, V_{Si} and c_1) we have that electrons located at c_1 and s_1 will remain in place whereas those at c_2 will swap place with c_3 (and s_2 will swap with s_3).

Expressing all 6 of these transformations in the B basis we find:

$$
E = \begin{bmatrix} 1 & 0 & 0 & 0 & 0 & 0 \\ 0 & 1 & 0 & 0 & 0 & 0 \\ 0 & 0 & 1 & 0 & 0 & 0 \\ 0 & 0 & 0 & 1 & 0 & 0 \\ 0 & 0 & 0 & 0 & 1 & 0 \\ 0 & 0 & 0 & 0 & 0 & 1 \end{bmatrix} \quad
\sigma_v = \begin{bmatrix} 1 & 0 & 0 & 0 & 0 & 0 \\ 0 & 0 & 1 & 0 & 0 & 0 \\ 0 & 1 & 0 & 0 & 0 & 0 \\ 0 & 0 & 0 & 1 & 0 & 0 \\ 0 & 0 & 0 & 0 & 0 & 1 \\ 0 & 0 & 0 & 0 & 1 & 0 \end{bmatrix}
$$

$$
\sigma_v' = \begin{bmatrix} 0 & 1 & 0 & 0 & 0 & 0 \\ 1 & 0 & 0 & 0 & 0 & 0 \\ 0 & 0 & 1 & 0 & 0 & 0 \\ 0 & 0 & 0 & 0 & 1 & 0 \\ 0 & 0 & 0 & 1 & 0 & 0 \\ 0 & 0 & 0 & 0 & 0 & 1 \end{bmatrix} \quad
\sigma_v'' = \begin{bmatrix} 0 & 0 & 1 & 0 & 0 & 0 \\ 0 & 1 & 0 & 0 & 0 & 0 \\ 1 & 0 & 0 & 0 & 0 & 0 \\ 0 & 0 & 0 & 0 & 0 & 1 \\ 0 & 0 & 0 & 0 & 1 & 0 \\ 0 & 0 & 0 & 1 & 0 & 0 \end{bmatrix} \tag{3.1}
$$

$$
C_3^- = \begin{bmatrix} 0 & 0 & 1 & 0 & 0 & 0 \\ 1 & 0 & 0 & 0 & 0 & 0 \\ 0 & 1 & 0 & 0 & 0 & 0 \\ 0 & 0 & 0 & 0 & 0 & 1 \\ 0 & 0 & 0 & 1 & 0 & 0 \\ 0 & 0 & 0 & 0 & 1 & 0 \end{bmatrix} \quad
C_3^+ = \begin{bmatrix} 0 & 1 & 0 & 0 & 0 & 0 \\ 0 & 0 & 1 & 0 & 0 & 0 \\ 1 & 0 & 0 & 0 & 0 & 0 \\ 0 & 0 & 0 & 0 & 1 & 0 \\ 0 & 0 & 0 & 0 & 0 & 1 \\ 0 & 0 & 0 & 1 & 0 & 0 \end{bmatrix}
$$

Now, we want to find as many subspaces as we can that are invariant under all 6 symmetry. In short, we want to find a basis that simultaneously block-diagonalizes all of these matrices into as many subspaces as possible.

First, we notice that the c_i sites never mix with the s_i sites and thus we can write all of these in two distinct subspaces:

$$M = \begin{bmatrix} M_{3x3}^{(1)} & 0 \\ 0 & M_{3x3}^{(2)} \end{bmatrix} \tag{3.2}$$

Since here $M_{3x3}^{(1)} = M_{3x3}^{(2)}$ for all transformations in $\mathbb{S}$ we simplify our problem to block diagonalizing the following 3x3 matrix:

$$\begin{gathered} E_{3x3} = \begin{bmatrix} 1 & 0 & 0 \\ 0 & 1 & 0 \\ 0 & 0 & 1 \end{bmatrix} \quad (\sigma_v)_{3x3} = \begin{bmatrix} 1 & 0 & 0 \\ 0 & 0 & 1 \\ 0 & 1 & 0 \end{bmatrix} \quad (\sigma'_v)_{3x3} = \begin{bmatrix} 0 & 1 & 0 \\ 1 & 0 & 0 \\ 0 & 0 & 1 \end{bmatrix} \\ (\sigma''_v)_{3x3} = \begin{bmatrix} 0 & 0 & 1 \\ 0 & 1 & 0 \\ 1 & 0 & 0 \end{bmatrix} \quad (C_3^-)_{3x3} = \begin{bmatrix} 0 & 0 & 1 \\ 1 & 0 & 0 \\ 0 & 1 & 0 \end{bmatrix} \quad (C_3^+)_{3x3} = \begin{bmatrix} 0 & 1 & 0 \\ 0 & 0 & 1 \\ 1 & 0 & 0 \end{bmatrix} \end{gathered} \tag{3.3}$$

Here the best we can do is a 1D subspace and a 2D subspace. In particular, in the c_i subspace if we use the following state:

$$\begin{aligned} a_{(1)} &= \frac{1}{\sqrt{3}}(c_1 + c_2 + c_3) \\ e_{(1),x} &= \frac{1}{\sqrt{6}}(2c_1 - c_2 - c_3) \\ e_{(1),y} &= \frac{1}{\sqrt{2}}(c_2 - c_3) \end{aligned} \tag{3.4}$$

Where the names of the states were chosen according to group theory conventions (which we will not detail here). Also note that the $e_{(1),x}$, and $e_{(1),y}$ states chosen for our basis are not unique (other orthonormal combinations of these two states would have been just as good). This forms a new basis $\{a_{(1)}, e_{(1),x}, e_{(1),y}\}$, wherein our symmetry transformations are now expressed as:

$$E_{3x3} = \begin{bmatrix} 1 & 0 & 0 \\ 0 & 1 & 0 \\ 0 & 0 & 1 \end{bmatrix} \qquad (\sigma_v)_{3x3} = \begin{bmatrix} 1 & 0 & 0 \\ 0 & 1 & 0 \\ 0 & 0 & -1 \end{bmatrix} \qquad (\sigma_v')_{3x3} = \begin{bmatrix} 1 & 0 & 0 \\ 0 & \frac{-1}{2} & \frac{\sqrt{3}}{2} \\ 0 & \frac{\sqrt{3}}{2} & \frac{1}{2} \end{bmatrix}$$

$$(\sigma_v'')_{3x3} = \begin{bmatrix} 1 & 0 & 0 \\ 0 & \frac{-1}{2} & \frac{-\sqrt{3}}{2} \\ 0 & \frac{-\sqrt{3}}{2} & \frac{1}{2} \end{bmatrix} \quad (C_3^-)_{3x3} = \begin{bmatrix} 1 & 0 & 0 \\ 0 & \frac{-1}{2} & \frac{-\sqrt{3}}{2} \\ 0 & \frac{\sqrt{3}}{2} & \frac{-1}{2} \end{bmatrix} \quad (C_3^+)_{3x3} = \begin{bmatrix} 1 & 0 & 0 \\ 0 & \frac{-1}{2} & \frac{\sqrt{3}}{2} \\ 0 & \frac{-\sqrt{3}}{2} & \frac{-1}{2} \end{bmatrix} \tag{3.5}$$

Finally, doing the same with the s_i subspace we end up with two 1D spaces ($a_{(1)}$ and $a_{(2)}$) and two 2D spaces ($e_{(1)}$ and $e_{(2)}$). States within these subspaces cannot be transformed into states from another subspace by any of the six symmetry operations. Each subspace, therefore, represents states seeing a different overall potential (ie with a different eigenenergy). Here the states in the $e_{(1)}$ subspace form a degenerate pair with the same energy (and the same thing goes for the $e_{(2)}$ subspace).

Thus we have found our 6 possible orbital available for the electrons to sit in. Note that we have not said anything yet about the ordering of these states (ie which one has the higher energy). In general, this is a complicated problem that requires DFT to solve, but as noted by Maze et al. [97] one can also get a reasonable estimate of this ordering by using an electron-ion interaction of the type:

$$V = \sum_i v_c \left|c_i\right\rangle \left\langle c_i\right| + \sum_i v_s \left|s_i\right\rangle \left\langle s_i\right| + \sum_{i>j} h_c \left|c_i\right\rangle \left\langle c_j\right| + \sum_{i>j} h_s \left|s_i\right\rangle \left\langle s_j\right| + \sum_{i,j} h_{sc} \left|c_i\right\rangle \left\langle s_j\right| + h.c. \tag{3.6}$$

But we will not do this computation here. Instead, we will refer to results in the literature [53], which have ordered the states as $a_{(1)}a_{(2)}e_{(1)}e_{(2)}$ (with $a_{(1)}$ having the lowest energy and $e_{(2)}$ the highest). A few additional characteristics [53] of these levels are:

1. The $a_{(1)}$ levels falls below the valence band maximum (VBM).
2. The $a_{(2)}$ levels is close to (but perhaps slightly above) the valence band maximum (VBM).
3. The lowest of the two e levels ($e_{(1)}$) is associated with the C dangling bonds.

For this dissertation, we will not use the $e_{(2)}$ levels and thus the electron wavefunction will generally be closer to the C atoms than the Si atoms (or alternatively closer to the V_{Si} than the V_C site). Thus, in the next section, we will adopt the shorthand notation e to refer to the $e_{(1)}$ level and simply ignore the $e_{(2)}$ levels.

3.2.3 The full-system levels

In the last section, we have found the single electron orbitals, we now wish to look more globally at the full system. Here we will need to add 6 electrons (since we are talking about the "neutral" divacancy there are 6 participating electrons).

Since there are now multiple spin-carrying particles involved, we will need to add the spin degree of freedom to fully describe the system energies and symmetries. For example, since this system is composed of indistinguishable fermionic particles we know that it must be anti-symmetric under the exchange of particles [1]. This means that an anti-symmetric orbital state will always be associated with a symmetric spin state and vice-versa (you can check this in table 3.1)

We will place these electrons in the following 4 single electron levels: a_1, a_2, e_x and e_y (with e_x and e_y being the degenerate levels associated with $e_{(1)}$). Each of these levels can only support 2 electrons (spin up and spin down) due to Pauli exclusion principles, thus we have a total of eight possible locations for the 6 electrons.

---

[1] Here we will refer to states as being "symmetric" or "anti-symmetric" under the exchange of particle. By this, we simply mean that the eigenvalue is 1 or -1 when we exchange any two particles

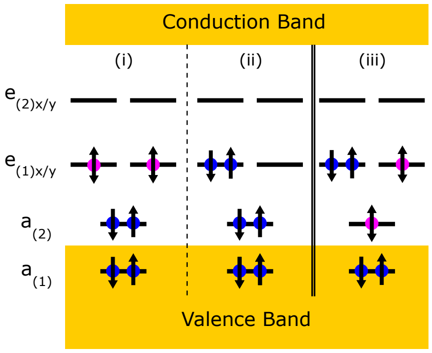

Figure 3.2: **Single particle model of the VV^0 in SiC**. The two structures on the left represent the ground state (i) triplet $^3A_2$, and (ii) singlets $^1E_1$, $^1E_2$ and $^1A_1$. (iii) The structure on the right corresponds to the two equivalent excited state orbitals $|X\rangle$ and $|Y\rangle$.

It is often simpler to frame this problem in terms of the location of the missing electrons (unfilled orbitals) since there are only 2 of these holes. And because these holes can leave unpaired electrons they also effectively carry a spin-half. Therefore, we can label the state of the full system using the $|h_0h_1s_0s_1\rangle$ basis where h_i represents which single-particle orbital hole i is in, and s_i represents its spin.

Looking only at the hole configuration, we can reasonably infer that the system will be in it's lowest energy configurations when both holes are in the e levels (Figure 3.2 (i and ii)). In this 4 dimensional subspace ($\{|e_x\rangle, |e_y\rangle\} \otimes \{|e_x\rangle, |e_y\rangle\}$), there is one anti-symmetric state ($|e_xe_y - e_ye_x\rangle$) and 3 symmetric states (under particule exchange). Because these are fermions, the anti-symmetric state will be a spin triplet (S=1) and the symmetric states will be spin singlets (S=0).

Then if we promote an electron to the e level we are left with the slightly more energetic configuration of holes ea. This subspace ($\{|a_1e_x\rangle, |a_1e_y\rangle, |e_xa_1\rangle, |e_ya_1\rangle\}$) is again 4-dimensional and can be decomposed into symmetric and anti-symmetric spaces. Once again, since we are dealing with a fermionic system, the symmetric subspace $\{|a_1e_x\rangle + |e_xa_1\rangle, |a_1e_y\rangle + |e_ya_1\rangle\}$ is going to be associated with spin singlets and the anti-symmetric subspace $\{|X\rangle = |a_1e_x\rangle - |e_xa_1\rangle, |Y\rangle = |a_1e_y\rangle - |e_ya_1\rangle\}$ is going to be associated with a spin triplet. Finally, once mixed with triplet spin states, the anti-symmetric subspace can

Table 3.1: **Eigenstates of the full VV^0 system.** Here we show the full eigenstates of the two lowest energy holes configurations (*ee* and *ea*) along with their spin (singlets are S=0 and triplets are S=1) and orbital (symmetric or anti-symmetric under particle exchange) characteristics [97]. We note that the spin triplets are always associated with anti-symmetric orbital (and singlets with symmetric orbitals) making the full state anti-symmetric under the exchange of particles. We also define $|E_\pm\rangle = \mp(|X\rangle \pm i\,|Y\rangle)$.

Holes config.	State Name	State	Spin	Orbitals	Full-state symmetry
ee	${}^3A_2$	$\lvert e_xe_y - e_ye_x\rangle \otimes \left\{ \begin{matrix} \lvert\downarrow\downarrow\rangle \\ \lvert\uparrow\downarrow + \downarrow\uparrow\rangle \\ \lvert\uparrow\uparrow\rangle \end{matrix} \right.$	Triplet	Anti-symmetric	$E_1 + E_2$ A_1 $E_1 - E_2$
	${}^1E_1$	$\lvert e_xe_x - e_ye_y\rangle \otimes \lvert\uparrow\downarrow - \downarrow\uparrow\rangle$	Singlet	Symmetric	E_1
	${}^1E_2$	$\lvert e_xe_y + e_ye_x\rangle \otimes \lvert\uparrow\downarrow - \downarrow\uparrow\rangle$	Singlet	Symmetric	E_2
	${}^1A_1$	$\lvert e_xe_x + e_ye_y\rangle \otimes \lvert\uparrow\downarrow - \downarrow\uparrow\rangle$	Singlet	Symmetric	A_1
ea	A_1	$\lvert E_-\rangle \otimes \lvert\uparrow\uparrow\rangle - \lvert E_+\rangle \otimes \lvert\downarrow\downarrow\rangle$	Triplet	Anti-symmetric	A_1
	A_2	$\lvert E_-\rangle \otimes \lvert\uparrow\uparrow\rangle + \lvert E_+\rangle \otimes \lvert\downarrow\downarrow\rangle$			A_2
	E_1	$\lvert E_-\rangle \otimes \lvert\downarrow\downarrow\rangle - \lvert E_+\rangle \otimes \lvert\uparrow\uparrow\rangle$			E_1
	E_2	$\lvert E_-\rangle \otimes \lvert\downarrow\downarrow\rangle + \lvert E_+\rangle \otimes \lvert\uparrow\uparrow\rangle$			E_2
	E_y	$\lvert Y\rangle \otimes \lvert\uparrow\downarrow + \downarrow\uparrow\rangle$			E_1
	E_x	$\lvert X\rangle \otimes \lvert\uparrow\downarrow + \downarrow\uparrow\rangle$			E_2
	${}^1E_x$	$\lvert a_1e_x + e_xa_1\rangle \otimes \lvert\uparrow\downarrow - \downarrow\uparrow\rangle$	Singlet	Symmetric	E_1
	${}^1E_y$	$\lvert a_1e_y + e_ya_1\rangle \otimes \lvert\uparrow\downarrow - \downarrow\uparrow\rangle$	Singlet	Symmetric	E_2

be further decomposed according to the symmetries of the full state (either A_1, A_2, E_1, E_2).

We summarize all of these states in table 3.1.

To conclude, we see that simple reasoning based on symmetry arguments can get us pretty far in determining the level structure of the divacancy. Using similar symmetry arguments, we can also predict what polarization (linear vs circular) of light will be required to excite transitions between these levels. However, there are two important caveats to mention:

1. This analysis does not give us directly the energy and ordering of the levels. Although some rough educated guesses (e.g. *ee* will be lower than *ea* based on the ordering from the previous section), a more complete analysis requires numerical methods such as density functional theory (DFT). The final ordering of the states can be seen in figure 3.3.

2. This analysis assumes a perfect C_{3v} symmetry. In the presence of transverse strain or electric field, this assumption is generally violated to some degree. This slight deviation effectively mixes the states shown in table 3.1 (most importantly it will mix the states in the *ea* triplet subspace).

3.3 The divacancy as a qubit

Now that we know what the level structure of the divacancy will look like, we want to explore the question of how we go from this level structure to a qubit. To build a proper qubit we need two distinct quantum states which have:

1. Long coherence time
2. An initialization mechanism
3. A readout mechanism
4. A method for implementing arbitrary rotations

3.3.1 Picking a subspace with long coherence

To fulfill the 1st criteria we generally embed our qubit states in the *ee* triplet subspace. Other subspaces (*ee* singlets and *ea* subspaces) all suffer from spontaneous decay which ultimately brings the state back to the *ee* triplet subspace.

For the rest of this dissertation, we will commonly employ the following shorthands subspace names (these are summarized in figure 3.3):

1. Ground State (GS): Referring to the *ee* triplet subspace. We will also use the notation $|0\rangle$, $|-1\rangle$, $|+1\rangle$ to refer to 3 possible spin states in the GS subspace.
2. Excited State (ES): Referring to the *ea* triplet subspace.

3. Intersystem Crossing (ISC): Referring generally to intermediate states in which the ES can decay via non-spin conserving transitions (this corresponds to the *ee* singlet subspaces [53]).

Of course, the GS is a spin-1 subspace and therefore has 3 different states ($m_s \in \{-1, 0, +1\}$). Since we can arbitrarily control any of these three levels we are free to choose any two of them as our "qubit levels".

We generally use $m_s = 0$ as one of the two "qubit levels" because, as we will see in the sections 3.3.2 and 3.3.3, both initialization and readout are easier this way. So ultimately, we generally use either $\{|0\rangle, |-1\rangle\}$ or $\{|0\rangle, |+1\rangle\}$ as our qubit space.

It is worth noting that the $\{|-1\rangle, |+1\rangle\}$ is also sometimes interesting because it is: (1) twice as sensitive to magnetic noise, but (2) much less sensitive to electric noise. Nevertheless, since our main noise source is generally magnetic (nuclear and paramagnetic defects) this is generally not a worthwhile tradeoff.

3.3.2 Qubit initialization

Initialization is an essential first step for most quantum circuits. In a sense, initialization is in direct conflict with the requirement for a highly coherent isolated quantum system because this operation is fundamentally non-unitary. Non-unitary operations in quantum mechanics are only possible in open systems when some information is lost to the qubit's environment.

There are two related, but conceptually slightly different, ways one can think about implementing initialization:

1. Use a high-fidelity single-shot projective readout to read the state of the qubit and then apply the appropriate quantum gate to initialize into the desired state.

2. Use a "one-way" depolarization channel that exchanges energy (most likely loses energy) with the environment to end up in a given state with high probability after some

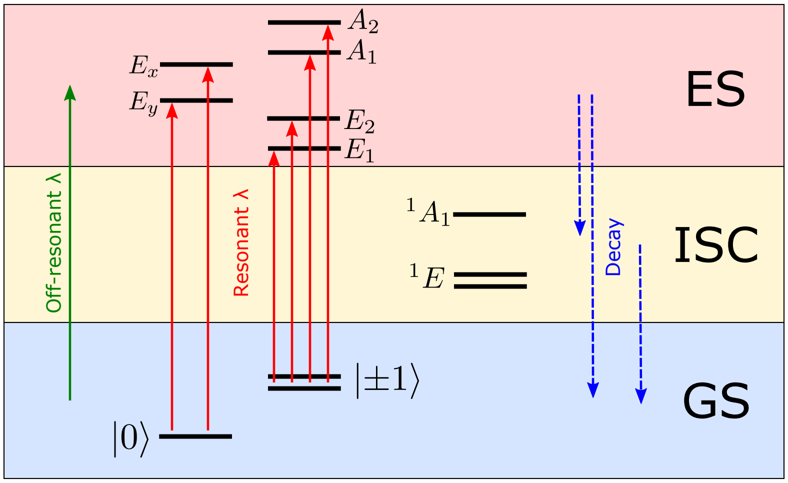

Figure 3.3: **Full-system energy structure of the divacancy.** The levels are ordered from the lowest energy state ($|0\rangle$) up to the highest energy state (A_2) and group into GS, ES, and ISC. The red arrow denotes allowed optical transitions. The first column denotes the triplet states with $m_s = 0$ along with the associated spin conserving transitions. The second column denotes the $m_s = \pm1$ states and associated transitions. The last column represents the ISC levels participating in the initialization. The dashed blue arrows illustrate that all states in the ES have decay channels both to the GS and ISC, and the states in the ISC have decay channels to the GS. Note that importantly the decay channels do not all have the same rates even though we've represented them with a single arrow for conciseness (this is critical for initialization!). Finally, we use a green arrow to represent off-resonant excitation which can be thought of as simultaneously causing all possible resonant transitions (red arrows) via the phonon sideband.

interaction time.

As we will see in section 3.3.3, method 1 is not an option (at least not yet!) because we do not currently collect enough photons per shot for a high-fidelity single-shot projective readout. So we need to find a way to use method 2.

There are 2 commonly used methods for constructing this "one-way" depolarization channel:

1. Off-resonant initialization: Using off-resonant excitation (generally ~900-975nm) we can simultaneously excite the divacancy to its ES regardless of the spin state in the GS. We then rely on differences in decay rates depending on the spin state. [2] The competition of these rates turns out to initialize the divacancy with about 90% fidelity.

2. Resonant initialization: This is a much more deliberate approach, where we selectively target a spin subspace in the GS (either $\{|0\rangle\}$ or $\{|-1\rangle,|+1\rangle\}$) and use one of the resonant transitions (red arrow in figure 3.3) to pump that spin state into the excited state. Because the ISC decay channel has some probability to flip the spin state when going back to the GS, we have effectively constructed a "one-way" depolarization channel. This approach is required when high fidelity ($> 99\%$) initialization is desired.

3.3.3 Qubit readout

Just like the initialization, we generally use optical transitions for reading out the state of our qubit. To this end, we can either use off-resonant excitation or resonant excitation.

First, off-resonant excitation once again relies on the competition of decay rates from the ES to the GS/ISC. For some defects (e.g. *hh*), it turns out that the $m_s = 0$ subspace emits on average slightly more photons than the $m_s = \pm 1$ subspace when excited continuously.

---

[2] Here differences between the "ISC to $|0\rangle$" rate (faster) and the "ISC to $|\pm 1\rangle$" rate (slower) is the most likely candidate. This hypothesis stems from the fact that some defects (e.g. *kk*) have a positive contrast (meaning that the $|\pm 1\rangle$ state is brighter than the $|0\rangle$ state) in off-resonant excitation but still initializes to the $|0\rangle$ state under off-resonant illumination.

For other defects (e.g. *kk*) the opposite is true. And for the basal defect, the $|+\rangle$, $|-\rangle$, and $|0\rangle$ all have different average brightness. Either way, this slight difference is sometimes enough to distinguish the various spin states after averaging. However, the contrast between the different spin states is not great so this is not the best method in general.

This brings us to the second method: using resonant excitation. Here we selectively excite only one of the resonant transitions associated with a given spin subspace. We often use the transitions associated with the $|0\rangle$ state because this transition is more cyclical meaning that it is more likely to decay back to the $|0\rangle$ without spin-flipping. This means that we can expect more photons on average before a spin-flip occurs. Importantly, using this method the system only emits photons when it is in the target qubit state (here $|0\rangle$) and theoretically emits no photon at all when in the other qubit state. This results in a greatly enhanced contrast which has been demonstrated up to be $> 99\%$ in some of the work presented in this dissertation.

However, having great contrast on average is not sufficient for performing projective single-shot readout. By this, we mean the following:

1. Single-shot readout: This refers to the ability to distinguish the two-qubit state in a single measurement (no averaging over many experiments). Here we see that even a perfect contrast:

$$\text{contrast} = \frac{(\text{average photon number for } |0\rangle) - (\text{average photon number for } |1\rangle)}{(\text{average photon number for } |0\rangle)} = 1 \tag{3.7}$$

   is not sufficient, we also need to ensure that the "average photon number for $|0\rangle$" is greater than 1! In general, to allow for some imperfections in the contrast (due to mixing, detector dark counts, background counts, etc...) we generally target a few (1-10) photons per shot (but of course the more photon the better!). This is necessary for many quantum protocols which involve feedback based on measurement.

2. Projective readout: This is an even stricter type of single-shot readout since it requires not only that we measure the current state of the system, but also, that our measurement does not flip the state we are measuring. This requires that the maximum possible number of photons per shot be much higher (> 100). If we had those numbers we could measure for only a fraction of the maximum time (set by the spin-flip rate) and thus avoid spin-flips while still collecting 1-10 photons. We also note that projective readout can by itself replace initialization. However, projective single-shot readout is not strictly necessary for building arbitrary quantum circuits since it can be replaced by a combination of initialization, single-shot measurement, and qubit rotation.

3.3.4 Qubit control

The requirement we need for ensuring we can use our divacancy as a qubit is the ability to perform arbitrary unitary rotations between the qubit states. Since we always operate our qubit in the GS except for measurements and initialization, it is sufficient for this section to discuss how we can perform arbitrary rotation between the various levels in the GS. Of course the theory we present here could also be applied to some extent to describe the optical resonant excitation to the excited state (the only difference being the optical frequency vs the microwave frequency, and the shorter coherence time of the ES), but we will stick to the GS only to simplify the picture. Nevertheless, we will treat the full GS rather than discuss an arbitrary qubit state and we will try to stay as close as possible to the underlying physical system.

Ground state Hamiltonian

First, let's write down the full GS Hamiltonian for a divacancy system. Here we'll include nuclear spins and nearby other paramagnetic spins for completeness. However, depending on what we are trying to analyze we generally simplify this to only include the relevant terms.

The full GS Hamiltonian for a divacancy and it's surrounding nuclear spins is [84]:

$$\hat{H}_{|GS\rangle} = \hat{\mathbf{S}}\cdot\mathbf{D}\cdot\hat{\mathbf{S}} + \gamma^e\hat{\mathbf{S}}\cdot\mathbf{B} + \sum_i \gamma_i^n\hat{\mathbf{I}}_i\cdot\mathbf{B} + \sum_i \hat{\mathbf{S}}\cdot\mathbf{A}_i\cdot\hat{\mathbf{I}}_i + \sum_i\sum_{j>i}\hat{\mathbf{I}}_i\cdot\mathbf{P}^n_{i,j}\cdot\hat{\mathbf{I}}_j + \sum_i \hat{\mathbf{S}}\cdot\mathbf{P}^e_i\cdot\hat{\mathbf{S}}_i \quad (3.8)$$

where:

- $\hat{\mathbf{S}}$ is the electron spin operator for the central divacancy,
- $\mathbf{D}$ is the crystal field splitting or zero-field splitting,
- γ^e is the electron gyromagnetic ratio,
- $\mathbf{B}$ is the applied external magnetic field,
- $\hat{\mathbf{I}}_i$ are the spin operators of the nearby nuclear isotopes (^{13}C and ^{29}Si),
- γ_i^n are the nuclear gyromagnetic ratio (either that of ^{13}C or ^{29}Si),
- $\mathbf{A}_i$ are the hyperfine tensor coupling the electron spin to neighboring nuclear spin,
- $\mathbf{P}^n_{i,j}$ are the dipole-dipole coupling between the nuclear spin in the environment,
- $\hat{\mathbf{S}}_i$ are the spin operators of all electron spins in the defect's environment ($\hat{\mathbf{S}}_0 = \hat{\mathbf{S}}$),
- $\mathbf{P}^e_i$ are the dipole-dipole coupling between the central divacancy and other nearby electron spins.

The first term generally arises from spin-orbit and spin-spin interactions [97] which can differ between the different spin states. This term is often broken down into:

$$\hat{\mathbf{S}}\cdot\mathbf{D}\cdot\hat{\mathbf{S}} = D_z\hat{S}_z^2 - E_x^0\left(\hat{S}_x^2 - \hat{S}_y^2\right) + E_y^0\left(\hat{S}_x\hat{S}_y + \hat{S}_y\hat{S}_x\right) \quad (3.9)$$

Where $\mathbf{E}^0 = 0$ for a perfect C_{3v} symmetry defects (in the absence of transverse strain and electric field) and $\mathbf{E}^0 \neq 0$ for the C_{1h} defects. This term generally creates a splitting between the $m_s = 0$ spin state and the $m_s = \pm 1$ states on the order of about 1 GHz and can also split the $m_s = +1$ from the $m_s = -1$ state if there is not a perfect C_{3v} symmetry. The exact value of $\mathbf{D}$ changes depending on the defect type we are looking at and as such is generally a good way (along with the PLE spectrum) to identify the defect type (*hh*, *kk*, *kh* or *hk*).

The second term represents the Zeeman splitting which separates the $m_s = +1$ and $m_s = -1$ levels.

The next three terms represent the energy associated with the nearby nuclear isotope as well as their interactions with the electron spin and other nuclear spins. These will be quite useful when implementing nuclear quantum memories, but will also be the cause of decoherence for the electron spin.

Finally, the last term corresponds to the dipole interactions between nearby electron paramagnetic traps. This interaction is generally undesired and can be a limiting factor to decoherence in certain scenarios (such as T_2 in isotopically purified samples).

Controlling the GS spin

We now wish to explore how one can use microwave magnetic fields to control the spin of the divacancy in its GS. Here we will simplify the derivation by temporarily ignoring the effect of surrounding nuclear and electronic spins (which are either too weakly coupled or too slowly varying to affect the dynamics at short timescales). For the sake of simplicity, we will also focus on the c-axis defect in the absence of strain or electric field ($\hat{\mathbf{S}} \cdot \mathbf{D} \cdot \hat{\mathbf{S}} = D_z \hat{S}_z^2$).

We begin by defining the divacancy axis (here the c-axis) as the z coordinate. Then, we select one of the perpendicular directions as our x drive axis. Finally, for this derivation we will assume a static B_z and a time-varying transverse magnetic field:

$$B_x(t) = s(t) \cdot \sin(\omega t + \phi) = I(t) \cdot \cos(\omega t) + Q(t) \cdot \sin(\omega t) \tag{3.10}$$

Where $s(t)$ corresponds to the amplitude envelope, ω is the drives frequency and ϕ is an arbitrary phase. We note that in practice it is often useful to decompose this signal into an in-phase quadrature $I(t) = s(t) \cdot \sin(\phi)$ and out-of-phase quadrature $Q(t) = s(t) \cdot \cos(\phi)$ since these can easily be generated using an IQ modulator and a high-frequency tone (at ω).

So taking all of these assumptions into consideration, we write down our effective Hamiltonian as:

$$\hat{H} = D_z \hat{S}_z^2 + \gamma^e \left(B_z \hat{S}_z + B_x(t) \cdot \hat{S}_x \right) \tag{3.11}$$

By defining $\hat{H}_0 = D_z \hat{S}_z^2 + \gamma^e B_z \hat{S}_z = \hbar\omega_+ \left|+1\right\rangle \left\langle+1\right| + \hbar\omega_- \left|-1\right\rangle \left\langle-1\right|$, we can then split the Hamiltonian into a time independent part and a time dependent part.

$$\hat{H} = \hat{H}_0 + \gamma^e B_x(t) \cdot \hat{S}_x \tag{3.12}$$

We can then use the static part of the Hamiltonian to define a rotating frame $\hat{M} = e^{i\hat{H}_0 t/\hbar}$. Following the standard interaction picture transformations, we can convert the effective state and operators from the lab frame to the rotating frame.

$$\left|\psi_{rot}\right\rangle = \hat{M} \left|\psi_{lab}\right\rangle \tag{3.13}$$

$$\hat{A}_{rot} = \hat{M} \cdot \hat{A}_{lab} \cdot \hat{M}^\dagger \tag{3.14}$$

With these definitions out of the way, we now want to examine our Hamiltonian in this rotating frame.

$$\hat{H}_{rot} = \hat{M} \cdot \hat{H} \cdot \hat{M}^\dagger \tag{3.15}$$

Computing this, we find:

$$\hat{H}_{rot} = \hat{H}_0 + \frac{\gamma_e s(t)}{\sqrt{2}} \cdot \sin(\omega t + \phi) \begin{pmatrix} 0 & e^{i\omega_+ t} & 0 \\ e^{-i\omega_+ t} & 0 & e^{-i\omega_- t} \\ 0 & e^{i\omega_- t} & 0 \end{pmatrix} \tag{3.16}$$

Here it is useful to start making approximations. In particular, we will make use of the rotating wave approximation (RWA) which argues that rapidly rotating terms in the Hamiltonian will average out. To be more specific, we say that a frequency ν is "fast" if $\nu \gg \frac{\gamma_e s(t)}{\sqrt{2}}$. In this case, we will eliminate every term rotating at $\omega + \omega_+$ and $\omega + \omega_-$. We will also define $\delta_+ = \omega - \omega_+$ and $\delta_- = \omega - \omega_-$. This transforms our Hamiltonian to:

$$\hat{H}_{rot} = \hat{H}_0 + i\frac{\gamma_e s(t)}{2\sqrt{2}} \begin{pmatrix} 0 & e^{-i(\delta_+ t+\phi)} & 0 \\ -e^{i(\delta_+ t+\phi)} & 0 & -e^{i(\delta_- t+\phi)} \\ 0 & e^{-i(\delta_+ t+\phi)} & 0 \end{pmatrix} \tag{3.17}$$

Here there are three interesting cases to consider:

- First, when $\omega = \omega_+ = \omega_-$. This is the situation when $B_z = 0$. Here diagonalizing the matrix yields a dark state $(|+1\rangle - |-1\rangle)$ which does not couple to the $|0\rangle$ state and a bright state $(|+1\rangle + |-1\rangle)$ which does couple under drive.
- Second, when $\omega = \omega_+ (\delta_+ = 0)$. Here we assume large δ_- and can therefore once again use the RWA to eliminate terms oscillating at frequency δ_-. Using these conditions, we get

$$\hat{H}_{rot} - \hat{H}_0 = i\frac{\gamma_e s(t)}{2\sqrt{2}} \begin{pmatrix} 0 & e^{-i\phi} & 0 \\ -e^{i\phi} & 0 & 0 \\ 0 & 0 & 0 \end{pmatrix} = \frac{\gamma_e}{2\sqrt{2}} \begin{pmatrix} 0 & I(t) + iQ(t) & 0 \\ I(t) - iQ(t) & 0 & 0 \\ 0 & 0 & 0 \end{pmatrix} \tag{3.18}$$

- Third, when $\omega = \omega_-(\delta_- = 0)$. Similarly, we get:

$$\hat{H}_{rot} - \hat{H}_0 = i\frac{\gamma_e s(t)}{2\sqrt{2}} \begin{pmatrix} 0 & 0 & 0 \\ 0 & 0 & -e^{i\phi} \\ 0 & e^{-i\phi} & 0 \end{pmatrix} = \frac{\gamma_e}{2\sqrt{2}} \begin{pmatrix} 0 & 0 & 0 \\ 0 & 0 & I(t) - iQ(t) \\ 0 & I(t) + iQ(t) & 0 \end{pmatrix} \tag{3.19}$$

From this, we can choose either the $\mathbb{S}_- = \{|0\rangle, |-1\rangle\}$ or $\mathbb{S}_+ = \{|0\rangle, |+1\rangle\}$ basis to implement our abstracted qubit state. In either case, the Hamiltonian in this reduced qubit space will be:

$$\left[\hat{H}_{rot}\right]_{\mathbb{S}_\pm} = \frac{1}{2}\left[\omega_\pm\left(\mathbb{I} - \sigma_z\right) + \frac{\gamma_e I(t)}{\sqrt{2}}\sigma_x + \frac{\gamma_e Q(t)}{\sqrt{2}}\sigma_y\right] \tag{3.20}$$

This means that by controlling $I(t)$ and $Q(t)$ we will be able to perform arbitrary single-qubit rotations around the x and y axes.

CHAPTER 4

EXPERIMENTAL TOOLS

Of course, even after we understand all the physics of the divacancy, a lot of the hard work consists in building the experimental tools to enable these measurements. In this chapter, we will aim to describe a few of the various experimental components developed throughout this work. We will touch on:

1. The sample mount and cryogenics
2. The optical setup
3. The electronics and waveform generation
4. The software infrastructure

4.1 Sample mount and cryogenics

Let's begin with a quick discussion of some of the considerations for the cryostat and sample mounts. The main considerations here are:

1. Cooling power at the sample (and Vacuum level)
2. Microwave and DC electronic lines
3. Optical access
4. Tunable DC magnetic fields

4.1.1 Two cryostat configurations

To achieve these goals we went through a few design iterations and settled on the two cryostat configurations shown in figure 4.1. These two configurations differ by only a few components and it is thus easy to switch between them when necessary.

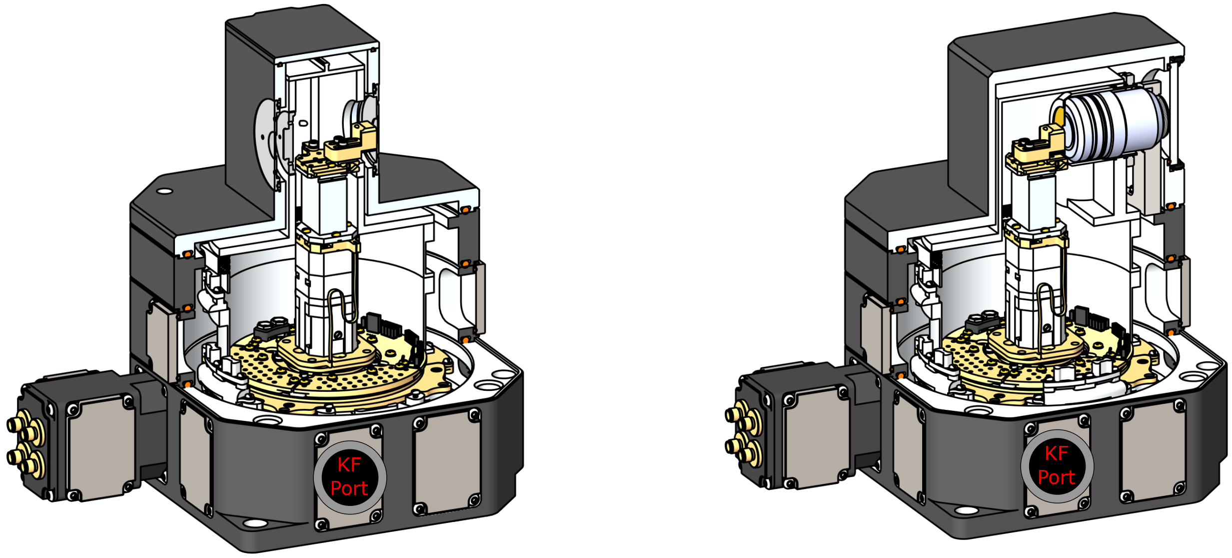

(i) "Out-of-cryo"

(i) "In-cryo"

Figure 4.1: **Cryostat configurations.** Shows the cryostat in two different configurations: (i) The “out-of-cryo” configuration where the objective is meant to be mounted on the XYZ periscope (see section 4.2.4), and (ii) an “in-cryo” configuration where the objective is mounted inside the vacuum shroud of the cryostat.

The “in-cryo” objective configuration has the advantage that it allows the objective to get closer to the sample. This gives us more clearance on top of the sample for things like wire bonds. Additionally, it allows us to minimize the area that is in direct line of sight to a 300K surface. Indeed in the “in-cryo” configuration, the entire objective (which is itself at 300K) is surrounded by an aluminum (Al) radiation shield (at 30K). The front of that shield is made of a piece of Al foil with a ∼5mm hole pierced into it for optical access. Beyond that ∼5mm hole, everything else is well enclosed in the radiation shield (at 30K). This means that in general, we can achieve a lower base temperature with the “in-cryo” configuration. On the downside, however, this configuration does not allow us to move the objective and we, therefore, cannot make use of the XYZ periscope to scan over the sample (instead we need to use a combination of the Attocube stack and the FSM scans). Additionally, since the objective is mounted on the vacuum shroud we have noticed a fair amount of vibration between the sample and the objective. This leads to some instability in the collection efficiency due to the cold head motion and thus periodic fluctuation of our PL count rate.

The "out-of-cryo" objective configuration, on the other hand, requires that we extend our sample mount outside of the radiation shield and bring the sample itself very close to the external vacuum window. Since this means that more of the sample is exposed to 300K radiations, this configuration generally results in a higher base temperature at the sample. Additionally, the thickness of the vacuum shroud can sometimes make it tricky to bring the sample within the short working distance of the objective. On the plus side, this configuration allows us to use the XYZ periscope (which is generally a very repeatable and precise motion control) and does not suffer as much from vibrations of the objective due to the cold head mechanical action.

Other interesting features of this cryostat are:

1. The SMA feedthrough which allows us to feed in MW signals. These are housed in a section that protrudes from the main housing to allow easy access to the back of the panel allowing us to make changes to these cables. We've also substituted the default SMP connector at the back of that panel from SMA connectors which prevents the cable from disconnecting due to thermal cycling.

2. The KF port, which allows us to connect an external turbopump to achieve a better vacuum before cooling down. In our cryostat, this KF flange is connected to a Tee which has a valve followed by an open port for the turbopump on the one side and a blank KF flange on the other. The blank KF flange is intended to be replaced by a fiber feedthrough in future experiments (where fiber access may be important).

3. There are several available DC lines accessible in the cryostat via the built-in header pins and accessible from outside the cryostat through a custom-built breakout board.

4. To monitor the temperature of our cryostat component we have access to several ther-

mometers. Three of them were installed with the unit ("Stage 1", "Stage 2" and "Platform" thermometers) and two were added at custom locations ("User" and "Sample" thermometers). The "User" thermometers are mounted on top of the piezo stack, while the "Sample" thermometer is mounted directly on the same copper piece as the sample (to get a temperature reading as close to the sample as possible).

On the subject of temperature monitoring, we note that although the base of the cryostat generally reaches below 4K, the "User" thermometer is generally at a higher temperature by 0.5-1K and the "Sample" thermometer is generally 1-2K above that. This means that the "Sample" thermometer usually reads 5-7K (and sometimes higher in the "out-of-cryo" configuration). Furthermore, it is actually difficult to know exactly the temperature at the top of the sample (where we are measuring defects) and this is generally all the more complicated due to heating from laser sources and MW driving. Given the importance of temperature to achieve narrow optical lines, care should be taken in future implementations of this setup to improve the temperature at the top surface of the sample (1 or 2 degrees lower would greatly help!).

4.1.2 Sample mount

To ensure the best possible thermal contact, we mount our sample directly on a gold-plated copper piece. We then use a custom PCB to connect to the MW and DC lines using wire bonds.

We make sure to use surface-mounted SMP connectors on the backside of the board (the part facing away from the objective) to because of the tight clearance on the top of the sample.

Our PCB features 4 different MW lines as well as 6 DC lines which is plenty for most of our experiments and can usually allow us to connect multiple samples at a time during a single cooldown

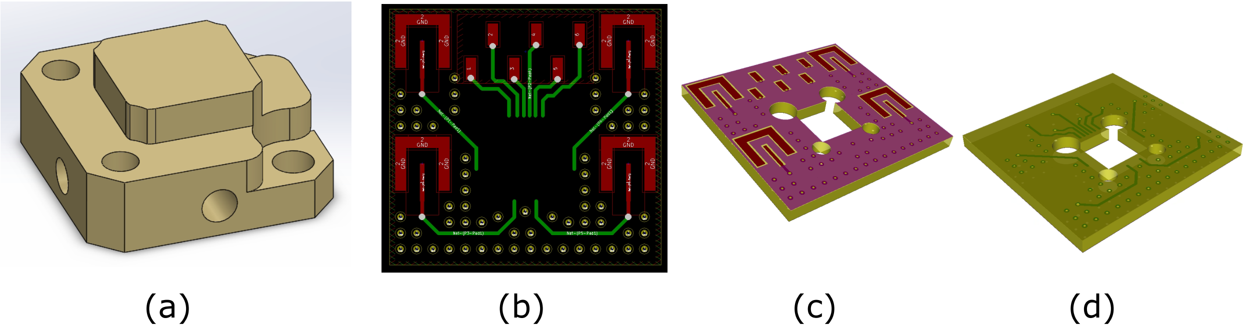

Figure 4.2: **Sample mount.** Shows both the gold-coated copped mount (a) and the associated PCB (b,c,d). The SiC sample is mounted on the center "post" to improve its thermal contact. The PCB is then screwed in with the copper post protruding from the middle and wire bond connections can be made in the wire bonder. The full assembly can then easily be mounted inside the cryostat. (a) Shows the gold-coated copper mount with screw hole to attach: the PCB, the sample thermometer, and the cryostat L-bracket mounting component. (b) Show the PCB with the back layout in red and the front layout in green. A 3d rendering of the back (c) and front (d) of the PCB showing the cutout for the post in the center (front side is facing the objective).

4.1.3 XYZ DC magnetic coils

When only low fields are necessary (for example for zeroing out the external field) we can use three-axis coils. This can generally allow us to reach a few 10s of Gauss at the sample.

These coils were 3D printed with a home-build printer in a PLA material. They were designed to include 4 ferrite cores to enhance the field. Once 3D printed the enameled wire was coiled using a second 3D part (specially designed for this task) and a manual drill. The ferrite cores were then glued in place and the three-axis were connected using standard metal L-brackets.

4.1.4 Goniometer

To apply larger fields (up to ~1000 Gauss), we constructed a goniometer which could rotate around 2 axes (α and β) and move in and out along a third linear axis (R) (shown in figure 4.4). By mounting this goniometer on an XYZ positioner we effectively have 6 axes of motion.

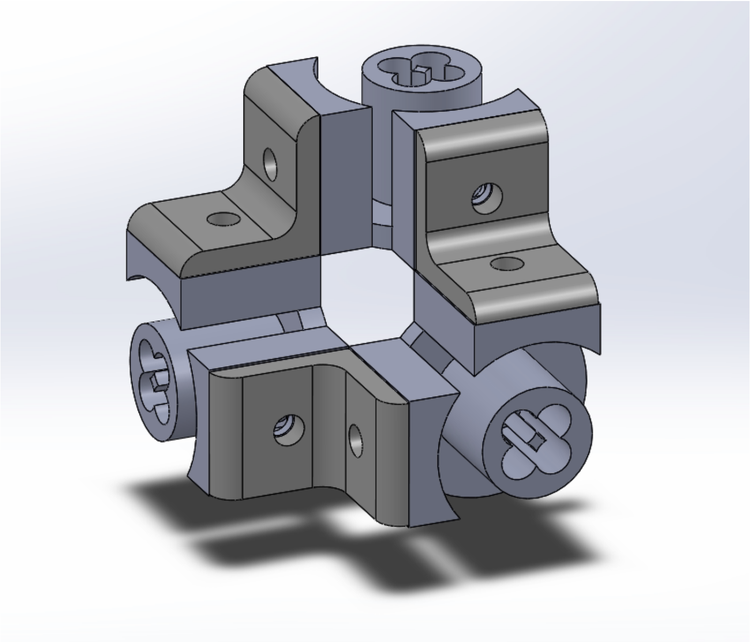

Figure 4.3: **CAD of XYZ magnetic coil.** CAD model showing the construction of or 3 axes coils for varying DC magnetic fields in the low field regime. We coil wires around the center post of each of the three-axis and glue 4 ferrite rods per axis in the center of these posts.

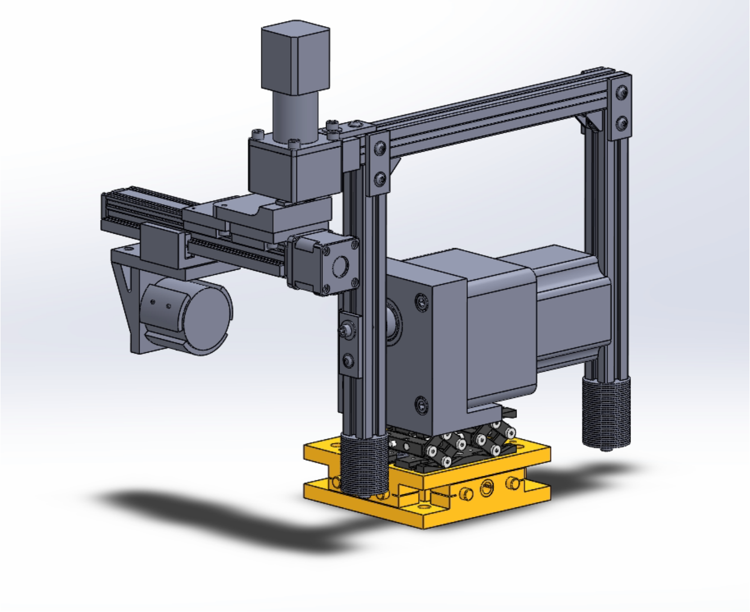

Figure 4.4: **CAD model of Goniometer.** This goniometer is used to precisely move a large permanent magnet around the cryostat. It uses two motorized rotation axis, one motorized linear motion axis, and a 3-axis manual XYZ stage used to align the center of rotation to the SiC sample.

The XYZ stages are manual stages allowing us to align the center of rotation of the goniometer to the sample. Then, we use the (α, β, and R) degrees of motion to move the magnet around the sample. The stepper motors for all three axes each have their motor drivers and are controlled by an Arduino microcontroller board. This board takes cares to remember the state of the goniometer (even when the computer software is reset), drives the correct number of steps to move the motors, and can also implement additional safety feature such as stopping the motion when a push-button is pressed (these push button can be mounted on the goniometer at positions where the motion could hit something is overrotated).

In general, since it is more convinient to work in a spherical coordinates frame centered at the sample, we map the $\{\alpha, \beta, R\}$ coordinates to the $\{\theta, \phi, R\}$ coordinates as follow (*this is implemented in lantz/drivers/arduino/gonioupdated.ino*[57]):

$$\begin{aligned} \cos\theta &= \sin\alpha\sin\beta \\ \cos\phi &= \sin\theta\cos\beta \end{aligned} \tag{4.1}$$

Because the motor itself has a bit of backlash, and some of the components have a bit of play, we have also added springs to the device to constantly pull on the two arms of the goniometer and minimize the effect of this backlash.

Overall, this construction allows us to programmatically tuned the angle of the field very repeatably with at least 0.1-degree accuracy. This is critical when aligning the magnet at high fields (when the magnet is close to the sample) where the field alignment needs to be within less than a degree.

4.2 Optical setup

At the center of all of the experiments presented in this dissertation is an optical setup to prepare and deliver laser light, to collect photoluminescence, and to image our sample.

This setup needs to be both highly reconfigurable/flexible and as simple/robust as possible. To achieve this goal, we have tried to make every part of this setup as modular as possible. Ideally, we isolate modules using single-mode optical fiber. This can allow us to swap modules as needed or realign a module without having to worry about the alignment of the rest of the setup. Of course, not everything can be easily separated into fiber-coupled modules, but to understand how this setup works, it is still useful to group into functionally distinct groups. So let's go through all these groups one at a time.

4.2.1 Modular structure of the laser preparation

To run our experiments, we require several different laser sources. In total, we currently have 5 main laser sources connected to our setup: 2 frequency tunable "resonant" lasers (1070-1145 nm), 1 "off-resonant" laser (905 nm), 1 laser with a wavelength longer than the ZPL ($\sim$1150nm), and 1 "red" laser (710 nm). However, over the course of our research, we have needed to accommodate plenty more wavelengths ranging from the UV to the NIR (see figure 5.5 for some examples).

To make it easy to swap these lasers we have made it a rule to isolate (using single-mode fibers) the "laser preparation modules" (AOM, EOM, polarization control, amplitude control, etc...) from the main confocal setup. The simplest solution here is to keep everything in fiber-coupled components. [1] However, due to some legacy hardware (AOM we already had for example), we also needed to build our laser preparation setups using free-space components. In this section, we'll present the two main laser preparation setup we use.

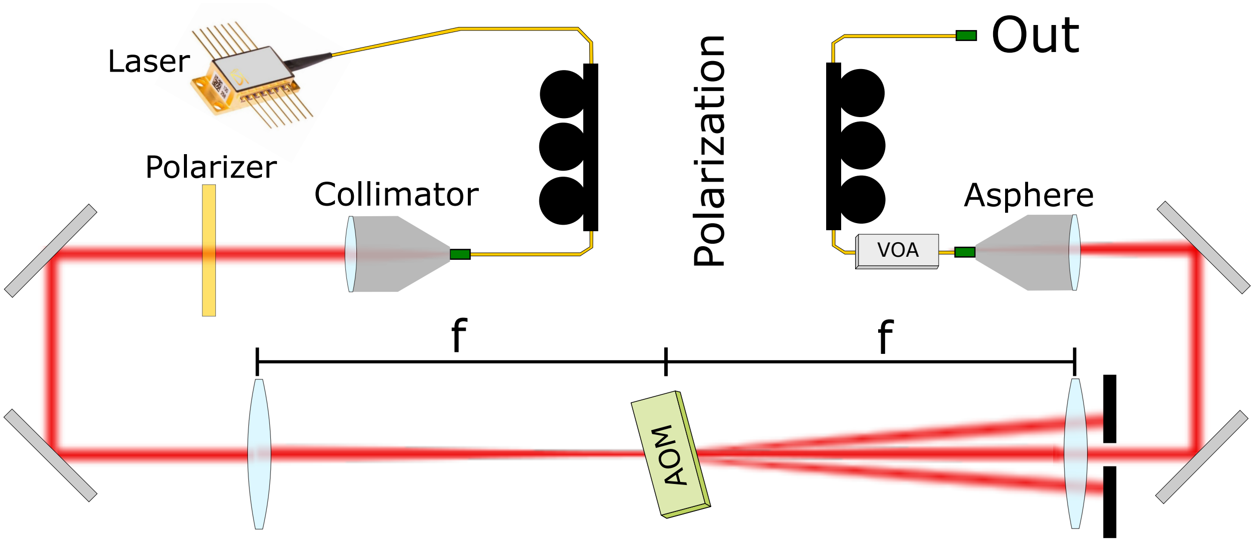

Figure 4.5: **Free-space AOM module.** Simple and compact setup for gating and controlling the polarization of a laser.

4.2.2 Free-space AOM module

First, we show a simple method to construct a modular AOM box. These AOM boxes were mostly built out parts we already had in the lab. These are currently used for the 905 nm, 1150 nm, and 710 nm lasers (and sometimes for some of the more experimental wavelengths as well).

Let's walk through the path here and explain the reasoning behind every component:

1. We begin at the laser. In most cases, we opted for fiber-coupled laser since they are both more modular (can be swapped easily) and have a clean spatial mode.

2. We pass the laser through polarization paddles to enable control of the polarization at the AOM (this is important to maximize efficiency).

3. We collimate the laser at a given beam size (d) using a fiber collimator.

---

1. As an aside, fiber-coupled components are sometimes slightly more expensive than their free-space counterparts (e.g. fiber AOM vs free-space AOM). However, we generally find that once we take into account the cost of building fiber collimation/coupling, mirrors, and mechanical mounts for all the optics, the fiber-coupled components often end up being more economical (as well as practical).

4. We use a linear polarizer to both align the polarization (using the paddle and a power meter) and clean up any residual orthogonal polarization.
5. We put our free space AOM at the waist of a beam focused by 2 lenses (focal length f).
6. We then use an iris on the collimated side of the lens to block all optical modes except the first-order mode from the AOM. Thus the zeroth order is ON by default when no MW is applied to the AOM and the first-order mode is predominant when MWs are applied to the AOM.
7. Then we use an aspheric lens to couple the light back into a single-mode fiber.
8. For some of our lasers, we then use a voltage-controlled optical attenuator (VOA) to tune the strength of the laser. This provides a very large tuning range (several orders of magnitude).
9. Finally, for some cases (where polarization matters), we can also use paddles at the output for controlling the polarization of the final beam in the confocal setup.

The beam size d and the focal length f are chosen to produce a specific beam waist diameter (w) at the AOM. The relationship between d, f, and w can be derived from the paraxial approximation to the Gaussian beam [127]:

$$d^2 = w^2 \left(1 + \frac{f^2}{L_F^2}\right) \tag{4.2}$$

where $L_F = \frac{\pi w}{\lambda}$ is the Rayleigh length of the beam and λ is the wavelength.

In turn, we select the waist size w based on the desired trade-off between efficiency and rise time (this information is usually found on the spec sheet of the AOM). We note here that if we think about how an AOM functions (an optical grating built out of phononic waves) this inherent tradeoff becomes apparent. Indeed for maximum efficiency, we would like a beam that is very large compare to the "grating pitch" (to approximate an infinite plane wave and thus get a better interference pattern). On the other hand, for faster rise time, we would prefer a small beam so that the phonon moving at the speed of sound in the crystal can traverse the beam faster.

4.2.3 Resonant laser characterization and preparation

The most critical laser in our setup is our narrow-line tunable NIR "resonant" laser. We refer to this laser (1070-1145nm) as "resonant" because we generally tune it in resonance with a GS to ES optical transition of our defect.

The wavelength tunability of this laser is critical, but also comes with some challenges. To start, there are a few knobs we can use to control both the emission wavelength and the output power:

1. The positioning of a stepper motor that changes the laser cavity length.
2. The voltage applied to a piezo actuator that can also change the laser cavity length.
3. The current applied to the laser diode.
4. The temperature setpoint of the laser.

Additionally, the laser is not guaranteed to be stable in all of these configurations. When it comes to the lasing frequency, two main issues can occur.

1. The frequency of operation of the laser can suddenly jump with only a small change in the control variable (e.g. piezo voltage). This occurs when the laser cavity suddenly, jumps to a different mode (mode hopping).
2. The laser cavity can be unstable with a particular set of control variables. When this happens the lasing becomes multi-mode and the emission has more than one frequency.

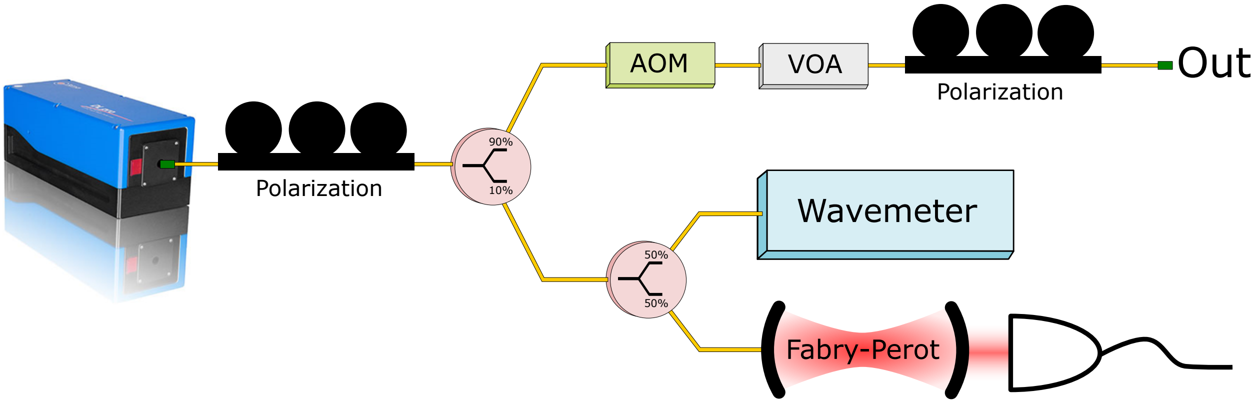

Figure 4.6: **Resonant laser preparation and characterization module.** All fiber-coupled for controlling the polarization, wavelength, and amplitude of the resonant laser while maintaining single-mode operation.

Both of these are very undesirable and means that we cannot simply send a wavelength to the laser and hope to get a narrow line single-mode frequency output. So how do we perform the laser frequency sweeps which are critical to our experiments? For this, we need to build beam characterization and feedback tools (figure 4.6)

Let's walk to the physical setup first and then we'll describe how we can build the associated feedback and control algorithms:

1. Using a Toptica laser and associated fiber coupling module, we couple the light to a single-mode fiber.
2. We then use fiber paddles to align the polarization of the light to the AOM axis.
3. We then split the light into two branches. We send 90% of the light to the "output branch" (this will ultimately go to the confocal setup) and 10% to the "characterization branch".
4. In the "output branch":
    (a) We use both the AOM and the VOA to control the amplitude of the signal. Here the AOM can be used for fast digital (ON/OFF) gating as well as fast

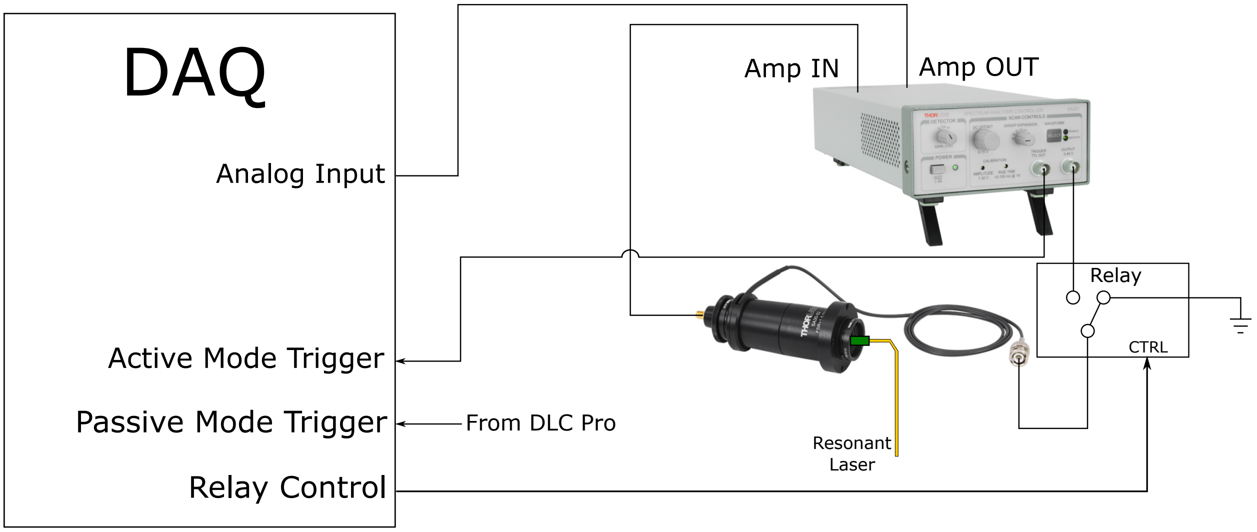

Figure 4.7: **Electrical connections for controlling the Fabry-Perot.** The electrical connections used to control and readout the Fabry-Perot. We generally switch between the "active" and "passive" mode using an external relay as shown above.

analog modulation (by tuning the amplitude of the RF). The VOA is slower, but generally has a larger dynamic range (orders of magnitude for the attenuation), so we usually use it statically to get roughly in the right output range.

(b) We finish with another fiber paddles to control the output polarization.

5. In the "characterization branch", we split the light 50-50 between a wavemeter and a Fabry-Perot. Note that the Fabry-Perot has a small piezo actuator that can be used to adjust the length of the cavity. This piezo is not to be confused with the "laser piezo" which adjusts the length of the laser cavity.

Finally, we note that the Fabry-Perot is operated in two different modes (see figure 4.7). An "active mode" where a piezo actuator in the Fabry-Perot is used to sweep the cavity length and a "passive mode", where the piezo in the Fabry-Perot cavity is kept at a constant voltage (grounded).

Now that we've described all the parts of the setup let's explain how we can automate various operations. As we go along, I will also point out where to find the various component algorithms in our codebases [26, 57] (these are the location at the time of this writing. They may get moved through the years and thus the links may become obsolete, but hopefully, they can still serve as a guide for the current generation of scientists in our lab.)

Ultimately, the goal here is to build out a fully automated method for doing laser frequency sweep. Of course, if we had a continuously tunable laser this would be a lot easier, but since these were not available at our required frequency, we need to do a little more work.

Coarse algorithm to approach target frequency

[This algorithm is implemented in the nspyre/user/gotolaserfreq.py [26]]

First, we need a method for coarsely reaching a given laser frequency (say within 5 GHz). In general, when we want to do a coarse frequency tuning, we use the stepper motor to tune the laser cavity. At a first level approximation one can simply calibrate a model to map the stepper motor value to a lasing frequency (this results in a roughly quadratic model written as $\omega \approx p_0 + p_1 \cdot x + p_2 \cdot x^2$). This gets us close to the right frequency, but because of the hysteresis inherent to the laser motor, it is generally not good enough.

To get closer, we use Newton's method and iteratively measure the current wavelength on the wavemeter and then take a step (using the gradient $\frac{\partial \omega}{\partial x} = p_1 + 2p_2 \cdot x$) toward the target frequency and then repeat until we get within the target range (~5 GHz).

Identify multi-mode lasing

[This algorithm is implemented in the lantz/drivers/thorlabs/fabryperot.py [57]]

The second critical algorithm we need is a method for checking whether or not our laser is multi-mode or not. This is done using the Fabry-Perot in active mode. In this mode, the laser is kept in the same state while we sweep the Fabry-Perot cavity. We synchronize (using a trigger from the Fabry-Perot controller) this piezo sweep with an analog acquisition of the

Fabry-Perot detector signal.

When the laser emission is single-mode, the resulting time-trace looks like a few[2] equally spaced peaks of approximately equal amplitude (each peak corresponding to the cavity length passing through a range where it is resonant with the current laser frequency).

When the laser emission is multi-mode, additional peaks of varying amplitude start appearing in the sweep. These are caused by the other modes of the laser.

Thus, if we take a sweep, counting the number of peaks (using a peak detection algorithm), and measure the variance in the amplitude of these peaks we can establish whether or not the laser is multi-mode. We consider the laser single-mode if the number of peaks is below a certain threshold (below 4 for our experimental parameters) and the variance in the amplitude of these peaks is also below a certain threshold.

Sweeping over a narrow range of laser frequencies

[This algorithm is implemented in the nspyre/user/taskvslaserfreq.py [26]. This code combines both the narrow and wide range frequency sweeps, but we will break it down into different subsections to help explain the various parts.]

Here we want to start building a narrow frequency sweep on the laser. To get to a given frequency, assuming that we are already close-by, we can adjust the piezo voltage. Although we can have a rough idea of how much the laser frequency changes per piezo volt, this is generally not precise enough (without constant calibration). To get around, this problem, we once again make use of Newton's method (with a fixed gradient).

In practice, this is the algorithm:

1. Step toward the right frequency using the laser piezo.

2. Measure the laser frequency on the wavemeter.

---

[2] The exact number of these peaks depends on the overall amplitude of the voltage sweep on the piezo. We have found that with our experimental parameters (Fabry-Perot FSR, voltage amplitude, wavelength, etc...) this is almost always about 2 to 3 peaks.

3. Repeat step 1 and 2 until we are close enough to the target frequency (within a certain delta value).

4. Verify that the laser is still single-mode and if not raise an error (this means the sweep was not narrow enough!).

5. Take a measurement (this measurement is often counting the number of photoluminescent single-photon from our defect).

6. Step the desired target laser frequency and go back to step 1.

Optimizing the dynamic range of the laser piezo sweep

[This algorithm is implemented in the nspyre/user/ctroptimize.py [26].]

As we have seen in the previous section, it is possible to controllably sweep the laser frequency over a “narrow range”. But how narrow does that range need to be? The answer to this question is determined by the “continuous tuning range” (CTR) of the laser. The CTR is the range in which it is possible to smoothly vary the laser frequency (by tuning the piezo voltage) without mode-hop or multi-mode behavior. This CTR is determined by various laser parameters: the emission frequency, the diode current, the piezo-feedforward value, and the diode temperature.

The DL pro (tunable laser) manual describes how one can manually maximize this CTR. However, since this process can be time-consuming and since we need to do it many times through a full frequency sweep, we want to automate this process.

For this purpose, we use our Fraby-Perot in the passive mode (where the Fabry-Perot piezo is grounded). We generate a triangular voltage sweep (generated at one of the output ports of the DLC-pro) and feed this control signal back into one of the input ports of the DLC-pro. This input is set up internally to adjust the laser piezo voltage, thus resulting in a piezo sweep which in turn results in a laser frequency sweep. We also use this sweep as a "digital trigger" to synchronize the acquisition of the Fabry-Perot signal on the DAQ. [3]

Ideally, this laser frequency sweep would result in equally spaced peaks corresponding to points in the sweep where the laser frequency goes into resonance with the Fabry-Perot cavity. However, when the laser mode-hops or goes multi-mode the signal from the Fabry-Perot, will feature uneven peaks (both in spacing and in height). Thus, by analyzing this signal we can get an idea of how wide we can expect the CTR to be.

To do this analysis, we first run a peak detection algorithm that returns the peak locations (x_i) and normalized amplitude (A_i, where $max_i A_i = 1$). We then compute one of the following error metrics as a proxy for how "good" our CTR is:

1. "Peak height uniformity"[4]: $N \cdot \left(\sum_{i=0}^{N} (1 - A_i)^2\right)^2$
2. "Average peak spacing maximization": $-\frac{1}{N} \sum_{i=0}^{N-1} (A_{i+1} - A_i)^2$

To put it all together, we write a function that sweeps the laser, measures the Fabry-Perot, and evaluates the CTR via an error metric. We can then feed this function into an optimizer which will vary the laser current and the piezo-feedforward to try to get the best possible CTR (the lowest value of the error metric). The exact optimizer that is used here can vary, but they should account for the fact that we do not have a derivative of the function to be optimized and the function can behave stochastically (ie some randomness in the output of the function). In the past, we have successfully used the following two optimizers:

1. DLib global search function
2. Covariance matrix adaptation evolution strategy (CMA-ES)

---

[3] Although it may not be ideal to use an analog signal as a digital trigger, we have found that in practice this results in a relatively stable phase of the acquisition with respect to the voltage sweep.

[4] Note that here since we multiply by N (rather than dividing by N like a mean) this equation also tends to penalize large numbers of peaks. This implicitly, means that we are also trying to maximize the peak spacing, so this could be seen as a "hybrid" error metric.

Using this automated algorithm we can generally find a large viable CTR at almost any user-specified frequency. Occasionally, if we notice that we are working in a frequency regime where it is hard to get a large CTR, we may also try to vary the laser temperature.

Finally, it is important to note that this algorithm is aimed at enabling large tunable sweeps, but this comes at the cost of variations in power. Indeed, because one of the optimization parameters is the diode current, every run of the optimizer potentially results in a different current, and thus in a different laser power. However, these variations are generally not too much of a problem when we simply aim at getting a broad and coarse PLE spectrum (this is what the sweep is most often used for).

Broad laser frequency sweep

[This algorithm is implemented in the nspyre/user/taskvslaserfreq.py [26].]

Finally, we can put all of the previous techniques together to implement a broad laser frequency sweep. This works as follow:

1. If necessary, use the laser cavity stepper motor to approach a target frequency (see “Coarse algorithm to approach target frequency”).
2. Optimize the current and piezo feedforward to maximize the CTR (see “Optimizing the dynamic range of the laser piezo sweep”).
3. Use the piezo to get to the exact target frequency (see “Sweeping over a narrow range of laser frequency”).
4. Test whether the laser is still single-mode (see “Identify multi-mode lasing”). If it’s multi-mode, go back to step 1, otherwise continue to the next step.
5. Take a measurement (e.g. counts from the defect).
6. Update the target frequency and go back to step 3.

This process is repeated until we have swept over the entire laser frequency range. Notice that since step 2 requires the passive mode on the Fabry-Perot and step 4 requires the active mode, we will also need to take care to flip the relay appropriately throughout the frequency sweep.

4.2.4 Confocal Microscope

Most of our experiments revolve around the use of a confocal microscopy setup. This setup's primary aim is to combine and deliver various lasers excitations to the defect and collect, from the same location on the sample, the photoluminescence from the defect. The word confocal simply refers to the fact that the focus of the excitation laser beam should be the same as the focus of the collection path.

In the following sections, we will explore all the various functional blocks (shown in figure 4.8) in this setup and then conclude with a discussion of one or two improvements we have recently made to the setup to improve the collection efficiency.

Laser Coupling

The main purpose of this block is to combine all the different excitation frequencies into one single optical path. In general, we need:

1. A "resonant" path to connect the output of the narrow-line tunable laser setup (OUT port in figure 4.6).
2. An "off-resonant" path to carry our 900-980nm excitation.
3. A short-wavelength path for the "repump" excitation. This is often red light (∼710 nm), but it can accommodate anything between 800 and UV (∼400 nm).

Ideally, every laser path first encounters a cleanup filter (although we do not currently have one in the repump path it may be a nice thing to add at some point). This cleanup

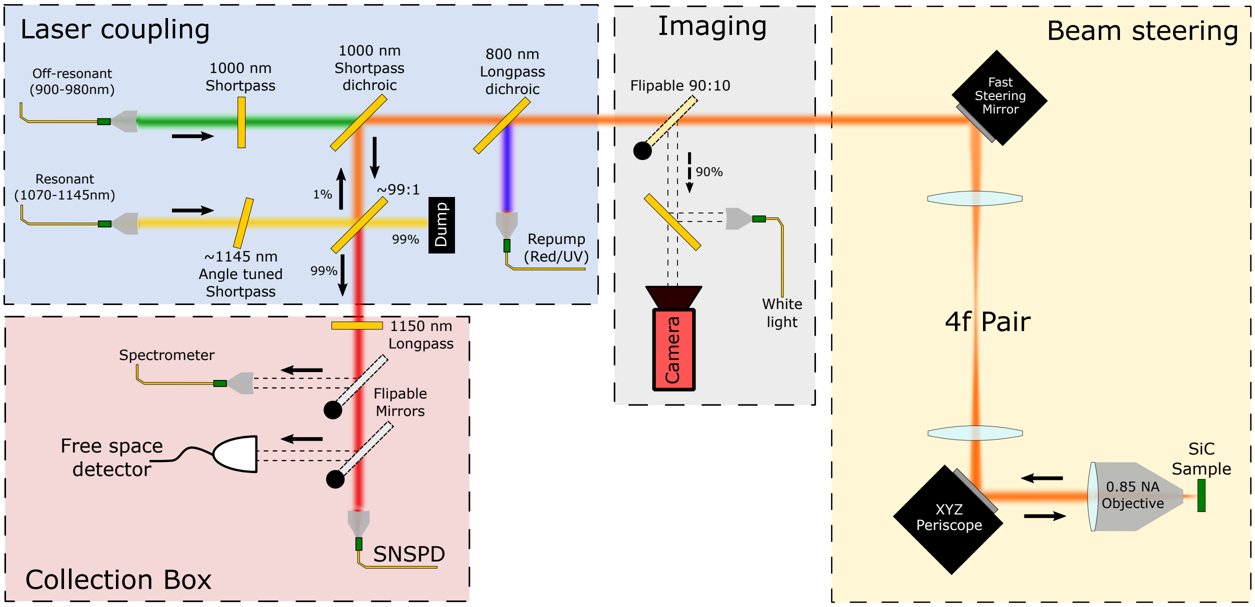

Figure 4.8: **Confocal microscope setup.** Schematics of the current confocal microscope setup. Although in practice this is all one free-space optical setup, we have grouped the various components into the different functional blocks. Note that for simplicity, we have omitted mirrors, irises, and other alignment components. Thus this schematic does not represent all the components on the optical table but rather aims to describe the setup functionally. Here, we've represented the highest energy visible wavelength (800nm and shorter) in blue/purple, the off-resonant laser (900-980nm) in green, the resonant laser (1070-1145 nm) in yellow, and the photoluminescence (at or above the ZPL wavelength). The orange beam represents a mixture of excitation wavelengths and photoluminescence. The dashed lines represent paths that are not active in the "standard photoluminescence experiments" because the associated optical component is flipped out of the optical path. These alternate paths are used for specialized tasks.

filter can be a bandpass or, more often, a short pass. This filter aims at eliminating any residual emission of the laser at a wavelength longer than the turn-on of the collection box's long pass filter.

For the "resonant" path this is especially important since the emission of that laser is very close to the turn-on of the collection filter. Here use a 1150nm short pass which we angle tune to achieve a cut-off around 1145nm.

Most lasers are coupled together using a 45-degree dichroic mirror which lets through one set of frequencies and reflects the others. To coupled in the resonant light we make use of a $\sim$99:1 splitter. This is implemented using a simple piece of glass coated with an anti-reflection coating. The reasoning for this technique comes from the following few criteria:

1. We want to transmit as much of the collected photons as possible.
2. To do entanglement we want to collect "ZPL photons" at the same frequency as the resonant laser.
3. We generally need very little resonant light to excite our defects.
4. We want to tune the polarization of the resonant light without changing the power of that laser at the sample too much.

Since dichroics generally don't satisfy criteria 2 and 4, we need something different. Here a polarization beam splitter could do satisfy 2, but would certainly not satisfy 4 and would probably hurt the collection efficiency (criteria 1). Here the realization that we need very little power at the defect (criteria 3), which stems from the fact that the defect transitions are very efficiently pumped by the resonant laser, is the condition which greatly helps us find a good solution (a piece of glass with an anti-reflection coating). This means, we simply discard $\sim$99% of our resonant laser (equivalent to an $\sim$OD2) at that interface.

In practice, we have found that the 45-degree AOI compensation plates from Thorlabs more or less satisfy our requirements. Two main criteria to look for when choosing which one to get are:

1. Largely transmissive 95-99%.
2. Reflections (∼1-5%) are not very polarization-sensitive around the resonant laser's wavelength.

Imaging

The purpose of this block is to get a live image of the sample and allow us to roughly align both the xy position and the z distance (to adjust the focus) within a few microns where we wish to do our experiments. This box is usually turned on when doing this alignment but is then turned off (the flippable beam-splitter is lifted out of the beam path) for the actual experiments.

Here are a few things to consider when aligning the imaging setup:

1. We need a lens in front of the camera CCD. Ideally, this lens is adjusted such that the focus of the camera is at "infinity". This is because the image produced by the objective will be almost collimated and thus appear to be coming from infinitely far.
2. We should try to keep the imaging setup as close to the sample as possible to avoid the image becoming too small on the camera.
3. When using a 4F-pair (in the beam-steering block) with a C-coating (anti-reflection coating for the NIR) we generally get a lot of reflection in the visible spectrum. This means that if our white light beam is perfectly parallel to the optical path, a lot of that white light will reflect off the lenses and go straight back into the camera. To mitigate this issue the solution is to align the white light such that it still hits the FSM at the same point, but not-parallel to the optical path (at an angle). This means that the light will still reach the objective (if it is at the same position on the FSM as

the optical path it will also also be at the same position on the objective. see "Beam steering" section), but will reflect on the lenses at an angle and not get coupled back in the camera.

Beam steering

Here the goal is to aim both the excitation beam and the collection path at a specific location on the sample. This process would ideally cover large areas of the sample, be precise (∼100nm scale), repeatable, and fast.

For maximum flexibility, our setup contained three different beam positioning system each with their own set of advantages and disadvantages:

1. Fast steering mirror (FSM): This mirror can rotate along two axes to deflect the optical path. The 4F system then ensures that the beam always hits the back of the objective and maps a deflection at the FSM to a variation in the angle of incidence of the beam in the objective (this, in turn, moves the focus on the sample). This method is fast, repeatable, and precise. Unfortunately, it can only cover a small range (order $100\mu m$) on the sample and must therefore be combined with more macroscopic movements.

2. XYZ periscope: This method can cover large areas of the sample, and is both precise and repeatable. Unfortunately, it can only be used in the "out-of-cryo" objective configuration and it is not as fast as the FSM.

3. XYZ Attocube piezo stack: Although not shown in figure 4.8, we also mount our sample on an Attocube piezo actuator. This actuator allows us to cover large areas even when working with an "in-cryo" objective configuration. Unfortunately, it lacks precision, repeatability, and speed. Here the repeatability issues are particularly limiting and stem from the fundamentally random steps inherent to the "stick-slip" actuators.

Collection box

This section of the setup is where all the photoluminescence from the divacancy is collected. Although the entire setup is enclosed for laser safety reasons, here the enclosure is also functionally important. Indeed it is important to isolate this part of the setup from outside light (e.g. room light) and from any lights from the lasers. Therefore the collection box is enclosed on all sides and we simply poke a hole of about 1 inch in the enclosure to let the collection path in. This hole is itself more or less covered by our long-pass filter which eliminates any shorter wavelengths.

Our most common/important detection method uses a fiber-coupled superconducting nanowire single-photon detector (SNSPD). Therefore, this optical path is prioritized by being the default path when the flip mirrors are lifted out of the path. This removes possible flip mirror repeatability issues and ensures that the alignment is maintained for that path.

The two additional paths are a spectrometer input, which is useful to take photoluminescence spectrums, and a free-space detector, which can be used for better collection efficiency on ensemble measurements.

Improvments

Over the last year or so, we decided to build a new setup both to increase the throughput of our experiments, but also to explore new ways to improve collection efficiency. These somewhat simple redesign changes, have already enabled us to increase the number of collected photons by roughly 80% (from about 50kcnts to 90kcnts) and are expected to deliver even more improvements in the months to come.

The basics two guiding principle for this redesign were:

1. Reduce the number of optical elements between the objective and the collection box.
2. Reduce the distance between the objective and the collection box.

To this end we made the following modifications:

1. Remove the 4F pair and use the out-of-cryo XYZ periscope for beam steering. This means that our objective needs to be outside the cryostat, which puts tight requirements on the distance from the outside of the cryostat to the sample (limited by the objective focal length ∼1mm). On the upside, this brings the collection much closer to the sample and removes some optics from the collection path.

2. Move the 1000nm short-pass dichroic right before the beam steering block (periscope). This again, bring the collection closer to the sample and remove some extraneous optics (ie the 800nm long-pass) from the collection path.

3. Addition of a deformable mirror in the collection box right before the fiber coupling. This adaptive optic will aim to reshape the mode of the light coming from the defect to help it to mode match with the gaussian mode of the SM fiber. This could result in significant improvements to collection efficiency (perhaps up to a factor of 2). For example, some results in the NV center [17] have shown about twice the count rates in multi-mode fibers vs their SM counterparts.

4.3 Electronics

Besides the optical setup, the experimental infrastructure we built also involved an electronic side. In this section, we will detail some of these electronics. Broadly, we will subdivide this section into a microwave (MW) generation electronic setup and a pulse counting electronics setup.

In addition to these two electronics setups, a critical component of our electronics is the arbitrary waveform generator (AWG). This device essentially acts as the central synchronization device and ideally would drive:

1. The AOMs gating and analog modulations

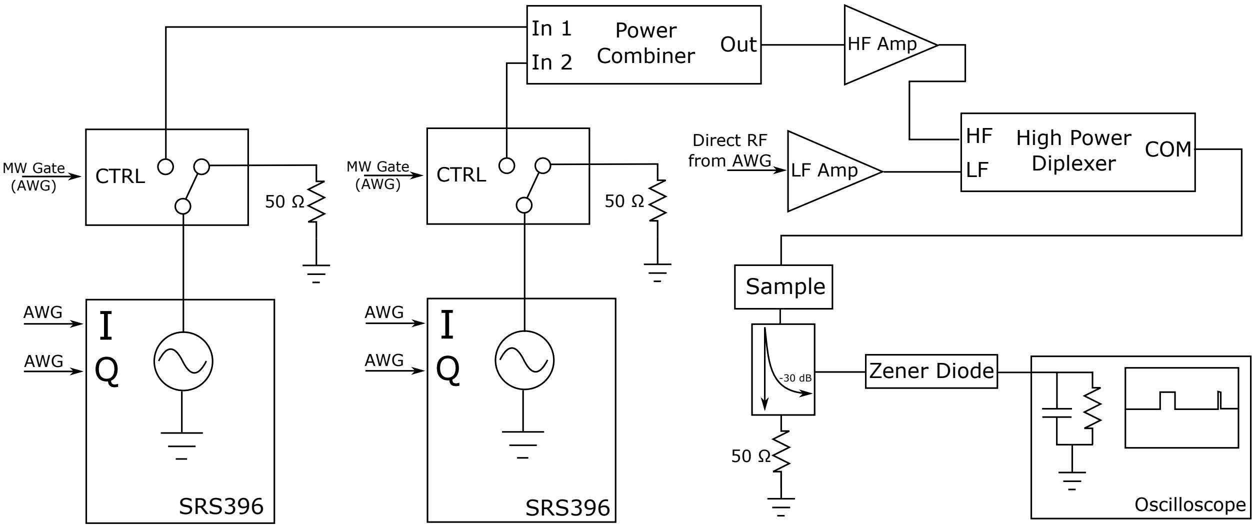

Figure 4.9: **Microwave Electronics.** Diagram of the electronics used to generate deliver the MW signals to the sample.

2. Providing IQ signals and gating the MW sources
3. Direct RF generation for frequency ∼100MHz or less (e.g. strongly coupled nuclear RF drive)
4. Gating and Routing of pulses from the SNSPD
5. Triggering of the time tagger

Because the number of potential AWG connections needed exceeds the total number of channels from the AWG, we often end up setting unplugging the unnecessary channels for a given experiment (for example when we don't perform strongly coupled nuclear spins experiments we may unplug the direct RF driveline). Ideally, we would get an AWG with more channels (or a second AWG), but for the experiment in this dissertation, everything was run using only AWG5014C (4 analog channels and 8 digital markers).

4.3.1 Microwave Generation

The goal of this setup is to produce all the necessary microwave (MW) signals to drive transitions in the GS. There are generally two ranges of frequency we are interested in:

1. The high-frequency (HF) range (referred to here as MW frequencies) from ∼700MHz to ∼4GHz
2. The low-frequency range (referred to here as RF frequencies) from the kHz regime to ∼100MHz

Although these ranges are approximative (we could certainly also drive between 100-700MHz by tweaking the connections or beyond 4GHz if we are willing to accept some losses), the signals that we need to generate generally in these ranges. We usually use the HF range to drive electron spin transitions (between $|0\rangle$ and $|\pm1\rangle$) and we use the LF range for driving strongly coupled nuclear spins. [5]

These two frequency ranges are amplified separately in a high-power amplifier adapted for that range and outputting respectively 10 and 30 W at saturation. Of course, we generally keep the powers much lower than this to ensure not to destroy the cryogenic cables, the wire bonds, or the sample striplines. The amplified signal is then combined on a high power diplexer and sent towards the sample. By sample here we mean the series of:

1. Cryogenic coaxial cables and connectors
2. Coplanar waveguides on the sample mount PCB
3. Wirebonds to the sample
4. Microstrip fabricated on top of the SiC sample
5. Symmetric output sequence (Wirebonds, CPW, and cryo coax.)

---

[5] This was also designed with mechanical drive in mind, which is certainly also something we can do

There are of course some variations in the way the samples are wired. Some frequent ones include:

1. "Wirebond over the top": It is often quicker to characterize samples without fabricating stripline. In this situation, we usually can simply string a wire bond over the top of the sample surface (trying to keep the wire bond as close to the surface as possible).
2. "Shorted stripline or wire bond": When we are either short on output lines or we "really" want to maximize the power delivery at the sample, we can short the stripline or wire bond very close to the region of interest. This effectively creates a standing wave with a current anti-node at the short. This is generally not the recommended way to operate however because it results in (A) power being reflected into the amplifiers, (B) a potentially varying drive amplitude depending on how far the current anti-node is located (at MW frequencies a few cm can be sufficient to affect the phase of the standing wave), and (C) a lost of visibility on power loss or broken line (when using the standard "transmission" configuration, we can check power transmission by measuring before and after the sample. This is very useful to diagnose when a cable, bond, or stripline is broken).

Once we are through the sample, we generally use a directional coupler to tap a small amount of MW ($\sim$-20dB) into a monitoring circuit. The monitoring is composed of a Zener diode which effectively rectifies the voltage followed by an oscilloscope which both filters out the rapid oscillation (since the input channel is BW limited) and displays the MW envelope (for monitoring). Placing this power monitoring system after the sample also allows us to verify that the MW generation is working correctly (ie pulses are being generated, no coax connection were disconnected and the wire bond and striplines are alive and well!). Finally, the MW are dumped into a high power 50Ω resistors to avoid reflections or standing waves. As much as possible, every part of this setup, including the samples, is designed to be 50Ω matched.

The generation of the RF is usually done directly from the AWG, but could also come from an external RF source.

The generation of the MW frequencies is done using the SRS396 which is a MW signal generator with IQ modulation. The IQ signals generate by the AWG and routed to the SRS396 signal generators. In addition to enabling us to modulate the MW in amplitude (digital gating, analog modulation, and pulse shaping), IQ modulation can also be used to frequency shift the output frequency. This works as follows:

1. The output of the SRS396 in the IQ modulation mode is:

$$S(t) = I(t) \cdot \cos(\omega t) - Q(t) \cdot \sin(\omega t) \tag{4.3}$$

2. We set

$$\begin{aligned} I(t) &= A(t) \cdot \cos\left(\omega_{\text{shift}} t + \phi\right) \\ Q(t) &= A(t) \cdot \sin\left(\omega_{\text{shift}} t + \phi\right) \end{aligned} \tag{4.4}$$

3. Then

$$S(t) = A(t) \cdot \cos\left(\left(\omega + \omega_{\text{shift}}\right) \cdot t + \phi\right) \tag{4.5}$$

This way, we can apply a pulse with an arbitrary frequency ($\omega + \omega_{\text{shift}}$) (within the bandwidth of the IQ modulator), an arbitrary phase ϕ, and a pulse amplitude $A(t)$.

The microwave output of the SRS396 is also gated using fast MW switches. These switches have both pros and cons:

- On the plus side, they completely shut off any microwave drive from reaching the amplifier and can therefore limit the residual MW tone which could accumulate over time and cause slow rotations of the electron spin.

- On the negative side, there is a significant amount of noise generated when these switches transition between their ON/OFF states.

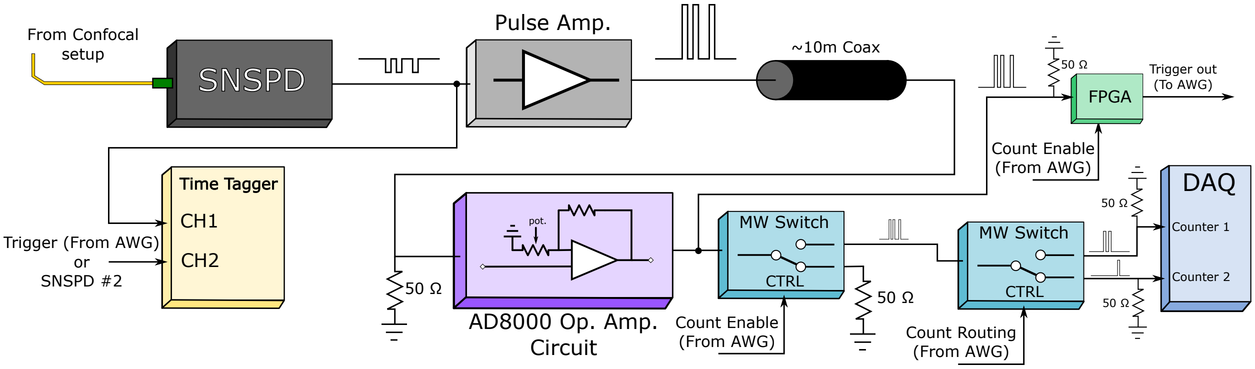

Figure 4.10: **Diagram of the pulse counting electronics.** Diagram showing how the pulses from the SNSPD are routed, amplified, and counted by the readout electronics. Note that although we have represented the SNSPD here as a single "box", it is itself composed of two parts: a cryostat containing the actual detector and an associated control electronics box (which handles the biasing of the detector and first stage amplification of the SNSPD pulses).

So in general, we used the switches when running long experiments with a low number of gates (e.g. T_1 or T_2), and we don't use the MW switches (or keep them in the ON state) when running experiments with a large number of gates (to avoid the state transition noise). Another strategy we could use is to detune the MW carrier (frequency of set on the signal generator) from all of the defects transition frequency and used IQ frequency shifting when performing gates.

4.3.2 Pulse counting electronics

On the collection side of the experiment, we also need electronics to amplify, process, and count pulses coming from our superconducting nanowire single-photon detector (SNSPD). The setup we use for this purpose is shown in figure 4.10. Throughout this circuit, one must be careful to properly terminate lines with 50 Ω to avoid reflection. If this is not done properly, photons could end up being double-counted.

Time tagger

We use a PicoHarp 300 time-correlated single-photon counting (TCSPC) system when we wish to perform experiments we require that we analyze the arrival time of photons. In general, we use the time tagger in two different settings

1. When we want to perform a correlation measurement between two SNSPD channel. This is the case, for example, when we want to do autocorrelation on the PL to confirm the emissions are from a single-photon source (g^2 measurement or auto-correlation measurement). In this case, we split our counts into two SNSPD channels (using a 50-50 fiber beam-splitter) and compare the arrival time of photons on each of the SNSPD channels.

2. When we want to see an average time trace of the photon counts on the detector. In this case, we use the AWG to send a "trigger" pulse on one of the channels of the Picoharp and compare the timing of that pulse with the SNSPD pulse on the other channel. This mode can be used simply as an "oscilloscope for PL" or can be used to accumulate "per experiment" statistics (rather than only average values).

Conveniently, from an instrument setup and software perspective both of these modes work exactly the same way. We can simply stream the time stamp of the pulses on each channel to the computer, which then performs a cross-correlation computation and outputs the resulting time trace.

Pulse amplification

To be able to keep a reasonable amplitude throughout the counting circuit we use various stages of amplification.

First, the SNSPD electronics itself has a low-noise amplifier built-in. We use the pulse from that output to feed-in directly into the time-tagger without any other amplification.

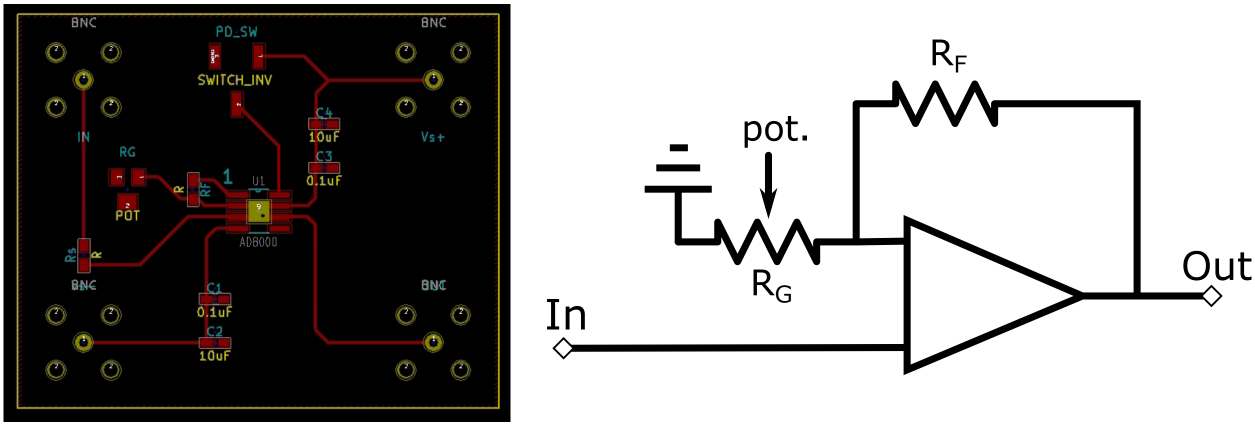

Figure 4.11: **Custom operational amplifier circuit.** On the left, is the PCB layout we design for this amplifier circuit. On the right, is a simplified version of the circuit it implements. The feedback resistor (R_F) is fixed while the resistance to ground is variable (R_G) through a potentiometer. The gain is $G = \frac{R_G}{R_G+R_F}$ and is generally kept around 2. Besides the elements shown in the circuit diagram we also have: an input resistor (R_S) which can help to impedance match the circuit, an enable switch that can toggle the state of the amplifier ON and OFF, and a few capacitors to regularize the power supply.

This allows us to minimize the timing jitter at the time tagger which can be important for measurement such as g^2. Since we are measuring dips of $\sim 15ns$, we would like the jitter to ideally remain smaller $\sim 0.1ns$.

The second stage is a pulse amplifier, which can both invert and amplify the incoming pulses to TTL level. This is generally sufficient in voltage amplitude to trigger instruments such as the DAQ counters.

However, if we want to connect more than 1 input device (each with a 50Ω input) in parallel, the pulse amplifier does not provide enough output current. This current limitation is further exacerbated by the fact that the SNSNPD and pulse amplifier are in a separate room from the rest of the counting electronics and are therefore separated by a 10-15m coaxial cable which can introduce loss. Furthermore, the 2 MW switches that gate the pulses and route them to the correct DAQ channels are also lossy. For all of these reasons, we need to ensure that our pulse can drive sufficient current to supply the various counters. We do this using a custom made operational amplifier circuit based on the AD8000 chip. The PCB we designed for this purpose can be seen in figure 4.11 and is essentially a non-inverting amplifier with a variable gain (adjusted using a potentiometer). We generally tune to about 2 (to compensate for losses and adjust the output voltage to $\sim 5V$), but its main utility is as a buffer which is able to drive the rest of the circuit with enough current.

DAQ counting

This is generally the main way we count photons in most of our experiments. We route the counts from the last amplifier through two switches:

1. A simple "Count Enable" switch: This allows us to register counts only during the readout portion of the experiments. Counts through other portions are ignored. This significantly reduces background noise on the counts (think of all the counts you might expect during off-resonant initialization for example!).

2. A "Count Routing" switch: This allows us to distribute the counts between two separate counters. This is useful to build 2-phases experiments that can be used in differential measurement to reject common-mode noise (in the same manner as a lock-in amplifier).

FPGA counting

Some of the experiments we are ultimately aiming to do with this setup involved fast feedback between the photon counting and the AWG. These generally take the following logical form:

- Wait for the count enable signal to go high (signifying the start of the readout).

- Count the number of photons until the "enable" signal goes low.

- Output a trigger to the AWG provided a certain condition on the count is met (e.g. counts are greater than some threshold).

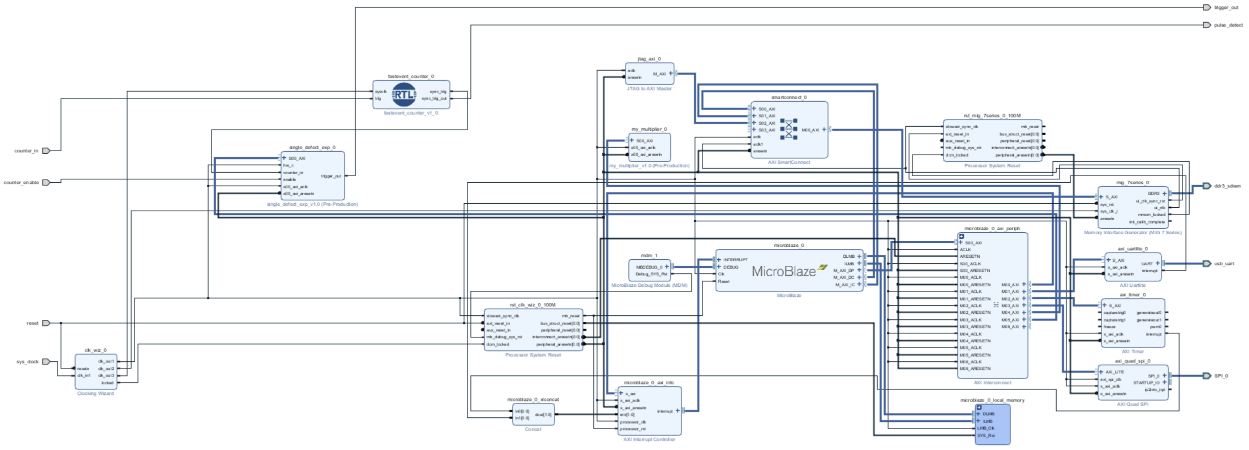

Figure 4.12: **Complete block diagram for FPGA implementation.** This shows the full structure of the logic which is implemented in the FPGA fabric. We include modules such as local registers, DDR3 memory controller, interrupt handler, clock distribution, SPI connections, timers, UART controller, interconnects, etc...

Unfortunately, neither the AWG5014C nor the DAQ can perform these types of conditional operation by itself. For this reason, we built a custom solution based on the Xilinx Kintex-7 FPGA (with some surrounding dev board from NumatoLab called the Skoll). We combine both available IPs and custom VHDL to build a system which can:

1. Count pulses asynchronously when triggered by the "count enable" channel.
2. Process the counts and output a hardware trigger if a certain condition is met (e.g. counts higher then threshold).
3. Provide a continuous counter mode.
4. Is both queryable and configurable from a computer via a USB serial interface.

Our system (shown in figure 4.12 and figure 4.13), is built around the MicroBlaze softcore processor. This processor continuously runs a custom C microcode, which listens for and responds to commands on the USB interface, configures the count processing module, and readout its output via module registers.

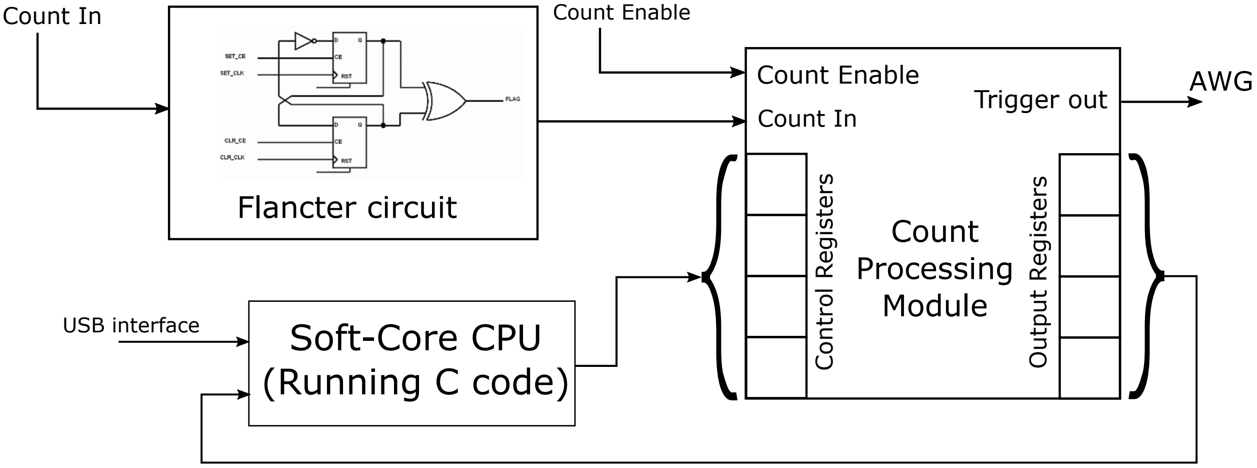

Figure 4.13: **Simplified block diagram for FPGA implementation.** This shows a simplified block diagram showing the main functional blocks. Flancter circuit converts the asynchronous counts to synchronous pulses and passes along to the count processing module. The count processing module handles the counting/triggering logic and can be configured and read out by the CPU. The CPU handles high-level tasks and communicates with the USB interface.

The task-specific blocks include a Flancter circuit and a count processing module. The Flancter circuit can take in asynchronous pulses of any length and convert them into synchronous pulses to be processed by the “count processing module”.

The count processing module has various configuration register to specify various parameters such as: the mode in which it should be counting (continuous, gated, or single-shot gated), the trigger mode (trigger when count are “greater than” or “less than” threshold) and a threshold count. It also features a count register which can be used to accumulate count and read them out through the CPU.

4.4 Software infrastructure

As might be obvious by now, these experiments rely on a large ensemble of instruments, techniques, and algorithms. Ideally, all of these components need to be expressed in a way that permits fast and flexible prototyping of new experiments. To achieve these goals, we wrote a lot of Python software infrastructure and frameworks. Since this code is now commonly used across our group and in other labs in the PME and at Argonne National Lab, I would like to give a brief overview of these tools, the basic ideas underlying them, and a quick overview of the features.

4.4.1 Lantz

Lantz[57] is a framework for standardizing the interface to instruments. Unlike the other software presented in this section, we did not write the core of the framework ourselves. Nevertheless, we used this framework to write custom device drivers for all of our instruments.

Because there is already good documentation for this software, we will not repeat the details here, but it merits a mention here since we have used it extensively to implement our instrument drivers. In short, the strength of this framework is that it provides a uniform interface to communicate with instruments regardless of the underlying way to physical connections (COM port, USB, Raw Socket, TCP server, DLL, GPIB, etc...). At the end of the day, once we've implemented the driver, everything comes down to an initialize/finalize function, along with Feats/DictFeats/Actions attributes. This means that higher-level software can assume this interface and build on top of it. Additionally, Lantz provides unit handling and limits on attributes range (useful to limits instrument to a safe operating regime)

4.4.2 Easy Wave

Easy wave [24] is the language we created to write sequences to the AWG. This language is meant to make it easy to write complex experiments by simply concatenating and superposing pulses using the "+" and "&" operation and standard Python syntax.

For example, figure 4.14 shows how we can construct a series of lines (each line corresponding to a different mw time) by simply concatenating init, mw, readout, and delay pulses. This framework has been very useful when building complex experiments involving hundreds or even thousands of pulses because it allows us to use all the Python features

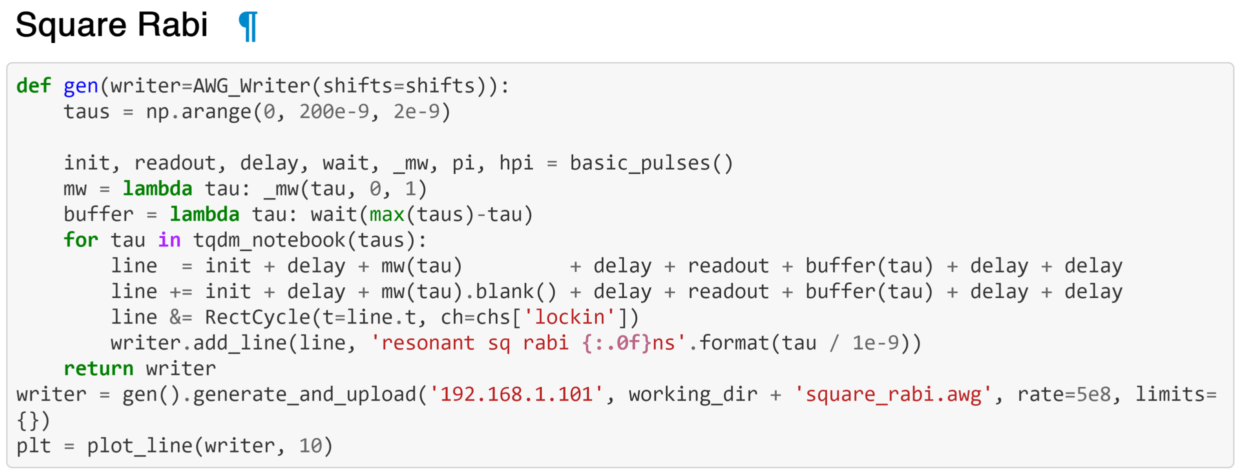

Square Rabi ¶

```
def gen(writer=AWG_Writer(shifts=shifts)):
    taus = np.arange(0, 200e-9, 2e-9)

    init, readout, delay, wait, _mw, pi, hpi = basic_pulses()
    mw = lambda tau: _mw(tau, 0, 1)
    buffer = lambda tau: wait(max(taus)-tau)
    for tau in tqdm_notebook(taus):
        line  = init + delay + mw(tau)         + delay + readout + buffer(tau) + delay + delay
        line += init + delay + mw(tau).blank() + delay + readout + buffer(tau) + delay + delay
        line &= RectCycle(t=line.t, ch=chs['lockin'])
        writer.add_line(line, 'resonant sq rabi {:.0f}ns'.format(tau / 1e-9))
    return writer
writer = gen().generate_and_upload('192.168.1.101', working_dir + 'square_rabi.awg', rate=5e8, limits=
{})
plt = plot_line(writer, 10)
```

Figure 4.14: **Example code for Rabi sequence using Easy Wave.** Example code for building a Rabi oscillation sequence with Easy Wave.

(functions, loops, etc...) to generate waveforms with minimal code. All the phase coherence of the pulses are handled at generation time to allow the user to also prepend pulses (in addition to appending).

More complicated pulse sequences also can use the Block_Writer to described compiled sequences that can help the user save on hardware memory.

4.4.3 NSpyre

NSpyre [26] (Networked Scientific Python Research Environment) is the central framework we have used to coordinate all the experiments presented in this dissertation. In general, this framework aims at making it easy, fast, and user-friendly to develop complex experiments involving: many instruments distributed across the lab, responsive live plotting and GUI, and command-line/notebook scripting capabilities.

Prior attempts

NSpyre is my third attempt at trying to build a software framework to make prototyping of new experiments fast and easy (the third time is the charm!). The first two attempts included:

1. A-Lab: This is a framework I wrote before joining the University of Chicago with the goal of providing a simple way to write GUI that would be decoupled from the underlying experimental code. Because this was so easy to set up, we were able to get it going immediately and used it for about a year.

2. Spyre (Scientific Python Research Environment): This framework was developed in collaboration with my colleagues at the University of Chicago and was aimed at enabling quick prototyping of new experiments that included plotting, and GUI inputs while keeping things simple for the user building new experiments. We largely realized these goals, however, the infrastructure ended up being bulky and monolithic. For instance, if we wanted to add a new experiment or if an uncaught exception occurred, we would need to reload the entire software which could take over a minute.

By combining the lessons from these two previous attempts, I decided to start from scratch and rewrite a third version of the framework: NSpyre!

Basic principles

The basic principles underlying the design of NSpyre are as follow:

- Decentralization: Experiments like the ones presented in this dissertation are complex and involve many instruments distributed across the lab. These instruments cannot always be directly connected to a single computer (some of them may be directly tied to a specialized computer or may have to be shared by many users running different experiments at the same time.). Similarly, we may want to control equipment run experiments, or plot data from different computers (either at different times or simultaneously).

- Modularity: Beyond achieving the goal of decentralization, modularity is also critical to ensure the flexibility of the framework. In particular, one of the core goals of NSpyre is to enable fast prototyping of user code (to implement their own experiments and GUIs). In practice, this means we need a way to inject new user code while minimizing load time and ensuring that bugs in this user code (there will certainly be some!) doesn't crash the whole system.

- User-friendliness: Not everyone running physics experiments is interested in learning the fine details at the core of the system. Most users will simply want to use this as a tool to run their experiments. Therefore, the part of the code that needs to be written by the user should be simple and require only entry-level programming experience.

- Flexibility and extensibility: On the other hand, there will be some users that will want to dive deep and developed new custom modules. For this reason, NSpyre should remain flexible and extensible. Here the modularity plays a big role in accomplishing this objective. Overall, the framework should try as much as possible to get out of the way and not be too restrictive. There is a balance here to be struck with "user-friendliness and standardization" on one side and flexibility on the other. I think the key to this balance is extensibility.

- Collaboration: This is perhaps the single most important principle and philosophy behind NSpyre. NSpyre aims at growing a community of developers and users that can contribute new modules, and maintain/improve the framework. Over time, my hope is that the development will become decentralized, follow industry best practices (code review, unit test, typing, etc...), and that I will become obsolete to the project[6]! It is important that every one sufficiently involved in the project (ideally from different groups or teams) feels like they can have a say in influencing the directions the frame-

---

[6] In fact, as of now, this is already happening with Jacob Feder (University of Chicago) and Micheal Solomon (Argonne National Lab) having taken the lead in the next step for this project!

work takes and the design decisions. If this fails, everybody is likely to go their own way and the project as a whole will not endure.

How it works

[This section will present how the framework works at the moment, but given that this is still evolving, the NSpyre documentation should be the main resource for the most up-to-date information.]

To ensure modularity, extensibility, and decentralization, NSpyre is in reality a combination of several blocks all linked together via a TCP interface. The lower level building blocks include:

- Mongo database: This NoSQL database serves to synchronize the whole system. Experiments (called spyrelets!) can write data to this database and instrument servers can store the latest state of the equipment. The data in this database can then be monitored for changes by other modules which can update whenever something changes (for example the live plotting can update as soon as the experimental data is modified in the database by monitoring for changes).

- Instrument servers: Instrument servers contain the direct connection to the instrument via the Lantz drivers. They can receive commands via TCP from other modules to set/query Feats (or DictFeat) or execute Actions. The server then relays the command to Lantz driver instances and returns the result over TCP. Instrument servers can also post to the Mongo database every time a Feat/DictFeat is either set or query (this helps maintain a good approximation of the current state of all the equipment on the server). The communication was originally implemented via the ZMQ protocol, but it is now being converted to use the RPyC library. Importantly, instrument servers can serve multiple clients asynchronously (not a 1 to 1 connection), and similarly, clients can connect to multiple instrument servers. Instrument servers can contain any number of physical instruments. For simplicity, we can put all the drivers in the same instrument server, or alternatively, we can have multiple servers each running a single device (these servers can either be on the same machine or distributed across the network).

- Instrument Manager: The instrument manager is essentially a list on the client-side that can query all the available instruments on a server and make them available to the user in a seamless way. Using the instrument manager, the user can simply get a list of all the available instruments and then execute operations on them without having to worry about which server contains this instrument.

The "more visible" part of NSpyre is the GUI modules (see some screenshots in figure 4.15). Here are a few of the basic GUI modules built-in:

- View Manager: As data is acquired, it is appended to a Mongo collection in the database. This collection can then be monitored for changes by other processes. In particular, the "View Manager", is a GUI that loads all the default "Views" specified by the various spyrelets currently in the database. A "view" is a way of visualizing the data (ie it specify how the raw data from a pandas Dataframe should be plotted). You can have multiple "Views" for the same data, plotting the data in different ways (e.g. averaged values vs latest values). The "View Manager" is thus a GUI, that enables you to switch between various views for the same spyrelet or different spyrelets. This GUI also allows you to define custom "Views" which allows you to change how the live data is being plotted.
- Instrument Manager GUI: Because Lantz has a standardized interface, we can easily, list all of the instruments Feats/DictFeat/Action and create a GUI which can display them in real-time based on the values in the Mongo database. This means that: (1) any process that query or sets an instrument will send a call to the instrument

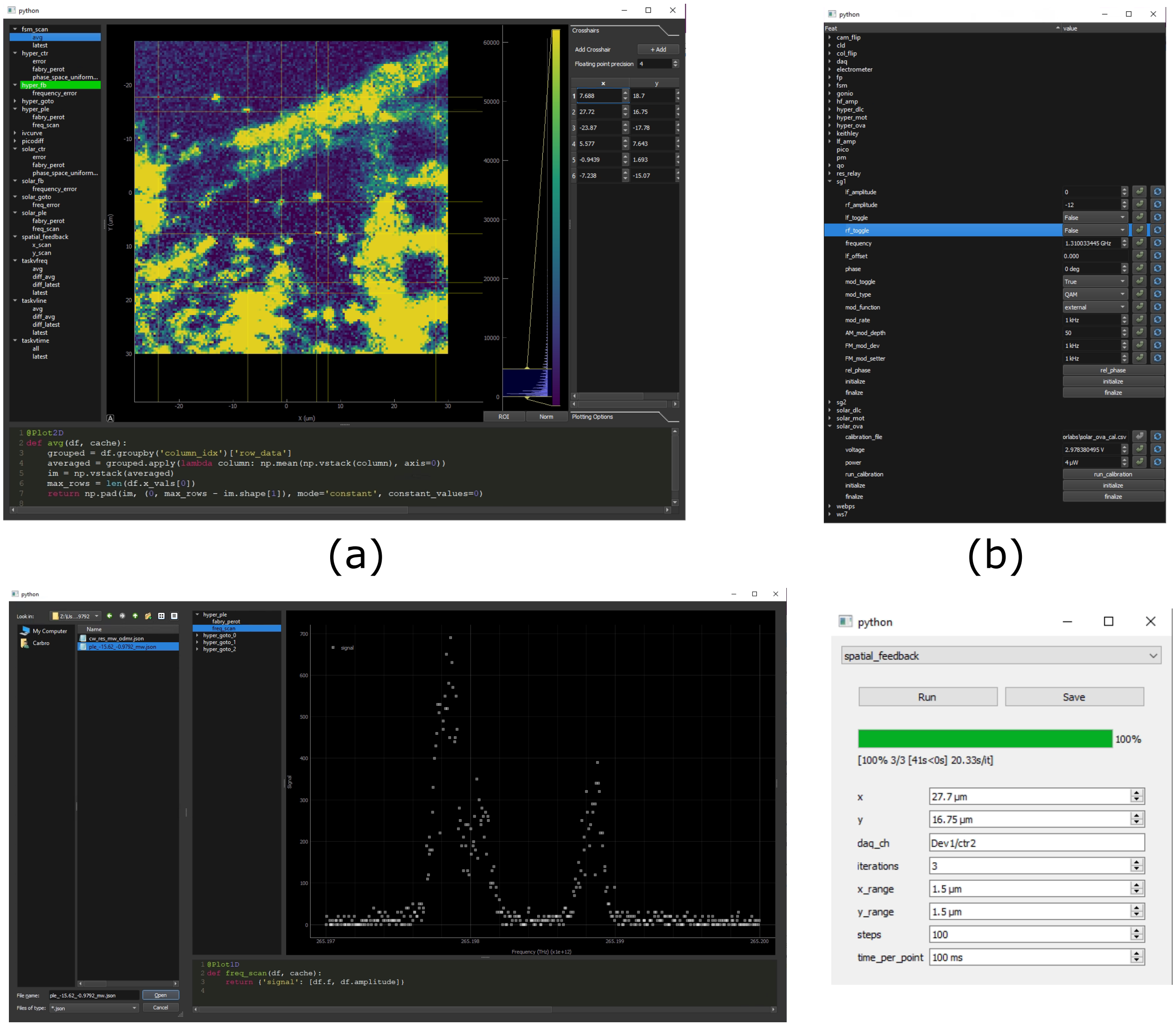

```
@Plot2D
def avg(df, cache):
    grouped = df.groupby('column_idx')['row_data']
    averaged = grouped.apply(lambda column: np.mean(np.vstack(column), axis=0))
    im = np.vstack(averaged)
    max_rows = len(df.x_vals[0])
    return np.pad(im, (0, max_rows - im.shape[1]), mode='constant', constant_values=0)
```

(a)

sg1
lf_amplitude 0
rf_amplitude -12
lf_toggle False
rf_toggle False
frequency 1.310033445 GHz
lf_offset 0.000
phase 0 deg
mod_toggle True
mod_type QAM
mod_function external
mod_rate 1 kHz
AM_mod_depth 50
FM_mod_dev 1 kHz
FM_mod_setter 1 kHz

solar_ova
calibration_file orlabs\solar_ova_cal.csv
voltage 2.978380495 V
power 4 μW

(b)

```
@Plot1D
def freq_scan(df, cache):
    return {'signal': [df.f, df.amplitude]}
```

(c)

spatial_feedback

[100% 3/3 [41s<0s] 20.33s/it]

x 27.7 μm
y 16.75 μm
daq_ch Dev1/ctr2
iterations 3
x_range 1.5 μm
y_range 1.5 μm
steps 100
time_per_point 100 ms

(d)

Figure 4.15: **Examples of NSpyre GUI.** (a) "View Manager" showing the various loaded spyrelets on the left panel, the plotting function used in the code editor at the bottom, the plot itself in the middle with various crosshair pointing to interesting locations in the plot (this can be applied to both 1D and 2D plots). (b) The Instrument Manager GUI, showing a menu of attributes for all the connected instruments which can be monitored and tweaked by the user. (c) Data Explorer, combining a file explorer with a View Manager. This can be used to quickly preview saved data in the form of JSON files. (d) Spyrelet launcher that allows the user to quickly select a spyrelet, set the input arguments, and launch the experiment.

server, (2) the instrument server will execute the command and post any changes in the device state to the Mongo database, (3) the instrument manager GUI will be updated automatically by monitoring for changes in the database. The result is that the Instrument manager is aware of any calls to any instrument made by any of the processes and can react accordingly. Finally, the instrument manager can of course allow the user to set instrument values directly from the GUI allowing for easy configuration.

- Spyrelet Launcher: Although the spyrelet can simply be called from the notebook or the Python interpreter, Spyrelets are also made to be compatible with a GUI interface. In this GUI, the user can select which spyrelet they want to run with what parameters and then simply hit the run button.
- Data Explorer: This essentially combines a “View Manager” and a file explorer to load dataset save as json files. This allows the user to quickly navigate through their file structures and preview/plot the data.

Of course, the idea here is that this framework is extensible, so we can write many more custom GUI modules (each running in their respective process), and they should all be able to synchronize via the Mongo database. Some example of these custom modules could include GUI motion control (with arrows to move a motorized actuator), front panel to monitor an instrument, GUI to allow you to interact with plotted data (for example take a spatial scan and then point and click at a given location to make the confocal microscope point there), and much more...

The last piece of this framework is the structure of the user code itself. This is in the form of spyrelet, which defines an experiment. Currently, the main elements of a spyrelet are:

1. REQUIRE_DEVICES: This specifies the name and device type of every device that

needs to be passed to the spyrelet to run this experiment.

2. PARAMS: This is partially used to generate the Launcher GUI and the handle default units. These specify the type of the arguments to the initialize/main/finalize functions.

3. REQUIRED_SPYRELETS: This is a list of sub-spyrelets which can be used as a subroutine to execute inside the parent spyrelet. This allows the user to reuse subroutine created in the form of spyrelets. For example, one may create a “spatial feedback” spyrelet which can either be used by itself, or as part of a sweep in which we periodically and synchronously want to apply that feedback.

4. CONSTS: This is a list of extra parameters that are unlikely to change from run to run and must thus be specified at the time we instantiate the spyrelet (rather than at the time we run it).

5. initialize/main/finalize functions: These form the core logic of the experiments. “initialize” is run first, then “main”, and then “finalize”. The “initialize” and “main” are functionally equivalent (one is simply run right after the other), but can be used by the user to separate instrument setup from the core logic of the experiment. The “finalize” function, is run regardless of whether the experiment completes, is interrupted by the user, or errors out. This function can thus be used to clean up and safely turn off instruments when necessary.

6. Plot1D/Plot2D: These decorators mark functions that define “Views”. These functions have as input the current data (as a DataFrame) and a cache (which contains temporary information and data). These functions should return either a Dict[str, Trace] (where Trace is a list containing the x and y data as numpy arrays) if it is a 1D plot or a 2D numpy array it is a 2D plot.

CHAPTER 5

QUANTUM SPIN IN CLASSICAL ELECTRONICS

This chapter and figures were adapted from the following publication[5]:

C. P. Anderson*, A. Bourassa*, et al. **Electrical and optical control of single spins integrated in scalable semiconductor devices**. *Science*, 2019. (* Equal contribution)

5.1 Electrical and Optical Control of Single Spins in Scalable Semiconductor Devices

Spin defects in silicon carbide have the advantage of exceptional electron spin coherence combined with a near-infrared spin-photon interface, all in a material amenable to modern semiconductor fabrication. Leveraging these advantages, we integrate highly coherent single neutral divacancy spins in commercially available p-i-n structures and fabricate diodes to modulate the local electrical environment of the defects. These devices enable deterministic charge state control and broad Stark shift tuning exceeding 850 GHz. Surprisingly, we show that charge depletion results in a narrowing of the optical linewidths by over 50 fold, approaching the lifetime limit. These results demonstrate a method for mitigating the ubiquitous problem of spectral diffusion in solid-state emitters by engineering the electrical environment while utilizing classical semiconductor devices to control scalable spin-based quantum systems.

5.1.1 Introduction

Solid-state defects have enabled many proof-of-principle quantum technologies in quantum sensing [23], computation[140] and communications[9]. These defects exhibit atom-like transitions that have been used to generate spin-photon entanglement and high-fidelity single-shot readout[114], enabling demonstrations of long-distance quantum teleportation, entanglement distillation, and loophole-free tests of Bells inequalities[9].

However, fluctuating electric fields and uncontrolled charge dynamics have limited many of these technologies [23, 114, 73, 16, 21]. For example, lack of charge stability and of photon indistinguishability are major problems that reduce entanglement rates and fidelities in quantum communication experiments[114, 73, 16]. In particular, indistinguishable and spectrally narrow photon emission is required in order to achieve high-contrast Hong-Ou-Mandel interference [77]. This indistinguishability has been achieved with some quantum emitters through dc Stark tuning the optical lines into mutual resonance[13, 42]. Meanwhile, a variety of strategies [23, 16, 110, 3, 36] have been proposed to reduce spectral diffusion[150] and blinking[102], but consistently achieving narrow and photostable spectral lines remains an outstanding challenge[137]. In addition, studies of charge dynamics[15, 149] have enabled quantum sensing improvements[23, 30], and spin-to-charge conversion[123] allowing electrical readout of single spin defects[125]. However, these experiments have largely been realized in materials such as diamond where scalable nanofabrication and doping techniques are difficult to achieve.

In contrast, the neutral divacancy (VV^0) defect in silicon carbide (SiC) presents itself as a candidate spin qubit in a technologically mature host, allowing for flexible fabrication, doping control, and availability on the wafer scale. These defects display many attractive properties including all-optical spin initialization and readout[86], long coherence times[34], nuclear spin control[83], as well as a near-infrared high-fidelity spin-photon interface[35]. However, VV^0 have suffered from relatively broad optical lines[35], charge instability[149] and relatively small Stark shifts[42]. Furthermore, the promise of integration into classical semiconducting devices remains largely unexplored. Here, we utilize the mature semiconductor technology that SiC provides to create a p-i-n structure that allows tuning of the electric field and charge environment of the defect. First, we isolate and perform high fidelity control on highly coherent single spins in the device. We then show that these devices enable wide dc Stark tuning while maintaining defect symmetry. Interestingly, we also demonstrate that charge depletion in the device mitigates spectral diffusion thus greatly narrowing the linewidths in the optical fine structure. Finally, we use this device as a testbed to study the photoionization dynamics of single VV^0, resulting in a method for deterministic optical control of the defect charge state. The effects presented here suggest that doped SiC structures are flexible and scalable quantum platforms hosting long-lived single spin qubits with an electrically-tunable high-quality optical interface. The demonstrated reduction in electric field noise can lead to increased spin coherence[80], electrical tuning of dark spins in quantum sensing[58], whereas charge control could extend the memory time of nuclear spins[112]. Additionally, this platform opens unique avenues for spin-to-charge conversion, electrically-driven single-photon emission[145], electrical control[82] and readout[125, 106, 44] of single spins in SiC CMOS compatible and optoelectronic semiconductor devices.

5.1.2 *Isolated Single Defects in a Semiconductor Device*

We first isolate and control single VV^0 in a 4H-SiC p-i-n diode created through commercial growth of doped SiC epilayers. After growth, we electron irradiate and anneal our samples to create single, isolated VV^0 defects. We fabricate microwave striplines and Ohmic contact pads allowing for spin manipulation and electrical gating (Fig. 5.1A) (appendix 5.3). In contrast to other defects in SiC such as the isolated silicon vacancy[143], the divacancy is stable above 1600 $^\circ C$ [126] making it compatible with device processing and high-temperature annealing to form *Ohmic contacts*. Spatial photoluminescence (PL) scans of the device show isolated emitters corresponding to single VV^0 (Fig. 5.1B), as confirmed by second-order correlation ($g^{(2)}$) measurements (Fig. 5.1B, inset)(appendix 5.3). The location in depth of the observed defects is consistent with isolation to the i-type layer. This is to be expected because formation energy calculations[18] indicate that the neutral charge state is

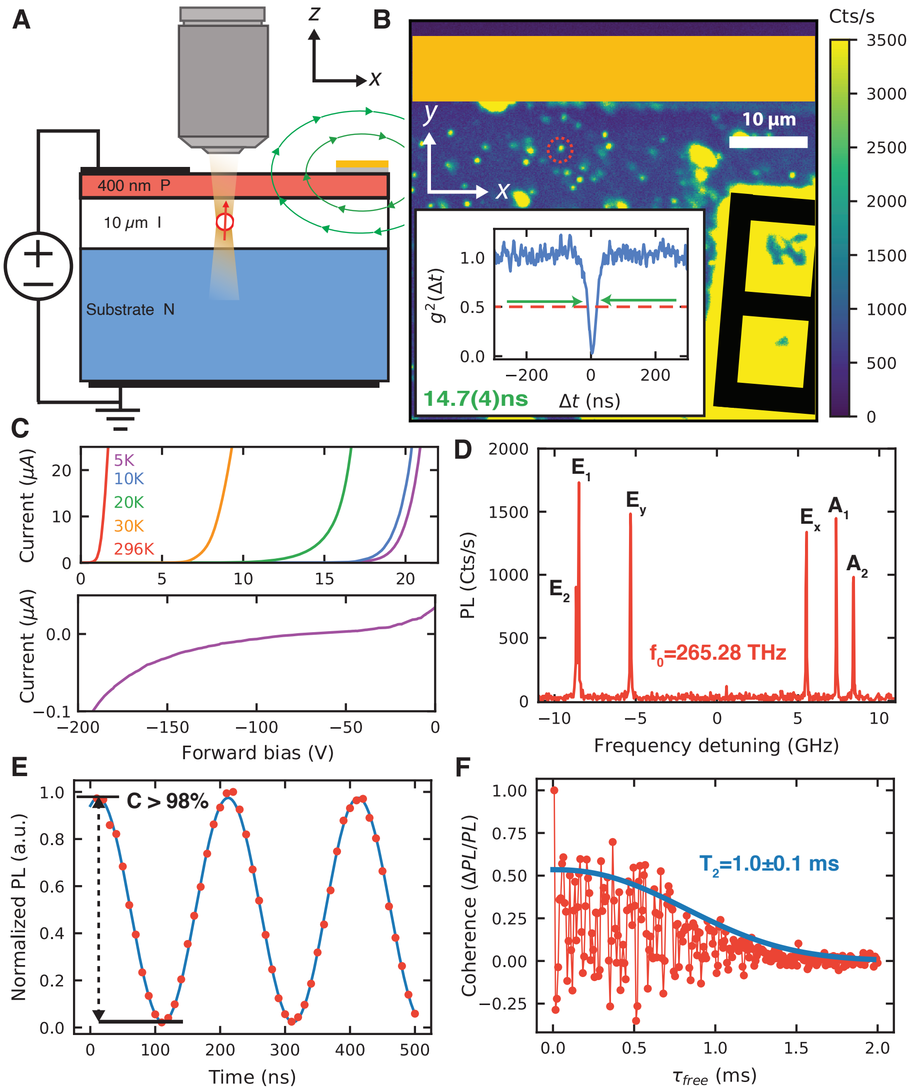

Figure 5.1: **Isolation of single VV^0 in a commercially grown semiconductor device. (A)** Schematic of the device geometry. **(B)** Spatial photoluminescence (PL) scan of an example device, showing isolated emitters (example circled in red) confirmed by autocorrelation (inset) showing $g^2(0) < 0.5$ (red line). Extracted emitter lifetime is 14.7 ± 0.4 ns (green arrows). Gate and microwave stripline features are drawn and color coded as in (A). **(C)** Top: I-V curves of the device at various temperatures; bottom: low temperature reverse bias behavior. **(D)** Photoluminescence excitation (PLE) spectrum of a single (kk) divacancy at 270 V of reverse bias. **(E)** Optically detected Rabi oscillations of a single (kk) VV^0 with >98% contrast (fit in blue) using resonant initialization and readout. **(F)** Hahn-echo decay of a single (kk) VV^0 in the diode. Rabi, Hahn and g^2 data are taken at 270 V of reverse bias and at approximately 240 Gauss at T=5 K.

energetically favorable when the Fermi level is between ∼1.1 eV to 2 eV and this condition must be satisfied somewhere in the i-layer [124](appendix 5.3). This depth localization provides an alternative to delta-doping[107], which is not possible with intrinsic defects, facilitating positioning and control in fabricated devices (Fig. S5.6). Additionally, owing to the diodes highly rectifying behavior at low temperature, large reverse biases are possible with low current (Fig. 5.1C)(appendix 5.3). Sweeping the frequency of a narrow-line laser, we obtain photoluminescence excitation (PLE) spectra of the optical fine structure of these single defects (Fig. 5.1D). Using the observed transitions for resonant readout and preparation, we perform high-contrast Rabi oscillations of isolated VV^0 in the p-i-n structure (Fig. 5.1E)(appendix 5.3). The contrast exceeds 98%, improving on previous demonstrations through the use of resonant spin polarization[35]. Additionally, a single spin Hahn-echo decay time of 1.0 ± 0.1 ms is measured for spins in the device (Fig. 5.1F), consistent with previous ensemble measurements[34]. The long Hahn-echo times and high-fidelity control demonstrate that integration into semiconductor structures does not degrade the spin properties of VV^0. This isolation and control of highly coherent spin qubits achieved in these functioning semiconductor devices unlock the potential for integration with a wide range of classical electronic technologies.

5.1.3 Large Stark Shifts in a p-i-n Diode

Because the (hh) and (kk) divacancies(appendix 5.3) in SiC are nominally symmetric along the c-axis (growth axis), the geometry of the diode allows for large electric fields which mostly conserve the symmetry of the defect. Therefore, wide tuning of the VV^0 optical structure is possible, while reducing unwanted mixing from transverse or symmetry-breaking components of the excited state Hamiltonian[13, 35, 97]. Because the i-type region can be relatively thin (10 μm here), the applied voltage is dropped over a much smaller region than if a bulk sample were used[42], leading to significantly larger Stark shifts for a given applied voltage.

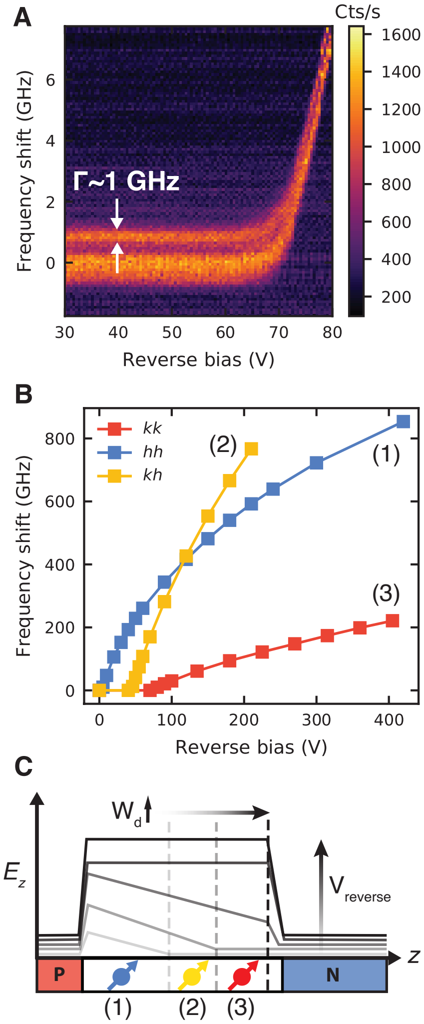

Figure 5.2: **Stark shifts in p-i-n diode. (A)** Low field Stark tuning of a single (kk) defect at T=5 K, showing a turn-on behavior for the Stark shifts and narrowing with voltage. This threshold is the same as in 5.4A. These scans contain the lower branch (E_1, E_2, E_y) where the linewidth of E_y is approximately 1 GHz and E_1 and E_2 are unresolved. The PLE lines show no shifting down to zero bias. **(B)** High field Stark shifts of multiple example defects (located at various depths and positions in the junction), showing >100 GHz shifts. **(C)** Schematic electric field distribution and depletion region width (W_d) in the diode for increasing reverse bias. Location in the junction can determine the local field experienced by the defects in (B). The error bars in (B) are smaller than the point size. All data were obtained at T=5 K.

In principle, this region can be reduced to a thickness that exceeds limitations from optical access with metal planar gates (limited by the optical spot size of $\sim 1\mu m$). Furthermore, it is possible to use doped layers as *in situ* transparent native contacts to Stark tune and control localized defects in suspended photonic or phononic structures[142] enabling complex hybrid electrical, photonic, and phononic devices. In our p-i-n junction device, we apply up to 420 V in reverse bias. Our results show Stark tuning of several hundreds of GHz on different defects of the same type and on inequivalent lattice sites where the Stark shift is between 0.4-3.5 GHz/V after a threshold is passed (Fig. 5.2A). For example, we observe a (hh) divacancy shifted by more than 850 GHz (2.5 meV) at a reverse bias of 420 V and a (kh) divacancy shifted by more than 760 GHz at a reverse bias of 210 V (Fig. 5.2B). These shifts are among the largest reported for any single spin defect to date and were only limited by the voltage output of our source. We expect that owing to the high dielectric breakdown field of SiC, even higher shifts of a few THz are possible (appendix 5.3). The high-field limit of these shifts correspond to estimated dipole moments ($d_{||}$) of 11 GHz m/MV and 4.5 GHz m/MV for (hh) and (kk) divacancies respectively, consistent with previous reports[42, 99]. For the (kh) basal divacancy observed, the estimated transverse dipole moment is around $d_{\perp}=$ 35 GHz m/MV. Furthermore, because the Stark shift represents a measure of the local electric field, we conclude that a negligible field is applied to the VV^0 before a certain threshold voltage where the depletion region reaches the defect[50]. This results from non-uniform electric fields in the diode caused by residual n-type dopants in the intrinsic region (Fig. 5.2C, (appendix 5.3)). Overall, our system could be used as a widely frequency-tunable, spectrally narrow source of single photons. In particular, our system enables one of the highest Stark shift to linewidth ratios ($> 40,000$) obtained in any solid-state single-photon source (Table 5.7). These characteristics make this system ideally suited for tuning remote defects into mutual resonance and for frequency multiplexing of entanglement channels[141]. Interestingly, the tunability range is so wide that it could even enable the tuning of a (hh) divacancy into resonance with a (kk) divacancy, allowing for interference and entanglement between different species of defects. This wide tunability stems from the rectification behavior of the diode which allows large electric fields without driving appreciable currents, which can degrade spin and optical properties. Furthermore, the observed sensitivity of the optical structure of single VV^0 defects could serve as a nanoscale electric field sensor enabling field mapping in these working devices with sensitivities of approximately 100 $(V/m)/\sqrt{Hz}$ or better, which is competitive with state of the art spin and charge based electrometry techniques [29, 136, 45](appendix 5.3).

5.1.4 Reducing Spectral Diffusion Using Charge Depletion

Uncontrolled fluctuating electrical environments are a common problem in spin systems where they can cause dephasing[80], as well as in quantum emitters where they result in spectral diffusion of the optical structure and lead to large inhomogeneous broadening. For example, adding and removing just a single electron charge 100 nm away causes shifts on the order of 100 MHz for the optical fine structure of VV^0 (Fig. 5.8). Previous work[35] has shown that by doing an exhaustive search through many defects in a specially grown material, one can find defects with lines as narrow as 80 MHz (typically 100-200 MHz or larger), however, this is still much larger than the Fourier lifetime-limit of ∼11 MHz[35]. In bulk intrinsic commercial material, the narrowest linewidths are significantly broadened to around or above 130-200 MHz[35] (Fig. 5.9). Overall, spectral diffusion has been a notoriously difficult outstanding challenge for nearly all quantum emitters in the solid-state. Here, we introduce a technique for mitigating spectral diffusion. We demonstrate that by applying electric fields in our device we deplete the charge environment of our defect and obtain single scan linewidths of 20±1 MHz (Fig. 5.3A) without the need for an exhaustive search. This reduction in PLE linewidth has a different voltage dependence than the transverse asymmetry in the defect, thus eliminating reduced mixing as a possible mechanism for narrowing (Fig. 5.3B). The temperature dependence of the linewidth is roughly consistent with a T^3 scaling at these low temperatures[74](fitted exponent 3.2 ± 0.3 and a zero-temperature linewidth of 11±5 MHz, appendix 5.3). Although the dominant temperature scaling may change at lower

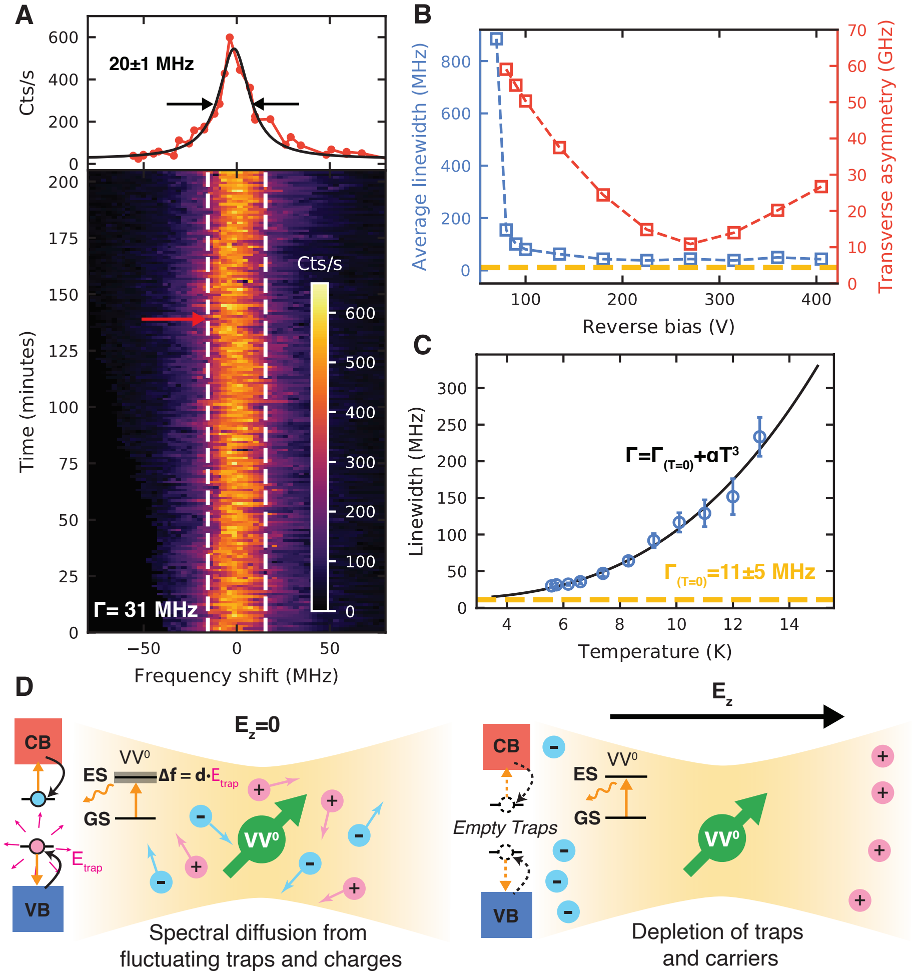

Figure 5.3: **Optical linewidth narrowing by tuning the electrical environment of a solid-state emitter.** **(A)** Multiple PLE sweeps taken over 3.5 hours of the E_x line, showing small residual spectral diffusion (fitted inhomogeneous linewidth of 31 ± 0.4 MHz). The red arrow corresponds to the single scan shown with a fitted linewidth of ≈ 20 MHz. **(B)** Comparison of the average linewidth (blue) and defect transverse asymmetry (red) with respect to applied reverse bias. The yellow line is the lifetime limit. **(C)** Temperature dependence of the linewidth. A free power-law fit gives an exponent of 3.2 ± 0.3. Constraining the fit to a T^3 relation, we extract a zero temperature linewidth of 11 ± 5 MHz (yellow line). Errors on the plot represent a 95% confidence interval. **(D)** Model for the effect of charge depletion on spectral diffusion in the illuminated volume (yellow). To the left of each diagram is a schematic band diagram with the relevant transitions. Errors for the fit values in (A) and (C) represent one standard deviation. All data is from a single (kk) VV^0. In (B), the laser power is slightly higher than in (A), causing some broadening. For (A) and (C) the E_x line is shown at 270 V of reverse bias. Data in (A) and (B) were obtained at T=5 K.

temperatures, this trend hints at a possible explanation for the remaining broadening and is consistent with a temperature limited linewidth. Furthermore, the observed line is extremely stable, with a fitted inhomogeneous broadening of 31 ± 0.4 MHz averaged for over 3 hours (Fig 5.3A). This stability over time, narrowness, tunability, and photostability demonstrate the effectiveness of engineering the charge environment with doped semiconductor structures for creating ideal and indistinguishable quantum emitters. At zero bias the linewidth in our samples is much higher than in bulk material (around 1 GHz, Fig. 5.2A). We attribute this to a greater presence of traps and free carriers (under illumination). Thus, in these samples, the observed narrowing corresponds to an improvement in the linewidth by a factor of more than 50. We speculate that a combination of this charge depletion technique with lower sample temperatures, a lower impurity material, and further annealing could enable measurements of consistent transform-limited linewidths[36, 66]. This use of charge depletion for creating spectrally narrow optical interfaces (Fig. 5.3D) could be widely applicable to other experiments in SiC, or to other solid-state emitters such as quantum dots[132, 92]. Indeed, by applying the same techniques developed here to intrinsic SiC materials, lines as narrow as ~ 21 MHz are observed[99]. Crucially, these results demonstrate that depleting local charge environments can transform a very noisy electric environment into a clean one, turning materials containing unwanted impurities into ideal hosts for quantum emitters.

5.1.5 Charge Gating and Photodynamics of Single Defects

Our observation of large Stark shifts and linewidth narrowing relies on understanding and controlling charge dynamics under electric fields. To achieve this, we study the stability of the observed single defects under electrical bias. This allows a careful investigation of the charge dynamics of single VV^0 under illumination, from which we develop an efficient charge reset protocol. In our experiments, we observe that with 975 nm off-resonant light, the photoluminescence (PL) drops dramatically once the reverse bias is increased past a threshold voltage

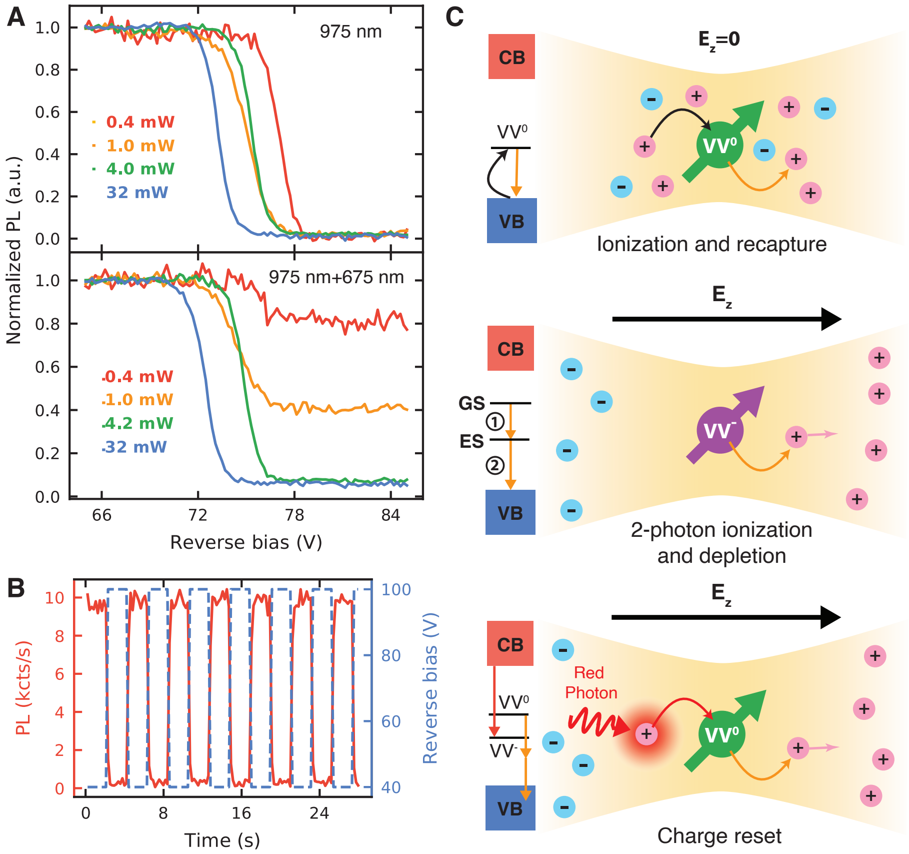

Figure 5.4: **Electrical and optical charge control of a single VV^0.** **(A)** Voltage and power dependence of the photoluminescence of a single (kk) VV^0 with 975 nm excitation (top), and with additional 188 μW of 675 nm illumination (bottom), showing a sharp threshold under reverse bias. With high 975 nm power, the two-photon ionization process dominates and the PL signal is low. **(B)** By controlling the voltage in time (blue) the emission from the single (kk) defect is switched on and off (red). **(C)** Model of rapid ionization and recapture at zero electric field (top). Two-photon ionization and formation of a depletion region under reverse bias (middle). Charge reset under applied electric field using red light (bottom). All data were obtained at T=5 K.

(Fig. 5.4A). This threshold varies between defects, which is expected given differences in the local electric field experienced stemming from variations in position, depth, and local charge trap density. We attribute the PL reduction to photoionization to an optically dark charge state[149]. We use this effect to create an electrically gated single-photon source[33, 119, 78], where emission is modulated in time with a gate voltage (Fig. 5.4B)[42]. The threshold voltage has a slight hysteresis (Fig. 5.10) and laser power dependence (Fig. 5.4A) suggesting

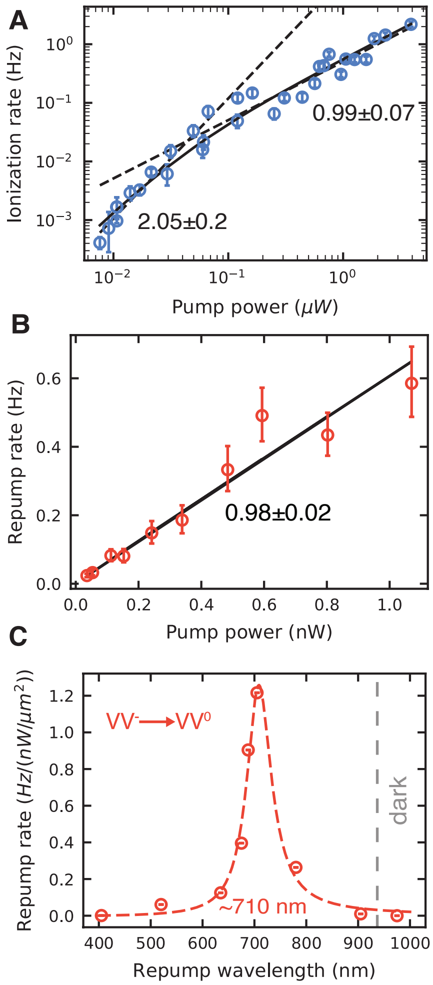

Figure 5.5: **Ionization and charge reset rates for VV^0. (A)** Dependence of the ionization rate on resonant laser power. Low and high power regime fits (black dotted lines) and their power laws ($m = 2.05 \pm 0.2$ and $m = 0.99 \pm 0.07$, respectively). The solid black line shows a full model fit. **(B)** Repump power dependence of the 688 nm laser, showing a linear exponent of $m = 0.98 \pm 0.2$. Fluctuations in the polarization or power of the laser limits the true error. (A) and (B) were taken at 90 V of reverse bias. **(C)** Repumping rate as a function of illumination wavelength at 270 V of reverse bias with a Lorentzian fit centered around 710 nm. With wavelengths longer than 905 nm (and at these powers) no PL is observed and the defect is dark. All error bars represent 95% confidence intervals from the fit of the raw data from a single (kk) VV^0. All data were obtained at T=5 K.

that trapped charges may play a role[13, 64]. We note that the electric field dependence of the photoionization could also be used to extend sensitive electrometry techniques[147] to the single defect regime, while controlled ionization of the spin can extend the coherence of nuclear registers[112]. The threshold for Stark shifts (Fig. 5.2A) corresponds approximately to the same voltage where significant photobleaching occurs when using off-resonant excitation. This links the sharp photoionization threshold in Fig. 5.4A to the presence of moderate electric fields and the onset of carrier depletion. A possible explanation for this voltage-dependent PL is that at zero electric field, illumination constantly photoionizes the VV^0 and other nearby traps. However, the divacancy rapidly captures available free carriers returning it to the neutral charge state. Under applied fields, carrier drift depletes the illuminated region of charges. Thus, when a VV^0 photoionization event occurs in this depleted environment, no charges are available for fast recapture, resulting in a long-lived dark state (Fig. 5.4C). Past works have shown that PL is enhanced in ensembles by repumping the charge with higher energy laser colors[149, 56, 95]. We extend this work to the single defect regime by applying various illumination energies and studying single defect photodynamics at 90 V of reverse bias (past the threshold voltage of approximately 75 V of reverse bias for this defect). We observe under resonant illumination the PL quickly drops to zero and does not recover, indicating that 1131 nm (1.09 eV) light (resonant with the ZPL of a (kk) VV^0) ionizes the defect, but does not reset the charge state. However, after applying higher energy light (688 nm, for example) the charge is returned to a bright state even with < 1 nW of applied power. This repump of the defect charge state is vital for restoring PL for ionized or charge unstable VV^0 in SiC (Fig. 5.4A) and is essential to observe the effects discussed in the previous sections (Fig. 5.4C). When both NIR resonant (1131 nm) and red (688 nm, 1.8 eV) light is applied to the defect, hopping between the bright (VV^0) and dark (VV^+ or VV^-) charge states results in a blinking behavior. From this blinking (Fig. 5.11), we can extract photoionization and repumping rates of the defect[7]. We first examine the ionization rate of a single VV^0 (Fig. 5.5A) and observe that the power dependence is quadratic below defect saturation (exponent $m = 2.05 \pm 0.2$) and linear at higher powers ($m = 0.99 \pm 0.07$). We note that our observed data provide evidence for a two-photon process to VV^- (appendix

5.3) suggested in previous ensemble studies[149, 95], and are less consistent with a recently proposed three-photon model converting to VV^+ [18, 56]. Thus, we conclude that the dark state caused by NIR resonant excitation is VV^-. Further study of the spin dependence of this ionization may lead to the demonstration of spin-to-charge conversion in VV^0. Similarly, we study the charge reset kinetics by varying the power of the repumping laser. We find a near-linear power-law with $m = 0.98 \pm 0.05$ (Fig. 5.5B). This linear dependence of the repumping rate can be described by two potential models. One possibility is that the dark charge state is directly one-photon ionized by repump laser. The other possible explanation is that nearby traps are photoionized by this color and the freed charges are captured by the divacancy to convert back to the bright state. By varying the color of this reset laser, we find repumping to be most efficient around 710 nm (1.75 eV), suggesting a particular trap state energy or a possible defect absorption resonance[22, 125] (Fig. 5.5C). Overall, we observe negligible ionization from the optimal red repump laser and no observable reset rate from the resonant laser. This results in fully deterministic optical control of the defect charge state (discussion in appendix 5.3), allowing for high-fidelity charge state initialization for quantum sensing and communications protocols.

5.1.6 Conclusions and Outlook

The electrical tuning of the environment demonstrated here constitutes a general method that could be applicable to various quantum emitters in semiconductors where spectral diffusion or charge stability is an issue[89], or where electric field fluctuations limit spin coherence[80](appendix 5.3). Furthermore, using our p-i-n diode as a testbed to study charge dynamics, we develop a technique to perform deterministic optical control of the charge state of single divacancies under electric fields[144]. The techniques presented will be vital to achieving single-shot readout and entanglement in VV^0 by enabling charge control and enhancing photon indistinguishability, suggesting doped semiconductor structures as ideal quantum platforms for defects. This work also enables high-sensitivity measurement of nanoscale electric fields and charge distributions in working devices[29] and facilitates spin-to-charge conversion[123] for enhanced quantum sensing and electrical readout protocols[125]. Finally, the introduction of VV^0 into classical SiC semiconductor devices such as diodes, MOSFETs and APDs may enable the next generation of quantum devices.

5.2 Materials and Methods

5.2.1 Defect Formation

Single defects can be isolated in commercially available and laboratory-grown wafers of SiC. In particular, custom grown wafers containing intrinsic, non-intentionally doped epilayers have sufficiently low enough defect density to isolate sparse single defects through confocal microscopy. After growth, we use 2 MeV electron irradiation at a dose of $3e13$ cm^{-2} to introduce vacancies in the lattice, that upon annealing (850 $°C$, 30 minutes, Ar ambient), form VV^0 and other defect complexes and traps. These defects form in the neutral charge state if the Fermi level is near mid-gap. In these samples, PL1 (hh), PL2 (kk), and PL4 (kh) divacancies are observed, consistent with previous reports as confirmed by photoluminescence (PL) spectra, ODMR signatures, and photoluminescence excitation (PLE) resonances. Interestingly, as in other work, we do not observe single (hk) divacancies. In this work, we use the ($V_C V_{Si}$) convention for the divacancy where k and h refer to the quasi-cubic and hexagonal sites, respectively.

5.2.2 Device Fabrication

In this work, we use a commercially grown (by Norstel AB, now ST Microelectronics) wafer of 4H-SiC. The wafer has a n-type substrate ($[N] = 1e18 - 1e19 cm^{-3}$, $12 - 30$ $m\Omega \cdot cm$) with $10\mu m$ i-type ($[N] < 1e15$ cm^{-3}, $[Vc] \sim 1e15$ cm^{-3}) and 400 nm p-type ($[Al] = 7e18$ cm^{-3})

epilayers grown on top, creating a vertical p-i-n junction. After forming isolated VV^0 in these wafers, Ohmic contact is made uniformly on the back n-type surface using $\sim 300\ nm$ of NiCr (80/20). This n-type contact is made Ohmic using a 5 minute RTA anneal in Ar ambient at 950 $^\circ C$. Subsequently, lithographically patterned Ohmic contact is made to the top p-type layer (30 nm Ti, 100 nm Al, 30 nm Au). The top contact is made Ohmic with an anneal in a quartz tube furnace in Ar at 850 $^\circ C$ for 10 minutes. These patterned structures allow for optical access to the defects under bias. Ohmic contact is confirmed through the linearity of the I-V response between two pads on the same layer for both the top and bottom contact. After the top and bottom contact formation, nearby microwave striplines are fabricated (10 nm Ti, 150 nm Au), allowing microwave coherent control of the spins.

Additionally, the slight 4° off-axis cut of our sample (used for high-quality epitaxy) means we also apply a slight transverse field to our defect with Stark tuning. In some defects, this accentuates the inherent strain asymmetry, but in other defects, it works against the local transverse strain and improves the symmetry of the defect. This is a convenient way to both tune the optical lines and restore symmetry with a single gate demonstrated in Fig. 5.3B.

5.2.3 Device Characterization

Although the exact interpretation of the I-V characteristics of the device is beyond the scope of this work, the behavior in Fig. 5.1C is consistent with the temperature dependence of the built-in voltage and possible non-Ohmic behavior of the top p-contact as the relatively deep ($\sim 0.2\ eV$) aluminum acceptors become frozen out at low temperature. Voltages of up to -420 V without exceeding a leakage current of 1 μA ($\sim 100\ A/m^2$) are possible. Reduction of the leakage current is important to reduce charge dynamics and heating, while allowing for large electric fields.

5.2.4 Confocal Microscope

Our measurements are performed in a home-built confocal microscope using a 100x near-infrared (NIR) objective with a numerical aperture (NA) of 0.85. The sample is at 5 K (unless otherwise specified) inside a Montana Cryostation s100 closed-cycle cryostat. The emission is collected through a 1060XP fiber and detected on a Quantum Opus Superconducting Nanowire Single-Photon Detector (SNSPD). All quoted powers are measured at the sample, accounting for losses in the setup.

5.2.5 Instrument Error and Linewidth

Photoluminescence excitation (PLE) scans of the optical fine structure convolve the resolution of our wavemeter and the laser stability (Gaussian) on the true linewidth (Lorentzian). This results in a Voigt profile. We estimate an upper bound on this total instrumentation error of 8 MHz from scans on a control cavity. Thus, using the Voigt equation our true linewidth (from 20 MHz in Fig. 5.3A) may be as narrow as 16 MHz.

5.2.6 Pulse Sequences and Hahn-echo

For Fig. 5.1B (inset), 5.1D, 5.1E, 5.1F only resonant lasers are used to reduce ionization. In the inset of Fig. 5.1B lasers tuned to the A_1 and E_x line are used simultaneously to produce constant PL. With the low powers used, the exponential $g^{(2)}$ fit corresponds to the optical lifetime, from which we can extract an expected lifetime limited linewidth of approximately 11 MHz. In Fig. 5.1E, 5.1F, 5.1 A laser pulse on the A_1 optical line polarizes the spin state to $m_s = 0$ with high fidelity. Subsequent pulsed microwave control drives the spin. For readout, counts are collected during a pulse on the cycling E_x transition. In the Rabi data in Fig. 5.1E, the contrast is not dark count subtracted. In principle the contrast could exceed 99% with this correction. For Fig. 5.1F, the measurement is differential by projecting the coherence to either $m_s = 0$ or $m_s = \pm 1$ and taking the difference. The Hahn-echo is fit with an envelope $e^{-(\tau_{free}/T_2)^2}$.

5.2.7 Photoluminescence Excitation (PLE) Scans

For PLE, a tunable resonant laser (Toptica DLC PRO) is scanned over the optical fine structure. For all scans presented here, a constant microwave drive is applied to prevent initialization into a dark spin state. This drive is fast enough to not interfere with the slow ionization dynamics. PLE scans are performed at zero magnetic fields unless otherwise noted. For the illumination color dependence in Fig. 5.5, these experiments are run with a rapidly interleaved pulse sequence where the resonant and repumping laser are never on at the same time to avoid multi-photon interplay between the two lasers.

5.2.8 Interleaved Charge Control Sequences

All measurements unless otherwise noted are at zero magnetic fields. This regime allows us to use a single microwave tone to mix both $m_s = +1$ and $m_s = -1$ with the $m_s = 0$ state. This prevents a "dark" spin state where some spin population could get trapped and thus enables continuous PLE experiments without the need for an off-resonant reset. For Fig. 5.5, the power dependence of the ionization and repump was taken with a total sequence duration of 1.25 ms, red pulse time 100 μs, resonant on for 1.1 ms. The repump and resonant are not on at the same time. The 688 nm diode laser is directly modulated. For Fig. 5.5C an optical chopper was used synced to pulse the repump when the resonant was off. The total sequence duration was 2 ms, repump pulse time of 1 ms (50:50 duty cycle chopper) and the resonant laser was on for 800 μs.

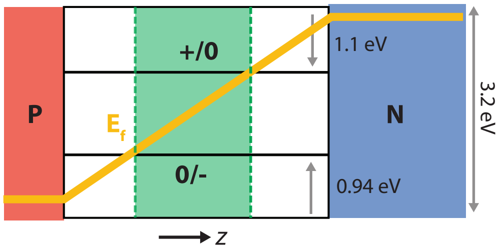

Figure 5.6: **Charge stability region of VV^0 in a p-i-n diode.**

5.3 Supplementary Details

5.3.1 *Depth Control Using Doping*

For defects complexes that lack a dopant (intrinsic defects), localization cannot be achieved by the traditional method of local implantation[133] or delta-doping through growth[107]. In SiC, for example, this limits precise depth localization for both VV and V_{Si} defects and can be problematic for applications such as near-surface sensing or photonic crystal integration. Using doped structures to tune the local Fermi level, we can control the defects' stable charge state[102] and thus provides an alternative method for depth localization. In general, the VV is only stable in its neutral charge state (in equilibrium) when the Fermi level lies within the charge stability region of VV^0. This charge stability region can be understood through DFT calculations, which place this region $E_V + 1.1\ eV < E_f < E_c - 1.1\ eV$[149, 95]. With the total bandgap being $\sim 3.2\ eV$, this roughly localizes the VV^0 to only form and be stable in the middle 1/3 of the i region (Fig. 5.6) in a p-i-n diode. Specifically, i-type layers can be grown near the surface and be very thin $< 100\ nm$ for sensing, and localized i-type layers in the center of photonic cavities could increase coupling efficiencies while also offering *in situ* charge control and linewidth tuning techniques.

5.3.2 Limits of Stark Tuning

We estimate that the limit for Stark tuning will be the shift that occurs right before dielectric breakdown. From[91], the breakdown field at 300 K is around 300-500 MV/m (at cryogenic temperatures we expect this to be higher, but the 300 K value is used here). Therefore, we conservatively estimate a maximum possible Stark shift using the (hh) divacancy dipole of around 11 GHz/(MV/m) to be above 3 THz and expect to exceed this in an optimally engineered cryogenic sample. This corresponds to 30 V in a 100 nm layer (easily achieved with growth) or 300 V on a 1 μm intrinsic layer.

5.3.3 Threshold Voltages and Stark Shift Dipoles

In general, the displayed Stark tuning in Fig. 5.2B represent just one example defect of each species in the diode. Within each defect configuration (hh), (kk), (kh) the threshold voltage where shifts start to occur changes. However, within each species, the high field Stark shift slope remains roughly consistent. At high voltages, the 10 μm i-layer can become completely depleted and drop the voltage uniformly over the layer thickness (Fig. 5.2C). For example, we find four (hh) divacancies that have different reverse bias thresholds (5, 15, 40, 70 V), but have similar shift per volt at high fields (1.15, 1.10, 1.20, 1.10 GHz/V). Since we expect that at high voltages the field will be uniform in the i-region, we can estimate the field as a function of V to be E=V/10 μm. With this field estimate we obtain similar values for the (hh) electric dipole moment (11.5, 11.0, 12.0, 11.0 GHz/(MV/m)). Similarly, for (kk) divacancies, we measured two defects that had reverse bias thresholds of 80 V and 100 V, with dipoles of 4.8 and 4.1 GHz/(MV/m) respectively. By averaging these Stark dipole moments, we therefore estimate the Stark electric dipole for (hh) to be 11 GHz/(MV/m) and for (kk) to be 4.5 GHz/(MV/m). We only report one (kh) defect Stark shift (equivalent to a dipole of 35 GHz/(MV/m)), but similar data can be found in [99]. In our estimate, we do not take into account the exact angle of the (kh) VV^0 with respect to the c-axis. The small dipole of the (kk) divacancy makes it more resilient to electrical noise and spectral diffusion. As described in the main text, we attribute the differences in threshold voltages to the effect of a finite charge depletion region (at low voltage) slowly reaching different depths in the sample as we increase the applied voltage (Fig. 5.2C). In a sense, the depletion voltage needed represents the exact depth of the defect and could be presumably be used to precisely locate the defect in depth.

5.3.4 Electric Field in the Diode

In general, as described in the previous section, the electric field is non-uniform in the diode. As mentioned in 5.1, this results from a small residual n-type (“unintentional doping) of the nominally “intrinsic i-type layer. The fact that the i-type layer is not perfectly i-type means that the field can be dropped over small areas near the p-i or the i-n interfaces (depending on the residual dopant), instead of being uniformly dropped over the full i-type region. In particular, for our unintentionally n-doped (n^{-}) layer, a “trapezoidal depletion in the p-i-n diode occurs starting near the $p - n^{-}$ interface (Fig. 5.2C)[93]. The exact shape of this trapezoidal field and charge distribution as a function of voltage can be calculated from semiconductor transport equations. When this trapezoidal depletion reaches through the entire intrinsic layer, it is commonly referred to as “punch-through, above which the field can be uniformly dropped over the intrinsic region. The width of the depletion and punch through voltage can be estimated with equation $W_d = \sqrt{\frac{2\varepsilon\varepsilon_o|V|}{eN_d}}$ [91, 42]. Using $N_d = [N] \sim 1e15\ cm^{-3}$, we can estimate a “punch-through voltage of around 100 V (for a 10 μm i-layer). This is roughly consistent with the largest threshold voltages for Stark shifts and depletion observed. The electric field distribution also reflects the regions that are depleted. This is also sometimes referred to as a “space charge region. The carrier concentration in diodes is known to follow an exponential relation in voltage/electric field[93].

5.3.5 Stark Shifts and Linewidths of Various Quantum Emitters

Here, we define Δ as the ratio of the maximum frequency tuning to the observed linewidth. This metric balances the needs for emitters of tunability and narrowness. In the past, large tunability has been achieved at the cost of inhomogeneous broadening, and conversely, some narrow lines have been demonstrated at the cost of tunability. This makes sense since the shift ($S \sim d \cdot E$) and linewidth ($\Gamma \sim \Gamma_0 + d \cdot \delta E$) are both related to the dipole moment (d) and thus present an inherent tradeoff (note that Γ_0 is proportional to the "transition dipole moment but is different from the Stark shift dipole d). Therefore, to account for this tradeoff, Δ is an interesting metric. Moreover, this metric also has practical relevance since it represents the number of resolvable spectral channels that could be used in a spectral-multiplexed quantum network. A summary of the demonstrated linewidths and tuning ranges for different solid-state single-photon emitters is shown in Table 5.7. Recent work has demonstrated that strain tuning can be a valuable substitute for the Stark effect in systems with weak dipole moments (d). This tuning capability was used to achieve a large Δ (Table 5.7) and to demonstrate dynamically stabilized single-photon emission [94]. We would also like to mention recent work in non-solid state systems (single molecules) [118], quoting this metric (Δ) and achieving $\Delta \sim 40,000$.

5.3.6 Estimate of the Sensitivity of the Optical Fine Structure to Electric Fields.

Using the following Lorentzian model for our count rate as a function of excitation frequency c(f):

$$c(f) = \frac{A}{\pi\gamma\left[1 + \left(\frac{f-f_0}{\gamma}\right)^2\right]} \tag{5.1}$$

where f_0 is the resonant frequency, γ is the half-width at half-maximum (i.e. half of the linewidth), $A = c_{max} \cdot \gamma\pi$, where c_{cmax} is the maximum counts per second on resonance.

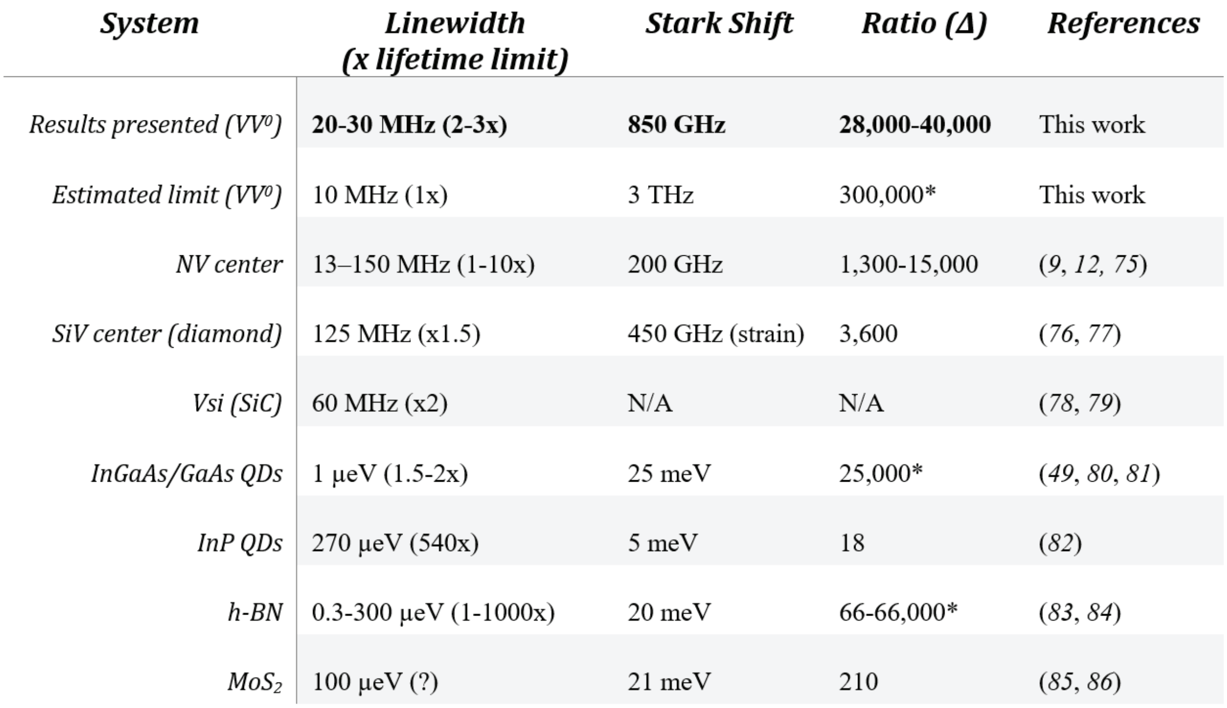

System	Linewidth (x lifetime limit)	Stark Shift	Ratio (Δ)	References
Results presented (VV^0)	**20-30 MHz (2-3x)**	**850 GHz**	**28,000-40,000**	This work
Estimated limit (VV^0)	10 MHz (1x)	3 THz	300,000*	This work
NV center	13–150 MHz (1-10x)	200 GHz	1,300-15,000	(*9*, *12*, *75*)
SiV center (diamond)	125 MHz (x1.5)	450 GHz (strain)	3,600	(*76*, *77*)
Vsi (SiC)	60 MHz (x2)	N/A	N/A	(*78*, *79*)
InGaAs/GaAs QDs	1 μeV (1.5-2x)	25 meV	25,000*	(*49*, *80*, *81*)
InP QDs	270 μeV (540x)	5 meV	18	(*82*)
h-BN	0.3-300 μeV (1-1000x)	20 meV	66-66,000*	(*83*, *84*)
MoS_2	100 μeV (?)	21 meV	210	(*85*, *86*)

Figure 5.7: **Comparisons of Δ, the tuning-to-linewidth ratio.** Comparison of the tuning range to linewidth ratio for solid-state single-photon emitters (Δ). Numbers with "*" have not been realized experimentally and are a simple combination of the best linewidths with the largest tuning reported. Numbers without "* have been experimentally realized. The references in this table are not adapted to this thesis and the corresponding references can be compared in [5]

First, we must compute:

$$\frac{dc}{df} = \frac{-2A}{\gamma^2\pi}\frac{(\frac{x-x0}{\gamma})}{(1+(\frac{x-x0}{\gamma})^2))^2} \tag{5.2}$$

Then we note that our signal for an electric field of magnitude E is:

$$E\frac{dc}{dE}\cdot t = E\frac{dc}{df}\frac{df}{dE}\cdot t \tag{5.3}$$

And if we assume a shot-noise limited signal we see that our noise is $\sqrt{c\cdot t}$. Therefore, we are trying to maximize:

$$\max_{f_{pai}} \frac{E\frac{dc}{df}\frac{df}{dE}\cdot t}{\sqrt{c\cdot t}} \tag{5.4}$$

We find that the extrema of that expression are at $f = f_0 \pm \frac{\gamma}{\sqrt{2}}$ and at that point, the signal-to-noise per second is:

$$\frac{S}{N \cdot t} = \mp \frac{df}{dE} \frac{4E}{(3\gamma)^{3/2}} \sqrt{\frac{At}{\pi}} \cdot \frac{1}{t} = \mp \frac{1}{\eta} \cdot E \frac{1}{\sqrt{t}} \tag{5.5}$$

Where *eta* is the sensitivity which we defined as the electric field necessary for the signal-to-noise (per $\sqrt{Hz}$) to be 1. Therefore:

$$\eta = \frac{3\gamma}{4 \cdot \frac{df}{dE}} \sqrt{\frac{3\gamma\pi}{A}} = \frac{3\gamma}{4 \cdot \frac{df}{dE}} \sqrt{\frac{3}{c_{\max}}} \tag{5.6}$$

Using $\gamma = 40\ MHz$, and an isotropic (this approximation will suffice for this estimation) $\frac{df}{dE} = 10\mathrm{GHz} \cdot \left(\frac{\mathrm{MV}}{\mathrm{m}}\right)^{-1}$ we get a single spin sensitivity of about $116 \frac{\mathrm{V}}{\mathrm{m}} / \sqrt{\mathrm{Hz}}$ (a conservative estimate). State-of-the art in spin based electrometry has sensitivities of $20,000 \frac{\mathrm{V}}{\mathrm{m}} / \sqrt{\mathrm{Hz}}$ [45] for single spins and $10 \frac{\mathrm{V}}{\mathrm{m}} / \sqrt{\mathrm{Hz}}$ for extremely large ensembles [100].

5.3.7 Stark Shifts from Single Charges

One way to understand the spectral diffusion in this work is to assume some nearby traps are capturing or releasing charges. So it is relevant to calculate the effect of a single point charge “appearing in a trap near the defect. For this we simply use the Coulomb law:

$$\vec{E} = \frac{1}{4\pi\epsilon} \frac{e}{r^2} \tag{5.7}$$

Then if we assume a dipole strength of about $4 - 11$ GHz$\cdot$(MV/m)$^{-1}$ we get the rough relation shown in Fig. 5.8. This suggests a very high sensitivity to free carriers and fluctuating trapped charges and helps us understand why charge depletion is useful.

We expect that the linewidth $\Gamma \propto \sqrt{N}$ from N uniform-strength fluctuators. With our measured reduction of the linewidth by a factor of 50, this corresponds to over three orders

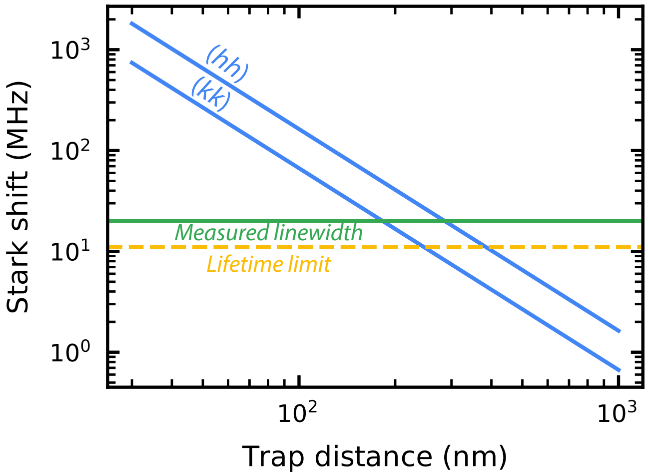

Figure 5.8: **Stark shifts from single trapped charges.** Stark shift caused by a single trap at a given distance. The green line is the minimum measured linewidth and the yellow dashed line is the expected lifetime limit.

of magnitude reduction in fluctuating electrical charge traps. Note that the only relevant traps in these estimates are the fluctuating traps. For shallow traps like Nitrogen, most dopants will be fluctuating between charge states under illumination with almost any color.

5.3.8 Optical Linewidths in Other Commercial SiC Material, Generalizability

The narrowest linewidths achieved in commercial i-type material from the same company that provided the p-i-n diode material is around 120 MHz at best. For example, in the data in [99], the undepleted linewidth of a (kh) VV^0 is over 200 MHz for all observed defects for material from the same company (Fig. 5.9A). A relatively good (hh) divacancy with a linewidth of 135 MHz is shown in Fig. 5.9B. For specially grown material, one defect was found with an 80 MHz linewidth, but most defects from that sample were above 120 MHz in linewidth[35]. These linewidths are sample dependent and depend on the impurity density that causes spectral diffusion.

We note that in Ref. [99], a similar narrowing effect with comparable magnitude is

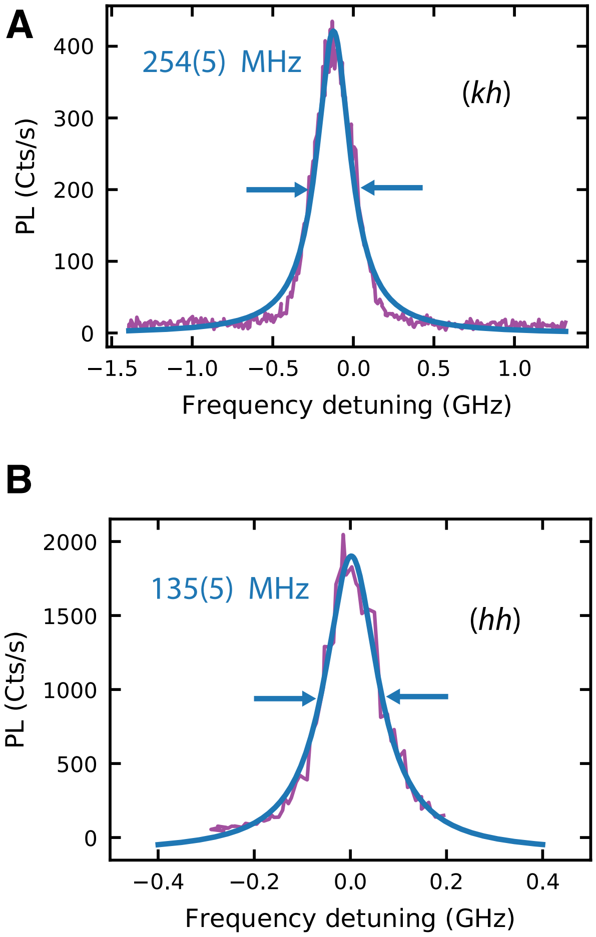

Figure 5.9: **PLE spectra of defects in bulk intrinsic material. (A)** Example PLE scan of a single (kh) and a **(B)** single (hh) VV^0 in intrinsic commercial material (not the p-i-n diode measured here).

demonstrated as an extension of this work. Furthermore, all observed defects here displayed qualitatively similar linewidth reductions. In general, the techniques shown in this work offer a possibility to mitigate noise from residual impurities in a wide range of solid-state materials (not limited to SiC) with charge depletion.

5.3.9 Temperature Dependence of the Linewidth

The temperature dependence of the linewidth gives a physical understanding of the dephasing mechanism. At higher temperatures than those studied here ($> 15\ K$) [35] the linewidth for single VV^0 follows a T^5 power law. This power law is consistent with a Raman two-phonon dephasing that exists for the NV^- center[51]. However, these previous studies were limited by broad lines that did not allow a study of the temperature dependence below 15 K (limited by impurities). At these low temperatures, the power-law deviates from T^5 and is fitted to be closer to a T^3 power law for single (kk) VV^0. Power laws of the PLE linewidth in single emitters have been described ranging from linear to T^7, but a T^3 power law has been found to arise from two possibilities:

1. A two-phonon process in the limit where the strain is small compared to the spin-orbit interaction in the excited state [68], where at high strain it transitions to a T^5 power law.
2. A one-phonon process in a piezoelectric material [74].

Following [68], we believe case 1 is less likely due to the negligible effect of transverse asymmetry (strain) on the linewidth observed (Fig. 5.3B). Case 2 is plausible since SiC is a slightly piezoelectric material, in contrast to diamond. However, further investigation will be required to completely understand the origin of the observed power law. Furthermore, different temperature dependences and behaviors can be expected for the PL4 (hk) divacancy, due to the differences in orbital structure.

5.3.10 Threshold Hysteresis

The observed charge switching behavior under variable voltage has a hysteresis behavior, potentially related to trapping charges[13, 71]. An example curve is shown Fig. S5.10. Such trapping of charge under cyclic voltage waveforms forms the basis of performing EDMR[38] measurements in SiC.

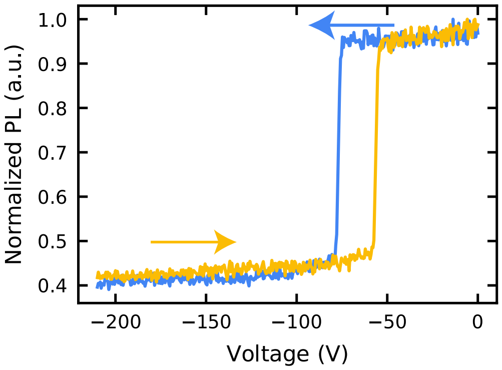

Figure 5.10: **PL charge transition hysteresis.**

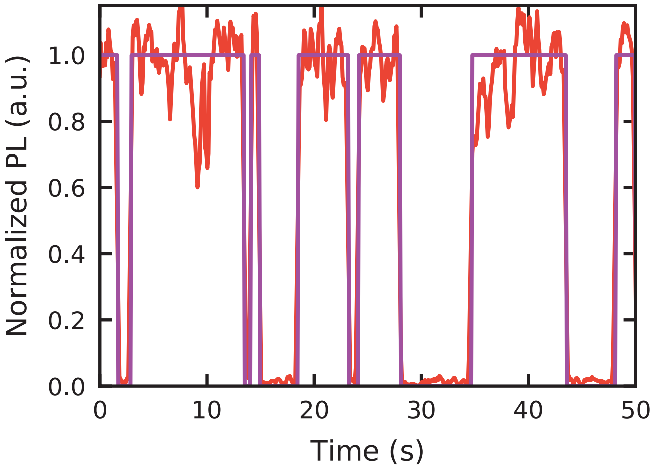

Figure 5.11: **Blinking dynamics.** Example of blinking dynamics of PL (red) under continuous 688 nm and resonant excitation, with binning for analysis (purple).

5.3.11 Single Defect Charge Dynamics (Blinking)

In the main text, we mention a blinking behavior with continuous repump and ionization tones. An example of such behavior is shown in Fig. 5.11. The binning of this “telegraph behavior results in periods of high and low PL (near zero). In Fig. 5.5, we use the average time spent in the high state as a measure of the ionization rate and the average time spent in the low state as a measure of the repump rate. In this section, we demonstrate more formally why using these average times as a proxy for the rate is a valid approach.

First, we assume that when we are in VV^0 state, there is a constant probability of

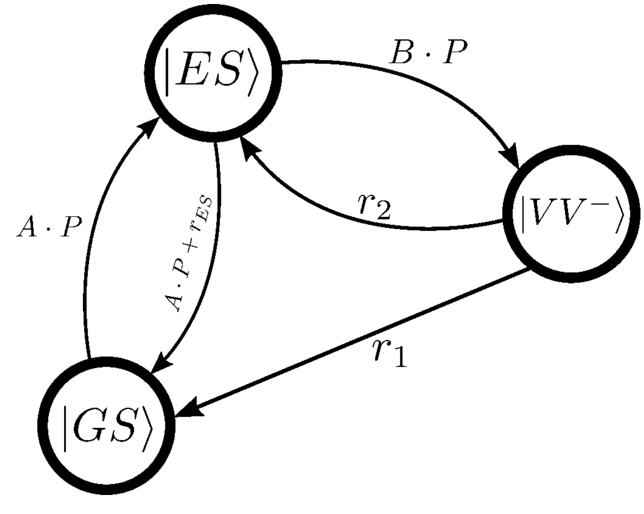

Figure 5.12: **Markov chain of charge dynamics.** Markov chain diagram representing the transition rates involved in the ionization and repump processes.

ionizing (see the Markov chain in Fig. 5.12). Therefore, the process is memoryless and the only memoryless continuous function is the exponential function. Thus, the probability of a "high event" having a duration t is:

$$P(t) = \frac{1}{\tau} e^{-t/\tau} \tag{5.8}$$

where $\frac{1}{\tau}$ is the ionization rate. In our analysis, we take the duration of several "high events" and consider them as sampling $[X_0, \ldots, X_N]$ of a random variable X sampled from the probability distribution above. Since we know that:

$$E[X] = \int_{x=0}^{\infty} x \cdot \frac{1}{\tau} e^{-\frac{x}{\tau}} dx = \tau \int_{\alpha=0}^{\infty} \alpha e^{-\alpha} d\alpha = \tau \tag{5.9}$$

We estimate the ionization rate τ^{-1} using the maximum likelihood estimator which corresponds to the sample mean $\hat{\tau} = E[X] \approx \bar{x}$. Additionally, we can calculate the error bar we should use for the sample mean by estimating the confidence interval. This is done first by transforming our random variable to $\tilde{X} = \frac{2 \cdot X}{\tau}$ (where τ is the actual distribution mean (as opposed to the estimator) and therefore $\tilde{X}$ now has a mean of 2). Then, by noting that the distribution of the sum of N exponential random variables $\tilde{X}_0 \ldots \tilde{X}_N$ (with mean 2) is equal to the Gamma distribution:

$$\sum_i \tilde{X}_i = \Gamma_{N,2}(\tilde{x}) = \frac{1}{\Gamma(N)2^N}\tilde{x}^{N-1}e^{-\tilde{x}/2} \tag{5.10}$$

This is simply the pdf of the chi-square distribution with $2N$ degrees of freedom $\chi^2_{2N}(\tilde{x})$. Therefore,

$$\frac{2}{\tau}\sum_i X_i = \sum_i \tilde{X}_i = \chi^2_{2N}(\tilde{x}) \tag{5.11}$$

If we define the quantile function Q as the inverse of the χ^2_{2N} cummulative distribution function (CDF) (i.e. $Q_{2N}\left(CDF_{2N}(\tilde{x})\right) = \tilde{x})$) we see that $Q_{2N}(p) = \tilde{x} : p = P(\tilde{X} \leq \tilde{x})$ (for a continuous and strictly monotonic CDF). Therefore, for a confidence interval of $(1-\alpha)\%$ we want:

$$Q_{2N}(1-\alpha/2) < \frac{2}{\tau}\sum_i X_i < Q_{2N}(\alpha/2) \tag{5.12}$$

Therefore, we have:

$$\frac{2\sum_i X_i}{Q_{2N}(1-\alpha/2)} < \tau < \frac{2\sum_i X_i}{Q_{2N}(\alpha/2)} \tag{5.13}$$

which reduces to

$$\frac{2N\hat{\tau}}{Q_{2N}(1-\alpha/2)} < \tau < \frac{2N\hat{\tau}}{Q_{2N}(\alpha/2)} \tag{5.14}$$

Where $\hat{\tau} = \bar{x}$ is our sample mean. In our analysis, we use the Python scipy.stats.chi2.ppf function to compute $Q_{2N}(p)$. For our error bars, we used a 2-sigma equivalent interval of 95.6% ($\alpha = 4.4\%$). This analysis is modeled after [116].

5.3.12 Theory of Two-Photon Ionization

Two explanations have been suggested for the ionization of the divacancy in SiC. One proposes a two-photon ionization into the negative charge state VV^- [95, 149], the other suggests a four steps process into VV^+ [18, 56] involving a total of three photons in the process. Our results (Fig. 5.5A) show a quadratic behavior (consistent with two-photon) below saturation and a linear relation after saturation is reached. The only way two reconcile these results with the proposed VV^+ scenario is to assume the second photon excitation ($\Delta\mathrm{E}_2^{\mathrm{a}}$ in Fig. 3 of[18] is much more efficient at $\sim 265\ THz$ then the initial excitation ($\Delta\mathrm{E}_1^{\mathrm{a}}$ in the same figure). We find this unlikely since the first excitation is specifically made to be resonant and the second excitation would most likely be off-resonant. Therefore, for the purpose of this section we will assume a simple two-photon ionization process consisting of:

- One excitation from the ground-state ($|GS\rangle$) to the excited state ($|ES\rangle$).
- One excitation from the excited-state ($|ES\rangle$) to the ionized state ($|VV^-\rangle$).

Two-photon ionization events are usually assumed to be quadratic in power. However, this is only a valid assumption in the limit of a very short (or even virtual) intermediate state lifetimes. For an intermediate state lifetime similar to excitation times or above (saturation), the behavior becomes linear. To see the analytical form of the power dependence, let's use the following states (shown in Fig. 5.12)

$$\vec{\phi} = \begin{bmatrix} \phi_0 \\ \phi_1 \\ \phi_2 \end{bmatrix} = \begin{bmatrix} GS \\ ES \\ VV^- \end{bmatrix} \tag{5.15}$$

And set up the following rate equations:

$$\frac{\partial \vec{\phi}}{\partial t} = \begin{bmatrix} -AP & AP + \Gamma_{\mathrm{ES}} & r_1 \\ AP & -AP - BP - \Gamma_{\mathrm{ES}} & r_2 \\ 0 & BP & -r_1 - r_2 \end{bmatrix} \cdot \vec{\phi} \tag{5.16}$$

We can get the steady-state solution by getting the eigenvector corresponding to an eigenvalue of 0. In this case, the non-normalized solution is:

$$\begin{aligned} \phi_0 &= \tfrac{(r_1+r_2)(AP+\Gamma_{\mathrm{ES}})}{ABP^2} + \tfrac{r_1}{AP} \\ \phi_1 &= \tfrac{r_1+r_2}{BP} \\ \phi_2 &= 1 \end{aligned} \tag{5.17}$$

From these, we can calculate various quantities of interest.

Ionization Rate

For the ionization rate, we are looking for the probability of transition to VV^- given that we are in VV^0. First, we compute:

$$\mathrm{Prob}\left(\mathrm{ES}|VV^0\right) = \frac{\mathrm{Prob(ES)}}{\mathrm{Prob(ES)} + \mathrm{Prob}(GS)} = \frac{\phi_1}{\phi_0+\phi_1} = \frac{AP}{2AP + BP\frac{r_1}{r_1+r_2} + \Gamma_{\mathrm{ES}}} \tag{5.18}$$

Then the ionization rate is given by:

$$\mathrm{Prob}\left(\mathrm{ES}|VV^0\right) \cdot BP = \frac{ABP^2}{2AP + BP\frac{r_1}{r_1+r_2} + \Gamma_{\mathrm{ES}}} \tag{5.19}$$

This is used in the fit of Fig. 5.5A.

PL From Off-Resonant with a Red Repump

Here we assume the main source of repump is from the red (not the off-resonant NIR laser). If we hold the red power constant, the effective repump rates can still be empirically described by r_1 and r_2. Here we are interested in:

$$\mathrm{Prob}(ES) = \frac{AP}{\frac{BP(AP+r_1)}{r_1+r_2} + 2AP + \Gamma_{\mathrm{ES}}} \tag{5.20}$$

In the high power regime,

$$\text{Prob}(ES) \approx \frac{r_1 + r_2}{BP} \tag{5.21}$$

Since PL $= \Gamma_{\text{ES}} \cdot$ Prob(ES) this demonstrates why at high power the PL disappears for both singles and ensembles.

PL From Off-Resonant with an Off-Resonant Repump

In the case of 905 nm illumination, for example, the repump power is proportional to the pump power therefore if we substitute r_i for $P \cdot r_{i,P}$ we find:

$$\text{Prob}(ES) = \frac{AP}{\frac{BP(A+r_{1,P})}{r_{1,P}+r_{2,P}} + 2AP + \Gamma_{\text{ES}}} \tag{5.22}$$

Therefore, at high power we have a finite constant equilibrium population:

$$\text{Prob}(ES) \approx \frac{A}{\frac{B(A+r_{1,P})}{r_{1,P}+r_{2,P}} + 2A} \tag{5.23}$$

5.3.13 Possible Resonances for the Charge Reset

The observed charge repumping and reset can have multiple origins (as described in the main text). Here we suggest two possibilities for this resonance.

Charge Trap Photoionization

The energy of 710 nm is approximately 1.75 eV, corresponding to a charge trap having a photoionization resonance [88] at this energy. Upon ionization, this trap can provide a carrier for the VV to capture. Looking for possible candidates for this resonance by matching with formation energies calculations [95] we identify V_c, which is the most common compensating defect in our SiC samples. Therefore, we find V_c to be the most plausible trap candidate. V_c

transitions from $0 \to +$ can occur at energies above $E_g - 1.8\ eV \sim 1.5\ eV$ and its transition from $+ \to 0$ can occur above $\sim 1.8\ eV$. Therefore, once that photon energy is reached, V_c can freely cycle between $0 \leftrightarrow +$ resulting a source of free carriers (both electrons and holes) which can recombine with the divacancy.

Direct Ionization

The other possibility is a direct ionization of VV^-. Direct ionization to the conduction band (CB) is predicted to occur at a pump energy $E_p > 1.3\ eV$ from experiment and theory [149, 95]. However, VV is known to have a second set of $e_x,\ e_y$ single-particle orbitals that lay in or near the CB. These orbitals could result in a resonance in the band (near 1.75 eV) that very efficiently converts VV^- to VV^0. Such a resonance for ionization has been proposed for both the NV^- center in diamond [125] and for the VV[56]. Initial DFT results point to several possible resonances in the charge dynamics from the singlet and triplet states[22] that could be related to this or changes in the DOS in the CB.

5.3.14 Spectral Diffusion and Ionization Under Various Illumination Wavelengths

In optimizing the repump, we show that the reset rate is most efficient around 710 nm (Fig. 5.5C). Here, we show that this wavelength is also ideal in that there this little added spectral diffusion or ionization added (Fig. 5.13). Sweeping over the PLE resonance many times (Fig. 5.14) and integrating the total intensity over many sweep gives the time-averaged intensity of the line. This time-averaged PL is high when there is no added ionization and low when significant photoionization is present. The inhomogeneous linewidth quoted represents the time-averaged PLE width over many scans and many minutes. This metric captures added spectral hopping from the choice of repump wavelength.

We observe that around 710 nm negligible ionization and broadening is added to the PLE

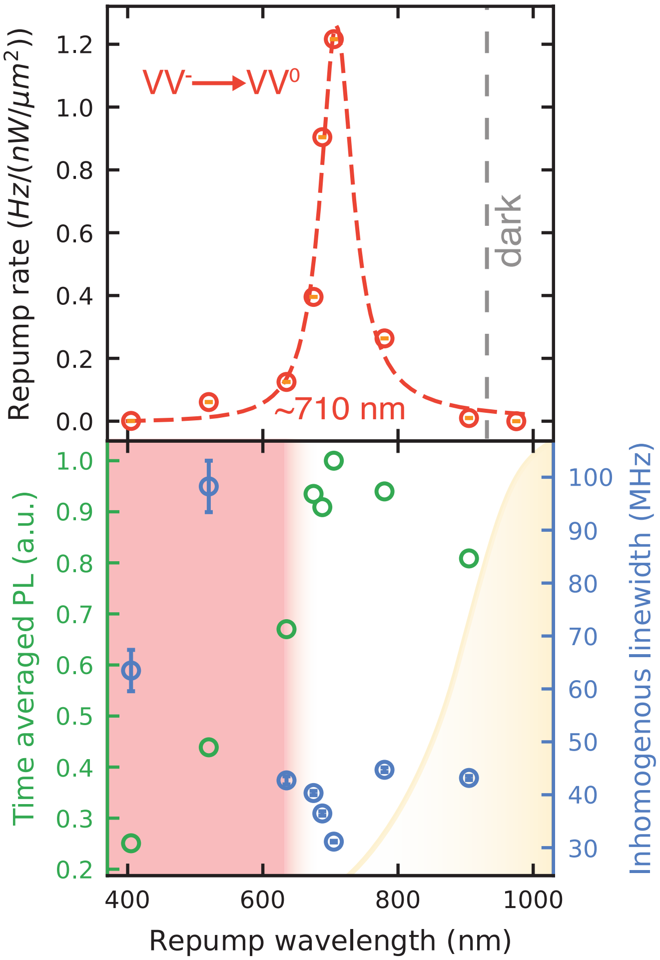

Figure 5.13: **Optimizing the charge reset laser color.** (top) shows the data from 5.5C. (bottom) shows the total PLE integrated intensity (green) over many sweeps (such as in 5.3D), this metric includes blinking and any other photo-instability which manifests as a reduced signal. PLE inhomogeneous linewidth (blue) over many scans with no compensation for jumps or drifts as a function of wavelength. Each wavelength has the same power at the sample ($\approx$ 180 nW). The shaded areas are guides to the eye representing the onset of two-photon ionization (yellow) due to the absorption sideband of VV^0 and the energy by which VV^0 is directly one-photon ionized (red). All error bars represent 95% confidence intervals from the fit of the raw data and are from a single (kk) VV^0.

lines, while higher energy illumination such as 520 nm (2.38 eV) is found to greatly increase the added ionization and spectral diffusion, consistent with a direct ionization process predicted through defect formation energies[18]. In ensembles, off-resonant light around 905 nm (1.37 eV) was found to be near-optimal in producing PL, as that wavelength both excites

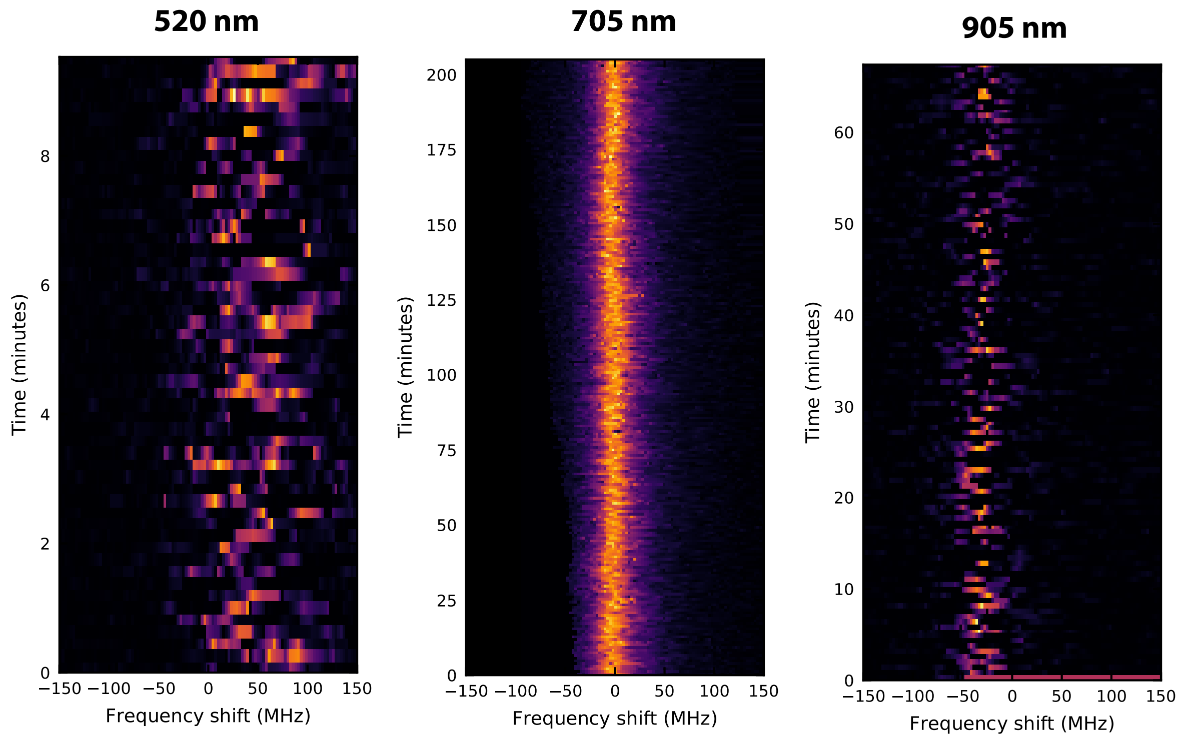

Figure 5.14: **Color dependence of blinking and spectral diffusion.** PLE sweeps over many scans at different wavelengths. These scans were used to generate the data in 5.13. Plots share the same x-axis but different total times. Increased spectral diffusion is apparent with the 520 nm and additional blinking is observed with the 905 nm. These scans are at the same optical power. The 705 nm plot corresponds to Fig. 5.3A.

the defect and repumps the charge state [149, 56, 95]. Here, we confirm those dynamics in a single defect, where 905 nm adds a small amount of repumping, while a 975 nm (1.27 eV) laser bleaches the defect without recovery with these powers (Fig. 5.13). However, 905 nm excitation also increases the ionization rate and is much less efficient than red laser colors around 700 nm in resetting the charge (Fig. 5.14). In addition, due to the higher powers necessary to stabilize the charge, 905 nm similarly adds to spectral diffusion of the PLE lines resulting in a broadening [150]. In general, because the absorption of resonant light is very efficient, it is preferable to use off-resonant light whose greater power causes much higher two-photon ionization rates. However, some off-resonant illumination energies (such as 905 nm) can additionally repump the divacancy into the correct charge state, while resonant

λ (nm)	σ_a **(cm^{-2})**	σ_i **(cm^{-2})**	σ_r **(cm^{-2})**
1131	$8 \pm 2 \times 10^{-12}$	$5.0 \pm 0.2 \times 10^{-19}$	0
975	$9.4 \pm 0.3 \times 10^{-12}$	$1.2 \pm 0.2 \times 10^{-17}$	0
905	$4.0 \pm 0.4 \times 10^{-17}$	$8.5 \pm 0.4 \times 10^{-18}$	$2.90 \pm 0.03 \times 10^{-20}$
705	0	-	$3.5 \pm 0.04 \times 10^{-18}$

Figure 5.15: **Ionization and reset cross sections.** Cross sections for absorption (σ_a), ionizing (σ_i) and repumping (σ_r) with various illumination wavelengths. For reference, the saturation power at sample is 14 mW for 905 nm and 9 mW for 975 nm.

light does not reset the charge of VV^0. Therefore, to reduce all unwanted ionization and to have independent and efficient control of the charge state, the ideal scenario is to use resonant light and a designated charge reset laser to stabilize the defect (red, ∼710 nm).

5.3.15 Charge Ionization and Repumping Cross Sections

With the power dependences of Fig. 5.4A, and Fig. 5.5A, along with the equations in section 5.3.12, we can extract the relevant ionization and repumping cross-sections as shown in Table S25.15. This uses the relation:

$$\text{Rate } = \frac{P\sigma}{A\hbar\omega} \tag{5.24}$$

Where P is the optical power over area A (the spot size), and $\hbar\omega$ is the energy of a single photon of a given wavelength. We also use the fact that the saturation of the emitter occurs: $PL(P) = \frac{A}{1+P/P_{\text{sat}}}$, where $\frac{1}{\tau} = \frac{P_{\text{sat}}\sigma_a}{A\hbar\omega}$ and is the emitter lifetime of $\sim 15\ ns$.

5.3.16 Deterministic Charge Control

In the main text, deterministic charge control is claimed to be possible. Here, we will discuss that claim. In general, the charge control is deterministic if there is independent control of

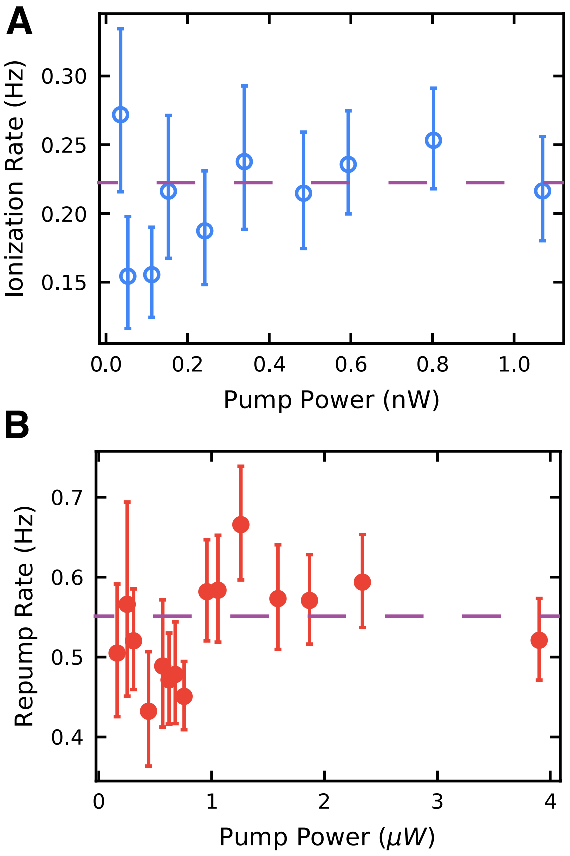

Figure 5.16: **Deterministic charge control.** **(A)** Ionization rate with changing repump power. **(B)** Reset rate with changing resonant power. The independence of the charge reset rate on ionization power and the charge ionization rate on reset power demonstrated independent and therefore deterministic control.

both $VV^0 \to VV^-$ and $VV^- \to VV^0$, such that upon applying that control, the desired charge state can be set with high fidelity. The selectivity of these rates determines the maximum fidelity possible of the desired charge state, and the rates themselves determine the time the control needs to be on for a given fidelity. First, at these temperatures the charge states are extremely stable [149], so no thermal process can interfere with the control. Second, we demonstrate that upon changing the repump power, the ionization rate does not change (Fig. 5.16A) and that upon changing the resonant power, the repump rate does not change (Fig. 5.16B).

Thus, the red repump and the resonant two-photon ionizing laser are independent controls of the defect charge state. By pumping with red for an extended period of time, very high fidelity charge state initialization into VV^0 is possible. However, from Fig. S7 we note that the red repump may add a small amount of ionization. A conservative estimate from the errors on Fig. 5.16 puts the ratio of the added change to about 1/10 to 1/20 of the total ionization and reset rate, giving a lower limit of 90-95% deterministic charge state preparation fidelity. This fidelity is also for 688 nm repump wavelength, not the much more efficient reset around 710 nm. This already competes with the best charge state manipulation of the NV^- in diamond, and we expect the true fidelity to be higher [123]. In principle, the well-resolved periods of low and high PL demonstrated means that single-shot charge readout is attainable, allowing for measurement and correction towards a particular charge state. We note that this deterministic charge state control is optimal under electric fields, where ionization events cause the charge to drift and be lost, instead of being able to be recaptured by the defect. For example, at zero electric fields, most single defects are stable under resonant excitation, as they live in a bath of photoionized charges (undepleted).

5.3.17 Distinction Between Different Types of Inhomogeneous Broadening

In the main text, we show how one can use electric fields to reduce spectral diffusion of the optical lines which contributes to the overall “inhomogeneous linewidth. However, the term “inhomogeneous linewidth is used in various contexts to refer to several different effects which can broaden the line from the fundamental “homogeneous linewidth. As such, we would like to make a distinction here between a few different types of “inhomogeneous broadening and discuss the relevance of these effects and how they relate to our system. First, for a single defect, spectral diffusion over time can cause inhomogeneous broadening of the optical lines. Well call this “temporal inhomogeneous broadening. This “temporal broadening as compared with the homogeneous linewidth is indeed of critical importance and is one of the main issues addressed in this work. As we have shown in Fig. 5.3, the

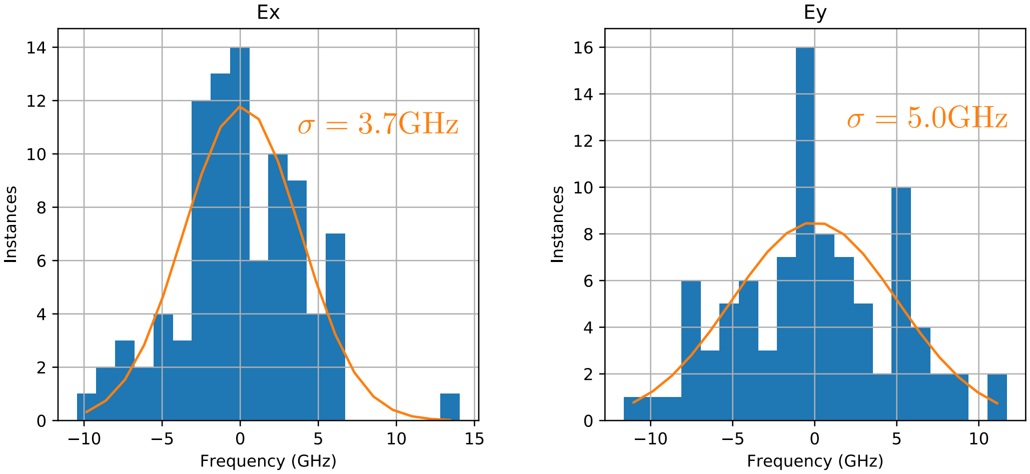

Figure 5.17: **Histograms of PLE center frequencies.** Spatial inhomogeneous (defects at different spatial locations) optical frequency distribution for (kk) defects in a semi-insulating sample for both the E_x (left) and E_y (right) transitions.

“temporal inhomogeneous broadening seems to be mainly due to electric field noise and can be mitigated to a great extent by charge depletion. In Fig. 5.3A, we observe this temporal inhomogeneous linewidth to be around 31 MHz over 3 hours. As mentioned in Fig. 5.3C and in section 5.2 section, we believe this could be further improved by slightly lower sample temperature and less instrumentation errors on the wavelength readout. Second, for a set of defects spatially distributed in a sample, we can observe some shifts in the exact position of the optical lines most likely due to local strain variations. Well call this “spatial inhomogeneous broadening. This is an important criterion since it sets a lower bound for the Stark shift necessary to enable two random defects to be tuned into resonance with one another. Here, we have provided an estimate based on statistics taken on a semi-insulating sample (see Fig. 5.17). This data suggests that the “spatial inhomogeneous broadening is roughly around 5 GHz, well below the demonstrated tuning range.

Third, one could also wonder about the variation between significantly different samples (for example, different wafers may have different strains, epilayer compositions, or growth conditions). Well call this “sample-to-sample variation. A precise measure of “sample-to-sample variation is tricky since we only have a distinct number of wafers and we generally try to have these wafers as similar as possible. However, our experience with several types of wafers (both commercially and custom grown, and with different epilayers) suggest variations to be on the order of ~100-200 GHz. Of course, the more extreme the changes to the host material is, the higher these variations are expected to be. However, in a practical implementation of a quantum node, the samples at play would most likely be chosen to be nominally identical, thus greatly reducing this number. In short, our demonstrated tuning range of ~850 GHz easily covers both the "temporal and "spatial inhomogeneous linewidth (by orders of magnitude) and would undoubtedly cover the "sample-to-sample variations present in nominally similar chips.

5.3.18 Effect of Charge Depletion on Spin Coherence

In this work, we demonstrate the effect of charge depletion on the optical linewidth. However, one could also wonder what effects depletion might have on the spin coherences. Although this is beyond the scope of this paper (and we did not directly observe any obvious effects), we do believe this is an exciting research avenue. There are two possible ways in which charge depletion could contribute to longer coherences. First, the direct reduction in E-field noise could help to mitigate dephasing due to the E-field coupling terms in the spin Hamiltonian. Second, by changing the charge state of nearby traps, the depletion region could modify the total spin of these traps, potentially changing the effective induced B-field noise.

5.3.19 Charge Feedback Protocol and Rates

Charge dynamics are a major problem that many solid-state systems need to contend with. In the NV^-center in diamond, for example, this issue has been addressed using feedback protocols [114]. In particular, these protocols require readout and control of the charge state of the defect. This manuscript demonstrates two aspects of our system which will make it amenable to these types of feedback protocols. First, the divacancy simply goes dark once ionized (without a red repump) and does not return to the neutral state even when a resonant readout laser is applied. This facilitates reading out the charge state, as a weak resonant tone (such that two-photon ionization is negligible) can confirm the presence or absence of the divacancy in the correct charge state, without causing unwanted charge flipping. Second, we show that we can use red light to deterministically repump into the neutral charge state, giving us an ideal control for the feedback loop. Since this repump could be fast (by increasing the red power to a few mW) it would have minimal effect on the duty cycle. In general, the charge conversion rates demonstrated here are slow. However, this was mostly done for ease of experiment and to avoid timescales associated with the intersystem crossing. Despite this, there is no obvious limit for the ionization and reset rates, where we expect timescales of μs are readily accessible by increasing the powers from nW to mW [42].

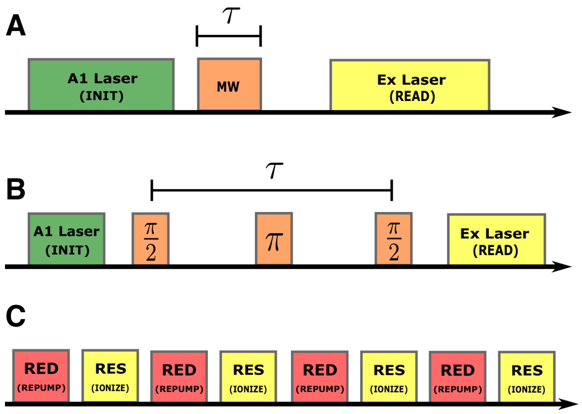

Figure 5.18: **Pulse sequences.** Pulse sequences for **(A)** Rabi oscillations, **(B)** Hahn echo, and **(C)** charge hopping experiments. These correspond to the descriptions in 5.2.

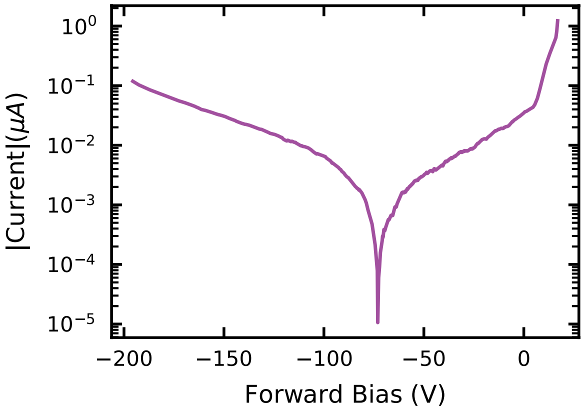

Figure 5.19: **Semi-log plot of the absolute value of current from the IV curve for the device at 5K.**

CHAPTER 6

QUANTUM MEMORIES AND ISOTOPIC ENGINEERING

This chapter and figures were adapted from the following publication [25]:

A. Bourassa*, C. P. Anderson*, et al. **Entanglement and control of single nuclear spins in isotopically engineered silicon carbide**. *Nature Materials*, 2020. (* Equal contribution)

6.1 Entanglement and control of single nuclear spins in isotopically engineered silicon carbide

Nuclear spins in the solid-state are both a cause of decoherence and a valuable resource for spin qubits. In this work, we demonstrate control of isolated 29Si nuclear spins in silicon carbide (SiC) to create an entangled state between an optically active divacancy spin and a strongly coupled nuclear register. We then show how isotopic engineering of SiC unlocks control of single weakly coupled nuclear spins and presents an *ab initio* method to predict the optimal isotopic fraction which maximizes the number of usable nuclear memories. We bolster these results by reporting high-fidelity electron spin control (F=99.984(1)%), alongside extended coherence times ($T_2 = 2.3\ ms$, $T_2^{DD} > 14.5\ ms$), and a >40 fold increase in dephasing time (T_2^*) from isotopic purification. Overall, this work underlines the importance of controlling the nuclear environment in solid-state systems and provides milestone demonstrations that link single-photon emitters with nuclear memories in an industrially scalable material.

6.1.1 Introduction

Nuclear spins are one of the most robust quantum systems, displaying relaxation times that can exceed hours or days [61, 105, 131]. This makes them exciting candidates for quantum technologies requiring long memory times. In particular, nuclear spins are attractive quantum registers for optically active spin defects in the solid-state [27]. For example, nuclear registers can be used for repetitive quantum non-demolition (QND) optical readout [96], to enhance the signal-to-noise in quantum sensing [155], to implement quantum error correction schemes [128], or as vital components of quantum repeater [113] and quantum communications [76] nodes. Additionally, electron-nuclear hybrid systems provide a platform for studying measurement back-action [41] and the emergence of classicality in quantum mechanics [135].

Recently, commercial SiC has been shown to provide a technologically mature semiconductor host for multiple defect spin qubits [34, 86, 143, 43, 148]. In particular, this material allows the integration of isolated color centers into classical electronic devices which can be used to engineer and tune the spin-photon interface [5]. Combining such a tunable near-infrared emitter [35, 40] with a long-lived quantum memory is a promising basis for quantum network nodes fabricated at wafer scale by the semiconductor industry. To realize these quantum memories, SiC provides both carbon and silicon isotopes with non-zero nuclear spin. These isotopes have been shown to couple to various electronic spin defects [83, 103]; however, the isolation and control of single nuclear spins [129] in SiC has remained an outstanding challenge.

In this work, we report coherent control and entanglement of nuclear spin quantum registers strongly coupled to a single neutral divacancy spin (VV^0) in naturally abundant SiC. We then extend this control to weakly coupled nuclear spins, where isotopic purification enables the isolation of robust quantum memories. Using isotopic engineering, we also report both record coherence times and record single-qubit gate fidelities [115] for spins in SiC. Throughout this work, we present both experiment and *ab initio* theory that explores the inherent tradeoffs between spin coherence and nuclear memory availability which are involved when isotopically engineering materials. These results develop a full suite of nuclear spin controls

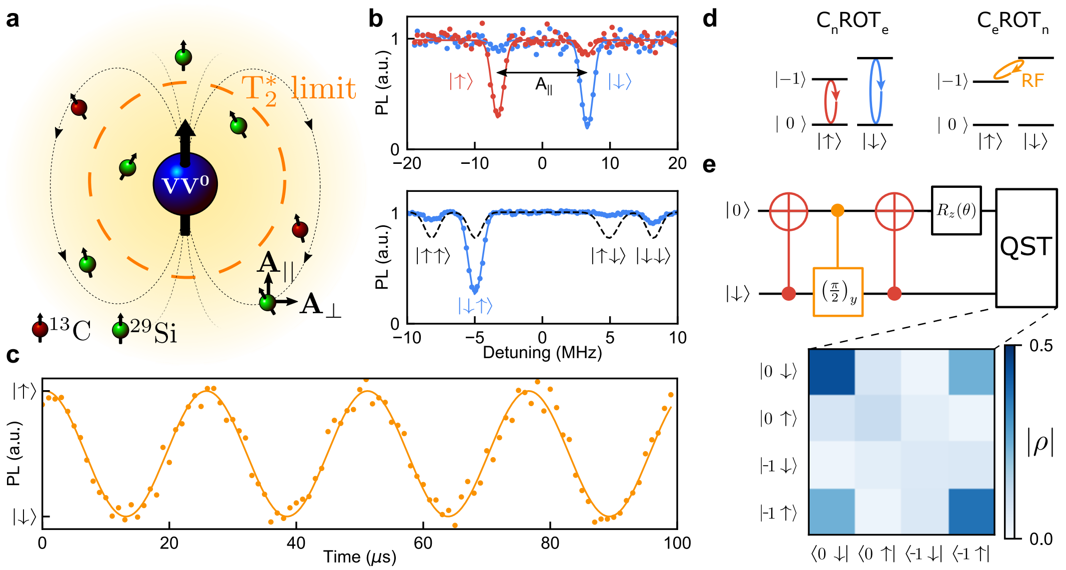

Figure 6.1: **Initializing, controlling, and entangling strongly coupled nuclear spins.** **a**, Schematic of a single divacancy with surrounding nuclear spins. **b**, Optically detected magnetic resonance of a single (kk) VV^0 after initialization of both the electron and either 1 (top) or 2 (bottom) strongly coupled nuclear spins. Top: initialization in either the $|\uparrow\rangle$ (red) or $|\downarrow\rangle$ (blue) nuclear spin states. Detuning is from 1.139 GHz. Bottom: the dashed line (black) represents the expected results from an uninitialized state, the blue line is the experimental initialized state. Detuning is from 2.153 GHz. **c**, Nuclear Rabi oscillations (between $|1 \downarrow\rangle$ and $|-1 \uparrow\rangle$) obtained by driving an RF tone implementing a C_eROT_n. **d**, level structure schematic of a divacancy spin coupled to a single nuclear register. The $|+1\rangle$ electron spin state is not shown. (left) C_nROT_e manipulation drives colored as in **b**. (right) C_eROT_n RF drive corresponding to the oscillations in **c**. **e**, (top) Quantum circuit used to generate a bipartite entangled state between an electron and nuclear spins. Gates are driven using the manipulations shown in **d**. (bottom) Resulting density matrix ($|\rho|$). The third initialized qubit is omitted. All data are taken at T= 5 K.

in SiC and provide a guide for future materials design of spin-based quantum technologies.

6.1.2 Strongly Coupled Nuclear Registers

In natural SiC, 1.1% of the carbon atoms and 4.7% of silicon atoms possess an I=1/2 nuclear spin. Thus, about a third of all single c-axis oriented (hh and kk, appendix 6.3) divacancies will have a ^{29}Si register on one of the nearest-neighbor lattice sites (denoted Si_I, Si_{IIa} or Si_{IIb}) [126]. When the hyperfine coupling exceeds the linewidth (order $1/T_2^*$) of the electronic state (Fig. 6.1a), oscillations due to these nuclear spins are observable in Ramsey experiments. We refer to such nuclear spins as strongly coupled. This strong coupling splits the $m_s = \pm 1$ electronic ground state levels, which results in pairs of resolved transitions that enables direct selective control of this two-qubit state using external radio frequency (RF) magnetic fields.

Here, we demonstrate such a strongly coupled system by isolating a single c-axis (kk) VV^0 with a nearby ^{29}Si at the Si_{IIa} site (parallel hyperfine $A_{\parallel} = 2\pi \cdot 13.2\ MHz$) in natural 4H-SiC. In this case, because the electron spin linewidth (~1 MHz) is much lower than the hyperfine splitting $A_{\parallel}$, we observe two individually addressable transitions corresponding to the two nuclear spin states (Fig. 6.1b). To polarize this nuclear register, we make use of two iterations of algorithmic cooling in which we optically polarize the electron spin and then swap this polarized state to the nuclear spin [140]. Using this method, we can achieve a high initialization fidelity (~93%) as measured by the peak asymmetry in the optically detected magnetic resonance spectrum shown in Fig. 6.1b (appendix 6.3).

After nuclear initialization, we prepare the electron spin in the $m_s = -1$ state and use a 13.2 MHz RF magnetic field to drive nuclear Rabi oscillations (Fig. 6.1c), which we read out by projecting onto the electron spin. Since these oscillations are only driven in the $m_s = \pm 1$ states, this allows us to demonstrate a $C_{\pm 1}NOT_n$ gate [83] which can be performed in 12.7 μs. Throughout these measurements, we also make use of fast (limited only by the hyperfine splitting of the lines) C_nNOT_e gates by applying a microwave pulse at one of the two frequencies shown in Fig. 6.1b (see Fig. 6.1d).

Having demonstrated control over a single nuclear spin, we then increase the number of registers by finding a (kk) divacancy which is strongly coupled to two ^{29}Si spins (with 6% probability for naturally abundant SiC). For this defect, we show that using both algorithmic cooling and dynamical nuclear polarization [83, 48] (DNP), we can polarize the full three-qubit system (Fig. 6.1b). We then demonstrate individual control of these registers and calibrate gates operating on either register (appendix 6.3).

In this three-qubit spin system, we apply the quantum circuit in Fig. 6.1e on the electron and one of the two coupled nuclear spins to create an electron-nuclear entangled state, and measure its full density matrix using quantum state tomography [83] (QST). We evaluate this density matrix using the positive partial transpose test, confirming unambiguously the entanglement in this system with an estimated entangled state fidelity of $\sim 81\%$ (appendix 6.3).

These results demonstrate that single, strongly coupled nuclear spins can be used as quantum registers in SiC with relatively fast gate times. This type of register is useful for QND measurement of the nuclear spin and more generally for any applications that require fast operations [52] on ancilla qubits [111, 60]. However, the number of available nearby nuclear sites which can be controlled in this way is limited. Additionally, the high coupling strength makes these nuclear registers more sensitive to stochastic noise from the electron spin and limit applications where repeated electron initialization and control is necessary [113, 75], such as in long-distance quantum communications [62] or entanglement distillation [76].

6.1.3 Weakly Coupled Nuclear Memories

To complement these strongly coupled registers, we therefore investigate nuclear spins which are weakly coupled to divacancy electron spins. In order to access these memories and go beyond the $1/T_2^*$ limit, we use a XY8-based dynamical decoupling sequence to perform nanoscale NMR [129, 2, 8, 101] of the nuclear environment of a (kk) divacancy (Fig. 6.2a). This sequence (Fig. 6.2b) not only protects the electron spin from decoherence, but also allows for selective control of nuclear spins even when their hyperfine coupling is lower than the electron spin linewidth. In this measurement, each nuclear spin produces a series of dips in the coherence function at a pulse spacings [129] $\tau_k \approx \frac{(2k+1)\pi}{2\omega_L+A_1}$ at integer order k

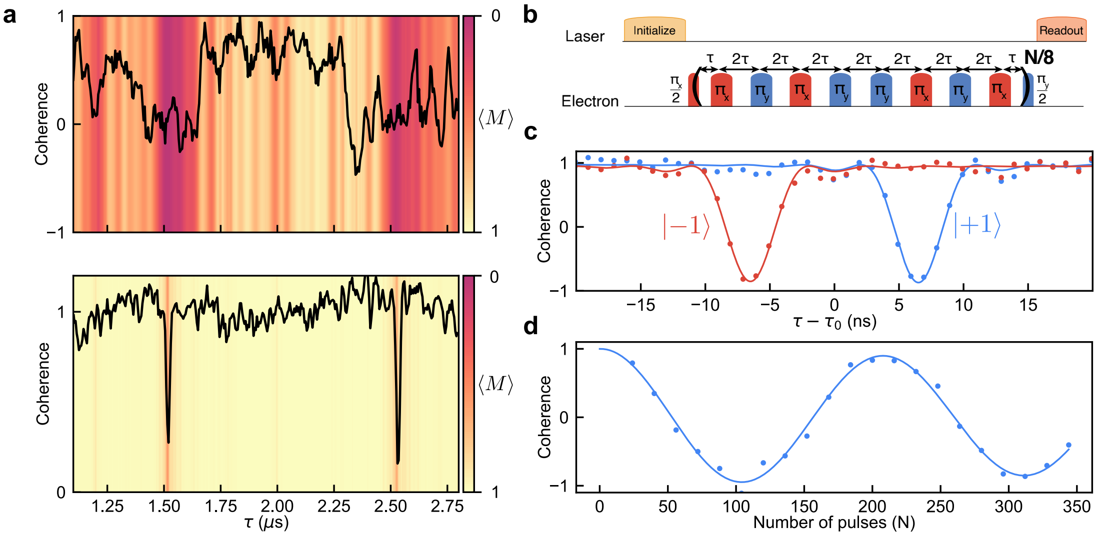

Figure 6.2: **Spectroscopy and control of weakly coupled nuclear spins.** **a**, CPMG based NMR spectroscopy of the nuclear environment of an example kk divacancy in a natural (top) and isotopically purified (bottom) sample. The data is shown as a black solid line. The background gradient represents the calculated average coherence function obtained over many nuclear configurations $\langle M \rangle$, which represents the expected density of coherence dips. **b**, Schematic of the XY8 pulse sequence. **c**, Coherence dips (8th order ($k = 8$), $\tau_0 = 6.125\ \mu s$) using either the $|-1\rangle$ (red) or $|+1\rangle$ (blue) electron spin state, providing a measure of $A_\partial \approx 2\pi \cdot 650\ Hz$. **d**, A $C_eROT_{x,n}(\pm\theta)$ oscillation demonstrated on the 6th order ($k = 6$) of the isolated nuclear spin and achieved by varying the number of XY8 subsequence repetitions. After seven XY8 repetitions (total pulse number $N = 56$), a conditional $\pm\pi/2$ rotation is achieved with a fidelity of F=97(1)%. All data are taken at T= 5 K and B = 538 G.

and Larmor frequency ω_L, corresponding to its specific nuclear precession frequency. With this spectroscopy, we observe that natural SiC has a crowded nuclear resonance spectrum due to the relatively abundant ^{29}Si, making it difficult to isolate single spins with low hyperfine coupling [75] (defined here to be $< 2\pi \cdot 60\ kHz$). This spectrum, along with *ab initio* cluster-correlation-expansion [120] (CCE) simulations of various possible nuclear spin configurations (Fig. 6.2a), demonstrates that natural SiC is not well suited for isolating single weakly coupled nuclear spins with low hyperfine values.

To address this issue, we use isotopically purified gases to grow 4H-SiC with 99.85% ^{28}Si and 99.98% ^{12}C (appendix 6.3). In this sample, we once again measure the nuclear environment of a few (kk) divacancies and find one with a single isolated dip in the coherence function (Fig. 6.2a). We find that the dip positions very closely match the different orders (k) of the Larmor frequency of a ^{29}Si (differing only through the hyperfine value [129]). We further confirm the gyromagnetic ratio for this nuclear spin species by repeating the experiment at a different magnetic field (appendix 6.3).

Having confirmed that the dips correspond to a ^{29}Si nuclear spin, we perform spectroscopy in both the $[m_s = 0, m_s = +1]$ and the $[m_s = 0, m_s = -1]$ basis (Fig. 6.2c), and measure a small $A_{\|} \approx 2\pi \cdot 650\ Hz$ [129], which would not be resolvable in a Ramsey experiment. Low $A_{\|}$ nuclear spins are especially useful as robust quantum memories because the dephasing of the nuclear spin caused by stochastic noise from the electron is particularly sensitive to the parallel component of the hyperfine tensor, $A_{\|}$ [113].

Fixing the pulse spacing (2τ) to a specific coherence dip ($k = 6$), we then vary the number of pulses (N) to coherently control this weakly coupled single nuclear spin [129, 128]. The corresponding $C_eROT_{x,n}(\pm\theta)$ oscillations observed (Fig. 6.2d) allows us to measure the perpendicular hyperfine component $A_{\perp} \approx 2\pi \cdot 11.45\ kHz$ (where $\theta \approx \frac{A_{\perp} \cdot N}{\omega_L}$) and confirms the successful application of a maximally entangling two-qubit gate [128](appendix 6.3). If no other nuclear spins were present, one could choose any resonance order (k) to perform the two-qubit gate. In practice however, as k increases, the resonance of the isolated nuclear spin separates from the rest of the bath which drastically increases the two-qubit gate fidelity. Here, even in the isotopically purified sample where the nuclear spectrum is sparse, the electron-nuclear gate fidelity increases greatly at higher orders (k) as the resonance separates from the bath (up to 97(1)% at $k = 6$, appendix 6.3). These results demonstrate the importance of reducing the nuclear spin bath for high fidelity control of isolated quantum memories with weak hyperfine interactions.

With these results in mind, we now turn our attention to estimating the optimal isotopic fraction required to maximize the number of isolated and controllable nuclear memories. Here, we need to strike a balance between too much purification which removes most usable nuclear spins and too little which results in a crowded and unresolvable spectrum. Limiting the gate time to a regime where nuclear-nuclear interactions are negligible (appendix 6.3), we developed a method to predict the average number of resolvable nuclear memories as a function of isotopic concentration. This is achieved by considering both the intrinsic gate fidelity from the electron-nuclear interaction and the average effect of unwanted rotations from all other nuclear species (appendix 6.3). Our analysis demonstrates several important aspects of nuclear availability in SiC.

First, there exists an optimal nuclear spin concentration (Fig. 6.3a) that maximizes the average number of available nuclear memories which can be controlled within a maximum gate time and at a given minimum gate fidelity. Here, we find that naturally abundant SiC has a prohibitively high concentration of ^{29}Si, which prevents the isolation of nuclear memories with low hyperfine coupling ($< 2\pi \cdot 60\ kHz$). This reinforces the importance of isotopic engineering for nuclear memories in SiC and explains the spectrum observed in Fig. 6.2a. Second, the hyperfine values of the resulting controllable memories vary with isotopic concentration (Fig. 6.3b). At high concentrations, nuclei with moderate hyperfine ($> 2\pi \cdot 60\ kHz$) contribute to most of the available memories, while low hyperfine nuclear spins are unresolvable. On the other hand, a lower isotopic concentration results in a less crowded spectrum and allows for the isolation of nuclei with lower hyperfine. The choice of nuclear concentration thus not only determines the total number of available quantum memories, but also the distribution of hyperfine values for these controllable nuclei.

Furthermore, we note that there is a tradeoff between the maximum allowable gate time and the number of available nuclear memories. While longer gate times allow for the resolution of more distant nuclei, this increase is shown to be only sublinear (appendix 6.3). Additionally, when both nuclear species are utilized, the SiC binary lattice may provide roughly double the number of resolvable nuclear registers compared to a monoatomic crystal.

While the range of desired hyperfine values may differ depending on the particular ap-

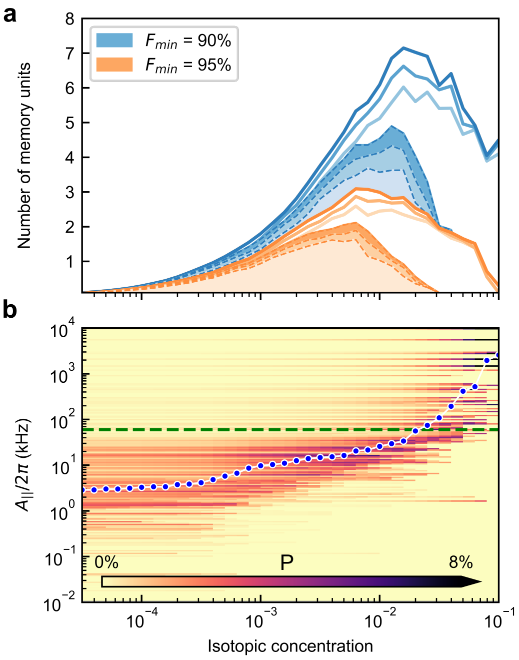

Figure 6.3: **Isotopic optimization of nuclear memories.** **a**, Calculated average number of memory units as a function of isotopic concentration where $[^{13}C] = [^{29}Si]$. A memory unit is defined as a nuclear spin that can be isolated and controlled above a given gate fidelity (F_{min}) within the maximum gate time. Solid lines correspond to all memory units whereas the dotted lines with shaded areas correspond to only memories with $A_{||} < 2\pi \cdot 60\ kHz$. Three different maximum allowable gate times are represented (lightest to darkest: 1 ms, 1.5 ms and 2 ms). **b**, Distribution of the hyperfine values for usable memory units as a function of isotopic concentration. Darker color corresponds to a higher probability (P) that memory units, if present and usable, will have the corresponding hyperfine value (maximum gate time = 1.5 ms, $F_{min} = 0.9$). Blue circles show the median of the distribution at the given concentration. The green dotted line corresponds to $A_{||} = 2\pi \cdot 60\ kHz$. The values are computed at the magnetic field of 500 G.

plication, a careful selection of the isotopic fraction is critical to maximizing the number of nuclear spins available in this range. This careful selection also determines the resulting average gate speeds and fidelities, allowing further optimization for the application at hand. These results therefore constitute not only a proof-of-principle demonstration of single weakly coupled nuclear spin control in SiC, but also provide guidance for future isotopic growth of materials for a variety of spin-based quantum technologies.

6.1.4 High-fidelity Qubit Control and Extended Coherences

Broadly, these experiments are all predicated on the divacancy electronic spin being a controllable and long-lived qubit. In this section, we discuss in detail the main factors that limit the coherence of divacancies in SiC and quantify our ability to perform single-qubit manipulation.

We begin by measuring both T_2^*(Ramsey spin dephasing time) and T_2 (Hahn-echo coherence time) of both c-axis (*kk*) and basally (*kh*) oriented defects in isotopically purified material. We measure the c-axis defects at B=48.8 G and the basal defects at B=0 G (to benefit from the magnetic insensitivity arising from a clock-like transition [99, 98]).

We report (Fig. 6.4a and 6.4b) T_2^* times of 48.4(7) μs and 375(12) μs for the c-axis (*kk*) and basal (*kh*) defects, compared to 1.1 μs [34] and 70-160 μs [99] in naturally abundant material. These numbers correspond to record dephasing times for spins qubits in SiC [103]. Additionally, despite only moderate isotopic purity, these results are very competitive with NV centers in diamond with much lower nuclear spin concentration [23, 14, 67]. This favorable scaling most likely arises from the SiC binary lattice and longer bond length, which results in reduced nuclear flip-flops [120]. These improvements in T_2^* are vital for DC quantum sensing schemes and for achieving strong coupling in hybrid systems [37, 142].

The significant increase in dephasing times arising from the isotopic purification for the c-axis defects shows that magnetic field noise from the nuclear environment is by far the main limiting factor to T_2^* for these defects. We provide further evidence of this by investigating the dephasing in isotopically purified SiC with *ab initio* cluster-correlation-expansion (CCE) simulations. Taking into account the remaining nuclear spin bath, these calculations predict average T_2^* values which are consistent with our experimental observations (Fig. 6.4a).

On the other hand, while basal divacancies benefit from first-order insensitivity to magnetic field noise at B=0 G, this magnetic noise protection comes at the cost of increased sensitivity to electrical fields [69]. Since charge fluctuations can cause significant electric

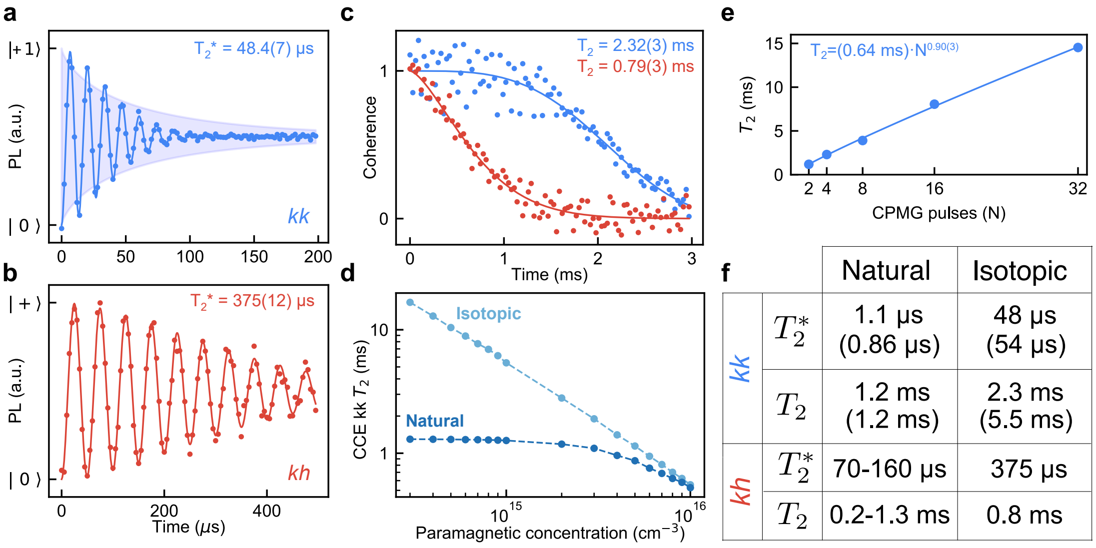

		Natural	Isotopic
kk	T_2^*	1.1 μs (0.86 μs)	48 μs (54 μs)
	T_2	1.2 ms (1.2 ms)	2.3 ms (5.5 ms)
kh	T_2^*	70-160 μs	375 μs
	T_2	0.2-1.3 ms	0.8 ms

Figure 6.4: **Divacancy dephasing and decoherence times in isotopically purified material.** **a**, Dephasing of a c-axis (kk) defect in the isotopic sample at B=48.8 G. The shaded region represents the predicted average results from CCE (B = 50 G and paramagnetic density of 1×10^{15} cm^{-3}). **b**, Dephasing of a basal (kh) defect at B = 0 G. **c**, Coherence function under a Hahn echo sequence for kk (blue) and kh (red) single defects. **d**, CCE calculations (including the effects of paramagnetic traps) for a kk defect showing that the expected Hahn echo T_2 varies greatly based on paramagnetic spin density for both natural (dark blue) and isotopic (light blue) material (at B = 500 G). **e**, Coherence time for a (kk) defect in the isotopic sample under a varying number of CPMG pulses (N) shows that T_2 increases roughly linearly with pulse number (B = 48.8 G). **f**, Table summarizing representative numbers for T_2^* and T_2 (Hahn echo) in kk and kh defects in both natural and isotopic samples. Natural SiC coherences are taken from literature [34, 99, 98]. Numbers in parentheses are the theoretical numbers obtained by CCE (at B = 50 G) with both the nuclear spin bath and a paramagnetic spin bath of 1×10^{15} cm^{-3}. All data are taken at T= 5 K.

field noise [5], this may explain why the increase in T_2^* obtained from isotopic purification (Fig. 6.4b) is less pronounced than that of the c-axis divacancies. Furthermore, this magnetic protection also makes nuclear control difficult in the basal (kh) divacancies. This underlines the tradeoffs involved when choosing a defect species to work with.

Next, we perform Hahn-echo experiments to measure T_2 in isotopically purified SiC (Fig. 6.4c). Although we find a factor of ~2 improvement in the coherence time for (kk) defects in this material (2.32(3) ms versus 1.1 ms [34]), we remark that this is a more modest improvement than that of T_2^*. Nevertheless, this T_2 is comparable to the longest observed

Hahn-echo coherence time in isotopically purified diamond samples with much greater isotopic purity [11, 63]. Interestingly, but the measured T_2 deviates from the predictions from nuclear spin induced decoherence obtained with CCE calculations, which yield an average coherence time of ∼37 ms. To understand these results, we carried out second order CCE simulations to study the effect of non-interacting electron spin pairs on the coherence time [146]. At the estimated paramagnetic density (impurities and radiation-induced defects in the $3 \times 10^{14} - 3 \times 10^{15} cm^{-3}$ range, appendix 6.3) we find good agreement with the experiment (Fig. 6.4d), thus confirming both the accuracy of our theoretical model and the important role of paramagnetic defects in limiting coherence. Our results are consistent with magnetic noise from a weak, but quickly fluctuating paramagnetic spin bath combined with noise from a strong, but slowly fluctuating, nuclear spin bath [12]. As a consequence, T_2^* is limited by nuclear spins, while T_2 is limited by paramagnetic impurities for the c-axis defects. On the other hand, differences in the basal divacancys coherence compared to other reports [98, 99] likely stems not only from the isotopic purification, but also from sample-to-sample variations in electric field noise, which could be mitigated using charge depletion techniques [5].

The demonstrated coherence can be further extended by additional refocusing pulses. We provide a proof-of-principle demonstration by varying the number of pulses (N) in a dynamical decoupling sequence. At $N = 32$, the coherence is increased to 14.5 ms (for a kk defect, Fig. 6.4e). With more pulses, the coherence should continue to increase linearly until the T_1 limit is reached, which we measure to be on the order of one second under these experimental conditions (appendix 6.3).

Finally, we characterize our single-qubit gate fidelities through randomized benchmarking experiments and obtain an average gate fidelity of 99.984(1)% (Fig. 6.5). These bare fidelities are amongst the highest for single spins in the solid-state [115, 152, 154] and exceed the threshold for error correction codes [85, 139, 31]. Furthermore, high fidelity control of the

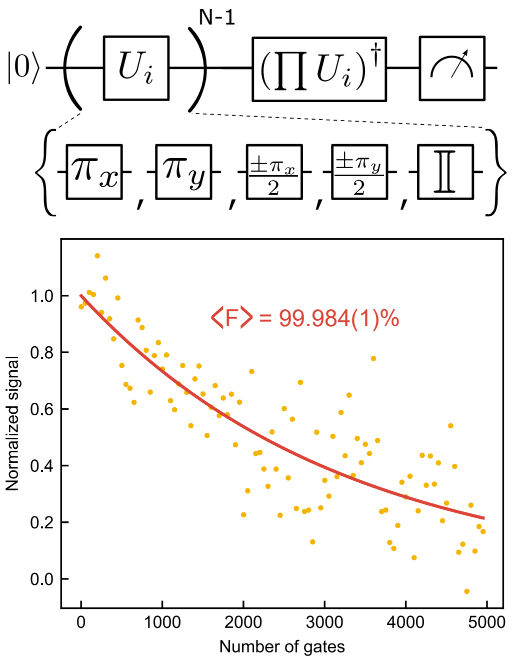

Figure 6.5: **Average single-qubit gate fidelity as measured by randomized benchmarking.** Results obtained by applying N Clifford gates (as represented by the quantum circuit) on a *kh* defect in the isotopically purified material at T= 5 K, B= 0 G. From this decay we extract an average gate fidelity of 99.984(1)%

electron spin is crucial to prevent reduced coherence in nuclear spin memories [75]. The long coherence ($T_2^{DD} > 14.5\ ms$) and high fidelity control (99.984(1)%), combined with a > 99% resonant initialization and readout fidelity (appendix 6.3) demonstrated in this work establishes the divacancy in SiC as a promising system for future solid-state quantum devices.

6.1.5 Conclusion

Defect spins in SiC are exciting candidates for wafer-scale quantum technologies requiring stationary qubits and a photonic quantum communication channel. In this work, we provide milestone demonstrations of nuclear memory control of both strongly and weakly coupled nuclear memories in a technologically mature semiconductor material. This work also examines, both experimentally and theoretically, the tradeoffs that are inherent to isotopic purification and offers a pathway towards optimizing nuclear spin concentration to maximize the number of usable nuclear memories.

Our results underline the importance of isotopic engineering in designing materials for solid-state quantum applications. Such engineering can provide a two-fold benefit for quantum memories: it enables control of more nuclear spins by unlocking access to memories with low hyperfine coupling, while also drastically increasing the coherence of these nuclear spins [109]. Moreover, isotopic engineering enables the selection of a hyperfine distribution that can optimally trade off the effect of the "frozen core [59] against the electron spin induced noise inherent in realistic quantum communications protocols [75]. Further optimization may also be achieved by considering differing nuclear control methods [27, 46]. Additionally, the demonstrated proof-of-principle nanoscale NMR detection of a single nuclear spin (at a distance of ∼1.2 nm) in SiC provides a route for a functionalizable, biocompatible platform for quantum sensing with polarization and readout in the biological near-infrared window [108]. Overall, these results cement defects in SiC as attractive systems for the development of quantum communication nodes and underline the importance of isotopic control in material design for future quantum technologies.

6.2 Methods

6.2.1 Single Defect Observation and Control

Single defects are observed in a home-built confocal microscope operating at T= 5 K with a Montana Cryostation s100 closed-cycle cryostat. We utilize a high NA (0.85) NIR objective and single-mode fiber-coupled (1060XP) IR-optimized SNSPD (Quantum Opus) and observe single defects with 40-50 kcts at saturation. 905 nm excitation is used along with a weak 705 nm tone for charge stabilization [5]. Microwave striplines are fabricated alongside an electrical control planar capacitor (10 nm Ti, 150 nm Au) using electron beam lithography.

In 4H-SiC, single PL1 (hh), PL2 (kk), and PL4 (kh) defects are observed and are labeled following the $V_c V_{Si}$ convention and where h represents the hexagonal lattice site and k the quasi-cubic lattice site. The c-axis refers to the crystallographic axis in SiC which corresponds to the stacking direction of the hexagonal layers of SiC ([0001]). Basal defects are oriented along one of the basal planes. Resonant readout and initialization [5, 35] (realized using a tunable Toptica DLC PRO laser) can result in Rabi contrast exceeding 99% in optically detected magnetic resonance (ODMR) (Fig. 6.6). This corresponds to the highest Rabi contrast reported in SiC and provides an achievable lower bound for initialization and readout errors combined. Reported coherences are for representative single defects.

For the strongly coupled nuclear spin experiments, Gaussian pulse shaping is used to perform spectrally narrow manipulation of the quantum registers. ^{13}C registers are also available [126], but occur with lower probability in both the natural and isotopic samples. For nuclear spin spectroscopy and control, randomized benchmarking, and coherence measurements, square pulses were used with π pulse times ranging from 50 ns to 1 μs. Magnetic fields are applied with a large permanent magnet on a goniometer. Alignment at high field is achieved by reducing the mixing from off-axis magnetic fields, visible through the PLE magnitude after initializing the spin (a measure of cyclicity). In order to zero the magnetic field for kh divacancies, we utilize a three-axis electromagnet. Using a nearby c-axis kk defect as a magnetometer, the field is zeroed by reducing the splitting between the very narrow CW ODMR lines in the isotopically purified sample (<20 kHz).

6.2.2 Materials Growth

Natural 4H-SiC was obtained from Norstel AB (now ST Microelectronics) in the form of a 20 μm intrinsic epitaxial layer grown on 4 off-axis HPSI 4H-SiC. This layer contains $< 1 \times 10^{15}\ cm^{-3}\ V_c$. For the isotopically purified ("isotopic) sample, epitaxial 4H-SiC was CVD grown on a 4-degree off-axis n-type 4H-SiC substrate at a thickness of ~90 μm using isotopically purified Si and C precursor gasses. The purity is estimated to be 99.85% ^{28}Si and 99.98% ^{12}C, which was confirmed by secondary ion mass spectroscopy (SIMS). C-V measurements show a slightly n-type behavior of this layer with a free carrier concentration of $6 \times 10^{13} cm^3$. This roughly matches the measured concentration ($3.5 \times 10^{13} cm^{-3}$) of nitrogen through comparisons of the bound exciton lines. DLTS places the V_c concentration at the mid $10^{12} cm^{-3}$ range before irradiation.

In the naturally abundant material, single defects are created using a $110^{13} cm^{-2}$ dose of 2 MeV relativistic electrons. Subsequent annealing at 810 C in an Ar environment produces spatially isolated single VV^0. For the isotopically purified material, an electron dose of $1 \times 10^{13} cm - 2$ (Fig. 6.5) and $5 \times 10^{14} cm^{-2}$ (Fig. 6.1,6.2,6.3) are used. Despite the low impurity and defect content of the starting material, this means that the number of induced displacements [90] in the lattice after irradiation can be as high as $0.5 - 3\ cm^{-1} \times (dose) = (0.25 - 1.5) \times 10^{15}\ cm^{-3}$. These defects can be paramagnetic and most likely consists of V_C, V_{Si}, and associated vacancy complexes. This is also a relatively common range even before irradiation in commercially available materials. Upon annealing, divacancies are created along with other paramagnetic defects. Higher spin species or laser-induced scrambling of the charge states of these paramagnetic impurities may also increase the effect of impurities with respect to CCE.

Furthermore, the observed optical linewidth is significantly broadened by spectral diffusion. In this material, lines are in the 150-350 MHz range. We can use this broadening to estimate18 the trap density to be $3 \times 10^{14} - 3 \times 10^{15} cm^{-3}$ for the kk defect, which would be consistent with the observed Hahn echo times if these traps are assumed to be paramagnetic.

6.2.3 Calculations of Coherence Functions

Cluster-correlation expansion (CCE) calculations of the coherence function for the nuclear spins were carried out according to the method outlined by Yang and Liu [153] with the choice of parameters described by Seo et al. [120]. We apply the CCE up to second-order under the assumption that the flip rate of each pair of electron spins is not impacted significantly by interactions with the spins outside a given pair. The total coherence function (L) can be factorized into contributions from electron and nuclear spins, respectively: $L(t) = L_{electron} \cdot LL_{nuclear}$.

6.2.4 Calculations of Nuclear Memory Availability

In order to decide whether the nuclear spin at the lattice site i can be used as a memory, we evaluated the state fidelity of the electron spin state after a nuclear-induced rotation. The fidelity can be inferred from the electron magnetization along the x-axis. Assuming that nuclei-nuclei interactions are negligible, the expectation value of the electron magnetization along the x-axis at a given N and τ in the presence of a nucleus i can be expressed as

$$\tilde{M}_i = E\left(M | M_i \in M\right) = M_i \prod_{j \neq i} E\left(M_j\right) \tag{6.1}$$

where $M_i(M_j)$ is the conditional magnetization when only one nucleus (at lattice site $i(j)$) interacts with the electron, j runs over all other possible nuclear positions, and $E(M_j)$ is the expectation value of the conditional magnetization. A nucleus at lattice site j is considered to be useable as a memory unit if there exist at least one set of N and τ with $N2\tau$ smaller than a maximum gate time, such that the fidelity of the electron spin after rotation $\tilde{M}_i(N, \tau)$ is higher than a certain threshold F_{min}. The average number of nuclei i present at this lattice site is equal to the concentration of the spin-$\frac{1}{2}$ isotope c_i. The resulting total number of usable memory units is computed as the sum of c_i for all i that meet the fidelity criterion for at least one set of N, τ:

$$N_{\mathrm{mem}} = \sum_{i}^{F\left(\tilde{M}_i\right) \geq F_{\min}} c_i \tag{6.2}$$

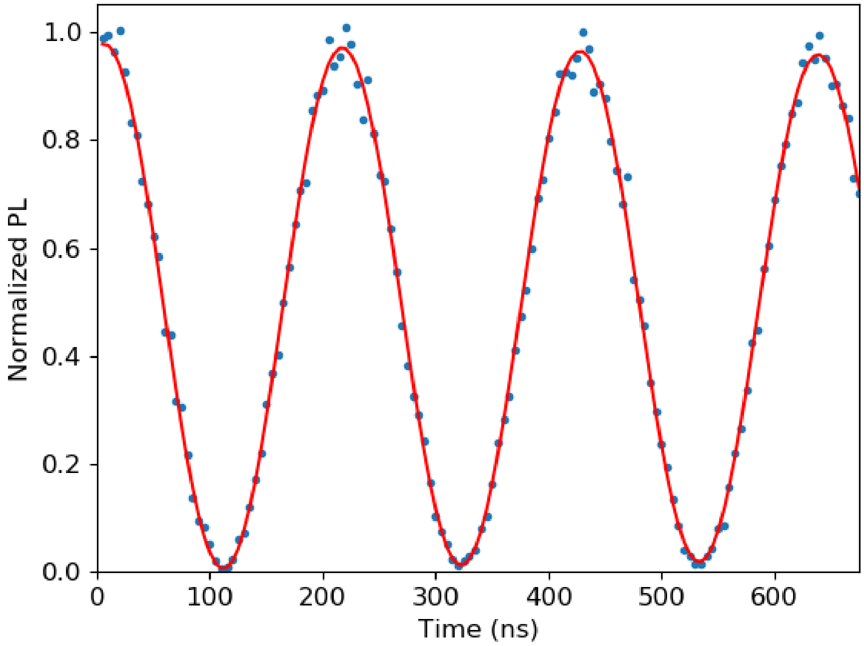

Figure 6.6: **99% Rabi.** Rabi with $> 99\%$ contrast indicating that we can initialize, control, and readout our electron spin qubit with less than 1% combined error.

6.2.5 Hyperfine Cutoff Value

A cutoff of $A_{\|} = 2\pi \cdot 60\ kHz$ is used in this work as a rough guideline for when hyperfine are low enough to act as optimal quantum memories. This corresponds to hyperfine values that were found to be ideal for communication protocols with the NV^- in diamond [75, 113]. Coincidentally, this cutoff is also roughly the same order of magnitude as the ODMR linewidth we measure in isotopic samples (20 kHz) and provides an approximate limit for the lowest hyperfine spin which could be considered strongly coupled.

6.3 Supplementary Details

6.3.1 Probability to Have Strongly Coupled ^{29}Si Spins

When considering c-axis divacancy defects and only the 3 nearest sites [126], there are 12 possible ^{29}Si locations that result in a strongly coupled electron-nuclear system. The isotopic concentration of ^{29}Si is 4.685%. Thus, the probability of finding 0 or 1 strongly coupled ^{29}Si spins is:

$$\begin{aligned} P_0 &= (1-0.04685)^{12} \\ P_1 &= 12 \cdot (1-0.04685)^{11} \cdot 0.04685 \end{aligned} \tag{6.3}$$

In order to evaluate the probability to find 2 strongly coupled ^{29}Si spins, we need to ensure we do not count cases where the two ^{29}Si are at degenerate sites. Since there are two 3-fold degenerate cases and one 6-fold degenerate case, we have:

$$P_2 = (1-0.04685)^{10} \cdot 0.04685^2 \cdot (6 \cdot 3 \cdot 3) \tag{6.4}$$

Finally, for all three non-degenerate sites having exactly 1 ^{29}Si we have:

$$P_3 = (1-0.04685)^{9} \cdot 0.04685^3 \cdot (6 \cdot 3 \cdot 3) \tag{6.5}$$

Number of ^{29}Si	Probability	
	0	56.23%
	1	33.16%
	2	6.11%
	3	0.36%

(6.6)

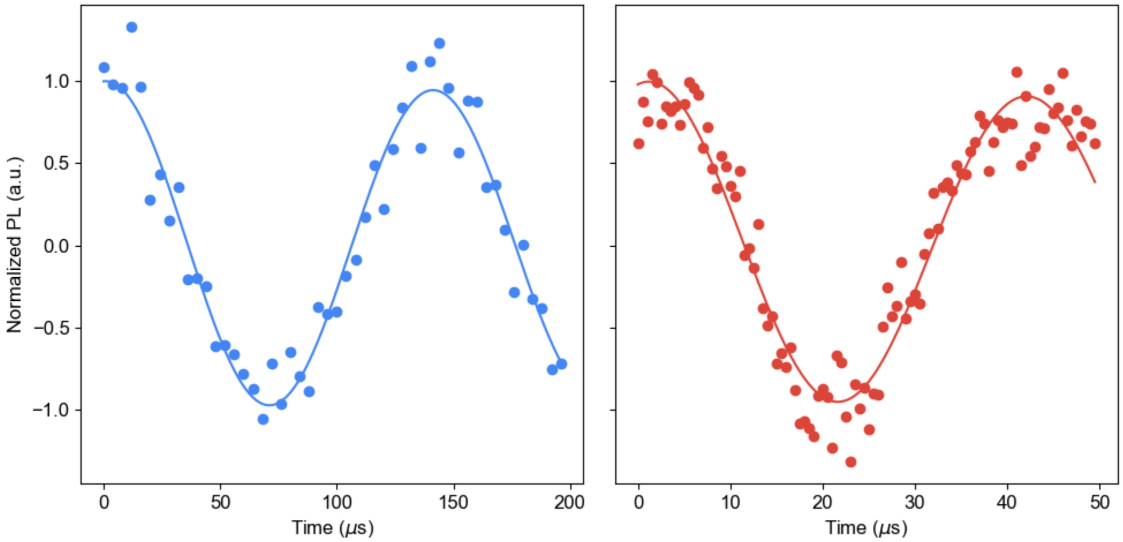

Figure 6.7: **Two register control.** Independent control of the two nuclear registers in the strongly coupled 3-qubit system described in the main text. These correspond to a $C_{\pm 1}NOT_n$ rotation performed using a direct RF drive.

6.3.2 Initialization Fidelity of Strongly Couple Nuclear Spins

To determine the initialization fidelity, we use the fitted peak amplitudes in Fig. 6.1b, which correspond to the electron spin transitions at two different frequencies which depend on the nuclear spin state. We then simply use these peak amplitudes as the diagonal elements (populations) of a density matrix (with off-diagonal terms = 0). We then renormalize the elements such that the trace is 1 and then compare to the ideal target density matrix using the qutip.fidelity function which implements the following metric:

$$F(\rho, \sigma) = \sqrt{\mathrm{Tr}[\sqrt{\rho}\sigma\sqrt{\rho}]} \tag{6.7}$$

6.3.3 Independent Control of Nuclear Spins in the 3-qubit System

After finding a defect with 2 distinguishable strongly coupled nuclear spins, we demonstrate that we can control them independently by performing a nuclear Rabi oscillation on each of them. The results are shown in Fig. 6.7.

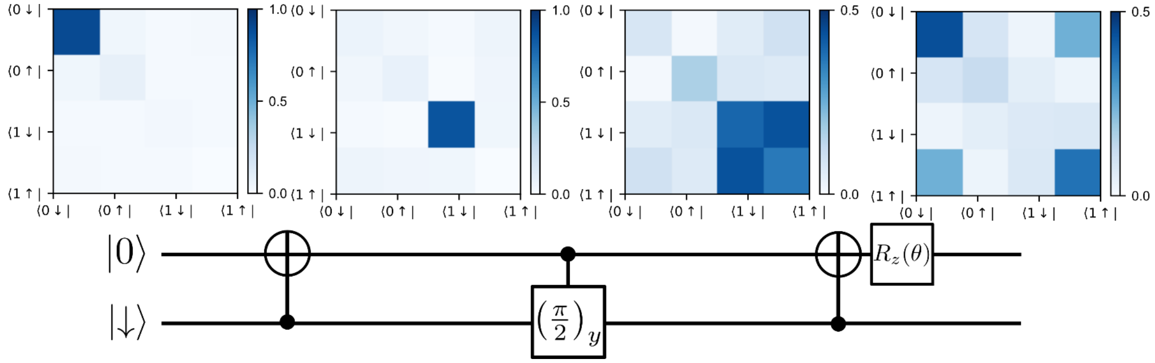

Figure 6.8: **QST.** — Quantum state tomography showing the absolute value of the density matrix at every stage of the entanglement process shown in Fig. 6.1.

6.3.4 Quantum State Tomography

To obtain the complete density matrix from our experiment we first need to perform the same experiment several times while swapping the readout sequence to probe the different terms of the density matrix [83]. Since we know that the density matrix is self-adjoint ($\rho_{ij} = \rho^*_{ji}$) we do not need to measure ρ_{ij} if we already know ρ_{ji}. Additionally, we know that the diagonal terms must be real and positive. Therefore, for a 4×4 density matrix we are left with 6 complex numbers (12 measurements) and 4 real numbers (4 measurements) to be determined, which will require a total of 16 measurements. In addition, we record 1 value for a “zero measurement (to subtract any systematic background) and 2 values that we can use to determine K (the brightness difference between the two electronic states in optical readout) by simply initializing the electron spin with a certain known fidelity (here we have used a conservative estimate of 90%). The off-diagonal terms are then simply obtained by normalizing the appropriate measurements by 2K. The diagonal terms can be found by solving the linear system composed of the 4 measurements. Note, that by using all 4 measurements we do not explicitly enforce that the trace should be one. Instead, we simply need to find the closest match of non-negative diagonal values such as to minimizes the square error and ensure a trace of 1. Thus we are essentially trying to fit an overdetermined set of linear equations.

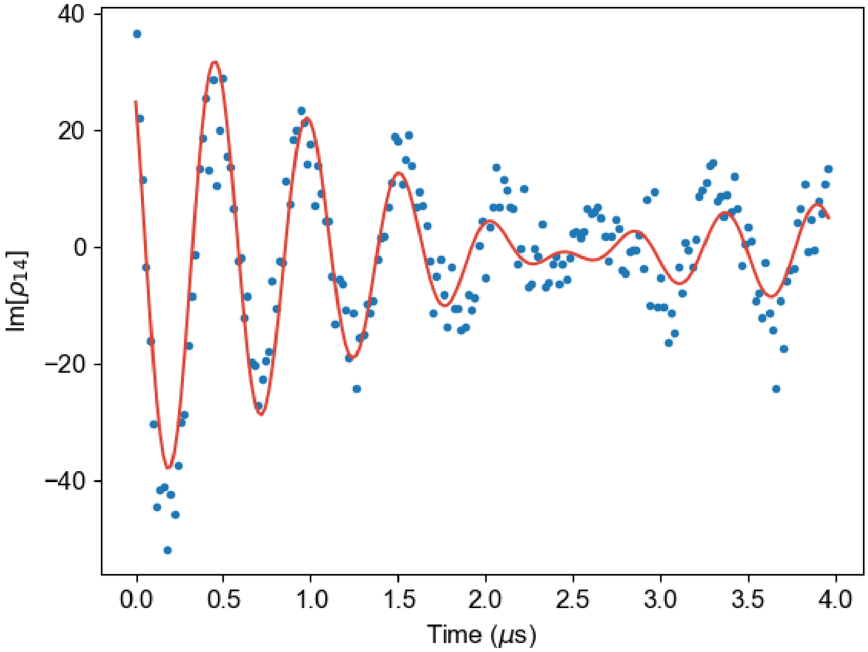

Figure 6.9: **Entangled state oscillations.** Rotation that occurs as we increase the wait time before the state tomography.

6.3.5 Entangled State Fidelity

To create an entangled state, we use the quantum circuit shown in Fig. 6.1d and expanded in Fig. 6.8. In this circuit, the last gate (Z-gate) is not explicit, but rather simply results from the fact that the state rotates under magnetic fields in the standard rotating wave basis. We can show this rotation by varying the time delay between state preparation and readout (Fig. 6.9). Therefore, to extract the true state fidelity, we can simply find the maximum fidelity with respect to a Z rotation angle (Fig. 6.10). Doing so, we find a rotation angle of 32.1 degrees for the particular measurement delay in experiments, corresponding entangled state fidelity of 80.76% (as computed using the qutip.fidelity function [72]).

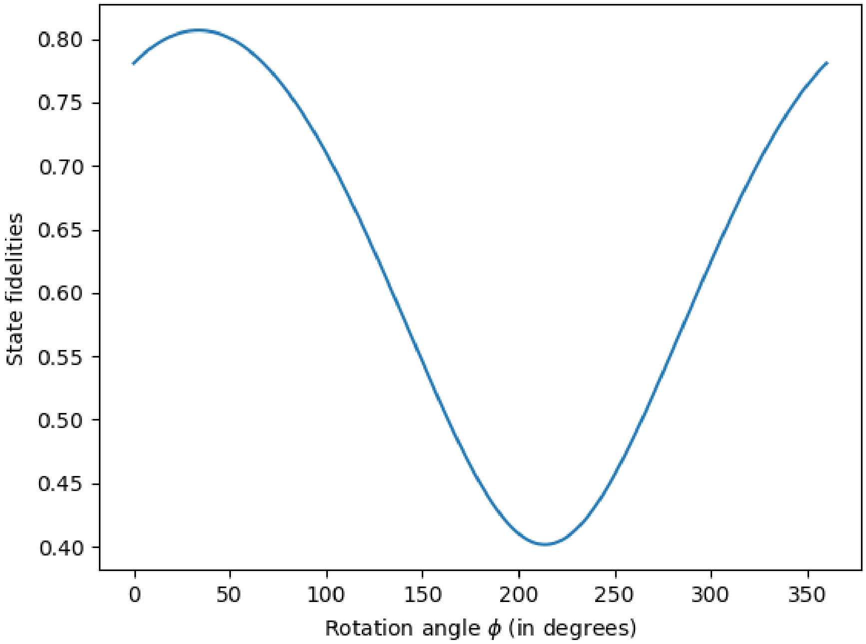

Figure 6.10: **Entangled state fidelity as a function of assumed z-rotation**

6.3.6 Positive Partial Transpose (PPT) Test

To confirm that we have an entangled state, we wish to check that the state corresponding to the density matrix is not separable. The PeresHorodecki criterion (also known as the positive partial transpose (PPT) test) states that if $\rho^(T_A)$ has negative eigenvalues, then it cannot be separable. Applying this test to our density matrix we get one of the eigenvalues at -0.171 thus confirming a non-separable state

6.3.7 XY8 Pulse Sequence

For CPMG based control of the nuclear spins, we utilize an XY8-based sequence by alternating between X(I) and Y(Q) quadrature π pulses in the scheme:

$$\tfrac{\pi}{2} - \left(\tau - \pi_x - 2\tau - \pi_y - 2\tau - \pi_x - 2\tau - \pi_y - 2\tau - \pi_y - 2\tau - \pi_x - 2\tau - \pi_y - 2\tau - \pi_x - \tau\right)^{N/8} - \tau - \tfrac{\pm\pi}{2} \qquad (6.8)$$

With the spacing between the π pulses defined as 2τ, and the XY8 subsequence repeated N/8 times for total pulse number N. The $\pm\pi/2$ maps the coherence onto the $m_s = 0$ and $m_s = \pm 1$ basis for a differential measurement. The alternating control phases effectively correct for pulse imperfections [4]. Our detection of weakly coupled nuclear spins involves varying the interpulse spacing and total pulse number.

6.3.8 *Weakly Coupled 2-qubit Gates*

Control of the weakly coupled nuclear spin is achieved using a sequence of successive π pulses spaced by $2\tau_k$ with [129].

$$\tau_k = \frac{\pi(2k-1)}{\omega_L + \omega} \tag{6.9}$$

where $\omega = \sqrt{\left(A_\parallel + \omega_L\right)^2 + A_\perp^2}$, ω_L is the Larmor frequency, $A_\parallel$ and $A_\perp$ are the hyperfine components and k is the dip order. At high magnetic fields, this dynamical decoupling period rotates the nuclear spin around the $\pm x$ axis depending on the electronic spin state implementing an effective $C_eROT_{x,n}(\pm\theta)$. More specifically, for N/8 repetitions of the XY8 sequence, the nuclear spin rotates by [129].

$$\theta \approx \frac{N \cdot A_\perp}{\omega_L} + O\left(\left(\frac{A}{\omega_L}\right)^2\right) \tag{6.10}$$

We note that this constitutes a fully entangling gate for $\theta = (2m-1)\pi/2$. Using single electron rotations we can transform a $U = C_eROT_{x,n}(\pm\pi/2)$ into a $CnNOTe$ like gate in the electron x-basis. This can be achieved for example using a sequence of

$$\frac{\pi_{e,x}}{2} - U - \frac{\pi_{e,y}}{2} \tag{6.11}$$

Additionally, when the resonance condition is not met, the dynamical decoupling se-

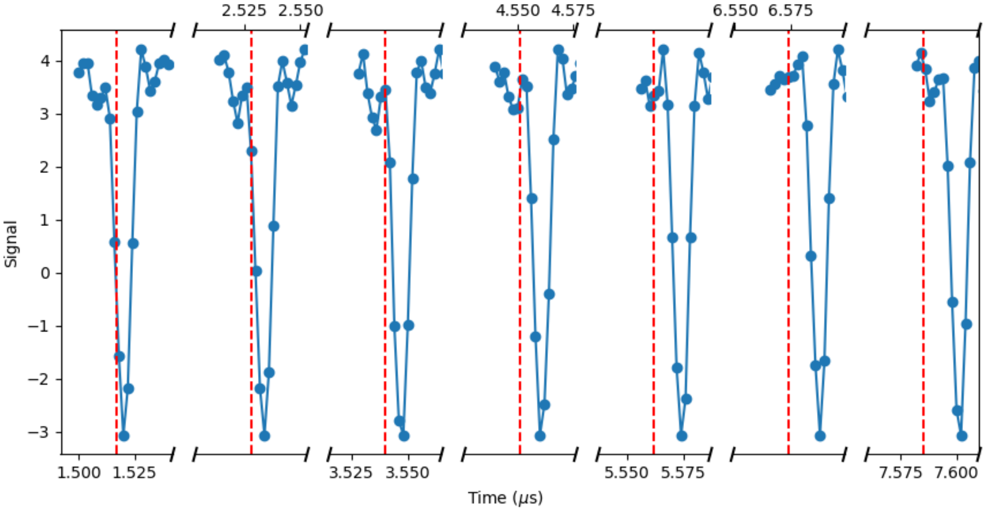

Figure 6.11: **Nuclear spectroscopy.** Multiple order of the nuclear dips, with the red dotted line corresponding to the expected Larmor without a hyperfine (with the B field measured by the separation of the +1 and -1 electronic resonances)

quence results in an unconditional z rotation of the nuclear spin. Combining conditional and unconditional rotations, full initialization and control of nuclear registers is possible

6.3.9 Control Fidelity of Weakly Coupled Nuclear Spin as a Function of τ Order (k)

In our nuclear spectroscopy (Fig. 6.11), each nuclear spin results in a series of periodic dips in coherence at specific τ (with the space between π pulses of 2τ):

$$\tau_k \approx \frac{\pi(2k-1)}{\omega_L + \omega} \tag{6.12}$$

Since every nuclear spin has its own frequency ω (due to the hyperfine), the dips caused by one nuclear spin becomes more isolated compared to dips caused by different nuclear spins. This allows for higher fidelity control of the nuclear spin at higher k, albeit by sacrificing gate speed. This is shown in Fig. 6.12 and 6.13 for the isolated nuclear spin in the main text.

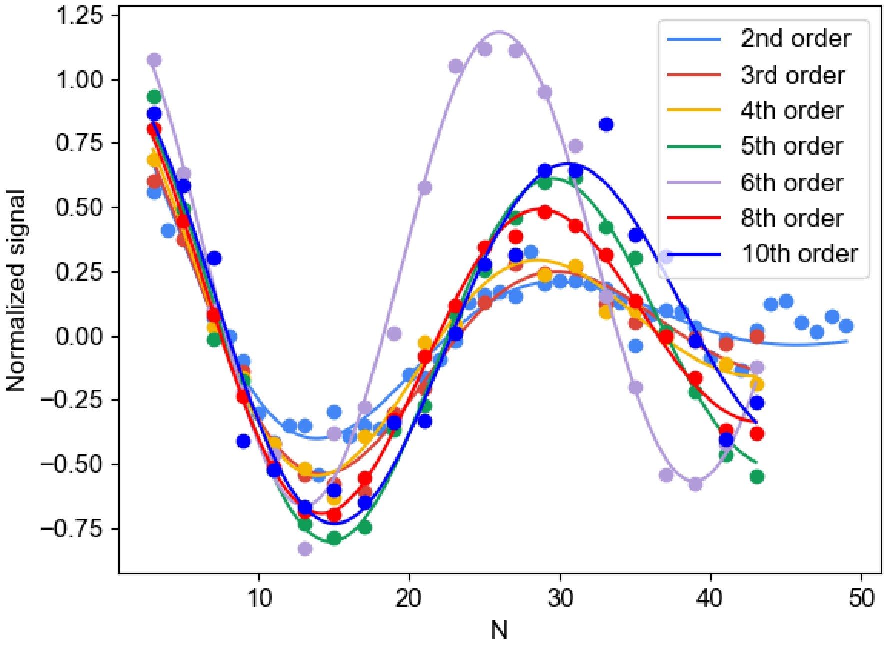

Figure 6.12: **Nuclear oscillations obtained from different peak orders (k).**

6.3.10 Measurement of the Nuclear Spin Gyromagnetic Ratio

We perform CPMG NMR spectroscopy on the weakly coupled nuclear spin in the main text at two different magnetic fields. From the positions of the coherence dips, we can extract the gyromagnetic ratio by calculating the frequency difference corresponding to the nuclear dip at two different values of B. We measure $|\gamma_n| \sim 8.50$ MHz/T (Figure 6.14), identifying this nuclear spin to be a single ^{29}Si ($|\gamma_n| = 8.47$ MHz/T). This is expected since ^{29}Si is the most probable nuclear species available given the isotopic balance in the sample.

6.3.11 Calculating the Hyperfine Values for Weakly Coupled Nuclear Spin

To calculate the hyperfine value ($A_{\parallel}$ and $A_{\perp}$) we use the following equations [20]:

$$A_{\parallel} = \frac{\omega_+^2 - \omega_-^2}{4\omega_L} \tag{6.13}$$

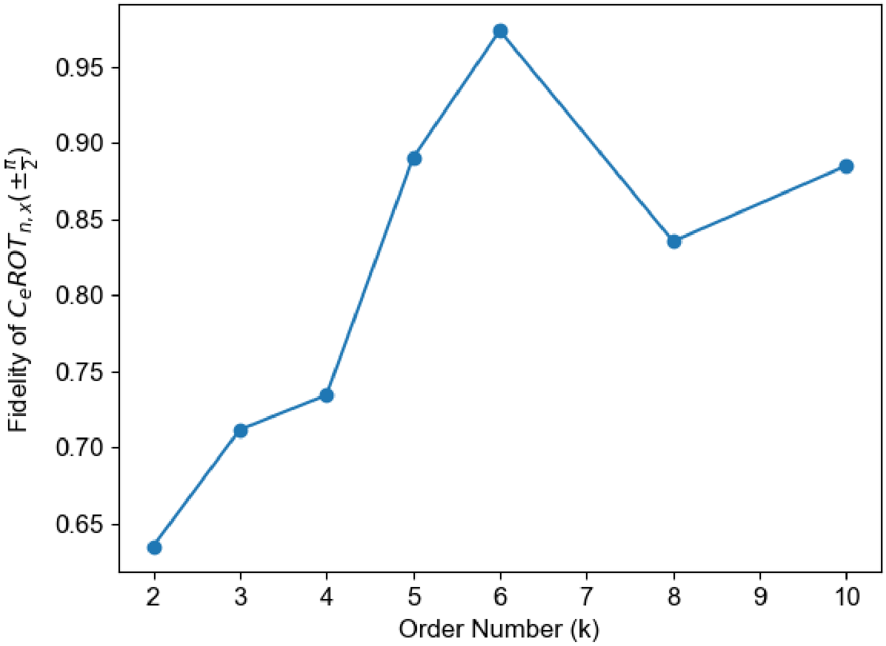

Figure 6.13: **Fidelity of a conditional $\pi/2$ nuclear rotation as a function of the order number.**

Where $\omega_\pm = \frac{\pi\cdot(2k-1)}{2\cdot\tau_\pm}$. $\tau_\pm$ are the coherence dip locations and k is the dip resonance order number. Additionally $\omega_L = B\cdot\gamma_{^{29}Si}$ is the Larmor frequency computed directly from the splitting of the $m_s = +1$ and $m_s = -1$ electron spin resonance lines. The perpendicular hyperfine is calculated from [129].

$$A_\perp = \sqrt{\frac{\left(A_\| + \omega_L\right)^2}{\left(\frac{N_\pi}{\pi}\right)^2 - 1}} \tag{6.14}$$

Where N_π is the number of pulses necessary to get a full π in the nuclear oscillations. In the limit of $\omega_L \gg A_\|$ and $N \gg \pi$ this simplifies to

$$A_\perp \approx \frac{\omega_L \pi}{N_\pi} \tag{6.15}$$

Note that these give the result in angular frequency (rad/sec) and we simply need to

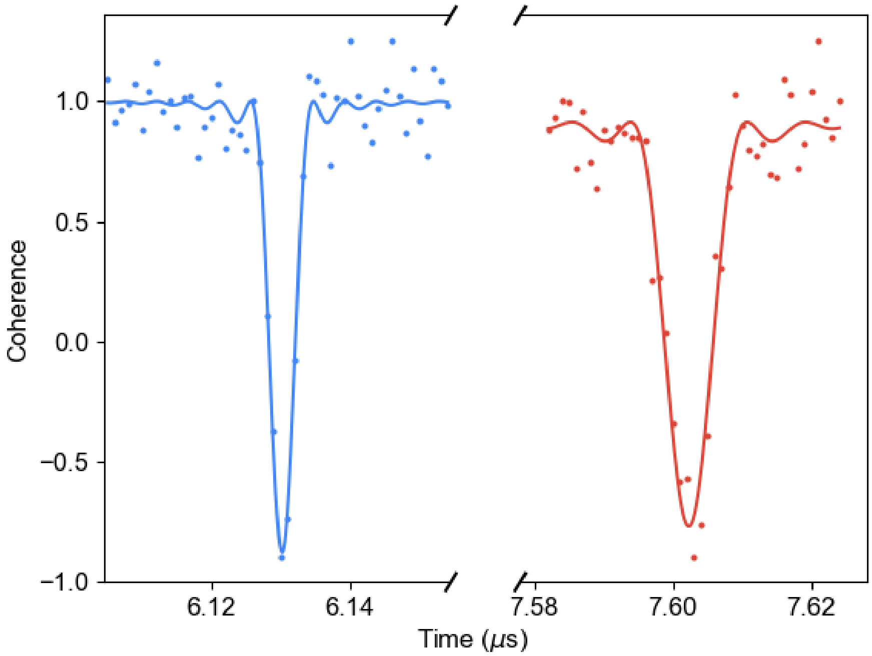

Figure 6.14: **Gyromagnetic ratio check.** Checking $|\gamma_n|$ using the 8th order resonance at two different magnetic fields (58 mT in red and 72 mT in blue). Solid lines correspond to the fit.

divide by 2π to get Hz. In our case, we calculate $A_{||} \approx 2\pi \cdot 650\ Hz$ and $A_{\perp} \approx 2\pi \cdot 11.45kHz$.

6.3.12 Locating Weakly Coupled Nuclear Spins

We assume that the hyperfine for distant nuclear spins is dominated by the dipole magnetic field of the electron which is oriented along z, with polar and azimuthal angles θ, ϕ:

$$\mathrm{B} = \frac{\mu_0}{4\pi r^3}|m|(3\hat{r}(\hat{z}\cdot\hat{r}) - \hat{z}) \tag{6.16}$$

The magnetic field at the nuclear spin is multiplied by the nuclear magnetic moment, and using the dipole moment of the electron $m = \gamma_e \hbar$ results in the hyperfine vector strength A

(the elements of the hyperfine tensor along z):

$$\begin{gathered}\frac{A_0}{\hbar} = \frac{\mu_0 \gamma_n \gamma_e \hbar}{4\pi r^3} \\ \overrightarrow{\mathrm{A}} = A_0(3\hat{r}(\hat{z}\cdot\hat{r}) - \hat{z})\end{gathered} \tag{6.17}$$

We can rewrite the radial unit vector and expand, using $(\hat{z}\cdot\hat{r}) = \cos(\theta)$

$$\overrightarrow{\mathrm{A}} = A_0(3\cos(\theta)(\cos(\phi)\sin(\theta)\hat{x} + \sin(\phi)\sin(\theta)\hat{y} + \cos(\theta)\hat{z}) - \hat{z}) \tag{6.18}$$

In particular, we can break up the hyperfine in terms of those along z $(A_{\|})$, and those perpendicular $(A_{\perp})$ [156]

$$\begin{gathered}A_{\perp} = 3A_0\cos(\theta)\sqrt{(\cos(\phi)\sin(\theta))^2 + (\sin(\phi)\sin(\theta))^2} \\ A_{\perp} = 3A_0\cos(\theta)\sin(\theta)\end{gathered} \tag{6.19}$$

And:

$$A_{\|} = A_0\left(3\cos(\theta)^2 - 1\right) \tag{6.20}$$

We can see that with these two equations, and by knowing the parallel and perpendicular hyperfine values we can locate our nuclear spin on a cone determined by θ at a distance r. ϕ is eliminated due to the symmetric nature of the dipole field. In our experiment, $|A_{\perp}| = 2\pi\cdot 11.45$ kHz, $A_{\|} = 2\pi\cdot 0.65$ kHz . We then solve for A_0 and θ, with $0 < \theta < \pi$ (spherical coordinates) and $A_0 < 0$ because the silicon gyromagnetic ratio is negative. Similarly, we know that our nuclear precession frequency increases (a measure of $A_{\|}$) with the use of $m_s = -1$ compared to $m_s = +1$. We know then that $A_{\|} > 0$ [156]. With this, we get solutions at:

$$\begin{gathered}A_0 = 2\pi\cdot -8.273 \text{ kHz} \\ \theta = 56 \text{ \& } 124 \text{ degrees}\end{gathered} \tag{6.21}$$

Solving for r using A_0, and using the gyromagnetic ratio for the silicon nuclei, r=1.24 nm. Measuring the sign of $A_\perp$ determines between the two possible polar angles, and then measuring the azimuthal angle is possible with similar techniques [156].

6.3.13 Electron Driven Nuclear Memory Decoherence

Besides obtaining a higher number of registers, weakly coupled nuclear spins are also desired because of their robustness to electronic spin manipulation. In particular, important protocols in quantum communication [76] requires one to store a state in the nuclear spin while manipulating the electron spin. While microwave manipulations are unitary and have a deterministic time (which could presumably be accounted for [75]), the electron spin reinitialization or readout is inherently stochastic. Thus, this process (with a characteristic time related to the spin-flip rate and the ISC) can impart a random phase on the nuclear spin, thus causing the state to dephase. This is due to the difference in nuclear precession frequency when the electron is in $m_s = 0$ or $m_s = \pm 1$ arising from the hyperfine interaction. For the NV^- center in diamond, one of every $\sim 10^3$ attempts produce entangled photons, with the Barret Kok scheme requiring $> 10^6$ attempts [111]. Therefore, the nuclear memory needs to withstand many thousands of entangling attempts, which involve reinitializing the electron spin. Using a model [20, 111] of the dephasing of weakly coupled nuclei caused by this process, we can get the fidelity of the nuclear state given N initializations of the electron.

$$F = \frac{1}{2} + \frac{1}{2^{N+1}} \left(1 + e^{-\frac{(\Delta\omega\tau)^2}{2}} \right)^N \tag{6.22}$$

Where $\Delta\omega = \omega_0 - \omega_{\pm 1} \cong 2\pi \times A_{\parallel}$, and τ is the average reinitialization time. We can see then that controlling nuclear spins with very small $A_{\parallel}$ is crucial to developing robust memories. The reinitialization time (τ) for the VV^0 system is expected to be faster because of short ISC shelving times. Additionally, lower spin mixing [35] may make these memories particularly robust to manipulations of the electron [75]. Additionally, control errors on the electron play a role in decoherence [75] of the nuclear spins, emphasizing the results in Fig. 6.5. Infidelity in the initialization of the electron similarly may limit the number of entanglement attempts. For the VV^0, we know that the initialization can be at least $> 99\%$ (Fig. 6.6). However, both of these mechanisms decrease as $A_{||}$ is reduced [75]. For these weakly coupled nuclei, T_2 decay is not the limiting factor for the number of entangling attempts. In experiments for the NV^- center, the memories are around 20 KHz [76, 75]. However, this is because more robust spins with less than 20 KHz are difficult to resolve in natural isotopic abundance in diamond. However, these memories are sufficient to survive ∼1000 entangling attempts as needed for the demonstration of entanglement purification [113, 75]. Moving to more weakly coupled registers through isotopic engineering may provide exponentially improved nuclear memories.

6.3.14 Coherence extension for the VV^0

In the main text, we demonstrate CPMG coherence extension on the *kk* divacancy (shown in Fig. 6.15). This allows us to extend T_2^{DD} to 14.5 ms at N=32 with longer times being possible with more pulses. For completeness, we also performed CPMG coherence extension on a basal (*kh*) divacancy and obtained the results shown in Fig. 6.16, extending the coherence to a maximum of T_2^{DD} ∼3.5 ms with N=32. Further improvement in field alignment could potentially improve these coherences times. Additionally, charge depletion [5] could also help reduce paramagnetic traps from creating magnetic noise while charge switching.

6.3.15 T_1 Lower Bound

At low temperature, T_1 is predicted to be well in excess of a second in comparison to the NV center in diamond [1]. However, T_1 times for the divacancy in SiC at low temperature (5 K) have not been reported to date. Unfortunately, in practice, laser leakage through the AOM and other experimental imperfections can artificially lower T_1 which may affect coherences.

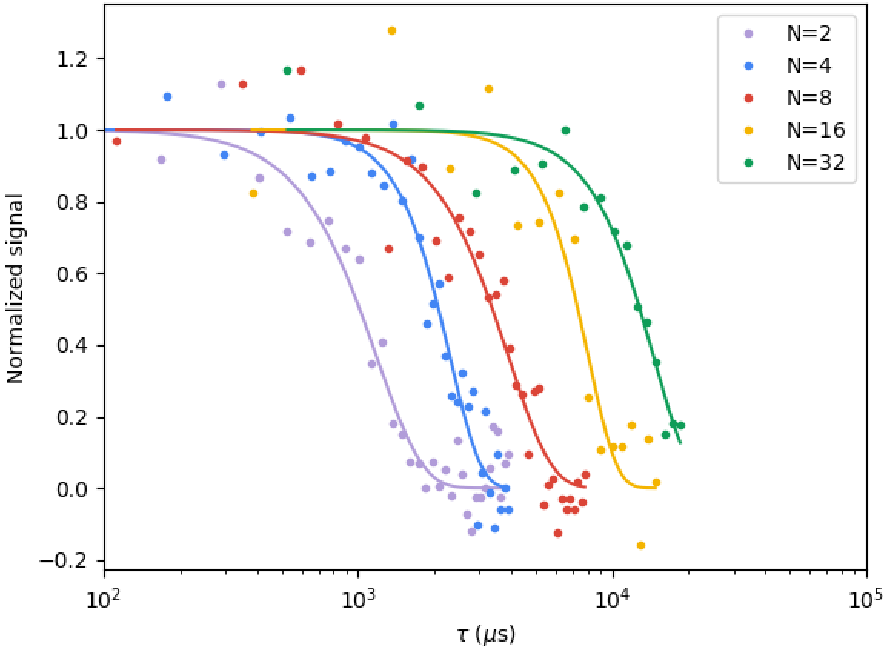

Figure 6.15: **CPMG-N on a *kk* divacancy.** The time constant obtain from these traces are plotted in the main text (Fig. 6.4)

To ensure we were not limited by such mechanisms we measured T_1 up to 500 ms. We see very little decay within this time scale, confirming that experiments were not limited by T_1 and that the relaxation times for divacancy defects in SiC at low temperatures can be extremely long.

6.3.16 Randomized Benchmarking

To put a lower bound on the gate fidelities we first select a set of Clifford gates to test. For our measurements, we selected the following set: $[I, x, y, x/2, y/2, -x/2, -y/2]$ Note that we omitted the z, z/2, and z/2 gates since these can have a simple instantaneous and error-free virtual implementation (i.e. change the frame of reference). Thus, including these would inflate the average gate fidelity. Additionally, we note that this set is complete in the sense that for every combination of N-1 randomly chosen gates in the set, we can find a single

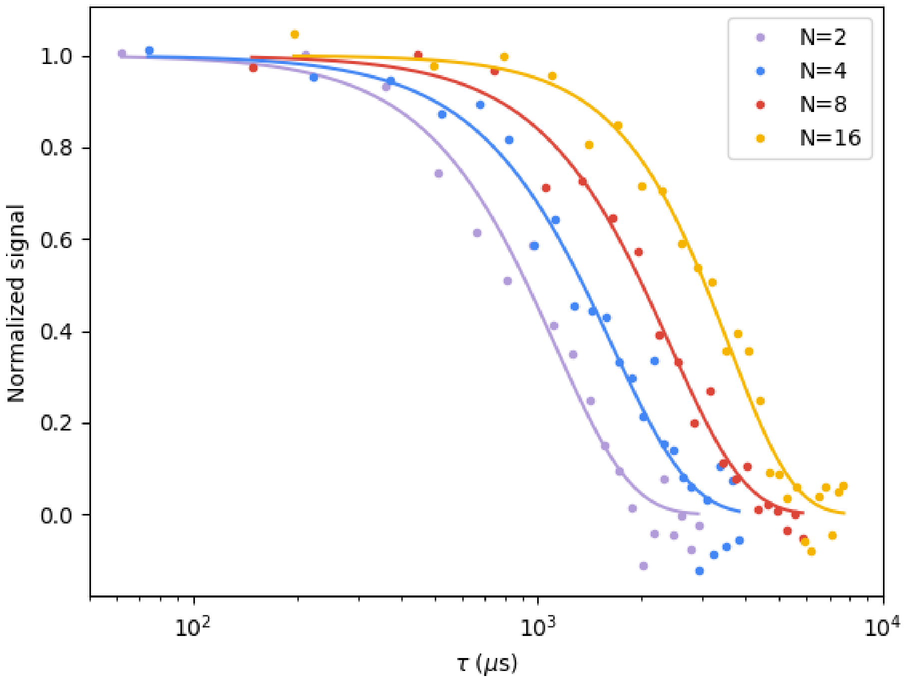

Figure 6.16: **CPMG-N on a kh divacancy near B=0.** Only moderate coherence enhancement is observed.

gate that will reverse the effect of that sequence. In practice, we ensure that every gate has exactly the same length in time (200 ns). An x gate, for example, would consist of [50 ns buffer][100 ns pulse][50 ns buffer], and an x/2 gate would be [75 ns buffer]-[50 ns pulse]-[75 ns buffer]. Once we have this universal set of gates, we can simply pick N-1 random gates, compute the matrix product of all of these, and then we simply add a final gate which projects to $m_s = +1$ (seq1) or $m_s = 0$ (seq2). By taking the difference of seq1 and seq2 we get the randomized benchmarking signal for N gates. To avoid using only a single sequence, we repeat the process with 5 different randomized sequences for each N and average the results together. We then fit our results to $f(N) = A \cdot \alpha^N$N and extract the Error per Clifford Gate [154] as:

$$r = 1/2(1 - \alpha) \tag{6.23}$$

This gives an error of 0.000156, or conversely a gate fidelity of 99.984%

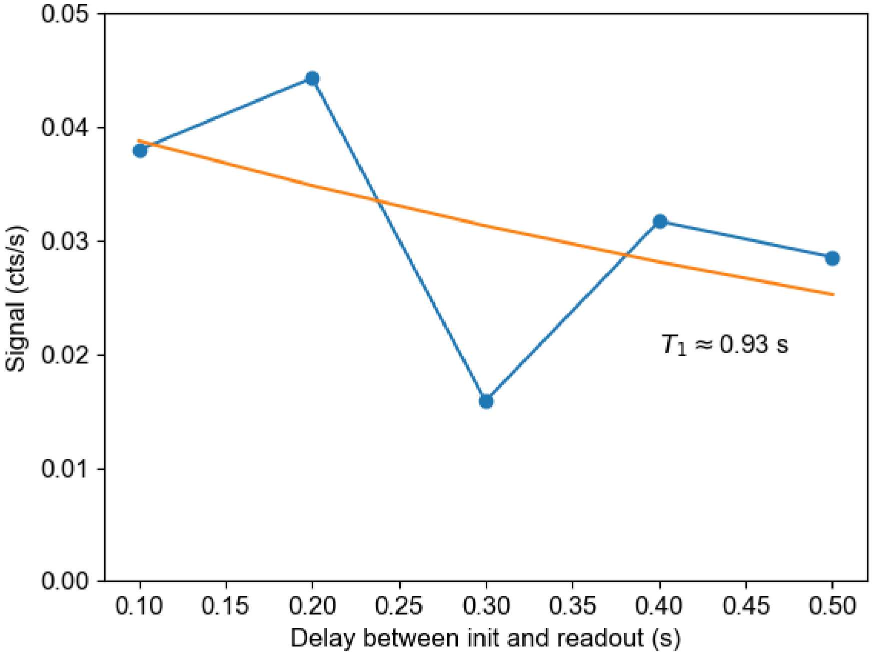

Figure 6.17: T_1 **of a single** kk **defect in an isotopically purified sample.**

6.3.17 Rabi Q

In the main text, we measure the single-qubit gate fidelity using randomized benchmarking. Here we will use Rabi Q, a different (but related) metric, to confirm that gate fidelity number. In Fig. 6.18, we see some slices of a continuous Rabi. We set the power such that the π time is ~200 ns. We then globally fit the data to the following function:

$$y(t) = A \cdot e^{-\frac{t}{\gamma}} \cdot \cos\left(2\pi\left(\frac{t}{2T_\pi}\right) + \phi_i\right) \tag{6.24}$$

Where ϕ_i is different for each slice and allows us to account for slight phase drifts which are possibly due to heating at long times. From this fit we get $\gamma = 199 \pm 6\ \mu s$ and $T_\pi = 199.63 \pm 0.02\ ns$. This gives a Rabi oscillation quality factor $Q = \gamma/T_\pi = 997 \pm 30$

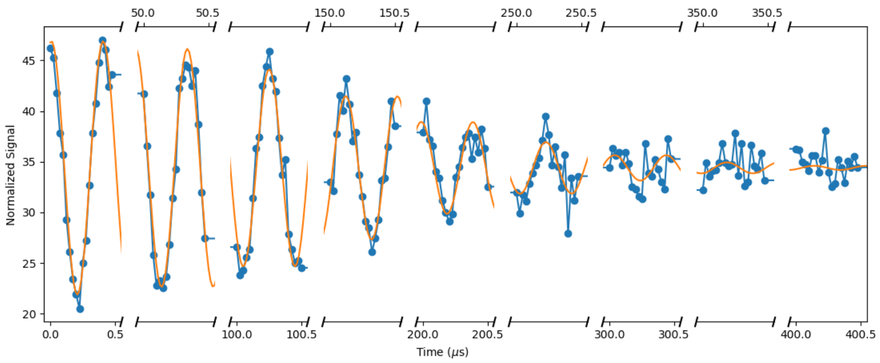

Figure 6.18: **Continuous electron Rabi oscillation on shows Rabi $Q = 997 \pm 30$.**

6.4 First-principles Calculations of the Coherence Function

6.4.1 System Hamiltonian

For a system consisting of central electron spin-1 and impurity spins-$\frac{1}{2}$ in an external magnetic field; the Hamiltonian is given by:

$$\widehat{H} = D\left(\hat{S}_z^2 - \frac{1}{3}S(S+1)\right) - \gamma_e B_z \hat{S}_z - \sum_i \gamma_n B_z \hat{I}_{iz} + \sum_i \boldsymbol{S}\boldsymbol{A}\boldsymbol{I}_i + \sum_{i \neq j} \boldsymbol{I}_i \boldsymbol{P} \boldsymbol{I}_j \tag{6.25}$$

where S is the central spin, S is the total spin quantum number of the central spin, and I_i are the bath (nuclear or electron) spins. The A tensor denotes the hyperfine interaction (spin dipole-dipole interaction) between the central spin and the bath nuclear (or electronic) spins. The P tensor denotes the spin dipole-dipole interaction between the spins belonging to the bath. We assume that the diagonal elements of the density matrix of the central electron do not change in time; hence the terms in the Hamiltonian containing $\hat{S}_x$ and $\hat{S}_y$ are negligible (secular approximation). Under this approximation, we can rewrite Eq. 6.25 for the spin bath driven [153] by the $m_s = 0$ ($|0\rangle$ qubit state) or $m_s = -1$ ($|1\rangle$ qubit state) levels of the central electron spin as:

$$\begin{aligned}
\widehat{H}_0 &= -\gamma_n B_z \widehat{I}_z + \sum_{i,j} \vec{I}_i \boldsymbol{P} \vec{I}_j \\
\widehat{H}_1 &= -\sum_i \gamma_n B_z \hat{I}_{iz} - \sum_i \left[A_{zz} \widehat{S}_z \widehat{I}_z + A_{zx} \widehat{S}_z \widehat{I}_x + A_{zy} \widehat{S}_z \widehat{I}_y \right] + \sum_{i,j} \vec{I}_i \boldsymbol{P} \vec{I}_j
\end{aligned} \tag{6.26}$$

6.4.2 Hyperfine Tensor Calculations

Hyperfine tensors for nuclear spins were computed using Density Functional Theory (DFT) [54]. DFT calculations were performed with Quantum Espresso code [55] using PBE functional. A kinetic energy cutoff of 40 Ry was adopted. GIPAW pseudopotentials were used to model electron-ion interactions. We used a supercell with 1438 atoms with Gamma-point sampling of the Brillouin zone. GIPAW code is used to evaluate hyperfine tensors for all atoms within the supercell. For atoms outside the supercell, hyperfine tensors were estimated using dipolar-dipolar approximation. For the electron impurities, the coupling tensors were computed using only dipolar-dipolar interactions, as exchange interactions between electrons are negligible at such distances.

6.4.3 Coherence Function

For the given delay between pulses (τ) and a number of pulses (N), which determines the total time of the experiment $t = N \cdot 2\tau$, the coherence function of the qubit is given by:

$$L(t) = \frac{\operatorname{Tr}\left[\hat{\rho}(t)\hat{S}^+\right]}{\operatorname{Tr}\left[\hat{\rho}(0)\hat{S}^+\right]} \tag{6.27}$$

Where $\hat{\rho}$ is the density matrix of the qubit. If the qubit is prepared in $|+x\rangle = \frac{1}{\sqrt{2}}(|0\rangle + |1\rangle)$ state, the coherence function at time t is given by:

$$L(t) = \operatorname{Tr}\left[\widehat{U}_0 \widehat{U}_1^\dagger\right] \tag{6.28}$$

With conditional propagators $\widehat{U}_0$ and $\widehat{U}_1$, which are defined differently for different experiments. For free induction decay (FID, n=0, t=τ):

$$\begin{aligned} \widehat{U}_0 &= \exp\left[-i\widehat{H}_0\tau\right] \\ U_1 &= \exp\left[-i\widehat{H}_1\tau\right] \end{aligned} \tag{6.29}$$

For Hahn-Echo experiment (N=1):

$$\begin{aligned} \widehat{U}_0 &= \exp\left[-i\widehat{H}_0\tau\right]\exp\left[-i\widehat{H}_1\tau\right] \\ \widehat{U}_1 &= \exp\left[-i\widehat{H}_1\tau\right]\exp\left[-i\widehat{H}_0\tau\right] \end{aligned} \tag{6.30}$$

For the experiments with number of pulses ≥ 2, the propagators are given by $\widehat{U}_0 = \widehat{V}_0^{N/2}$ and $\widehat{U}_1 = \widehat{V}_0^{N/2}$, where:

$$\begin{aligned} \hat{V}_0 &= \exp\left[-i\widehat{H}_0\tau\right]\exp\left[-i\widehat{H}_1 2\tau\right]\exp\left[-i\widehat{H}_0\tau\right] \\ \hat{V}_1 &= \exp\left[-i\widehat{H}_1\tau\right]\exp\left[-i\hat{H}_0 2\tau\right]\exp\left[-i\widehat{H}_1\tau\right] \end{aligned} \tag{6.31}$$

The coherence time is obtained by fitting the coherence function to the form $L(t) = exp[(t/T)^n]$, where T is the coherence time. We denote as T_2^* the coherence time T obtained for FID, and as T_2 the coherence time T obtained in Hahn-Echo experiments.

6.4.4 Cluster-Correlation Expansion

The coherence function $L(t)$ from (Eq. 6.28) can be approximated as a product of cluster contributions using the cluster-correlation expansion (CCE) method:

$$L(t) \approx \prod_{C \subseteq \{1,2,\ldots N_C\}} \tilde{L}_C(\mathrm{t}) \tag{6.32}$$

Where $\tilde{L}_C$ is the irreducible contribution of the cluster C, and N_c is the total number of clusters included in the expansion, which determines the order of approximation. For

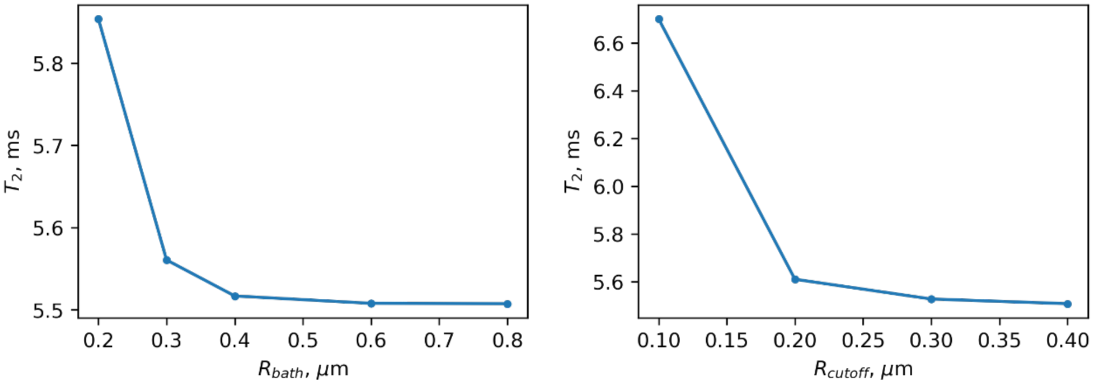

Figure 6.19: **The convergence of the electron-induced decoherence.** On the left the T_2 as a function of bath size, on the right as a function of the cutoff distance between electron spins to be considered a pair.

example, the notation CCE1 corresponds to accounting only for the contributions from isolated nuclear spins ($N_c = 1$), CCE2 corresponds to $N_c = 2$, and CCE3 corresponds to $N_c = 3$. The irreducible contributions are recursively computed as:

$$\tilde{L}_C(\mathrm{t}) = \frac{L_C(t)}{\prod_{C' \subseteq C} \tilde{L}_{C'}(\mathrm{t})} \tag{6.33}$$

Where $L_C(t)$ is the coherence function computed for bath, consisting only of cluster L_C using (Eq. 6.28).

6.4.5 Calculation Parameters

CCE calculations for nuclear spins were carried out according to [153] and convergence with respect to the order of the CCE was carefully checked in each case. The clusters were chosen according to the procedure described in [120]. In the case of electron spins, the strength of interactions between spins belonging to the bath is comparable to the coupling of the bath spins to the central spin, and the perturbative approach on which the cluster expansion is based is not justified. The break-down of the perturbative approach leads to CCE calculations of order 3 or higher to diverge [146]. We can however use an approximate description by assuming that CCE2 is sufficient to correctly estimate electron-electron interactions. This approximation likely yields underestimated coherence times at a given concentration of impurity electron spins, as in real systems the flip rate of electron pairs is reduced due to non-pair-wise interactions with other electrons. But at small electron spin concentration, high order effects are expected to be insignificant to determine the qualitative impact of electron spins on coherence times.

To compute the impact of the electron spins, we randomly placed the electron spins at the distances between 0 - 2 μm from the qubit. Following a procedure to choose the clusters similar to the one used for nuclear spins, in the calculation of coherence functions, we only included the pairs of electron spins with a distance smaller than a given cutoff distance, and we only considered clusters of spins in a finite bath. Both the pair distance cutoff and the bath size were chosen to be large enough to obtain converge of the coherence function as shown in Fig. 6.19.

Due to the different length scales of the nuclear-electron and electron-electron interactions, the two baths (electron and nuclear) can be considered decoupled. Therefore, the total coherence function can be factorized into contributions from electron and nuclear spins, respectively:

$$L_t = L_{electron} L_{nuclear} \tag{6.34}$$

The coherence function was obtained by averaging over the results of 200 (1000) calculations for different configurations of electron or nuclear spins, in the presence of a magnetic field of 50 G (500 G). In the experimental measurement, the pulse bandwidth used to control the qubit state allows us to simultaneously excite only a small subpopulation of the divacancies in the SiC sample. In this subpopulation, the energy splitting of the qubit levels does not deviate significantly from that of isolated divacancies. Hence, when computing the average coherence time to be compared with experiments, we need to exclude from the calculation

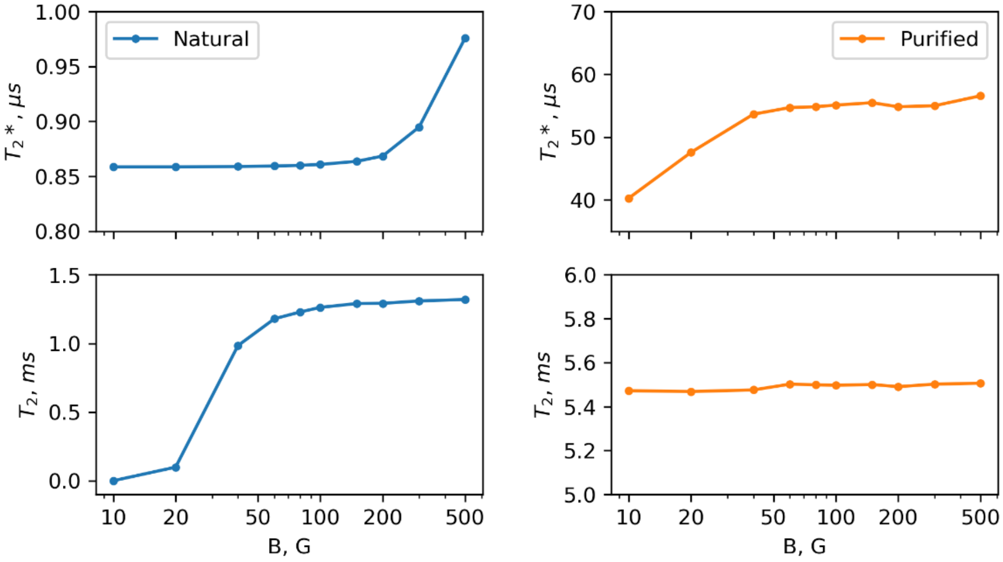

Figure 6.20: **Coherence times as a function of magnetic fields.** The coherence time T_2 of the natural material is shown on the left-hand side, and that of the isotopically purified material is on the right-hand side. The definitions of T_2 and T_2^* are given in the text.

the nuclear configurations whose hyperfine coupling would lead to significant deviation in energy splitting from that of an isolated divacancy. Therefore, only nuclear configurations with maximum parallel Hyperfine coupling <1 MHz were considered. However, we note that when including all the configurations, irrespective of their hyperfine coupling, we obtained very similar T_2 values and T_2^* values within 5-10%, for natural concentration.

6.4.6 Impact of the Magnetic Field

The computed values of T_2 and T_2^* for both isotopically purified and natural materials (with free electron concentration of $10^{15} cm^{-3}$) as a function of magnetic field is shown in Figure 6.20. In both cases, the T_2^* is not significantly impacted by changes in the magnetic field, while T_2 is impacted: in particular in the natural material we observed a considerable increase in nuclei-limited coherence time. Instead, in the case of electron-limited decoherence, the effect of magnetic fields in the range studied here (see Fig. 6.20) is negligible.

6.5 Nuclear Memory Optimization

6.5.1 Conditional Magnetization

Using the secular approximations for a system of one electron and one nuclear spin, we can rewrite the Hamiltonian (Eq. 6.25) as follows:

$$\widehat{H} = D\left(\hat{S}_z^2 - \frac{1}{3}S(S+1)\right) - \gamma_e B_z \widehat{S}_z - \gamma_n B_z \widehat{I}_z + A_{zz}\widehat{S}_z\widehat{I}_z + A_{zx}\widehat{S}_z\hat{I}_x + A_{zy}\widehat{S}_z\hat{I}_y \quad (6.35)$$

Using the notation for coupling parameters from [129] we can rewrite secular Hamiltonian (Eq. 6.35) as:

$$\widehat{H} = D\left(\hat{S}_z^2 - \frac{1}{3}S(S+1)\right) - \gamma_e B_z \widehat{S}_z - \gamma_n B_z \widehat{I}_z + A_{\|}\widehat{S}_z\widehat{I}_z + A_{\perp}\widehat{S}_z\hat{I}_x \quad (6.36)$$

With $A = A_{zz}$, being parallel hyperfine coupling, and $B = \sqrt{A_{zx}^2 + A_{zy}^2}$ the perpendicular hyperfine coupling. The magnetization of the central electron spin along x-axis can be computed as the real part of the coherence function L:

$$M = \operatorname{Re} L(t) = \operatorname{Re}\operatorname{Tr}\left[\widehat{U}_0\widehat{U}_1^{\dagger}\right] \quad (6.37)$$

6.5.2 The Gate Fidelity

In order to understand how many nuclei on average can be used as memory units at a given nuclear spin concentration, we proceed as follows. A given nuclear spin i can be used as a memory unit if the state of the electron spin can be preserved, following a rotation induced by the nuclear spin. For an electron qubit initially prepared in the $|+x\rangle$ state, the fidelity function F measures how well its state is preserved:

$$F(|-x\rangle, \rho) = \langle -x|\rho|-x\rangle \tag{6.38}$$

where ρ is the density matrix of the qubit. If the fidelity of the qubit rotation induced by nucleus i is higher than a chosen threshold value, then the nucleus is considered a usable memory unit. The threshold value is chosen depending on the purpose of the memory unit, and typical values are in the range of 0.9 - 0.99. The fidelity of the electron spin is related to the electron magnetization M at given N, τ:

$$F_{N\tau}(|-x\rangle, \rho) = \sqrt{\frac{1}{2} - \frac{M}{2}} \tag{6.39}$$

For short time scales (compared to the decay of the coherence function), the interaction between different nuclei can be neglected. Then the electron spin magnetization can be written as a product of conditional magnetizations [129] given by the magnetization of the electron interacting with a single isolated nuclear spin. In other words, CCE1 is used to evaluate the electron magnetization. As a function of delay between pulses (2τ) and a number of pulses (N) the magnetization is given by:

$$M(N, \tau) = \prod_i M_i(N, \tau) \tag{6.40}$$

To determine if a given nucleus i in the lattice is available as a memory unit, we consider the magnetization of the electron when the given nucleus is present. The expectation value of the magnetization when the nucleus i is present is:

$$\widetilde{M_i} = E\left(M|M_i \in M\right) = M_i \prod_{j \neq i} E\left(M_j\right) \tag{6.41}$$

Where j runs over all other possible nuclear positions. Then M_j is given as:

$$M_j = \begin{cases} M_j, & \text{if } \boldsymbol{j} \text{ is present} \\ 1, & \text{if } \boldsymbol{j} \text{ is not present} \end{cases} \tag{6.42}$$

At a given nuclear spin concentration c_j, the expectation value $E\left(M_j\right)$ is:

$$E\left(M_j\right) = 1 \cdot \left(1 - c_j\right) + M_j \cdot c_j \tag{6.43}$$

A given nucleus is considered usable as a memory register if the fidelity of electron spin after rotation at $\widetilde{M_i}$ is higher than a certain threshold F_{min}. The average number of nuclei i present at this lattice site is equal to the concentration of the isotope c_i. Therefore, the total number of usable registers can be computed as the sum of c_i for all i that meets the fidelity criteria at least one set of N,τ:

$$N_{\mathrm{mem}} = \sum_{i}^{F\left(\widetilde{M_i}\right) \geq F_{min}} c_i \tag{6.44}$$

6.5.3 Limitations of the Approach

The method adopted here assumes that the nuclei-nuclei interactions are negligible in determining the electron magnetization. The assumption can be verified by comparing coherence functions obtained at different orders of CCE for random nuclear configurations. A significant difference between the spectra obtained with the CCE1 and CCE2 approximations would indicate nonnegligible nuclei-nuclei interactions. Figure 6.21 shows the difference between the results of CCE2 and CCE1 for 6 different nuclear spin configurations at natural concentration (c(^{29}Si) = 4.7%, c(^{13}C) = 1.1%). We can see that at long delay times there are significant differences between coherence functions obtained with CCE2 and CCE1. The delay at which the deviations occur is inversely proportional to the number of pulses. Therefore, the maximum available gate time (equal to $N2\tau$) can be found from the value of the

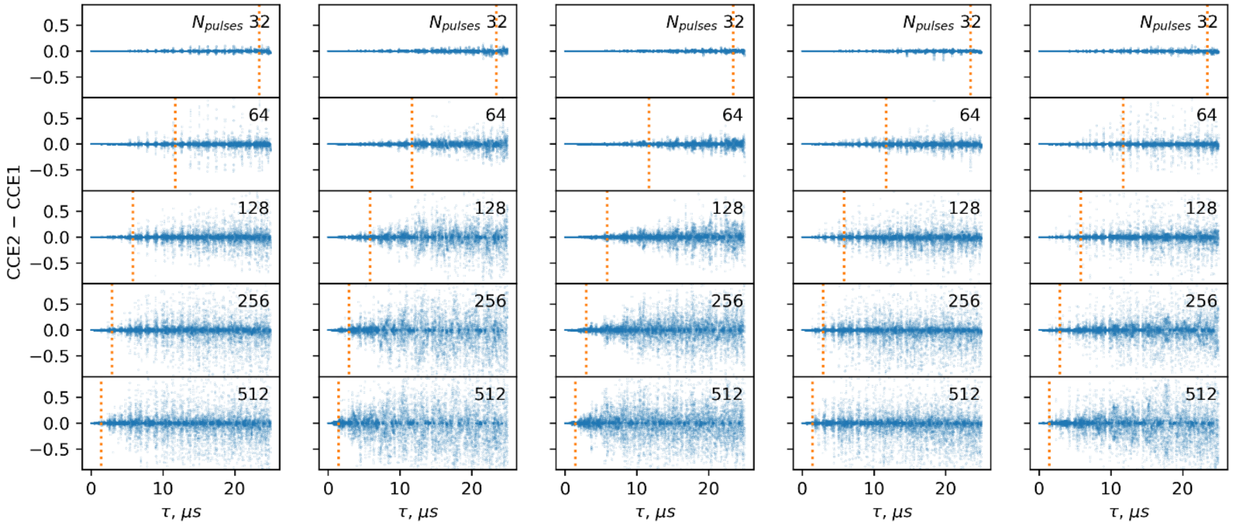

Figure 6.21: **Difference in coherence function predicted by CCE2 and CCE1 calculations.** Blue dots show the difference between the coherence functions obtained from CCE1 and CCE2 calculations, and the orange line shows the total gate time of 1.5 ms for six different nuclear configurations at a natural concentration of nuclear spins.

delay for a given number of pulses at which significant deviations occur. From the analysis of the CCE spectra for natural isotopic concentrations, the maximum gate time was established to be between 1-2 ms before significant deviations occur. This theoretical limit determines the maximum gate time, after which the fidelity of the rotation becomes limited by nuclear-nuclear interactions.

6.5.4 Convergence of the Results

Having established the theoretical maximum gate time, we checked the convergence of the number of memory units with respect to the size of the bath, timestep resolution, number of pulses, and the range of the delays between pulses. The convergence is shown in Figure 6.22. It was found that the number of memory units at the magnetic field of 500 G is converged at bath size 30 Angstrom, maximum τ of 25 μs, timestep of 0.5 ns, number of pulses of 512, which were used in Fig. 6.4.

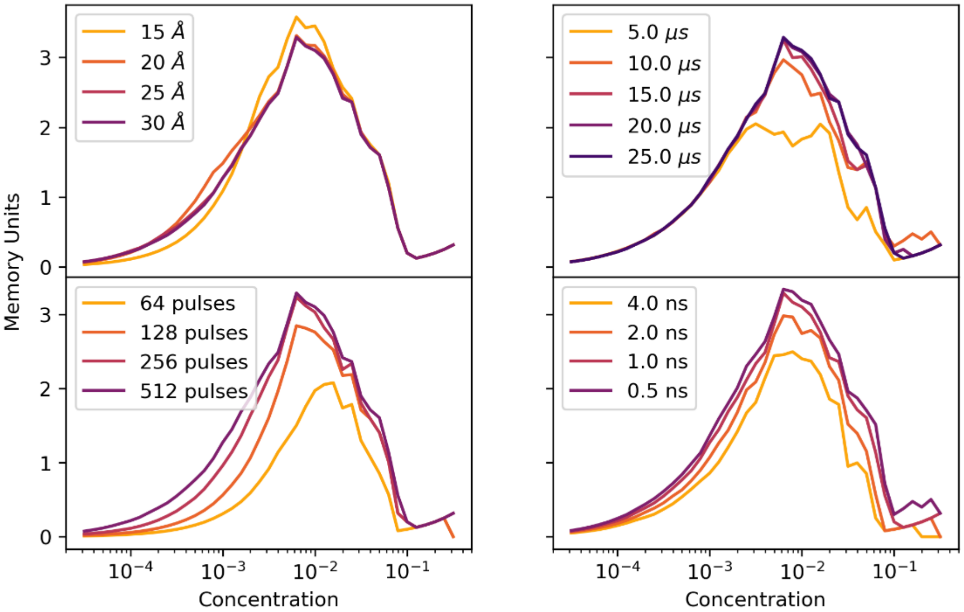

Figure 6.22: **Convergence tests for the calculation of usable memory units.** Left to right, top to bottom: computed number of usable memory units as a function of nuclear concentrations at a maximum gate time of 2 ms for varied bath size, maximum τ, number of pulses, and timestep. When parameters are not varied, default values of bath size = 30 , maximum $\tau = 25\mu s$, number of pulses = 512, and timestep = 1 ns are used.

6.5.5 Number of Memory Units as a Function of Gate Time

Figure 6.23 shows the increase in the average number of memory units as a function of the maximum gate time. We can see that the total number is proportional to the square root of the gate time. Furthermore, the purification of Si leads to a two-fold increase in the number of available memory units at long gate times, while the isotopic purification of carbon does not lead to any significant improvement.

It is interesting to note that the initial part of the curve corresponds to the nuclei with strong hyperfine coupling, and further increases in the number of usable nuclei include those with weak hyperfine coupling. The number of available memory units with weak hyperfine varies linearly with the maximum gate time within the chosen timescale.

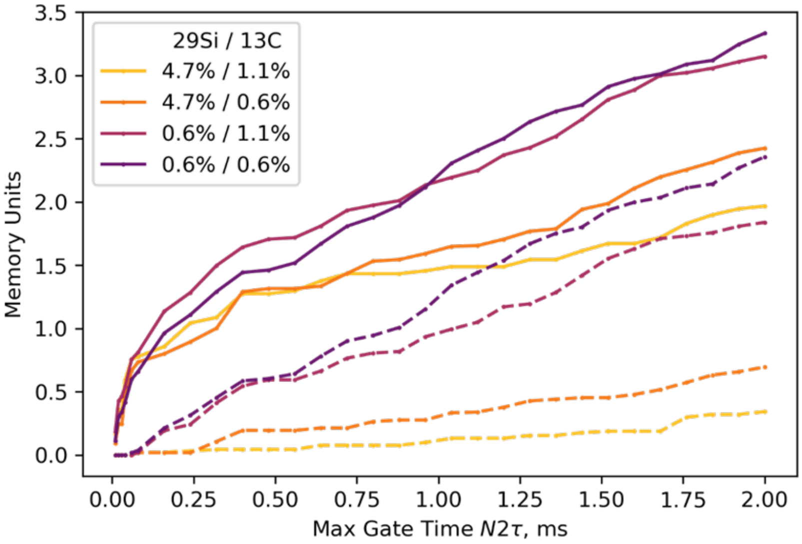

Figure 6.23: **Number of usable memory units as a function of the gate time.** The different color of the lines corresponds to different isotopic concentration, indicated in the inset. Dotted lines show the number of memory units with parallel hyperfine terms below $2\pi \cdot 60$ kHz. The minimum fidelity is equal to 0.95.

6.5.6 Hyperfine Distribution

Figure 6.24 shows the distribution of hyperfine couplings for memory units, available at different isotopic concentration/gate time. The gate time dependence further proves a point outlined above: usage of most of the nuclei with strong hyperfine coupling occurs at small timescales, and extended gate time allows one to access weakly coupled nuclei. Figure 6.25 shows the distribution for different minimum fidelities. Interestingly, the shape of the distribution is the same, albeit shifted towards higher concentrations at lower F_{min}.

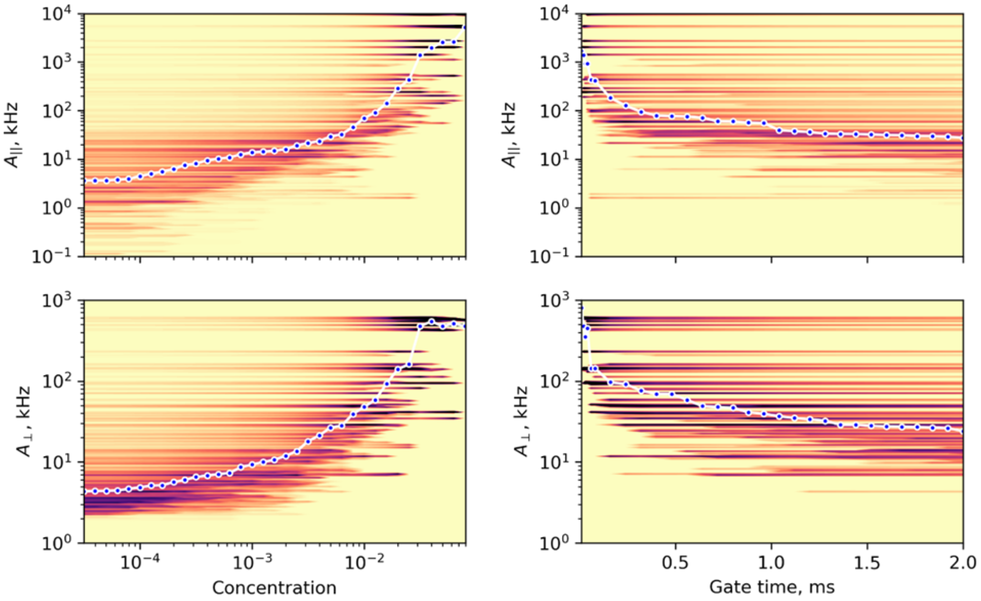

Figure 6.24: **Distribution of the most plausible hyperfine values for memory units.** Color maps show the probability of memory units in the sample with given nuclear concentration and gate time to have corresponding hyperfine coupling. On the left, the distribution is shown as a function of the nuclear concentration at maximum gate time $N2\tau$ 1.5 ms, with minimum fidelity of 0.95. On the right, the distribution is shown as a function of maximum gate time with concentration of $c(^{29}Si) = c(^{13}C) = 0.63\%$, which was found to be optimal at minimum fidelity of 0.95. Blue circles show the median of hyperfine values at the given concentration or gate time.

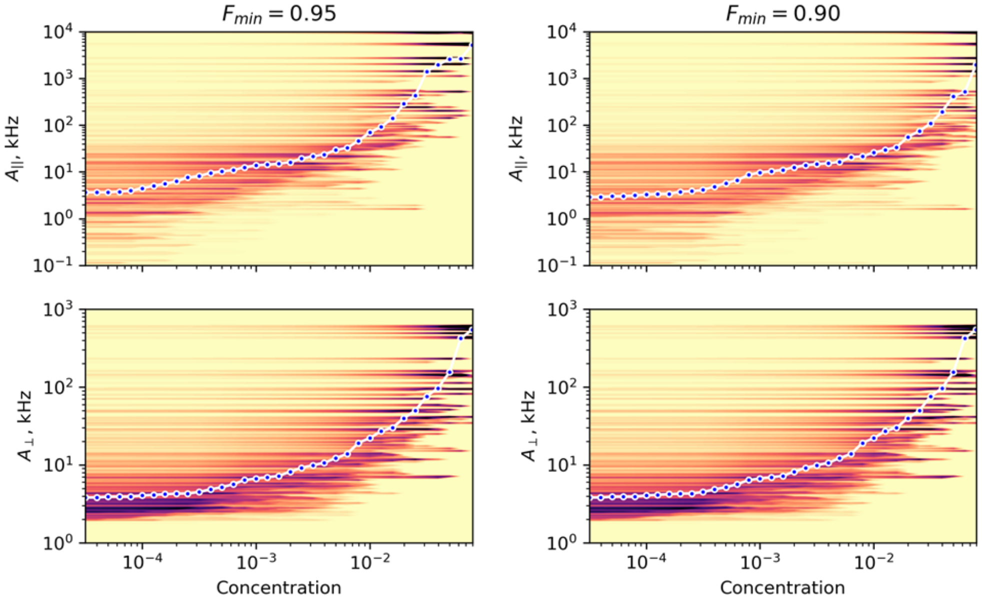

Figure 6.25: **Most plausible hyperfine values for memory units at different fidelities.** Color corresponds to the probability that memory units in the sample with given nuclear concentration will have the corresponding hyperfine term. The maximum gate time $N2\tau$ 1.5 ms, On the left the minimum fidelity of 0.95 is shown, on the right F_{min}=0.90. Blue circles show the median of hyperfine values at the given concentration.

CHAPTER 7

OTHER WORK

In this chapter, I will quickly summarize some of the other work I have had the chance to part of while at the University of Chicago. These are published works to which I have contributed, but have not been the project lead.

My goal here is not to repeat the content of these works in detail (I will instead link to the published versions of the manuscripts), but I will rather attempt to contextualize these results and frame them in the broader context of trying to achieve quantum technologies using defects in SiC.

7.1 Chromium defects in semiconductors

This work [87] explores the possibility of using chromium in SiC (and GaN) as an alternative defect system (instead of the divacancy presented in this dissertation for example). This work is emblematic of a broader class of research that is happening in our group [148, 43] which consists in finding new defect systems either in SiC or in another semiconductor. These types of experiments are the spiritual successors of the work [86] which laid the foundation for using the divacancy defect (discussed throughout this dissertation) as a spin qubit.

The premise of this search is that there may be a defect system out there that is better than the current leading candidate (NV, VV, V_{Si}, SiV, etc...) for quantum technologies. Although not all of these are directly addressed in this paper, I have compiled a non-exhaustive list of potential properties that could be desirable in a new defect system:

1. A higher Debye-Waller factor, meaning that more of the emission is concentrated in the zero-phonon line (ZPL). This would make photon interference experiment a lot better and perhaps even alleviate the need for photonic cavity enhancement (provided that the count rates are also high enough...).

2. Emissions closer to the telecommunication standard 1550 nm. Although the divacancy has emission in the NIR already (1140 nm), these are not quite at the standard telecommunication wavelengths (1550 nm). This is important because this range of wavelengths is efficiently (with minimal insertion loss) transmitted through optical fibers (hence why it was chosen by the telecommunication industry).

3. Higher coupling to mechanical phonons, which could help build hybrid quantum systems (see section 7.2).

4. Unlock new host materials. Some of these new defects could be portable to different host materials (this was demonstrated in this paper by measuring Cr in both SiC and GaN). Defects in silicon, for example, would be particularly interesting given how ubiquitous Si has become in the electronics industry.

5. Lower sensitivity to noise for both the optical and spin transitions.

6. Room temperature operation.

7. And much more!

7.2 Driving spins using Gaussian accoustics

This work[142] demonstrates the mechanical driving of divacancy ensembles in SiC. Mechanical degrees of freedom are interesting because they couple to a great variety of quantum systems and could thus potentially be used to bridge the gap between different qubit systems. For example, mechanical devices have been shown to couple to photons (optomechanics), superconducting circuits, and defects systems such as the NV center (and now the VV^0!).

In this manuscript, we aimed to demonstrate the use of surface acoustic wave (SAW) phonon for driving transitions in the GS of the VV^0. Because the mechanical coupling of VV^0 is not naturally large, we decided to build a phononic cavity around the defects.

Inspired by the curved mirrors in an optical Fabry-Perot we decided that using Gaussian-shaped mechanical "mirrors" (gratings) would allow us to maximize coupling between the mechanical mode and the defects. Our hope was to maximize the Q of the cavity while reducing the mode volume. Interestingly, SiC is ideal for this type of Gaussian-shaped resonator because the speed of sound is isotropic in that material.

Through this work, we achieved our goal and were able to demonstrate the mechanical driving of VV^0 spins in SiC. We also demonstrated interesting new X-ray spectroscopy techniques for measuring mechanical motion.

Although most of these demonstrations were done in ensemble devices, we believe these techniques should easily be transferable in a single defect system. However, to truly utilize spin-photon interaction to mediate state transfer between various quantum systems some major issues still remain. Namely, to achieve a bi-directional single quanta exchange, we need to significantly improve the coupling of the spin to the mechanics. To this end, 2 potential ideas could be explored. First, we could try a different defect than VV^0 which may have a larger mechanical coupling. In particular, we believe that defects associated with larger atoms impurities can display larger coupling to mechanics. Second, we believe that once applied to single defects, using the excited states orbital transition of the defect (instead of the GS spin transition) could enable larger coupling (although this may still not be quite sufficient for strong coupling).

7.3 Exploring the lower symmetry *kh* defects

This work[99] discusses some of the interesting properties of the basal divacancies (*kh*). This defect has a C_{1h} symmetry and thus a different energy structure then the c-axis VV^0 (*hh* and *kk*). This lower symmetry means less state degeneracy in general. In particular, the defect Hamiltonian has a non-zero $\mathbf{E}^0$ term (see section 3.3.4) leading to:

1. A splitting of the "$|+1\rangle$" and "$|-1\rangle$" states (which at B=0 are really the $|+\rangle$ and $|-\rangle$)

at B=0.

2. A higher sensitivity to the electric field around B=0.

In this work, we used both of these properties to demonstrate the following effects.

1. At B=0, the avoided crossing between the $|+\rangle$ and $|-\rangle$ state, results in a Zero First-Order Zeeman (ZEFOZ) transition. Put simply, the derivative of the energy of each state versus magnetic fields is zero (because the splitting is dominated by the $\mathbf{E}^0$ term) at B=0 so the state is not affected by small changes in magnetic fields. This of course comes at the cost of an increase in sensitivity to electric field noise, but since magnetic noise is generally the bigger problem of the two, we ultimately get a longer dephasing time ($\sim$75-150μs).

2. A dressing of the optical states using an external periodic E-field. Since these defects energies are more sensitive to E-field we can use a periodic E-field drive to modulate the transition energy between the GS and the ES. This dressing behavior can be described by Floquet theory because of the periodic nature of the Hamiltonian. This type of E-field coupling (using Stark shift modulation of the optical levels) is interesting because it seems to be more pronounced than the usual interactions with AC E-field of a c-axis defect for example. However, just as in the case of the mechanical coupling (from section 7.2), strong coupling is still a significant challenge.

In general, this work demonstrates that low symmetry defects such as the *kh* divacancies, could be good candidates for building quantum systems. However, the lower coupling to magnetic field noise (at B=0) comes at a cost. First, there is an increased sensitivity to E-field noise, but this is not too worrying since the tradeoff is worth it. Second and most critically, this lower sensitivity to B-field means that the defect does not couple to nuclear spins as strongly. This means that the control of nuclear memories may prove to be difficult. There are two sides to this problem:

1. The lower coupling means that it will be more difficult for the nuclear spin to have an impact on the electron spin and vice versa.
2. The requirement that we operate at B=0 (to benefit from the advantage of the avoided crossing) means that nuclear spins cannot rely on nuclear Zeeman to split the $|\uparrow\rangle$ and $|\downarrow\rangle$ states which may therefore remain degenerate (and therefore unusable as qubits).

Overall, this work ultimately demonstrates that having multiple types of defects to study in SiC is an interesting feature because they may lead to different tradeoffs.

7.4 Embeding VV^0 in photonic nanocavities

This work[40] demonstrates the fabrication of nanobeam cavities in SiC with embedded VV^0. This type of work is critical for several reasons:

1. Photonic cavities can enhance the emission fraction into the ZPL (and therefore the potential entanglement rate).
2. Photonic cavities can enhance the quantum efficiency of the VV^0 by increasing the ratio between the radiative transition rate to the non-radiative transition rate.
3. These devices are the stepping stone to building on-chip systems that would unlock device integration of quantum defects into real-world applications.

This work demonstrates the full process of device design, fabrication, characterization, and finally measurement of embedded quantum systems. Ultimately, this paper demonstrates a Purcell factor of ~ 50 which greatly enhances the ZPL photon emissions, while also maintaining control over the spin degree of freedom.

This type of work is all the more impressive because it inherently has to tackle some notoriously difficult problems with defects and semiconductors:

1. Device fabrication is always a tricky business and these devices are no different. These devices require both very small features (nm scales) and at the same time need to be undercut into suspended structures using a technique (photo-electro-chemical etch) that can selectively etch material with specific doping. All of this makes fabrication inherently complex, required building custom fabrication tools and techniques, and necessitated perfect execution of all the steps in the fabrication process.

2. The fact that these structures are so small means that the defect in them inherently suffers from all the problems associated with surfaces. Most defects (including the VV^0) see their properties degrade when they get close to surfaces. This is ultimately one of the biggest challenges of solid-state emitters.

Ultimately, device integration such as the one presented in this paper is critical to bringing defects systems to practical devices and this work opens the door to these possibilities.

7.5 Extending coherence with continuous drive decoupling

This work[98] demonstrates the use of a continuous drive to decouple the *kh* divacancy from noise in its environment, thus leading to an extended coherence time. This paper applies a constant E-field tone at the frequency of the transition between the $|+\rangle$ and $|-\rangle$ states at B=0. This tone effectively mixes the two spin states and results in the $|+1\rangle$ and $|-1\rangle$ as being the eigenstates of the new driven Hamiltonian. Overall, this effectively decouples the VV^0 from low-frequency noise from the environment. This behaves similarly to pulsed dynamical decoupling, by shifting the noise filter function to a higher frequency where the noise spectrum is lower. In this case, the decoupling is meant to address mostly E-field and temperature noise since the defect is already mostly insensitive to B-field noise around B=0 without the drive (see section 7.3). Ultimately, this work provides a nice alternative to pulsed dynamical decoupling to extend the T_2 of the VV^0 in SiC.

CHAPTER 8

OUTLOOK

Since the divacancy was first shown to be a viable quantum defect system, the field has come a long way. Having demonstrated a lot of the critical features, the divacancy in SiC now stands as a viable candidate for building quantum networks and as a real alternative to more established defect systems such as the NV^- center in diamond.

Furthermore, because this defect is hosted in a mature semiconductor host, the divacancy offers new possibilities perhaps best exemplified by the work presented in chapter 5. However, some numerous challenges remain to be solved for building practical quantum devices using SiC. This chapter will broadly explore some of these challenges and suggest avenues of research that could help overcome these obstacles.

8.1 Single-shot readout

Perhaps the single most important remaining milestone for VV^0 defects in SiC is to achieve Single-Shot Readout (SSR). High fidelity SSR is really the only thing currently standing in the way of achieving remote entanglement. Fortunately, there are several strategies we can use to achieve this goal and we are currently exploring a few of these options.

In current experiments, we collect about 0.15 photons per experiment (per shot) at most. To achieve SSR with reasonable fidelity, we would like to collect on average a few (∼2-10) photons, while maintaining a low noise count in the dark state (∼below 1). These numbers should not be viewed as hard-bound (they are not!), but rather as rough indicators of what we need to aim for.

Throughout this section, I will give my educated guess of how much we can hope to improve collection efficiency using every one of these methods. However, the reader should remember that these are just estimates and we will only know for sure, once we've tried out the changes.

8.1.1 Increasing collection efficiency

The most straightforward way to achieve SSR is to simply increase the collection efficiency from our defect. There are several ways to achieve this enhance using various modifications to the collection optics. This section presents a few examples.

Solid immersion lenses

Solid immersion lenses (SIL) to minimize total internal reflection: The main challenge to increasing collection efficiency in the current top-down collection configuration is that most of the light never makes it out of the SiC in the first place! This is because the critical angle for internal reflection at the interface of SiC and vacuum is about 22°. This means that any light emitted at an angle (with respect to the c-axis) greater than 22° is impossible to collect with a planar SiC-vacuum interface. This is where SIL comes into play. SILs are semi-spherical volume of material (typically etched in the SiC itself, but potentially also external with a different high-index material) with the emitter at the center. Since the emissions are coming from the center of the SIL every light ray hits the surface at 90° meaning no total internal reflection occurs. Only standard Fresnel reflections applied (∼20% reflected), and even those can be mitigated using anti-reflection coating.

One challenge associated with SIL is the alignment of the SIL and the defect. This alignment relies on both our ability to mark a defect position precisely and our ability to fabricate a SIL at a given location. We generally would like our defect to be located in the center of the SIL and as a rule of thumb, the allowed margin should be less then 20% of the SIL radius (so if we make SIL with$R = 5\mu m$, we want to have the defect at the center $\pm 1\mu m$). Obviously, the more precise the better!

In the XY directions (in-plane directions), the limiting number is generally related to the spot size which is “convoluted” with the “delta function” position of the defect. This spot size is generally about $1\mu m$ and by fitting a scan over the defect with sufficient signal-to-noise we can conceivably determine the defect position within $\sim 100nm$ or so. In fact, in the last few years, we have experimented with an automated procedure to align such defects within this type of precision range to external markers.

In the Z direction (direction of propagation or c-axis direction) however, determining the exact position of the defect is more tricky. First, traversing the SiC at an angle with the collection and excitation path (because of the large NA of the objective) makes the math to figure out the exact position in the material a bit tricky... But even if we do all of this correctly, we are still left with a Raleigh range of $\sim 10\mu m$ which drastically limits the precision we have in that direction. Interestingly, however, the work presented in chapter 5 may provide a very convenient solution here. Indeed, because the defects are mostly stable in the i-region we can make a PIN diode with a narrow i-region (let’s say $1\mu m$ or less) and then know from the start the depth of our defect without even needing to measure it! In fact, even when using the larger regions (such as the 10 μm) it should be possible to determine the exact location of the defect in depth by observing the turn-on threshold voltage for Stark tunning. This shows another neat application of semiconductor devices to emitters in SiC!

Overall, this technique alone could increase our collection efficiency by roughly a factor of 8.

Simplifying the confocal microscope

This was briefly discussed in section 4.2.4. The idea is to simplify the collection path of the confocal microscope by removing the 4F pair and bringing the “collection box” closer to the objective. Preliminary, results on this seem to indicate that we can increase our collection efficiency by approximately a factor of 2 using this modification.

Using adaptive optics

To collect light into our SNSPD detector, we first need to couple it to a single-mode fiber. The efficiency of the coupling of the collection photon into the fiber ultimately comes down to matching the spatial mode of these collection photons to the Gaussian model of the fiber. Unfortunately, the collimated emissions from the defect are not Gaussian. In fact, the emission profile of the resonant photons (ZPL photons) of the divacancy is that of a dipole with an in-plane dipole moment (which is essentially a donut shape on its side). This emission profile, whatever it is, is then collimated and results into a shape that is... well, not Gaussian!

This is where adaptive optics can play a role. In particular, we are currently exploring the possibility of using a deformable mirror in the collection path as a way to reshape the mode shape of the collection photon into something a little more Gaussian. This strategy has already been successful in the NV center community. Based on this literature and some rough measurement of loss going from multimode fiber to single-mode fiber, we estimate that this improvement could result in about a 2x improvement in collection efficiency.

Custom objective

Options for high numerical aperture (NA) objectives in the NIR can be limited. The best off-the-shelf option we have found so far is the Olympus LCPLN100XIR. This objective has a NA of 0.85 and transmission of about 75% at the ZPL (and can drop towards $\sim 65\%$ on the red side of the phonon sideband).

However, it seems like this is not a fundamental physical limitation of objectives at these wavelengths, but rather a lack of demand in the market for our wavelength of interest. Consequently, it may be possible to contract a company to design custom objectives that maximize NA and transmission. It is harder to estimate exactly what gain we expect for the NA improvements without knowing the physical system (SIL/ no SIL, emission profile, etc...) and doing some simulations, but my guess would be that getting an objective with about 90% transmission in throughout the phonon sideband and an NA of 0.9, could buy us a factor of ∼1.5x (50%).

SNSPD design

When we designed our collection setups, we designed the detectors to be maximally efficient at the ZPL and to function on all 4 defects orientation (*hh*, *kk*, *kh* and *hk*). This gave us a lot of freedom and, in the long run, this design wavelength will be critical to maximizing entanglement rates.

However, when trying to achieve SSR on the *hh* and *kk* defects this design wavelength is not ideal. Whereas the peak efficiency of the detector at the moment is $> 95\%$, the efficiency at 1250nm (the center of the phonon sideband) is down to $< 60\%$. This means that by shifting the peak frequency to about 1250nm and assuming an efficiency $> 85\%$ over the entire phonon sideband we could presumably achieve a gain in collection efficiency of about 1.5x (50%).

Summary

Given all of these improvements, we would end up with a gain of approximately: $8 \cdot 2 \cdot 2 \cdot 1.5 \cdot 1.5 = 72$. Starting at about 0.15 photons per shot, this would put us at around 11 photons per shot (well above the needed threshold!). However, experimental science is tricky, and given that not all of these may get fully realized, or may result in lower than expected gains, we should be prepared to get a lower final count even after implementing all of these strategies (call it “engineering margins”!). Nevertheless, this is a promising avenue to achieve SSR and it has the advantage that it does not require any drastic changes to the way we do experiments, but rather relies on a series of incremental improvements that are likely to be desirable over time anyways.

8.1.2 Spin-to-charge readout

Here the idea stems from the charge control experiment from chapter 5. Here we showed how resonant light can be used to ionize the divacancy. If that's the case then it is likely that we could successfully ionize the defect selectively when we are in a given spin state. We also demonstrated that at weak optical excitation powers the charge state can be stable for a very long time. This means that charge readout is relatively straightforward and should essentially benefit from an unlimited averaging time (ie unlimited signal-to-noise).

The main question is: what kind of spin-to-charge efficiency can we achieve? Since charge readout can have an arbitrarily good signal, this efficiency will really be the factor that will determine the overall fidelity of this type of SSR technique. We have already attempted some preliminary tests on that front and the results are looking promising...

Another factor we may need to be careful about if we go in this direction is the impact of the spin-to-charge readout process on the surrounding nuclear spins. Nuclear spins are absolutely essential to making a quantum communication node using the VV^0 and anything that is incompatible with nuclear memories is likely not a long-term solution.

8.1.3 Nuclear readout

Another option is to use nuclear spins themselves to store the quantum information and then read it out from there. This avenue for SSR is unlocked by the work presented in chapter 6. This technique would probably work best using the strongly coupled nuclear spins since these could benefit from fast C_nNOT_e gates (few 10-100s of ns). However, we may be forced to use more weakly coupled registers if trying to work in an isotopic regime that maximizes the number of nuclear memories.

Either way, the idea would be to transfer the state to be read out to the nuclear spin. Then repeatedly:

1. Initialize the electron spin

2. Perform a $C_n NOT_e$ gate

3. Readout the electron optically

Since we can repeat this cycle many times over (until the nuclear spin flips), this can significantly boost the number of photons available for readout. For instance, a 100 cycles sequence would bring us to ∼15 photon per shot.

The downside of this method is that we are forced to use one of our nuclear registers (a precious quantum resource) for readout, and it is then of very limited use for computation or storage.

8.1.4 Direct fiber coupling

Ultimately, we know our full coupling from the defect emission all the way to the fiber has many lossy steps. We can confirm this with a rough estimation of the number of photons we expect could be emitted.

1. With excitation saturation, we expect roughly 50% of the population in the excited state. With a lifetime of $\approx 18ns$ which we double because of the 50% population, we get on average a photon every $\approx 36ns$

2. With a spin-flip rate at saturation on the order of about $\approx 10\mu s$ (and let's assume a quantum efficiency of the emitter of 50% although we haven't actually measured this number...), this means that we should get about 150 photons emitted per shot.

3. With the current 0.15 photons collected per shot, we can infer a collection efficiency of about 0.1%.

We can also do another similar estimate using off-resonant CW counts. There,

1. We should get on average a photon every $\approx 36ns$ (see above).

2. We should count about $15 \cdot 10^6$ counts per second (assuming an emitter quantum efficiency of $\sim 50\%$).
3. In practice we only see about $50 \cdot 10^3$ counts per second at most. This means roughly a 0.3% collection efficiency.

Given how rough these estimates are, the numbers here have a large error margin, but I would probably expect the actual number to be less than 1%.

Ultimately, this very low estimated collection efficiency is the result of a series of lossy steps in the collection path (see section 8.1.1). One may ask whether we could reduce the number of steps involved... In particular, several recent works in the field of solid-state emitters have shown how they could use direct fiber coupling from their device to collect the emission defects located in (or coupled to) on-chip waveguides or nanocavities.

There seem to be two main techniques to couple fibers to on-chip devices:

- Edge coupling using lens fiber: The idea here is to have light emitted from the end of cantilevered beam-like structures. A fiber lens is then brought close (within order 10 μm) from the tip of the beam. The emitted light from the defect travels through the waveguide and exits the beam on the side of the chip and is immediately coupled to a single-mode fiber.
- Adiabatic tapered fiber: Here the idea is to fabricate a long tapered device and a long tapered fiber. We then place the tapered fiber in contact with the tapered waveguide. In this configuration, the light travels through the waveguide, and the size of the waveguide shrinks while the size of the fiber grows. Because of this adiabatic change, the spatial mode of the light is slowly transferred to the fiber, leading to an excellent coupling.

These techniques can lead to extremely efficient coupling (up to 80-90% coupling efficiency). Unfortunately, for maximal efficiency, these techniques generally require the emissions to be into a single-mode. This could be accomplished with waveguides or nanocavities but it brings along a whole set of other problems as we've seen in section 7.4. Nevertheless, even if we don't realize the full coupling efficiency potential by using nanostructures, there is still a lot of headroom between the current $\sim 0.1\%$ and the maximum $\sim 80-90\%$ efficiency. If for example, we could achieve a coupling efficiency of only 10%, this should be sufficient to get us to SSR (about 15 photons per shot)

8.1.5 Photonic devices

Finally, there is always a possibility of improving photonic devices themselves to increase collection efficiency. This can be done by:

1. Increasing the quantum efficiency and cyclicity of the defect via Purcell enhancement of the radiate decay in a photonic cavity.
2. Designing a photonic structure that can efficiently radiate towards the collection apparatus. For example, one could build a grating coupler structure with a far-field emission profile that is preferentially out-of-plane (and collect using the current top-down objective path).
3. Designing structures for better direct fiber coupling (see section 8.1.4)

8.2 New semiconductor devices

The work presented in chapter 5 unlocks a new world of possibilities for incorporating spins in doped semiconductor devices. In this section, we discuss a few possible devices which could be interesting to explore.

A first step would be to optimize the types of diodes structures we presented. In particular, we could try to reduce the size of the i-region to reduce the voltage of operations of the device (or increase the E-field at a given voltage). As we do this we will need to be careful not to bring the defects too close to a region the doped regions since the high carrier density in the p- and n- regions could introduce the electric noise back into our defect system. This effect could be somewhat mitigated by reducing the dopant concentration compared to what we presented in this dissertation. Finding new ways to reduce the i-region width without affecting the optical linewidth will definitely be an interesting engineering challenge.

Second, building more isolated devices such as mesa diodes would also have significant advantages. It would allow us to create widely scalable arrays of diode devices each individually controllable and would therefore be a step toward a more large-scale quantum device. Additionally, because of the elevation of these diodes, these structures could also be ideal for 3 axis control of electric fields. Engineering a device with 3-axis control of E-field would allow us to build systems in which defects can be tuned to be perfectly identical (not only with one optical line but with all of them!). This would addition of XY field would hopefully also enable us to restore the defect symmetry (to counter inhomogeneous strain) and increase the cyclicity of the optical transition.

Third, building avalanche photodiode (APD) devices and biasing them into the breakdown region, could potentially enable us to perform single-shot electrical readout of our defects. To do this, we would first need to apply the spin-to-charge techniques discussed in section 8.1.2. The charge carrier released in this process could then trigger an avalanche (under a large E-field) which would enable the resulting current to be read out electrically. In this type of scheme, mesa devices would also be interesting, because their smaller surface area would reduce the background leakage current leading to a better SNR for this APD readout.

Fourth, we could also think about fabricating pin structures into nanocavities. This would potentially enable us to tune the defect in the cavity in-situ by applying voltages on contacts far away from the device. Here we would essentially rely on the doped layer as transparent electrodes to “reach into the cavity” and tune the emitters. Furthermore, we could also try to apply the linewidth narrowing techniques presented in this dissertation to the defects inside the nanocavity. If this works, it would lead to a major advance in integrating spins in solid-state devices with nanophotonics. Note that this would achieve a widely tunable, narrow line, photonically enhance emitter while maintaining the defect spin properties in a system operating at 5K all in a scalable semiconductor material. To my knowledge, no system has yet achieved all of these requirements together and this would therefore represent a major advance in the field.

Finally, there are many more devices such as transistors, MOS capacitors, Schottky diodes, etc... Most of these are expected to be compatible with the techniques discussed in this dissertation, but some of them may also enable new tools and techniques. It will certainly be interesting how modern electrical devices can be leveraged to unlock new tools and techniques for defect systems in semiconductors!

8.3 New steps with nuclear spins

Although we have demonstrated how to control nuclear spins in chapter 6, a lot of work remains to be done. In particular, the next steps should be to measure the coherence of these nuclear spins, try to apply some new control techniques to access more nuclear spin with better fidelities, and create entangled states with more than one nuclear spin (and one electron spin) at the time. These would, in my opinion, be the next demonstrations with nuclear spins (along with using them for entanglement which we will discuss further in section 8.6).

First, let's discuss nuclear spins coherence. Nuclear spin coherence can actually be fairly tricky to measure because they are expected to be very long. This means that our experiment time quickly grows and it becomes difficult to measure enough signal.

For this reason, we decided to leave off the coherence measurements of nuclear spin until we've achieved SSR. Achieving this milestone will essentially mean that we would need to average less and therefore, long experiments will be more within reach.

We should also consider measuring the coherence of the nuclear spin while re-initializing and manipulating the electron spin since this is going to be necessary in the long run.

Second, we should aim to apply some recently developed techniques for controlling nuclear spins [27]. These techniques, although slightly more complex, offer a lot of flexibility and have already been shown to work in NV center systems. Thus, it should be possible to apply these techniques to SiC to get more selective and flexible nuclear spin gates.

Third, although this will require a bit more work, we should then try to entangle more than two spins at a time. As we start to create states with more and more qubit, we will hopefully approach a regime where small quantum algorithms or limited versions of error correction can be run. These types of small scale error correction algorithms will be a milestone demonstration to move ever closer to a fully-featured quantum repeater system.

8.4 Optical frequency conversion

Although the divacancy emissions are in the NIR, they are not quite at the ideal telecom wavelength (∼1550 nm). Although the loss penalty is much less than for visible photons, when working with a very long fiber link, it may become advantageous to do optical frequency conversion before transmitting the emitted photons.

A nice feature of being already in the NIR is that the energy needed for the conversion is quite low (about $4\mu m$). This means that two photons at the pump frequency are insufficient to reach the 1550nm energies. This is important since the pump needs to be strong for high conversion efficiency, but a strong pump with photon energy higher than half of that of 1550nm can cause significant background noise.

Therefore, we expect that frequency conversion from 1140nm to around 1550nm will be better than when starting from visible wavelength (as in the case of the NV^- center in diamond). The downside is that we will need to deal with uncommon laser frequencies for the pump (around $4\mu m$).

8.5 On-chip devices

There is a wide range of new photonics and electrical devices which should now be possible to create and explore. These on-chip devices will certainly be a critical part of integrating defects systems into practical devices. We have already touched on some of these (e.g. sections 8.1.1, 8.2, etc...) but I would like to throw in some additional examples here to really underscore the breadth of possibilities moving forward (some of these projects have already started in our lab, or at other institutions and have already been realized in other defects systems (e.g. NV center))):

1. SiC-on-insulator photonics: Integrating defects into photonic devices is very important for the future of on-chip systems. SiC-on-insulator provides an alternative to the current PEC method for producing photonic devices and could be a very valuable tool in the future. These could potentially be used to make photonic cavities, waveguides, on-chip beamsplitter, on-chip filters, and more...
2. Fabry-Perot using fiber mirrors: These devices, although not strictly "on-chip" devices, could potentially be used to integrate VV^0 into packaged devices. This type of technique has already been successfully applied in NV center systems [70, 117]. This type of system could provide better collection efficiency, Purcell enhancement, direct fiber coupling, and scanning capability all at the same time.
3. Building on-chip SNSPD: To completely remove the need for collection optics we could think of adding on-chip detectors. We would need to either work at a lower temperature or build SNSPD which can be operated at 5K. We would also need to be careful in shielding the detectors from outside lights and excitation laser (perhaps using on-chip filters and "black box"). This could again ultimately result in an increase in collection

efficiency and would widely simplify the integration into practical devices.

In the end, there are even more possible ideas (too long of a list to exhaustively go through) that have the potential for bringing this defect system into the world of practical applications.

8.6 Remote entanglement and quantum networks

Ultimately, the work in this dissertation and almost all the various possible next steps presented in this section all work towards a common final goal: building quantum networks. The steps to take in that direction would probably go as follows:

1. Demonstrate two-photon interference with ZPL emissions: Although we have decided to focus our effort in a different direction, this step could easily be in reach at the moment.

2. Small scale entanglement demonstrations: To realize this demonstration, we will first need to achieve SSR. Once we have SSR, we can combine it with the two-photon interference techniques to achieve entanglement between two nodes in the same lab. Such demonstrations, should be able to take advantage of the work presented in chapter 5 and chapter 6.

3. Larger scale entanglement demonstrations: This step will consist in scaling up the "in-lab" entanglement demonstration. Here new city-scale fiber network, such as the effort currently being developed at Argonne National Laboratory, will play a role. Although the same techniques learned from the small scale demonstration will still apply, this step will introduce a whole set of new challenges such as:

    (a) Fiber insertion losses

    (b) Fiber stability to ensure phase stability in transmission

    (c) Fiber isolation along the channel

   (d) Synchronization between the remote nodes

   All of these of course have possible solutions such as: optical frequency conversion, classical fiber trigger, and so on... Ultimately, I expect there will be an iterative process here between testing strategies at a lab-scale and implementing them on the larger scale.

4. Quantum error correction: Here we will need to scale up and further develop the techniques presented in chapter 6 to implement small scale error corrections. The goal here will be to make up for errors due to transmission (or decoherence). Initially smaller scale algorithms could focus on correcting for a single error quadrature. This approach may greatly relax the requirements in terms of the number of registers and operations needed, and may still be greatly advantageous.

References

[1] M. H. Abobeih, J. Cramer, M. A. Bakker, N. Kalb, M. Markham, D. J. Twitchen, and T. H. Taminiau. One-second coherence for a single electron spin coupled to a multi-qubit nuclear-spin environment. *Nature Communications*, 9(1):1–8, dec 2018.

[2] M. H. Abobeih, J. Randall, C. E. Bradley, H. P. Bartling, M. A. Bakker, M. J. Degen, M. Markham, D. J. Twitchen, and T. H. Taminiau. Atomic-scale imaging of a 27-nuclear-spin cluster using a quantum sensor. *Nature*, 576(7787):411–415, dec 2019.

[3] V. M. Acosta, C. Santori, A. Faraon, Z. Huang, K. M.C. Fu, A. Stacey, D. A. Simpson, K. Ganesan, S. Tomljenovic-Hanic, A. D. Greentree, S. Prawer, and R. G. Beausoleil. Dynamic stabilization of the optical resonances of single nitrogen-vacancy centers in diamond. *Physical Review Letters*, 108(20), 2012.

[4] Mustafa Ahmed Ali Ahmed, Gonzalo A. Álvarez, and Dieter Suter. Robustness of dynamical decoupling sequences. *Physical Review A - Atomic, Molecular, and Optical Physics*, 87(4):042309, apr 2013.

[5] Christopher P. Anderson, Alexandre Bourassa, Kevin C. Miao, Gary Wolfowicz, Peter J. Mintun, Alexander L. Crook, Hiroshi Abe, Jawad Ul Hassan, Nguyen T. Son, Takeshi Ohshima, and David D. Awschalom. Electrical and optical control of single spins integrated in scalable semiconductor devices. *Science*, 366(6470):1225–1230, 2019.

[6] A. Arvanitopoulos, N. Lophitis, S. Perkins, K. N. Gyftakis, M. Belanche Guadas, and M. Antoniou. Physical parameterisation of 3C-Silicon Carbide (SiC) with scope to evaluate the suitability of the material for power diodes as an alternative to 4H-SiC, oct 2017.

[7] N. Aslam, G. Waldherr, P. Neumann, F. Jelezko, and J. Wrachtrup. Photo-induced ionization dynamics of the nitrogen vacancy defect in diamond investigated by single-shot charge state detection. *New Journal of Physics*, 15, 2013.

[8] Nabeel Aslam, Matthias Pfender, Philipp Neumann, Rolf Reuter, Andrea Zappe, Felipe Fávaro De Oliveira, Andrej Denisenko, Hitoshi Sumiya, Shinobu Onoda, Junichi Isoya, and Jörg Wrachtrup. Nanoscale nuclear magnetic resonance with chemical resolution. *Science*, 357(6346):67–71, jul 2017.

[9] David D. Awschalom, Ronald Hanson, Jörg Wrachtrup, and Brian B. Zhou. Quantum technologies with optically interfaced solid-state spins. *Nature Photonics*, 12(9):516–527, 2018.

[10] Tesfaye Ayalew. *SiC Semiconductor Devices Technology, Modeling, and Simulation.* PhD thesis, 2004.

[11] Gopalakrishnan Balasubramanian, Philipp Neumann, Daniel Twitchen, Matthew Markham, Roman Kolesov, Norikazu Mizuochi, Junichi Isoya, Jocelyn Achard, Johannes Beck, Julia Tissler, Vincent Jacques, Philip R Hemmer, Fedor Jelezko, and Jörg Wrachtrup. Ultralong spin coherence time in isotopically engineered diamond. *Nature materials*, 8(5):383–7, may 2009.

[12] N. Bar-Gill, L. M. Pham, C. Belthangady, D. Le Sage, P. Cappellaro, J. R. Maze, M. D. Lukin, A. Yacoby, and R. Walsworth. Suppression of spin-bath dynamics for improved coherence of multi-spin-qubit systems. *Nature Communications*, 3(1):1–6, may 2012.

[13] L. C. Bassett, F. J. Heremans, C. G. Yale, B. B. Buckley, and D. D. Awschalom. Electrical tuning of single nitrogen-vacancy center optical transitions enhanced by photoinduced fields. *Physical Review Letters*, 107(26), 2011.

[14] Erik Bauch, Connor A. Hart, Jennifer M. Schloss, Matthew J. Turner, John F. Barry, Pauli Kehayias, Swati Singh, and Ronald L. Walsworth. Ultralong Dephasing Times in Solid-State Spin Ensembles via Quantum Control. *Physical Review X*, 8(3):031025, jul 2018.

[15] K. Beha, A. Batalov, N. B. Manson, R. Bratschitsch, and A. Leitenstorfer. Optimum photoluminescence excitation and recharging cycle of single nitrogen-vacancy centers in ultrapure diamond. *Physical Review Letters*, 109(9), 2012.

[16] H. Bernien, B. Hensen, W. Pfaff, G. Koolstra, M. S. Blok, L. Robledo, T. H. Taminiau, M. Markham, D. J. Twitchen, L. Childress, and R. Hanson. Heralded entanglement between solid-state qubits separated by three metres. *Nature*, 497(7447):86–90, 2013.

[17] Hannes Bernien. *Control, measurement and entanglement of remote quantum spin registers in diamond — TU Delft Repositories*. PhD thesis, TuDelft, feb 2014.

[18] Ariana Beste, Decarlos E. Taylor, D. Andrew Golter, and Chih W. Lai. Charge state switching of the divacancy defect in 4H -SiC. *Physical Review B*, 98(21), 2018.

[19] Stefan Birkner. Quantum Fourier Transform on Three Qubits.svg - Wikimedia Commons.

[20] M. S. Blok, N. Kalb, A. Reiserer, T. H. Taminiau, and R. Hanson. Towards quantum networks of single spins: Analysis of a quantum memory with an optical interface in diamond. *Faraday Discussions*, 184:173–182, 2015.

[21] Dolev Bluvstein, Zhiran Zhang, and Ania C.Bleszynski Jayich. Identifying and Mitigating Charge Instabilities in Shallow Diamond Nitrogen-Vacancy Centers. *Physical Review Letters*, 122(7), 2019.

[22] Michel Bockstedte, Felix Schütz, Thomas Garratt, Viktor Ivády, and Adam Gali. Ab initio description of highly correlated states in defects for realizing quantum bits. *npj Quantum Materials*, 3(1):1–6, dec 2018.

[23] C. Bonato, M. S. Blok, H. T. Dinani, D. W. Berry, M. L. Markham, D. J. Twitchen, and R. Hanson. Optimized quantum sensing with a single electron spin using real-time adaptive measurements. *Nature Nanotechnology*, 11(3):247–252, 2016.

[24] Alexandre Bourassa. https://github.com/alexbourassa/easy-wave.

[25] Alexandre Bourassa, Christopher P Anderson, Kevin C Miao, Mykyta Onizhuk, He Ma, Alexander L Crook, Hiroshi Abe, Jawad Ul-Hassan, Takeshi Ohshima, Nguyen T Son, Giulia Galli, and David D Awschalom. Entanglement and control of single nuclear spins in isotopically engineered silicon carbide. *Nature Materials*, 19(12):1319–1325, 2020.

[26] Alexandre Bourassa, Jacob Feder, and Michael Solomon. https://github.com/nspyre-org/nspyre.

[27] C. E. Bradley, J. Randall, M. H. Abobeih, R. C. Berrevoets, M. J. Degen, M. A. Bakker, M. Markham, D. J. Twitchen, and T. H. Taminiau. A ten-qubit solid-state spin register with quantum memory up to one minute. *Phys. Rev. X*, 9:031045, Sep 2019.

[28] L. Bradley, C. Donaghy-Spargo, G. Atkinson, and A. Horsfall. Evaluating suitable semiconducting materials for cryogenic power electronics. *The Journal of Engineering*, 2019(17):4475–4479, 2019.

[29] D. A. Broadway, N. Dontschuk, A. Tsai, S. E. Lillie, C. T.K. Lew, J. C. McCallum, B. C. Johnson, M. W. Doherty, A. Stacey, L. C.L. Hollenberg, and J. P. Tetienne. Spatial mapping of band bending in semiconductor devices using in situ quantum sensors. *Nature Electronics*, 1(9):502–507, 2018.

[30] Benjamin Brunel, Carles Blanch, Vanni Petrolli, Antoine Delon, Romain Pierrat, and Giovanni Cappello. Structure and dynamics of multicellular assemblies measured by coherent light scattering. *New Journal of Physics*, 2017.

[31] Earl T. Campbell, Barbara M. Terhal, and Christophe Vuillot. Roads towards fault-tolerant universal quantum computation, sep 2017.

[32] Kerem Y. Camsari, Brian M. Sutton, and Supriyo Datta. P-bits for probabilistic spin logic, mar 2019.

[33] Chitraleema Chakraborty, Laura Kinnischtzke, Kenneth M. Goodfellow, Ryan Beams, and A. Nick Vamivakas. Voltage-controlled quantum light from an atomically thin semiconductor. *Nature Nanotechnology*, 10(6):507–511, 2015.

[34] David J. Christle, Abram L. Falk, Paolo Andrich, Paul V. Klimov, Jawad Ul Hassan, Nguyen T. Son, Erik Janzén, Takeshi Ohshima, and David D. Awschalom. Isolated electron spins in silicon carbide with millisecond coherence times. *Nature Materials*, 14(2):160–163, 2015.

[35] David J. Christle, Paul V. Klimov, Charles F. de las Casas, Krisztián Szász, Viktor Ivády, Valdas Jokubavicius, Jawad Ul Hassan, Mikael Syväjärvi, William F. Koehl, Takeshi Ohshima, Nguyen T. Son, Erik Janzén, ádám Gali, and David D. Awschalom. Isolated spin qubits in SiC with a high-fidelity infrared spin-to-photon interface. 7(2), 2017.

[36] Y. Chu, N. P. De Leon, B. J. Shields, B. Hausmann, R. Evans, E. Togan, M. J. Burek, M. Markham, A. Stacey, A. S. Zibrov, A. Yacoby, D. J. Twitchen, M. Loncar, H. Park, P. Maletinsky, and M. D. Lukin. Coherent optical transitions in implanted nitrogen vacancy centers. *Nano Letters*, 14(4):1982–1986, 2014.

[37] A. A. Clerk, K. W. Lehnert, P. Bertet, J. R. Petta, and Y. Nakamura. Hybrid quantum systems with circuit quantum electrodynamics. *Nature Physics*, pages 1–11, mar 2020.

[38] C. J. Cochrane, P. M. Lenahan, and A. J. Lelis. Identification of a silicon vacancy as an important defect in 4H SiC metal oxide semiconducting field effect transistor using spin dependent recombination. *Applied Physics Letters*, 100(2), 2012.

[39] Jean-Pierre Colinge and Cynthia A. Colinge. *Physics of semiconductor devices*. Kluwer Academic Publishers, Boston, 2002.

[40] Alexander L. Crook, Christopher P. Anderson, Kevin C. Miao, Alexandre Bourassa, Hope Lee, Sam L. Bayliss, David O. Bracher, Xingyu Zhang, Hiroshi Abe, Takeshi Ohshima, Evelyn L Hu, and David D. Awschalom. Purcell enhancement of a single silicon carbide color center with coherent spin control. *Nano Letters*, mar 2020.

[41] K. S. Cujia, J. M. Boss, K. Herb, J. Zopes, and C. L. Degen. Tracking the precession of single nuclear spins by weak measurements, jun 2019.

[42] Charles F. De Las Casas, David J. Christle, Jawad Ul Hassan, Takeshi Ohshima, Nguyen T. Son, and David D. Awschalom. Stark tuning and electrical charge state control of single divacancies in silicon carbide. *Applied Physics Letters*, 111(26), 2017.

[43] Berk Diler, Samuel J. Whiteley, Christopher P. Anderson, Gary Wolfowicz, Marie E. Wesson, Edward S. Bielejec, F. Joseph Heremans, and David D. Awschalom. Coherent control and high-fidelity readout of chromium ions in commercial silicon carbide. *npj Quantum Information*, 6(1):1–6, dec 2020.

[44] M. W. Doherty, C. A. Meriles, A. Alkauskas, H. Fedder, M. J. Sellars, and N. B. Manson. Towards a room-temperature spin quantum bus in diamond via electron photoionization, transport, and capture. *Physical Review X*, 6(4), 2016.

[45] F. Dolde, H. Fedder, M. W. Doherty, T. Nöbauer, F. Rempp, G. Balasubramanian, T. Wolf, F. Reinhard, L. C.L. Hollenberg, F. Jelezko, and J. Wrachtrup. Electric-field sensing using single diamond spins. *Nature Physics*, 7(6):459–463, 2011.

[46] Wenzheng Dong, F A Calderon-Vargas, and Sophia E Economou. Precise high-fidelity electron–nuclear spin entangling gates in NV centers via hybrid dynamical decoupling sequences. *New Journal of Physics*, 22(7):073059, jul 2020.

[47] Abram L. Falk, Bob B. Buckley, Greg Calusine, William F. Koehl, Viatcheslav V. Dobrovitski, Alberto Politi, Christian A. Zorman, Philip X.L. Feng, and David D. Awschalom. Polytype control of spin qubits in silicon carbide. *Nature Communications*, 4(1):1–7, may 2013.

[48] Abram L. Falk, Paul V. Klimov, Viktor Ivády, Krisztián Szász, David J. Christle, WilliamF. Koehl, Ádám Gali, and David D. Awschalom. Optical Polarization of Nuclear Spins in Silicon Carbide. *Physical Review Letters*, 114(June):247603, 2015.

[49] Gabriel Ferro and Didier Chaussende. A new model for in situ nitrogen incorporation into 4H-SiC during epitaxy. *Scientific Reports*, 7(1):43069, mar 2017.

[50] J Forneris, S. Ditalia Tchernij, P Traina, E Moreva, N Skukan, M. Jakšić, V Grilj, F. Bosia, E. Enrico, G. Amato, I. P. Degiovanni, B. Naydenov, F. Jelezko, M. Genovese, and P Olivero. Mapping the Local Spatial Charge in Defective Diamond by Means of N- v Sensors - A Self-Diagnostic Concept. *Physical Review Applied*, 10(1):1–15, 2018.

[51] Kai Mei C. Fu, Charles Santori, Paul E. Barclay, Lachlan J. Rogers, Neil B. Manson, and Raymond G. Beausoleil. Observation of the dynamic Jahn-Teller effect in the excited states of nitrogen-vacancy centers in diamond. *Physical Review Letters*, 103(25):256404, dec 2009.

[52] G. D. Fuchs, G. Burkard, P. V. Klimov, and D. D. Awschalom. A quantum memory intrinsic to single nitrogen-vacancy centres in diamond. *Nature Physics*, 7(10):789–793, oct 2011.

[53] Adam Gali, Andreas Gällström, Nguyen Tien Son, and Erik Janzén. Theory of neutral divacancy in sic: A defect for spintronics. In *Silicon Carbide and Related Materials 2009*, volume 645 of *Materials Science Forum*, pages 395–397. Trans Tech Publications Ltd, 7 2010.

[54] P Giannozzi, O Andreussi, T Brumme, O Bunau, M Buongiorno Nardelli, M Calandra, R Car, C Cavazzoni, D Ceresoli, M Cococcioni, N Colonna, I Carnimeo, A Dal Corso, S. De Gironcoli, P Delugas, R. A. Distasio, A Ferretti, A Floris, G Fratesi, G Fugallo, R Gebauer, U Gerstmann, F Giustino, T Gorni, J Jia, M Kawamura, H. Y. Ko, A Kokalj, E. Kücükbenli, M Lazzeri, M Marsili, N Marzari, F Mauri, N. L. Nguyen, H. V. Nguyen, A. Otero-De-La-Roza, L Paulatto, S Poncé, D Rocca, R Sabatini, B Santra, M Schlipf, A P Seitsonen, A Smogunov, I Timrov, T Thonhauser, P Umari, N Vast, X Wu, and S Baroni. Advanced capabilities for materials modelling with Quantum ESPRESSO. *Journal of Physics Condensed Matter*, 29(46):465901, nov 2017.

[55] Paolo Giannozzi, Stefano Baroni, Nicola Bonini, Matteo Calandra, Roberto Car, Carlo Cavazzoni, Davide Ceresoli, Guido L Chiarotti, Matteo Cococcioni, Ismaila Dabo,

Andrea Dal Corso, Stefano de Gironcoli, Stefano Fabris, Guido Fratesi, Ralph Gebauer, Uwe Gerstmann, Christos Gougoussis, Anton Kokalj, Michele Lazzeri, Layla Martin-Samos, Nicola Marzari, Francesco Mauri, Riccardo Mazzarello, Stefano Paolini, Alfredo Pasquarello, Lorenzo Paulatto, Carlo Sbraccia, Sandro Scandolo, Gabriele Sclauzero, Ari P Seitsonen, Alexander Smogunov, Paolo Umari, and Renata M Wentzcovitch. QUANTUM ESPRESSO: a modular and open-source software project for quantum simulations of materials. *Journal of Physics: Condensed Matter*, 21(39):395502, sep 2009.

[56] D. A. Golter and C. W. Lai. Optical switching of defect charge states in 4H-SiC. *Scientific Reports*, 7(1):13406, dec 2017.

[57] Hernan Grecco, Alexandre Bourassa, Kevin C. Miao, Peter J. Mintun, Berk Diler, and Alexander L. Crook. https://github.com/awsch/lantz.

[58] M. S. Grinolds, M. Warner, K. De Greve, Y. Dovzhenko, L. Thiel, R. L. Walsworth, S. Hong, P. Maletinsky, and A. Yacoby. Subnanometre resolution in three-dimensional magnetic resonance imaging of individual dark spins. *Nature Nanotechnology*, 9(4):279–284, 2014.

[59] R. Guichard, S. J. Balian, G. Wolfowicz, P. A. Mortemousque, and T. S. Monteiro. Decoherence of nuclear spins in the frozen core of an electron spin. *Physical Review B - Condensed Matter and Materials Physics*, 91(21):214303, jun 2015.

[60] M. V. Gurudev Dutt, L. Childress, L. Jiang, E. Togan, J. Maze, F. Jelezko, A. S. Zibrov, P. R. Hemmer, and M. D. Lukin. Quantum register based on individual electronic and nuclear spin qubits in diamond. *Science*, 316(5829):1312–1316, jun 2007.

[61] J. Stephen Hartman, Bob Berno, Paul Hazendonk, Christopher W. Kirby, Eric Ye, Josef Zwanziger, and Alex D. Bain. Nmr studies of nitrogen doping in the 4h polytype of silicon carbide: Site assignments and spinlattice relaxation. *The Journal of Physical Chemistry C*, 113(33):15024–15036, 2009.

[62] B. Hensen, H. Bernien, A. E. Dreaú, A. Reiserer, N. Kalb, M. S. Blok, J. Ruitenberg, R. F.L. Vermeulen, R. N. Schouten, C. Abellán, W. Amaya, V. Pruneri, M. W. Mitchell, M. Markham, D. J. Twitchen, D. Elkouss, S. Wehner, T. H. Taminiau, and R. Hanson. Loophole-free Bell inequality violation using electron spins separated by 1.3 kilometres. *Nature*, 526(7575):682–686, oct 2015.

[63] E. D. Herbschleb, H. Kato, Y. Maruyama, T. Danjo, T. Makino, S. Yamasaki, I. Ohki, K. Hayashi, H. Morishita, M. Fujiwara, and N. Mizuochi. Ultra-long coherence times amongst room-temperature solid-state spins. *Nature Communications*, 10(1):1–6, dec 2019.

[64] F. J. Heremans, G. D. Fuchs, C. F. Wang, R. Hanson, and D. D. Awschalom. Generation and transport of photoexcited electrons in single-crystal diamond. *Applied Physics Letters*, 94(15), 2009.

[65] Harald Homulle. Cryogenic electronics for the read-out of quantum processors. 2019.

[66] S. O. Hruszkewycz, S. Maddali, C. P. Anderson, W. Cha, K. C. Miao, M. J. Highland, A. Ulvestad, D. D. Awschalom, and F. J. Heremans. Strain annealing of SiC nanoparticles revealed through Bragg coherent diffraction imaging for quantum technologies. *Physical Review Materials*, 2(8), 2018.

[67] Toyofumi Ishikawa, Kai-Mei C Fu, Charles Santori, Victor M Acosta, Raymond G Beausoleil, Hideyuki Watanabe, Shinichi Shikata, and Kohei M Itoh. Optical and Spin Coherence Properties of Nitrogen-Vacancy Centers Placed in a 100 nm Thick Isotopically Purified Diamond Layer. *Nano Lett*, 12:34, 2012.

[68] Kay D. Jahnke, Alp Sipahigil, Jan M. Binder, Marcus W. Doherty, Mathias Metsch, Lachlan J. Rogers, Neil B. Manson, Mikhail D. Lukin, and Fedor Jelezko. Electron-phonon processes of the silicon-vacancy centre in diamond. *New Journal of Physics*, 17, 2015.

[69] P. Jamonneau, M. Lesik, J. P. Tetienne, I. Alvizu, L. Mayer, A. Dréau, S. Kosen, J. F. Roch, S. Pezzagna, J. Meijer, T. Teraji, Y. Kubo, P. Bertet, J. R. Maze, and V. Jacques. Competition between electric field and magnetic field noise in the decoherence of a single spin in diamond. *Physical Review B*, 93(2):024305, jan 2016.

[70] Erika Janitz, Maximilian Ruf, Mark Dimock, Alexandre Bourassa, Jack Sankey, and Lilian Childress. Fabry-Perot microcavity for diamond-based photonics. *Physical Review A - Atomic, Molecular, and Optical Physics*, 92(4):043844, oct 2015.

[71] Harishankar Jayakumar, Jacob Henshaw, Siddharth Dhomkar, Daniela Pagliero, Abdelghani Laraoui, Neil B. Manson, Remus Albu, Marcus W. Doherty, and Carlos A. Meriles. Optical patterning of trapped charge in nitrogen-doped diamond. *Nature Communications*, 7(1):1–8, aug 2016.

[72] J. R. Johansson, P. D. Nation, and Franco Nori. QuTiP 2: A Python framework for the dynamics of open quantum systems. *Computer Physics Communications*, 184(4):1234–1240, apr 2013.

[73] Klaus D. Jöns, Katarina Stensson, Marcus Reindl, Marcin Swillo, Yongheng Huo, Val Zwiller, Armando Rastelli, Rinaldo Trotta, and Gunnar Björk. Two-photon interference from two blinking quantum emitters. *Physical Review B*, 96(7), 2017.

[74] Nicholas R. Jungwirth, Brian Calderon, Yanxin Ji, Michael G. Spencer, Michael E. Flatté, and Gregory D. Fuchs. Temperature Dependence of Wavelength Selectable Zero-Phonon Emission from Single Defects in Hexagonal Boron Nitride. *Nano Letters*, 16(10):6052–6057, oct 2016.

[75] N. Kalb, P. C. Humphreys, J. J. Slim, and R. Hanson. Dephasing mechanisms of diamond-based nuclear-spin memories for quantum networks. *Physical Review A*, 97(6):062330, jun 2018.

[76] N. Kalb, A. A. Reiserer, P. C. Humphreys, J. J. W. Bakermans, S. J. Kamerling, N. H. Nickerson, S. C. Benjamin, D. J. Twitchen, M. Markham, and R. Hanson. Entanglement distillation between solid-state quantum network nodes. *Science*, 356(6341):928–932, 2017.

[77] Benjamin Kambs and Christoph Becher. Limitations on the indistinguishability of photons from remote solid state sources. *New Journal of Physics*, 20(11):115003, nov 2018.

[78] Hiromitsu Kato, Marco Wolfer, Christoph Schreyvogel, Michael Kunzer, Wolfgang Müller-Sebert, Harald Obloh, Satoshi Yamasaki, and Christoph Nebel. Tunable light emission from nitrogen-vacancy centers in single crystal diamond PIN diodes. *Applied Physics Letters*, 102(15), 2013.

[79] Vinod Kumar Khanna. Temperature effects on semiconductors. In *Extreme-Temperature and Harsh-Environment Electronics*, 2053-2563, pages 3–1 to 3–33. IOP Publishing, 2017.

[80] M. Kim, H. J. Mamin, M. H. Sherwood, K. Ohno, D. D. Awschalom, and D. Rugar. Decoherence of Near-Surface Nitrogen-Vacancy Centers Due to Electric Field Noise. *Physical Review Letters*, 115(8), 2015.

[81] Tsunenobu Kimoto and James A. Cooper. Appendix C: Major Physical Properties of Common SiC Polytypes. In *Fundamentals of Silicon Carbide Technology*, chapter Appendix C, pages 521–524. John Wiley & Sons Singapore Pte. Ltd, Singapore, sep 2014.

[82] P. V. Klimov, A. L. Falk, B. B. Buckley, and D. D. Awschalom. Electrically driven spin resonance in silicon carbide color centers. *Physical Review Letters*, 112(8), 2014.

[83] Paul V. Klimov, Abram L. Falk, David J. Christle, Viatcheslav V. Dobrovitski, and David D. Awschalom. Quantum entanglement at ambient conditions in a macroscopic solid-state spin ensemble. *Science Advances*, 1(10), nov 2015.

[84] Paul Victor Klimov. *Quantum information processing with electronic and nuclear spins in semiconductors.* PhD thesis, The University of Chicago, January 2016.

[85] E. Knill. Quantum computing with realistically noisy devices. *Nature*, 434(7029):39–44, mar 2005.

[86] William F Koehl, Bob B Buckley, F Joseph Heremans, Greg Calusine, and David D Awschalom. Room temperature coherent control of defect spin qubits in silicon carbide. *Nature*, 479(7371):84–7, nov 2011.

[87] William F. Koehl, Berk Diler, Samuel J. Whiteley, Alexandre Bourassa, N. T. Son, Erik Janzén, and David D. Awschalom. Resonant optical spectroscopy and coherent control of Cr4+ spin ensembles in SiC and GaN. *Physical Review B*, 95(3):035207, jan 2017.

[88] A. Krtschil, H. Witte, M. Lisker, J. Christen, A. Krost, U. Birkle, S. Einfeldt, D. Hommel, F. Scholz, J. Off, and M. Stutzmann. Photoelectric properties of the 0.44 eV deep level-to-band transition in gallium nitride investigated by optical admittance spectroscopy. *Applied Physics Letters*, 77(4):546–548, jul 2000.

[89] Andreas V. Kuhlmann, Julien Houel, Arne Ludwig, Lukas Greuter, Dirk Reuter, Andreas D. Wieck, Martino Poggio, and Richard J. Warburton. Charge noise and spin noise in a semiconductor quantum device. *Nature Physics*, 9(9):570–575, 2013.

[90] A. A. Lebedev. *Radiation Effects in SiC*, volume 6. Materials research forum, 2017.

[91] M. E. (Mikhail Efimovich) Levinshtein, Sergey L. Rumyantsev, and Michael. Shur. *Properties of advanced semiconductor materials : GaN, AlN, InN, BN, SiC, SiGe.* Wiley, 2001.

[92] Matthias C. Löbl, Immo Söllner, Alisa Javadi, Tommaso Pregnolato, Rüdiger Schott, Leonardo Midolo, Andreas V. Kuhlmann, Søren Stobbe, Andreas D. Wieck, Peter Lodahl, Arne Ludwig, and Richard J. Warburton. Narrow optical linewidths and spin pumping on charge-tunable close-to-surface self-assembled quantum dots in an ultrathin diode. *Physical Review B*, 96(16), 2017.

[93] Josef Lutz, Heinrich Schlangenotto, Uwe Scheuermann, and Rik De Doncker. *Semiconductor power devices: Physics, characteristics, reliability.* Springer Berlin Heidelberg, 2011.

[94] B. MacHielse, S. Bogdanovic, S. Meesala, S. Gauthier, M. J. Burek, G. Joe, M. Chalupnik, Y. I. Sohn, J. Holzgrafe, R. E. Evans, C. Chia, H. Atikian, M. K. Bhaskar, D. D. Sukachev, L. Shao, S. Maity, M. D. Lukin, and M. Lončar. Quantum Interference of Electromechanically Stabilized Emitters in Nanophotonic Devices. *Physical Review X*, 9(3):031022, aug 2019.

[95] Björn Magnusson, Nguyen Tien Son, András Csóré, Andreas Gällström, Takeshi Ohshima, Adam Gali, and Ivan G. Ivanov. Excitation properties of the divacancy in 4H -SiC. *Physical Review B*, 98(19), 2018.

[96] P. C. Maurer, G. Kucsko, C. Latta, L. Jiang, N. Y. Yao, S. D. Bennett, F. Pastawski, D. Hunger, N. Chisholm, M. Markham, D. J. Twitchen, J. I. Cirac, and M. D. Lukin. Room-Temperature Quantum Bit Memory Exceeding One Second. *Science*, 336(6086):1283–1286, jun 2012.

[97] J R Maze, A Gali, E Togan, Y Chu, A Trifonov, E Kaxiras, and M D Lukin. Related content New Journal of Physics Properties of nitrogen-vacancy centers in diamond: the group theoretic approach. *New Journal of Physics*, 13(24pp):25025, 2011.

[98] Kevin C. Miao, Joseph P. Blanton, Christopher P. Anderson, Alexandre Bourassa, Alexander L. Crook, Gary Wolfowicz, Hiroshi Abe, Takeshi Ohshima, and David D. Awschalom. Universal coherence protection in a solid-state spin qubit. *Science*, 2020.

[99] Kevin C. Miao, Alexandre Bourassa, Christopher P. Anderson, Samuel J. Whiteley, Alexander L. Crook, Sam L. Bayliss, Gary Wolfowicz, Gergő Thiering, Péter Udvarhelyi, Viktor Ivády, Hiroshi Abe, Takeshi Ohshima, Ádám Gali, and David D. Awschalom. Electrically driven optical interferometry with spins in silicon carbide. *Science Advances*, 5(11), 2019.

[100] Julia Michl, Jakob Steiner, Andrej Denisenko, André Bülau, André Zimmermann, Kazuo Nakamura, Hitoshi Sumiya, Shinobu Onoda, Philipp Neumann, Junichi Isoya, and Jörg Wrachtrup. Robust and Accurate Electric Field Sensing with Solid State Spin Ensembles. *Nano Letters*, 19(8):4904–4910, 2019.

[101] C. Müller, X. Kong, J. M. Cai, K. MelentijeviÄ, A. Stacey, M. Markham, D. Twitchen, J. Isoya, S. Pezzagna, J. Meijer, J. F. Du, M. B. Plenio, B. Naydenov, L. P. McGuinness, and F. Jelezko. Nuclear magnetic resonance spectroscopy with single spin sensitivity. *Nature Communications*, 5(1):1–6, aug 2014.

[102] T. Murai, T. Makino, H. Kato, M. Shimizu, T. Murooka, E. D. Herbschleb, Y. Doi, H. Morishita, M. Fujiwara, M. Hatano, S. Yamasaki, and N. Mizuochi. Engineering of Fermi level by nin diamond junction for control of charge states of NV centers. *Applied Physics Letters*, 112(11), 2018.

[103] Roland Nagy, Matthias Niethammer, Matthias Widmann, Yu-Chen Chen, Péter Udvarhelyi, Cristian Bonato, Jawad Ul Hassan, Robin Karhu, Ivan G. Ivanov, Nguyen Tien Son, Jeronimo R. Maze, Takeshi Ohshima, Öney O. Soykal, Ádám Gali, Sang-Yun Lee, Florian Kaiser, and Jörg Wrachtrup. High-fidelity spin and optical control of single silicon-vacancy centres in silicon carbide. *Nature Communications*, 10(1):1954, 2019.

[104] Gerold Neudeck. *The PN junction diode.* Addison-Wesley, Reading Mass., 1983.

[105] Peter Niedbalski, Qing Wang, Christopher Parish, Fatemeh Khashami, Andhika Kiswandhi, and Lloyd Lumata. Magnetic-Field-Dependent Lifetimes of Hyperpolarized 13C Spins at Cryogenic Temperature. *Journal of Physical Chemistry B*, 122(6):1898–1904, feb 2018.

[106] Matthias Niethammer, Matthias Widmann, Torsten Rendler, Naoya Morioka, Yu-Chen Chen, Rainer Stöhr, Jawad Ul Hassan, Shinobu Onoda, Takeshi Ohshima, Sang-Yun Lee, Amlan Mukherjee, Junichi Isoya, Nguyen Tien Son, and Jörg Wrachtrup. Coherent electrical readout of defect spins in 4H-SiC by photo-ionization at ambient conditions. 2019.

[107] Kenichi Ohno, F. Joseph Heremans, Lee C. Bassett, Bryan A. Myers, David M. Toyli, Ania C. Bleszynski Jayich, Christopher J. Palmstrøm, and David D. Awschalom. Engineering shallow spins in diamond with nitrogen delta-doping. *Applied Physics Letters*, 101(8), 2012.

[108] Alexandra Oliveros, Anthony Guiseppi-Elie, and Stephen E. Saddow. Silicon carbide: A versatile material for biosensor applications. *Biomedical Microdevices*, 15(2):353–368, apr 2013.

[109] Evan S. Petersen, A. M. Tyryshkin, J. J.L. Morton, E. Abe, S. Tojo, K. M. Itoh, M. L.W. Thewalt, and S. A. Lyon. Nuclear spin decoherence of neutral P 31 donors in silicon: Effect of environmental Si 29 nuclei. *Physical Review B*, 93(16):161202, apr 2016.

[110] W. Pfaff, B. J. Hensen, H. Bernien, S. B. Van Dam, M. S. Blok, T. H. Taminiau, M. J. Tiggelman, R. N. Schouten, M. Markham, D. J. Twitchen, and R. Hanson. Unconditional quantum teleportation between distant solid-state quantum bits. *Science*, 345(6196):532–535, 2014.

[111] Wolfgang Pfaff, Tim H. Taminiau, Lucio Robledo, Hannes Bernien, Matthew Markham, Daniel J. Twitchen, and Ronald Hanson. Demonstration of entanglement by measurement of solid-state qubits. *Nature Physics*, 9(1):29–33, 2013.

[112] Matthias Pfender, Nabeel Aslam, Patrick Simon, Denis Antonov, Gergo Thiering, Sina Burk, Felipe Fávaro De Oliveira, Andrej Denisenko, Helmut Fedder, Jan Meijer, Jose A. Garrido, Adam Gali, Tokuyuki Teraji, Junichi Isoya, Marcus William Doherty, Audrius Alkauskas, Alejandro Gallo, Andreas Grüneis, Philipp Neumann, and Jörg Wrachtrup. Protecting a Diamond Quantum Memory by Charge State Control. *Nano Letters*, 17(10):5931–5937, 2017.

[113] Andreas Reiserer, Norbert Kalb, Machiel S. Blok, Koen J.M. van Bemmelen, Tim H. Taminiau, Ronald Hanson, Daniel J. Twitchen, and Matthew Markham. Robust quantum-network memory using decoherence-protected subspaces of nuclear spins. *Physical Review X*, 6(2):021040, jun 2016.

[114] Lucio Robledo, Lilian Childress, Hannes Bernien, Bas Hensen, Paul F.A. Alkemade, and Ronald Hanson. High-fidelity projective read-out of a solid-state spin quantum register. *Nature*, 477(7366):574–578, 2011.

[115] Xing Rong, Jianpei Geng, Fazhan Shi, Ying Liu, Kebiao Xu, Wenchao Ma, Fei Kong, Zhen Jiang, Yang Wu, and Jiangfeng Du. Experimental fault-tolerant universal quantum gates with solid-state spins under ambient conditions. *Nature Communications*, 6(1):1–7, nov 2015.

[116] Sheldon M. Ross. *Introduction to probability and statistics for engineers and scientists.* Elsevier Academic Press, 5th edition edition, 2014.

[117] Maximilian Ruf, Matthew J. Weaver, Suzanne B. van Dam, and Ronald Hanson. Resonant Excitation and Purcell Enhancement of Coherent Nitrogen-Vacancy Centers Coupled to a Fabry-Perot Micro-Cavity. sep 2020.

[118] Kevin G. Schädler, Carlotta Ciancico, Sofia Pazzagli, Pietro Lombardi, Adrian Bachtold, Costanza Toninelli, Antoine Reserbat-Plantey, and Frank H.L. Koppens. Electrical Control of Lifetime-Limited Quantum Emitters Using 2D Materials. *Nano Letters*, 19(6):3789–3795, 2019.

[119] C. Schreyvogel, V. Polyakov, R. Wunderlich, J. Meijer, and C. E. Nebel. Active charge state control of single NV centres in diamond by in-plane Al-Schottky junctions. *Scientific reports*, 5(1):12160, dec 2015.

[120] Hosung Seo, Abram L. Falk, Paul V. Klimov, Kevin C. Miao, Giulia Galli, and David D. Awschalom. Quantum decoherence dynamics of divacancy spins in silicon carbide. *Nature Communications*, 7(1):1–9, sep 2016.

[121] C E Shannon. A mathematical theory of communication. *The Bell System Technical Journal*, 27(3):379–423, jul 1948.

[122] Henry Maurice Sheffer. A Set of Five Independent Postulates for Boolean Algebras, with Application to Logical Constants. *Transactions of the American Mathematical Society*, 14(4):481–488, 1913.

[123] B. J. Shields, Q. P. Unterreithmeier, N. P. De Leon, H. Park, and M. D. Lukin. Efficient Readout of a Single Spin State in Diamond via Spin-to-Charge Conversion. *Physical Review Letters*, 114(13), 2015.

[124] Maki Shimizu, Toshiharu Makino, Takayuki Iwasaki, Kosuke Tahara, Hiromitsu Kato, Norikazu Mizuochi, Satoshi Yamasaki, and Mutsuko Hatano. Charge-state control of ensemble of nitrogen vacancy centers by n-i-n diamond junctions. *Applied Physics Express*, 11(3), 2018.

[125] Petr Siyushev, Milos Nesladek, Emilie Bourgeois, Michal Gulka, Jaroslav Hruby, Takashi Yamamoto, Michael Trupke, Tokuyuki Teraji, Junichi Isoya, and Fedor Jelezko. Photoelectrical imaging and coherent spin-state readout of single nitrogen-vacancy centers in diamond. *Science*, 363(6428):728–731, 2019.

[126] N. T. Son, P. Carlsson, J Ul Hassan, E Janzén, T. Umeda, J. Isoya, A. Gali, M. Bockstedte, N. Morishita, T. Ohshima, H. Itoh, E Janze, T. Umeda, J. Isoya, A. Gali, M. Bockstedte, N. Morishita, T. Ohshima, H. Itoh, J. Ul Hassan, E. Janz??n, T. Umeda, J. Isoya, A. Gali, M. Bockstedte, N. Morishita, T. Ohshima, and H. Itoh. Divacancy in 4H-SiC. *Physical Review Letters*, 96(November):8–11, 2006.

[127] Orazio Svelto. *Principles of lasers*. Springer US, 2010.

[128] T. H. Taminiau, J. Cramer, T. Van Der Sar, V. V. Dobrovitski, and R. Hanson. Universal control and error correction in multi-qubit spin registers in diamond. *Nature Nanotechnology*, 9(3):171–176, feb 2014.

[129] T. H. Taminiau, J. J.T. Wagenaar, T. Van Der Sar, F. Jelezko, V. V. Dobrovitski, and R. Hanson. Detection and control of individual nuclear spins using a weakly coupled electron spin. *Physical Review Letters*, 109(13):137602, sep 2012.

[130] M. Tanenbaum, L. B. Valdes, E. Buehler, and N. B. Hannay. Silicon n-p-n grown junction transistors. *Journal of Applied Physics*, 26(6):686–692, jun 1955.

[131] Cornelis J. Terblanche, Eduard C. Reynhardt, and Jan A. Van Wyk. 13C spin-lattice relaxation in natural diamond: Zeeman relaxation at 4.7 T and 300 K due to fixed paramagnetic nitrogen defects. *Solid State Nuclear Magnetic Resonance*, 20(1-2):1–22, aug 2001.

[132] Henri Thyrrestrup, Gabija Kirs, Hanna Le Jeannic, Tommaso Pregnolato, Liang Zhai, Laust Raahauge, Leonardo Midolo, Nir Rotenberg, Alisa Javadi, Diger Schott, Andreas D. Wieck, Arne Ludwig, Matthias C Lo, Immo So, Richard J. Warburton, Peter Lodahl, Gabija Kiršansk, Hanna Le Jeannic, Tommaso Pregnolato, Liang Zhai, Laust Raahauge, Leonardo Midolo, Nir Rotenberg, Alisa Javadi, Rüdiger Schott, Andreas D. Wieck, Arne Ludwig, Matthias C. Löbl, Immo Söllner, Richard J. Warburton, and Peter Lodahl. Quantum Optics with Near-Lifetime-Limited Quantum-Dot Transitions in a Nanophotonic Waveguide. *Nano Lett*, 18(3):49, mar 2018.

[133] David M. Toyli, Christoph D. Weis, Gregory D. Fuchs, Thomas Schenkel, and David D. Awschalom. Chip-scale nanofabrication of single spins and spin arrays in diamond. *Nano Letters*, 10(8):3168–3172, 2010.

[134] A M Turing. On Computable Numbers, with an Application to the Entscheidungsproblem. *Proceedings of the London Mathematical Society*, s2-42(1):230–265, 1937.

[135] T. K. Unden, D. Louzon, M. Zwolak, W. H. Zurek, and F. Jelezko. Revealing the Emergence of Classicality Using Nitrogen-Vacancy Centers. *Physical Review Letters*, 123(14):140402, oct 2019.

[136] A. N. Vamivakas, Y. Zhao, S. Fält, A. Badolato, J. M. Taylor, and M. Atatüre. Nanoscale Optical Electrometer. *Physical Review Letters*, 107(16):166802, oct 2011.

[137] S. B. Van Dam, M. Walsh, M. J. Degen, E. Bersin, S. L. Mouradian, A. Galiullin, M. Ruf, M. Ijspeert, T. H. Taminiau, R. Hanson, and D. R. Englund. Optical coherence of diamond nitrogen-vacancy centers formed by ion implantation and annealing. *Physical Review B*, 99(16), 2019.

[138] Bart Van Zeghbroeck. Principles of Semiconductor Devices. `https://ecee.colorado.edu/{~}bart/book/book/title.htm`, 2011.

[139] M. Veldhorst, J. C.C. Hwang, C. H. Yang, A. W. Leenstra, B. De Ronde, J. P. Dehollain, J. T. Muhonen, F. E. Hudson, K. M. Itoh, A. Morello, and A. S. Dzurak. An addressable quantum dot qubit with fault-tolerant control-fidelity. *Nature Nanotechnology*, 9(12):981–985, jan 2014.

[140] G. Waldherr, Y. Wang, S. Zaiser, M. Jamali, T. Schulte-Herbrüggen, H. Abe, T. Ohshima, J. Isoya, J. F. Du, P. Neumann, and J. Wrachtrup. Quantum error correction in a solid-state hybrid spin register. *Nature*, 506(7487):204–207, 2014.

[141] Sören Wengerowsky, Siddarth Koduru Joshi, Fabian Steinlechner, Hannes Hübel, and Rupert Ursin. An entanglement-based wavelength-multiplexed quantum communication network. *Nature*, 564(7735):225–228, dec 2018.

[142] Samuel J. Whiteley, Gary Wolfowicz, Christopher P. Anderson, Alexandre Bourassa, He Ma, Meng Ye, Gerwin Koolstra, Kevin J. Satzinger, Martin V. Holt, F. Joseph Heremans, Andrew N. Cleland, David I. Schuster, Giulia Galli, and David D. Awschalom. Spinphonon interactions in silicon carbide addressed by Gaussian acoustics. *Nature Physics*, 15(5):490–495, 2019.

[143] Matthias Widmann, Sang-Yun Lee, Torsten Rendler, Nguyen Tien Son, Helmut Fedder, Seoyoung Paik, Li-Ping Yang, Nan Zhao, Sen Yang, Ian Booker, Andrej Denisenko, Mohammad Jamali, S. Ali Momenzadeh, Ilja Gerhardt, Takeshi Ohshima, Adam Gali, Erik Janzén, and Jörg Wrachtrup. Coherent control of single spins in silicon carbide at room temperature. *Nature Materials*, 14(2):164–168, feb 2015.

[144] Matthias Widmann, Matthias Niethammer, Dmitry Yu Fedyanin, Igor A. Khramtsov, Torsten Rendler, Ian D. Booker, Jawad Ul Hassan, Naoya Morioka, Yu Chen Chen, Ivan G. Ivanov, Nguyen Tien Son, Takeshi Ohshima, Michel Bockstedte, Adam Gali, Cristian Bonato, Sang Yun Lee, and Jörg Wrachtrup. Electrical Charge State Manipulation of Single Silicon Vacancies in a Silicon Carbide Quantum Optoelectronic Device. *Nano Letters*, 19(10):7173–7180, 2019.

[145] Matthias Widmann, Matthias Niethammer, Takahiro Makino, Torsten Rendler, Stefan Lasse, Takeshi Ohshima, Jawad Ul Hassan, Nguyen Tien Son, Sang Yun Lee, and Jörg Wrachtrup. Bright single photon sources in lateral silicon carbide light emitting diodes. *Applied Physics Letters*, 112(23), 2018.

[146] Wayne M. Witzel, Malcolm S. Carroll, Aukasz Cywiński, and S. Das Sarma. Quantum decoherence of the central spin in a sparse system of dipolar coupled spins. *Physical Review B - Condensed Matter and Materials Physics*, 86(3):035452, jul 2012.

[147] G. Wolfowicz, S. J. Whiteley, and D. D. Awschalom. Electrometry by optical charge conversion of deep defects in 4H-SiC. *Proceedings of the National Academy of Sciences of the United States of America*, 115(31):7879–7883, 2018.

[148] Gary Wolfowicz, Christopher P. Anderson, Berk Diler, Oleg G. Poluektov, F. Joseph Heremans, and David D. Awschalom. Vanadium spin qubits as telecom quantum emitters in silicon carbide. *Science Advances*, 6(18):eaaz1192, may 2020.

[149] Gary Wolfowicz, Christopher P. Anderson, Andrew L. Yeats, Samuel J. Whiteley, Jens Niklas, Oleg G. Poluektov, F. Joseph Heremans, and David D. Awschalom. Optical charge state control of spin defects in 4H-SiC. *Nature Communications*, 8(1), 2017.

[150] Janik Wolters, Nikola Sadzak, Andreas W. Schell, Tim Schröder, and Oliver Benson. Measurement of the ultrafast spectral diffusion of the optical transition of nitrogen vacancy centers in nano-size diamond using correlation interferometry. *Physical Review Letters*, 110(2), 2013.

[151] W. K. Wootters and W. H. Zurek. A single quantum cannot be cloned. *Nature*, 299(5886):802–803, 1982.

[152] C. H. Yang, K. W. Chan, R. Harper, W. Huang, T. Evans, J. C.C. Hwang, B. Hensen, A. Laucht, T. Tanttu, F. E. Hudson, S. T. Flammia, K. M. Itoh, A. Morello, S. D. Bartlett, and A. S. Dzurak. Silicon qubit fidelities approaching incoherent noise limits via pulse engineering. *Nature Electronics*, 2(4):151–158, apr 2019.

[153] Wen Yang and Ren Bao Liu. Quantum many-body theory of qubit decoherence in a finite-size spin bath. *Physical Review B - Condensed Matter and Materials Physics*, 78(8):085315, aug 2008.

[154] Jun Yoneda, Kenta Takeda, Tomohiro Otsuka, Takashi Nakajima, Matthieu R. Delbecq, Giles Allison, Takumu Honda, Tetsuo Kodera, Shunri Oda, Yusuke Hoshi, Noritaka Usami, Kohei M. Itoh, and Seigo Tarucha. A quantum-dot spin qubit with coherence limited by charge noise and fidelity higher than 99.9%. *Nature Nanotechnology*, 13(2):102–106, feb 2018.

[155] Sebastian Zaiser, Torsten Rendler, Ingmar Jakobi, Thomas Wolf, Sang Yun Lee, Samuel Wagner, Ville Bergholm, Thomas Schulte-Herbrüggen, Philipp Neumann, and Jörg Wrachtrup. Enhancing quantum sensing sensitivity by a quantum memory. *Nature Communications*, 7(1):1–11, aug 2016.

[156] J. Zopes, K. S. Cujia, K. Sasaki, J. M. Boss, K. M. Itoh, and C. L. Degen. Three-dimensional localization spectroscopy of individual nuclear spins with sub-Angstrom resolution. *Nature Communications*, 9(1):1–8, dec 2018.